Corrosion and Erosion-Corrosion Behaviour of Lean Duplex Stainless Steels in Marine and Oilfield Environments

By

Sunday Aribo

Submitted in accordance with the requirements for degree of

Doctor of Philosophy

The University of Leeds

School of Mechanical Engineering

June, 2014

The candidate confirms that the work submitted is his own except where work which has formed part of jointly-authored publications has been included. The contribution of the candidate and the authors to this work has been indicated as appropriate. The candidate confirms that appropriate credits have been given within the thesis where reference has been made to the work of others.

In all papers, the primary author completed the experimental measurements and drafting of the papers. All authors listed completed proofreading prior to the submission of the papers

Papers contributing to this thesis

Sunday Aribo, Anne Neville, Xinming Hu (2012), Pitting Behaviour of Lean Duplex Stainless Steels in Marine and Oilfield Environments, SPE Oilfield Corrosion Proceedings, May 27-29, 2012, Aberdeen, Scotland, SPE 154811.

Featured in chapters 4, 5, and 9

Sunday Aribo, Michael Bryant**,** Xinming Hu, Anne Neville, (2013), Erosion-Corrosion Behaviour of Lean Duplex Stainless Steel (UNS S32101) in a CO_2-Saturated Oilfield Environment, NACE International Conference, Orlando Florida, USA, March 17-21, 2013, Paper No. 2382

Featured in chapters 4, 6, 7, and 9

Sunday Aribo, Richard Barker**,** Xinming Hu, Anne Neville, (2013), Erosion-Corrosion Behaviour of Lean Duplex Stainless Steels in 3.5% NaCl Solution, ***Wear*** 302 (2013) 1602–1608

Featured in chapters 4, 6, 7 and 9 of the thesis

Acknowledgements

I will like to express my profound gratitude to God Almighty for helping me throughout the period of my studies. I am deeply grateful to Prof. Anne Neville for her unequalled professional guidance, invaluable encouragement and motivation. It is my pleasure working under her supervision. My appreciation also goes to Dr. Xinming Hu and Dr. Chun Wang for their words of encouragement and professional advice during the early stages of this research.

My sincere gratitude to my friends and colleagues at the Institute of Functional Surfaces, School of Mechanical Engineering. I also appreciate all the technical and support staff of Mechanical Engineering for their support during the course of this programme. Special thanks to Late Graham Jakeman (you are greatly missed), Ron Cellier, Brian, Mark and other technicians in the laboratory. My sincere thanks also to Jackie Kidd (Mrs) and Fiona Slade (Mrs).

Special appreciation to my wife, Folake and our three wonderful kids (Oluwajomiloju, Oluwademilade and Oluwatobiloba-Joshua)-the PhD was fun having you guys at home after each hectic day in the lab. Thanks to my parents Noah Omolegeye Aribo and Comfort Omotayo Aribo for giving me a good start in life. Though you are no longer with me, I know you would be proud!

My special thanks to the ***Petroleum Technology Development Fund (PTDF)*** of the Federal Republic of Nigeria for the scholarship awarded me to pursue this PhD programme. I also appreciate the authority of ***Federal University of Technology, Akure, Nigeria*** for granting me a study leave throughout the period of this programme. Thanks also to Outokumpu Stainless Research Foundation Avesta, Sweden for giving us the alloys used for this research.

I dedicate this thesis to ***Charles Ilemobayo Aribo*** for believing and supporting my dreams- thank you good brother!

Abstract

Lean duplex stainless steels are becoming attractive for applications in oilfield and marine environments due to their economic advantages, very good mechanical properties and relatively good corrosion resistance. One such application is in the production of the carcass of flexible pipes. However, materials selection for such oilfield applications becomes more complex as a result of the interactions between corrosion and erosion. Much effort has been directed towards the study of erosion-corrosion behaviour of carbon steels and other passive alloys. However, the subject of erosion-corrosion of lean duplex stainless steels is still rarely reported. Moreover, data available in the literature on the localized corrosion resistance of the lean duplex stainless steels are limited to alkaline environments.

Efforts have been made in this thesis to add to the existing data and to the understanding of the subject of localized corrosion and erosion-corrosion resistance of lean duplex stainless steels UNS S32101, UNS S32304 and UNS S82441 in oilfield environments. The lean duplex alloy UNS S32101 has been studied in detail because of its combination of high strength and good corrosion resistance. This research also compared the corrosion and erosion-corrosion resistance of lean duplex stainless steels with standard austenitic stainless steels UNS S30403 and UNS S31603 as well as duplex stainless steel alloy UNS S32205. Aerated 3.5% NaCl and synthesized CO_2-saturated oilfield brines were considered as the corrosion media. Extreme erosion-corrosion conditions were simulated to design for severe environments often encountered in sand-containing oilfield pipeline systems.

Breakdown potentials, under static conditions, were found to be more positive in the aerated 3.5% NaCl than the CO_2-saturated oilfield brine solution. Also, lean duplex stainless steels and standard austenitic stainless steels exhibited similar resistance in both environments. X-ray Photoelectron Spectroscopy (XPS) analysis of the passive film indicated higher chloride incorporation in the CO_2-saturated oilfield brine. This, in addition to lower pH of the CO_2-saturated oilfield brine

appeared to be the reason why the breakdown potential was more negative in this environment.

Erosion-corrosion results showed that lean duplex stainless steels, UNS S32101 and UNS S32304, have higher resistance to pure-erosion damage than UNS S30403 and UNS S32205; better erosion-corrosion resistance than UNS S30403 austenitic stainless steel; and equivalent erosion-corrosion resistance to UNS S32205 standard duplex stainless steel. There was also a correlation between the erosion-corrosion resistance of the alloys and the sub-surface crystallography, microstructure and phase transformation. This, together with repassivation kinetics of the passive film, may be used to explain the erosion-corrosion behaviour of UNS S32101 and UNS S30403 in the oilfield slurry.

Contents

Figures

Tables

Chapter 1. Introduction

1.1 Introduction and Background of the Research

Material degradation in the form of corrosion and erosion-corrosion in offshore oil and gas field environments is of economic and safety importance to the operators. Damage of facilities by corrosion increases the operation expenditure and the potential costs run into millions of pounds/dollars each year. Recent studies (1) showed that corrosion costs in the United States rose above $1 trillion in 2012. This is said to account for almost 6.2% Gross Domestic Product (GDP) (1). Corrosion has also been reported to account for about 25% asset failures in the oil and gas sector (2). In Europe, research has shown that between 1980 and 2006, nearly 50% of hazards due to plant failure could be attributed to corrosion, erosion and fatigue (3).

Proper material selection is, therefore, important to control the huge economic losses caused by corrosion. Nonetheless, alongside satisfactory performance, cost considerations are another criteria used in selecting materials for pipeline applications in the oilfield environment (4-6). The choice of pipeline materials with the best combination of good properties and at the best cost is always a challenge to corrosion and materials engineers. It is noteworthy, however, that carbon steels remain the most selected alloys for pipeline applications because of cost considerations. Inhibitors are applied to prolong the life of such steels while relying on corrosion models to predict the corrosion rate. However, most models developed for such aggressive environments have their limitations. Sometimes the injection of

inhibitor could be difficult and the aggressiveness of the deep-water well environments has become too adverse for the carbon steel materials even with the best inhibitions (7-9).

Stainless steels have been selected for most oilfield applications where the aggressiveness of the field is too adverse for carbon steels. Duplex stainless steels are particularly selected because of their combination of high mechanical strength as well as their good corrosion resistance. However, the major limitation to the selection of these alloys has been their cost implications on the capital expenditure (CAPEX). The majority of such alloys have been found out to be 10 -15 times more expensive than carbon steels (9). However, the long term benefits from the selection of stainless steels include the lower corrosion rate, reduced inspection of pipelines, lower downtime period, lower risk of failure and the confidence that the operators display with the use of such alloys (9).

Duplex stainless steels are specifically designed for applications in aggressive oilfield and marine environments where both corrosion resistance and mechanical properties of 300 series austenitic stainless steels would perhaps be limited (10). The lean duplex stainless steels with much lower nickel and molybdenum contents have been developed as economic alternatives to the standard duplex and highly alloyed stainless steels (11-13). These lean duplex alloys have better mechanical properties than standard austenitic stainless steels UNS S30403 and UNS S31603 (14-18). They are less expensive and have corrosion resistance that is comparable to these alloys (14-18). The duplex phase in the lean duplex alloy is maintained by replacing part of the nickel content by manganese and nitrogen. The idea is to retain the duplex microstructure and retain reasonable quality of the steel while reducing the

production cost as much as possible (19). The austenite phase in such alloys has been maintained by adding more manganese and nitrogen.

Lean duplex stainless steels are becoming increasingly popular in the oilfield environments as a result of their attractive cost, good mechanical properties and relatively good corrosion resistance. One such application is in the production of carcasses of flexible pipes, Figure 1.1-1.2.

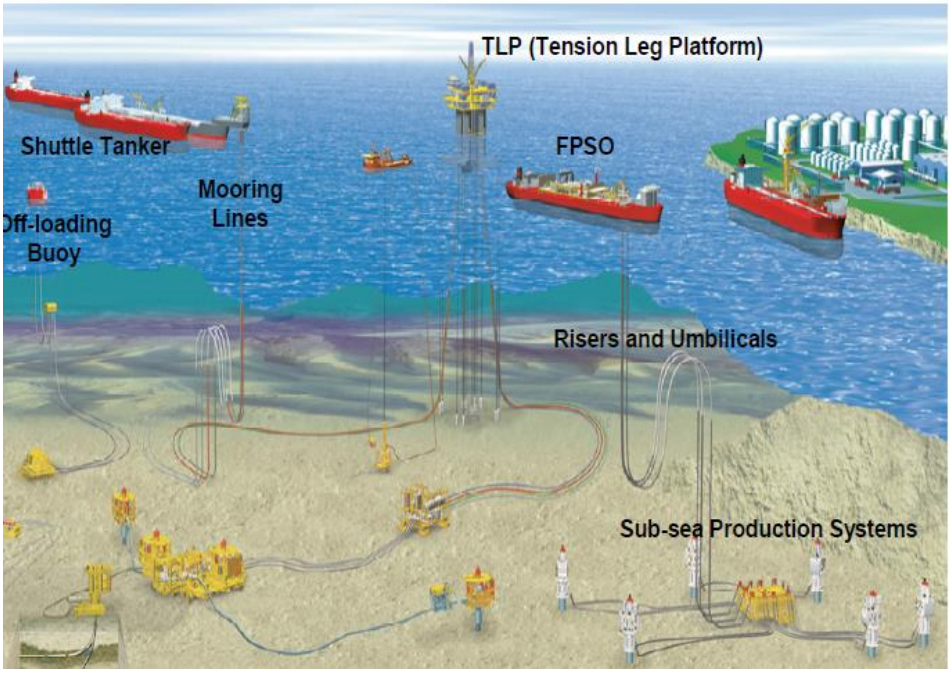

Figure 1.1: Offshore production system showing flexible pipes (risers and flowlines) (20)

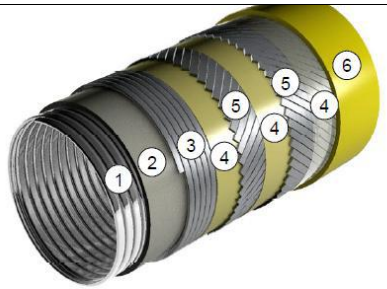

1. Stainless steel carcass (lean duplex now replacing UNS S32205,UNS S30403 and UNS S31603)
2. Polymer fluid barriers
3. Carbon steel pressure armour
4. Anti wear/friction tapes,
5. Carbon steel tensile armour
6. Polymer external sheath

Figure 1.2: Flexible pipe cross-section showing inner carcass layer (21)

Lean duplex stainless steels also find applications in the oilfield for the production of umbilical tubing, heat exchangers, separation units, cable trays and transportation vehicles (12, 13, 21, 22). Flexible pipes in deep water are exposed to hydrostatic pressure that might lead to failure of the carcass material by mechanical collapse (23, 24) Figure 1.3. For such flexible flow lines, the carcass material is always designed to withstand the aggressive produced fluids and sand mixtures as well as the external pressure exerted by seawater. Materials for such applications are, therefore, required to be corrosion resistant, erosion-corrosion resistant as well as having good fatigue and collapse resistance (23).

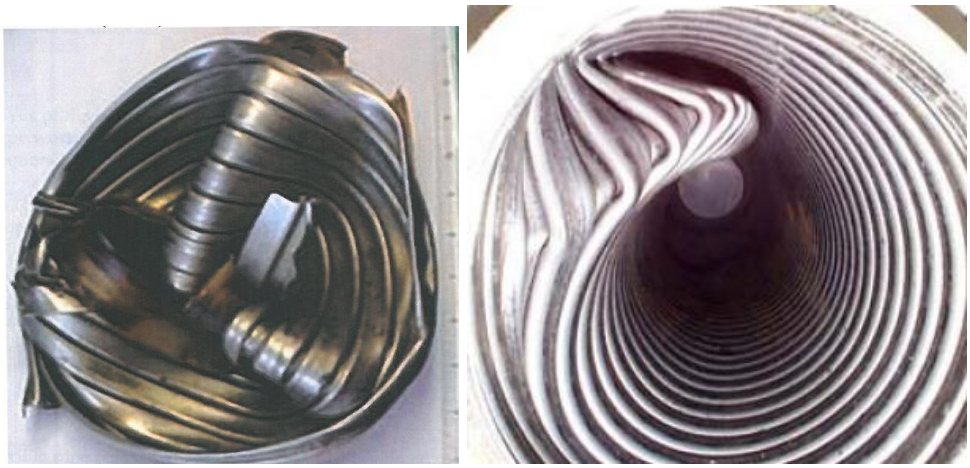

Figure 1.3: Failure of carcass of flexible pipes by mechanical collapse (23, 24)

Moreover, the failure modes of flexible pipes that lead to burst and leakage have been recently itemised to include sand erosion (24) (Figure 1.4), corrosion and mechanical collapse of the flexible pipe carcass amongst several other factors. One reason for considering the lean duplex stainless steels for such applications is their high yield strength which could help in resisting collapse from external hydrostatic pressure of the sea water.

Figure 1.4: Failure of carcass of flexible pipes by erosion (24)

Nevertheless, material degradation becomes more complex when wear and corrosion interact. The interactions between corrosion and erosion have been a subject of debate among scientists and engineers for several decades (25-31). The total material degradation when the two actions interact is often shown to be more than the individual processes acting separately. While much effort has been directed towards the study of corrosion behaviour of the lean duplex steels, oilfield environments have not yet been considered for evaluation. Also, there is still limited literature on the pitting behaviour of lean duplex stainless steels in CO_2-saturated oilfield environments. Moreover, the erosion-corrosion behaviour of these lean duplex alloys is still rarely reported. Furthermore, there is also limited literature on the properties of passive oxide films formed on the lean duplex stainless steels in aerated seawater and CO_2-saturated oil and gas environments. It is known that the

passive film stability is important to the pitting behaviour as well as the erosion-corrosion resistance of stainless steels (32-34). It is, therefore, necessary to study the repassivation kinetics of the damaged passive film of lean duplex stainless steels and compare these with standard austenitic stainless steels. The influence of the high manganese austenite phase on the passive film chemistry, repassivation rates, erosion-corrosion as well as the sub-surface crystallography orientation is an area of research interest.

It is of note that despite the abundant models available for the prediction of erosion-corrosion, there is still an incomplete understanding of the physical erosion-corrosion mechanism and synergy (interaction between erosion and corrosion). This has hindered the accurate prediction of material degradation by erosion and erosion-corrosion. For instance, the subject of erosion-corrosion synergism and antagonism has not been fully extended to the evolution of modified subsurface crystallography and microstructure (35, 36). For a metastable phase such as austenite, this becomes even more important as this phase could transform to a more stable strain-induced martensitic phase if it is heavily strained under sand impact (35, 36). Apart from this, alloys under such heavy impact could develop fatigue cracks, work-hardened layers, high dislocation density and grain refinement within the sub-surface (35-37). All these factors would modify both the corrosion and erosion resistance properties of the affected regions and subsequently this could affect the synergy between corrosion and erosion. To the best of the author's knowledge, the influence of strain-induced martensite and the other subsurface properties on erosion-corrosion has not been extended to duplex stainless steels and especially the lean duplex stainless steels.

1.2 Objectives of the Research

The main objective of this research is to improve the scientific and engineering understanding of lean duplex stainless steels in CO_2-saturated oilfield and aerated seawater environments. This is to help in facilitating material selection for oilfield applications under both quiescent and flowing conditions (erosion-corrosion). This research will achieve this by considering the following:

- The tendency for corrosion pits to initiate on the lean duplex steels in CO_2-saturated oilfield brine solution and aerated 3.5% NaCl environments. Behaviour of the lean duplex stainless steels will be compared with the austenitic stainless steels and the standard duplex stainless steels.
- Using X-ray Photoelectron Spectroscopy (XPS) to study the passive film properties formed on the lean duplex stainless steels in both aerated 3.5% NaCl and CO_2-saturated oilfield.
- The erosion-corrosion behaviour of the lean duplex stainless steels in both aerated 3.5% NaCl and CO_2-saturated oilfield environments. The lean duplex stainless steels will be compared with standard austenitic and standard duplex stainless steels.

This research will also relate the erosion-corrosion resistance of a lean duplex stainless steel, UNS S32101 and a standard austenitic stainless steel, UNS S30403 to their sub-surface crystallography and microstructure modifications during impact. The erosion-corrosion behaviour of these alloys will also be related to the repassivation rates of their surface passive film. This will be achieved by:

- Using X-ray Diffraction (XRD), Focused Ion Beam (FIB), Scanning Electron Microscope (SEM), Transmission Electron Microscope (TEM) and Selected Area Electron Diffraction (SAED) to study the influence of the sub-surface transformation on erosion-corrosion damage.
- Adopting the submerged impinging jet rig to study repassivation kinetics of damaged passive film under multiple sand impacts. The repassivation rate will then be used to explain the response of UNS S30403 and UNS S32101 to erosion-corrosion.

1.3 Outline of the Thesis

This thesis is presented in 10 chapters.

Chapter 2 presents the basic theory and literature review on the subject of corrosion, erosion and erosion-corrosion. The chapter discusses the general review of literature on the subject corrosion of passive alloys with emphasis on CO_2-corrosion and erosion-corrosion. General review of properties of alloys used in the CO_2-corrosion and erosion-corrosion environments is also discussed in this chapter.

Chapter 3 presents different types of stainless steels with emphasis on duplex and lean duplex stainless steel alloys. Literature review on the subject of corrosion and erosion-corrosion of duplex stainless steels with emphasis on lean duplex stainless steels is also presented in this chapter. Literature review on the repassivation behaviour of the passive film formed on duplex stainless steels is also presented. The chapter goes on to discuss the evolution of microstructure and crystallography of the subsurface of stainless steels subjected to either erosion or erosion-corrosion.

Chapter 4 presents the experimental techniques describing the sample preparation techniques, experimental rigs, methods and procedures used in this study. Procedures for the post-test examination are also explained in this chapter.

Chapter 5 presents the results obtained in static corrosion conditions in both aerated and CO_2-saturated conditions. Breakdown potential and surface analysis of the samples are presented in both environments.

Chapter 6 presents the experimental results obtained under pure-erosion and erosion-corrosion conditions for the alloys in both aerated and CO_2-satured environments.

Chapter 7 presents sub-surface changes with the use of X-ray Diffractometer (XRD), Focused Ion Beam (FIB) and Transmission Electron Microscope (TEM). Surface wear is also shown with Scanning Electron Microscope (SEM) while the hardness profile was determined by a micro-hardness tester. The relationships between the corrosion-wear and the subsurface morphology are explained in this chapter.

Chapter 8 presents the repassivation kinetics of the passive film formed on UNS S32101 and UNS S30403 in a CO_2-saturated oilfield. The repassivation index is determined from the log *i*- log *t* plots and the values related to the repassivation rates of the passive film. The repasivation index is also related to the resistance of the alloys to erosion-corrosion.

Chapter 9 presents a detailed discussion of the experimental results, comparing the work in this thesis with other reports in the literature and establishing the differences and contributions of this study.

Chapter 10 presents the conclusions drawn from this research and also explains the contribution of this research to the existing knowledge. The later part of this chapter suggests some work for further study.

Chapter 2. Fundamental Theories and Literature Review

2.1 Fundamentals of Aqueous Corrosion

Corrosion is said to be the gradual degradation of materials especially metals and alloys as they interact with their environments (38). Corrosion occurs at atomic /ionic scale within the alloy-environment interface. Several steps are involved with different reaction kinetics. However, the slowest of all the kinetics is the one that determines the reaction rate (38). Corrosion can also be classified as either dry or wet. Dry corrosion occurs at high temperature in the absence of liquid while wet corrosion which is also referred to as aqueous corrosion occurs in the presence of liquid. Most industrial corrosion falls under wet corrosion which is electrochemical in nature (39). Industrial/wet corrosion can, therefore, be defined as the chemical or electrochemical deterioration of an alloy in an aggressive environment (40, 41). The corrosion of alloys in aqueous solution is most times related to iron/steels and water. This is essentially due to abundance of water and its universal usage in most industries (39).

Electrochemical corrosion involves the movement of metallic atoms from their lattice. The atoms are oxidized into ions which enter into the environment. The oxidation and reduction reactions occur at the anode and cathode respectively. The reaction that occurs at the cathode is referred to as cathodic reaction while the reaction that takes place at the anode is referred to as anodic reaction (42). Equation

2-1 shows the dissolution of iron in aqueous solution. This is a typical corrosion reaction.

$$Fe^{o} => Fe^{2+} + 2e^{-} \quad \text{(anodic reaction)} \qquad 2\text{-}1$$

$$2H^{+} + 2e^{-} => H_2 \quad \text{(cathodic reaction)} \qquad 2\text{-}2$$

While equation 2-1 (anodic reaction) which is the oxidation reaction occurs at the anode, the reduction (equation 2-2) reaction occurs simultaneously at the cathode and referred to as the cathodic reaction.

The combination of equation 2-1 and 2-2 gives the overall reaction represented by equation 2-3.

$$Fe^{o} + 2H^{+} => Fe^{2+} + H_2 \qquad 2\text{-}3$$

However, it should be noted that the cathodic reaction which determines the reaction rate often depends on the condition of the aqueous environment. In a de-aerated environment, the cathodic reaction in equation (2-2) above determines the reaction rate. However, in an aerated environment, oxygen-reduction becomes the rate determining reaction. In this instance, at the cathode, the following reactions take place

$$4H^{+} + O_2 + 4e^{-} => 2H_2O \qquad 2\text{-}4$$
(acidic medium)

$$O_2 + 2H_2O + 4e^{-} => 4(OH)^{-} \qquad 2\text{-}5$$
(alkaline or neutral medium)

Combining equations 2-1 and 2-5 gives:

$$2Fe + 2H_2O + O_2 => 2Fe(OH)_2$$ 2-6

(ferrous hydroxide)-green colour pH of about 9.5)

Ferrous hydroxide can also be present in form of ferrous oxide ($FeO.nH_2O$).

Water, oxygen, carbon dioxide (dissolved in water), inorganic acids, hydrogen sulphide and strong organic acids are generally referred to as Electrochemically Active Species (EAS) because they produce ions or molecules that can be reduced by electrons. Most of these EAS are encountered in oil and gas environments (42).

2.1.1 The Corrosion Cell

Corrosion takes place through the action of electrochemical cell (Figure 2.1). An electrochemical cell comprises of four components. The corroding component is the anode while the cathode is the site where the environment reacts. The electrolyte (containing the electrochemical active species) provides the path for ionic conduction while the electrical connection provides path through which electrons flow from one electrode to another.

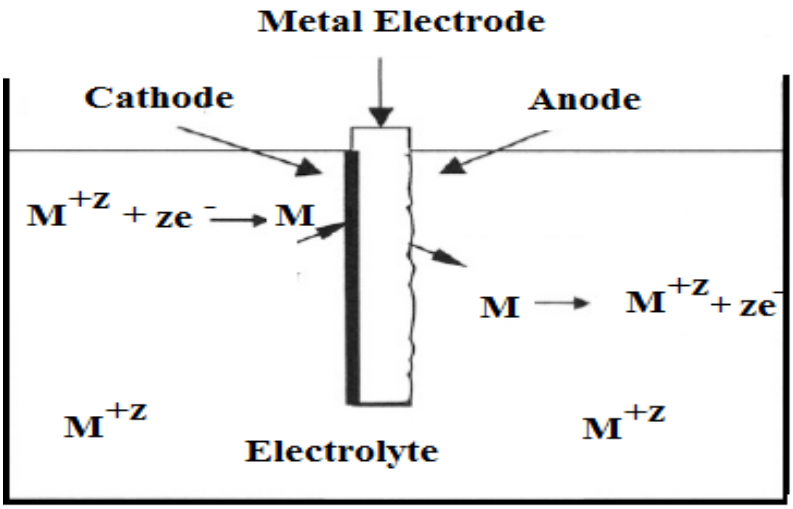

Figure 2.1: Simple corrosion cell (41)

The anodic and the cathodic sites in a corrosion cell may be physically separated from each other or adjacent to each other depending on the circumstance (39). However, most often in practice, they are not physically separated as shown in Figure 2.1.

2.1.2 Thermodynamics of Electrochemical Reactions

Metals in their natural state are ores which are chemical compounds with the metals combining with other elements and molecules. The separation of ore to its components requires the application of thermal energy. This applied energy increases the energy content of the metals as compared to the ores from which they are formed and make them unstable (38, 43). The tendency for these metals /alloys to revert back to their natural (lower energy state) is what leads to corrosion. According to basic thermodynamics, for these metals to revert back to their natural state, they must possess a negative free energy (-ΔG). Moreover, in electrochemical reaction, the driving force is the measure of potential difference and electric current. For corrosion reaction to proceed spontaneously, the thermodynamics of the system must be favourable. To determine if a reaction is thermodynamically favourable, Gibbs free energy equation:

$$\Delta G = \Delta G^{o} + RT\ln\frac{[Product]}{[Reactant]} \qquad 2\text{-}7$$

is considered.

Where, ΔG is the Gibb's free energy in KJ/mole, ΔG^{o} is the standard free energy of the cell in KJ/mole, R is the ideal gas constant (8.314 $Jmol^{-1}K^{-1}$), T is the absolute temperature in Kelvin (K), [Product] and [Reactant] are the concentrations of the product and the reactant in moles.

If $\Delta G > 0$, energy will be required to drive the reaction. However, if $\Delta G < 0$, the reaction occurs spontaneously. Having said this, it should also be noted that the entropy and the enthalpy of the reaction are also to be considered. The energy associated with the separation of charges between the metal surface and the solution is also important. The electric double layer (Figure 2.2) separates the metal surface and the test solution. This layer behaves like a capacitor and as such there is a rise in potential across the interface between the metal and the test solution.

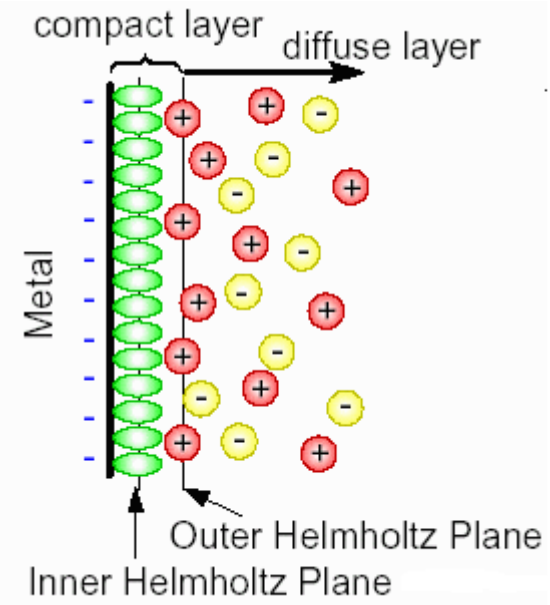

Figure 2.2: Electric double layer adapted from (41)

Potential across the EDL is represented as :

$$\Delta G = -nFE \qquad 2\text{-}8$$

Where G is the Gibbs free energy in kJ/mole, n is the number of electrons exchanged in the reaction and F is Faraday constant (96,496 Coulombs/mole) and E is the potential difference between the two half cells (Volts)

Under an equilibrium condition, both the electrical and chemical energy are said to be equal. They can thus be represented by the Nernst equation:

$$\Delta E = \Delta E^{o} - \frac{RT}{nF} \ln \frac{[Product]}{[Reactant]} \qquad 2\text{-}9$$

Where E is the potential difference between two half cells in Volts, E^{o} is the standard potential difference between a cell in Volts, R is the ideal gas constant (8.314 $Jmol^{-1}K^{-1}$), T is the absolute temperature in Kelvin (K), [Product], [Reactant] are the concentrations of the product and the reactant in moles and n is the number of electrons exchanged in the reaction.

2.1.3 The Pourbaix (E-pH) Diagram

The major factor in corrosion is the environment within which the alloy/metal is reacting (39). Potential-pH diagrams represent a summary of the thermodynamics of a metal/alloy and the associated species in the said environment. Potential-pH diagrams do not define the kinetics of the corrosion reaction but the thermodynamics prediction of corrosion reaction can be drawn from such diagrams as a function of potentials and pH (39, 44). Iron can be found in the states of immunity, passivity and corrosion in water depending on the pH and applied potential. The immunity state represents the state where corrosion is impossible. Metal deterioration is possible at the state of corrosion but this occurs at a particular rate (44, 45). The passive state represents the region where the corrosion products are insoluble in the environment. This corrosion products thus form a protective barrier on the alloy surface and thereby prevent the electrochemical interaction between the environment and the alloy (44, 45).

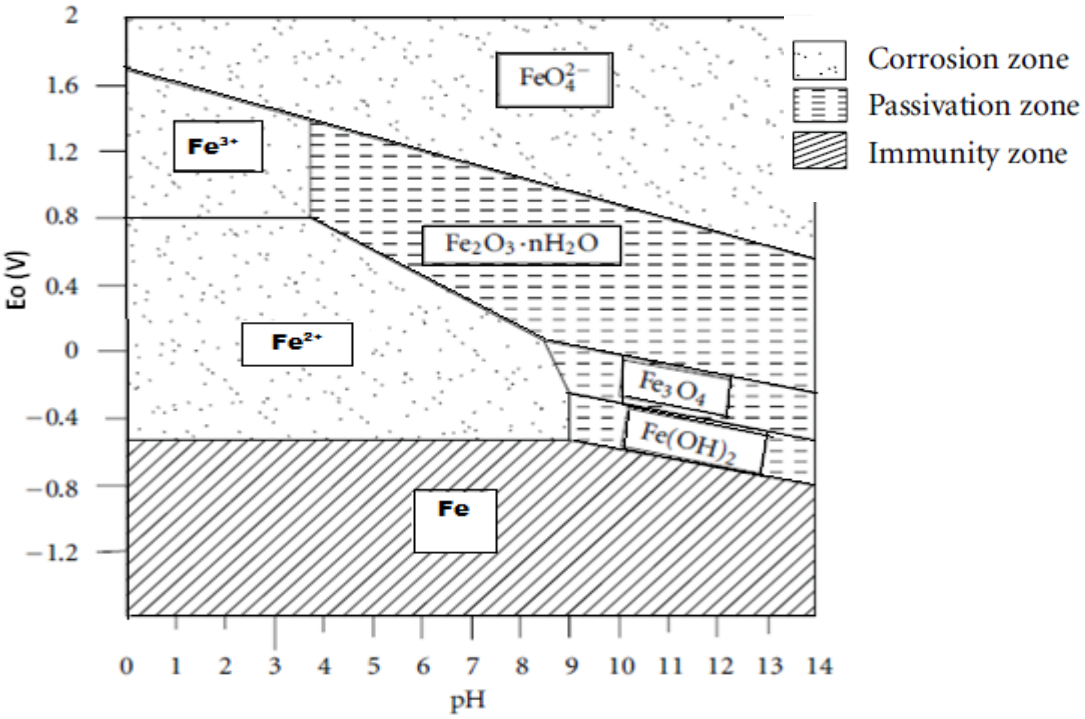

Figure 2.3: The E-pH diagram of iron in water (46)

2.1.4 Kinetics of Electrochemical Reactions

Thermodynamics describe the tendency of a system to corrode but do not give any information about the speed of the corrosion reaction. Consideration of the kinetics of a reaction on the other hand enable the rate at which such reactions will occur to be calculated (39).

2.1.4.1 Free energy and free activation energy

When two substances are involved in a chemical process, the general equation can be expressed as

$$A+B \text{ (reactants)} \longrightarrow C+D \text{ (Products)} \qquad 2\text{-}10$$

An activation barrier (activated complex) that is created during the reaction process is to be overcome before the products are formed. From the thermodynamic

point of view, the activation complex is at a higher energy level than the reactants. Figure 2.4 illustrates the activation complex. An energy difference (activation energy $\mathbf{\Delta G^{\#}}$) exists between the initial position and the activation complex.

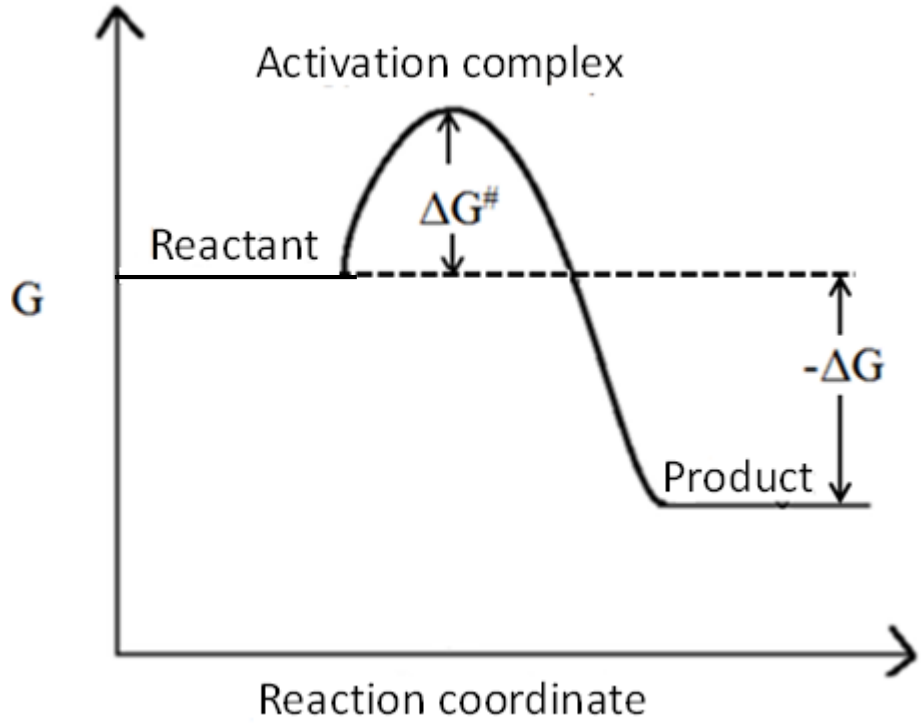

Figure 2.4: Energy profile adapted from (47)

The activation energy partly determines the rate of a chemical reaction. For a corrosion reaction, the corrosion rate v is defined thus:

$$v = kc \qquad 2\text{-}11$$

Where c is the concentration (moles) of the reactants. k is the constant of reaction derived from the Arrhenius equation (47).

$$k = Ae^{\frac{\Delta G^{\#}}{RT}} \qquad 2\text{-}12$$

k is the rate constant, A is the pre-exponential factor, $\Delta G^{\#}$ is the activation energy (Joules), R and T have been previously defined.

The rate of reaction partly depends on the activation energy. Lower activation energy increases reaction rate and vice-versa.

2.1.4.2 Exchange current density

The current flowing during any corrosion reaction is related to the corroding area and it is referred to as the corrosion current density. The net current at equilibrium is zero as illustrated by equation 2-13 (39). By convention, the anodic current, I_a, is taken to be positive and the cathodic current, I_c, as negative.

$$I_a + I_c = 0 \qquad 2\text{-}13$$

However, if the two complementary processes (as illustrated by Figure 2.5) occurring over the surface of a metallic material are considered, the potentials of such material is no longer at equilibrium. This deviation from equilibrium is termed polarisation. The difference between the equilibrium potential (ϕ_{eq}) and the resultant potential (ϕ) is the term referred to as overpotential, η. Overpotential is thus defined by the equation (2-14).

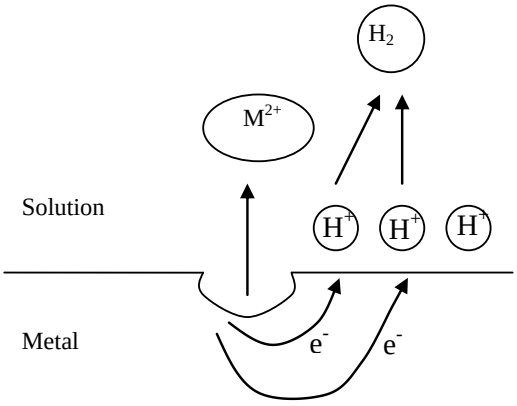

Figure 2.5: Electrochemical nature of the corrosion process

$$\eta = \phi - \phi_{eq} \qquad 2\text{-}14$$

η comprises of three components of the overall polarization across the electrochemical cell.

$$\eta_{act} + \eta_{conc} + iR \qquad 2\text{-}15$$

η_{act}, the activation polarisation, describes the charge transfer kinetics. It is the controlling factor during corrosion in strong acids or at small polarization currents or voltages. η_{conc}, the concentration polarization, is the potential change due to transportation inhibition caused by concentration differences. Concentration polarization becomes very importance when there is low concentration of the active species. Examples of this is dilute acids or in aerated water. Concentration polarisation is also said to be at play when there is a large polarization current or voltage. Transportation of active species is governed by diffusion, migration and convection. When the environment is stagnant, the convection force becomes negligible. Fick's Law describes the flux of the active species when the mass transport is purely diffusion controlled.

The Ohmic drop (iR) describes the polarization in the electrolyte or at interfaces as a result of the applied current. This is described by Ohm's law.

2.1.4.3 Activation Polarisation

When the rate of electron or charge flow is the determining step in a corrosion reaction, the reaction is said to be activation- or charge-transfer controlled. Under such conditions the electrochemical reaction is typically represented by two polarisation branches as illustrated in Figure 2.6.

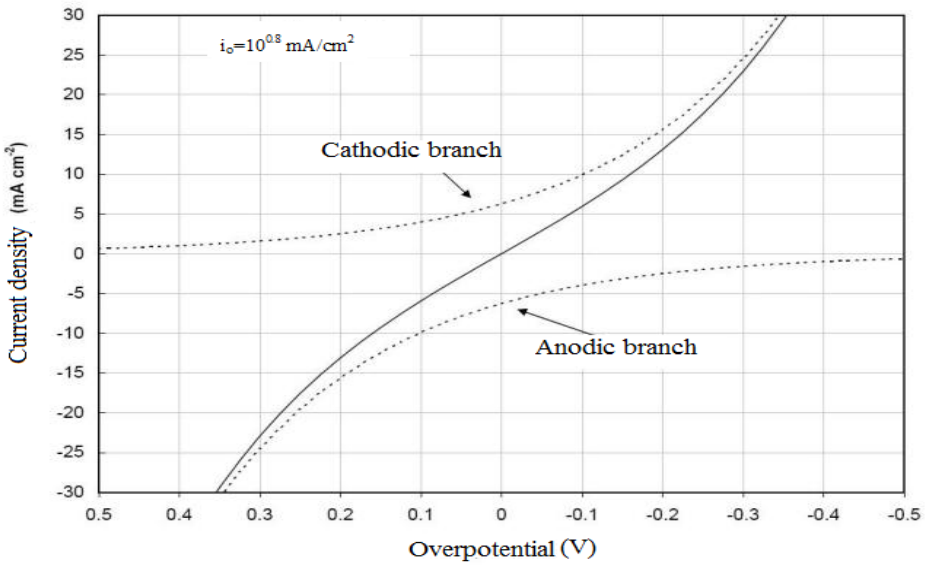

Figure 2.6: Current versus overpotential polarisation plot of ferric/ferrous ion reaction on palladium showing both anodic and cathodic branches of the resultant current behaviour (48)

The anodic and cathodic sides of the reaction can be studied using polarisation methods. The Butler-Volmer equation is used as a representation of such polarised surface.

$$i = i_o \left\{ \left[exp \propto \frac{nF}{RT} \eta \right] - \exp \left[-(1-\propto) \frac{nF}{RT} \eta \right] \right\} \qquad 2\text{-}16$$

i is the anodic or cathodic current, α is the charge transfer barrier for the anodic or cathodic reaction (approximately 0.5), Ƞ is overpotential ($E_{applied}$-E_{eq}), Volts, n is the number of participating electrons, R is the ideal gas constant (8.314 $Jmol^{-1}K^{-1}$), T is the absolute temperature (K) and F is 96, 485C/mole.

If the over potential becomes very high (positive/anodic), the second term in the equation becomes very negligible and i_a is given by the following expression:

$$i_a = i_o[\exp(\alpha_a \frac{nF}{RT} \eta_a)] \qquad 2\text{-}17$$

Where

$$\eta_a = \beta_a log_{10}(\frac{i_a}{i_o}) \quad 2\text{-}18$$

The Tafel coefficient β_a is the slope of the plot of η against log i

$$\beta_a = 2.303\frac{RT}{\alpha nF} \quad 2\text{-}19$$

When the overpotential is cathodic, the first term in the Butler-Volmer equation can be ignored. This gives rise to

$$i_c = i_o\{-\exp\left[-(1-\alpha_c)\frac{nF}{RT}\eta_c\right]\} \quad 2\text{-}20$$

$$\eta_c = \beta_c log_{10}(\frac{i_c}{i_o}) \quad 2\text{-}21$$

$$\beta_c = -2.303\frac{RT}{\alpha nF} \quad 2\text{-}22$$

2.1.4.4 Mixed Potential and Determination of Corrosion Current Density

The case described in Figure 2.6 is for a single equilibrium reaction involving Ferric/Ferrous reaction. Corrosion, however, occurs with two or more electrochemical processes happening on a metal surface. If we consider the acid corrosion for metal, M, as shown below,

$$\boldsymbol{M + zH^+ = M^{z+} + \frac{z}{2}H_2} \quad 2\text{-}23$$

Each of these reactions can be at equilibrium with individual equilibrium η_M and η_{H_2}. The total current-potential curve is then constructed from the four partial reactions (1-4) that superimpose one another with four individual partial current densities as shown in Figures 2.7 and 2.8.

1. Anodic metal dissolution

2. Cathodic metal plating

   With equation $\boldsymbol{i_M = i_M^+ + i_M^-}$ 2-24

3. Cathodic hydrogen evolution

4. Anodic hydrogen ionisation

With equation $\boldsymbol{i_H = i_H^+ + i_H^-}$ 2-25

The partial current densities can be expressed analogue to the Butler-Volmer equation. The total current-potential curve will then be a combination of both equations (2-24 and 2-25):

$$\boldsymbol{i_t = i_M + i_H = i_M^+ + i_M^- + i_H^+ + i_H^-} \quad \text{2-26}$$

The potential where i_M and i_H are equal (despite their different signs) is called the mixed potential or the corrosion potential (E_{corr}) Figure 2.7. The corresponding current is what is referred to as the corrosion current density (i_{corr}) Figure 2.7. This is also illustrated by the Tafel extrapolation in Figure 2.8.

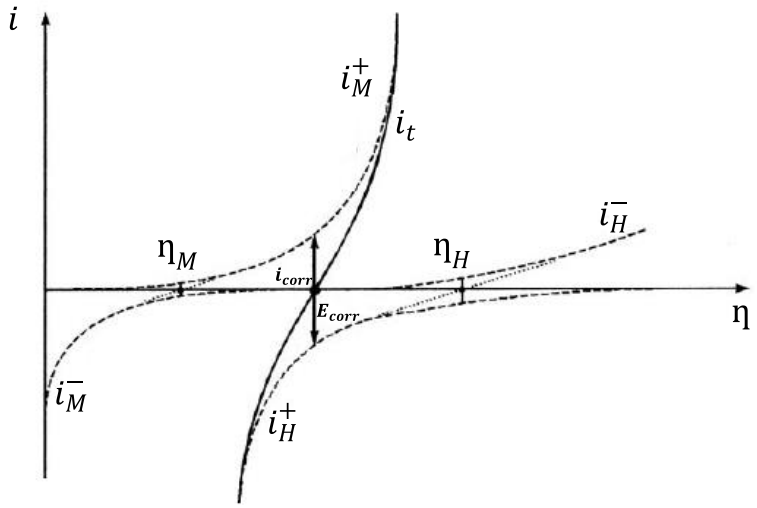

Figure 2.7: Total current-potential curve of acidic corrosion with formation of a mixed potential, E_{corr} (49)

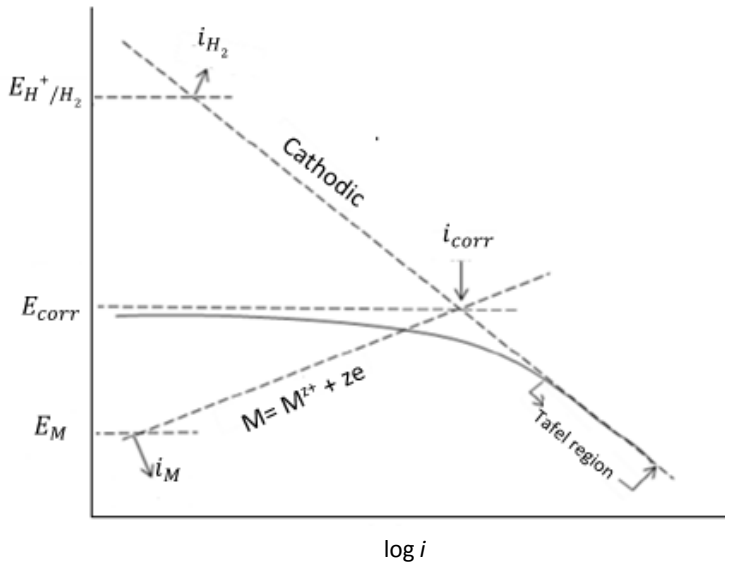

Figure 2.8: Mixed potential theory showing Tafel extrapolation, corrosion current and corrosion potential, adapted from (50)

2.1.4.5 Polarisation Resistance Measurement

The linear polarisation resistance method developed by Stern and Geary (1957) (51) can be used to measure corrosion rate under steady state conditions. Linear polarisation technique assumes that in activation controlled systems, the exponential anodic and cathodic polarisation curves are approximate to a straight line close to the free corrosion potential. A small external DC potential signal of ±10 to 20 mV is applied to the system, and the current flowing in the external circuit is measured. The polarisation resistance (R_p) is the ratio between the applied potential and the measured current.

$$\boldsymbol{R_p = \frac{\Delta E}{\Delta i}} \qquad 2\text{-}27$$

ΔE = applied voltage change with respect to the free corrosion potential

Δi = measured current density

The corrosion current density can then be determined thus:

$$i_{corr} = \frac{B}{R_p} \qquad 2\text{-}28$$

Where, B is the Stern-Geary constant which is dependent on the corrosion system.

$$B = \frac{\beta_a \beta_c}{2.3(\beta_a + \beta_c)} \qquad 2\text{-}29$$

Knowledge of polarization resistance R_p and the Tafel constants (β_a, β_c) can be used to determine the corrosion rate (52).

2.2 Classifications of Corrosion

Corrosion may be classified into general/uniform corrosion and localized corrosion. General corrosion occurs over the entire material's surface and it is very easy to predict. Localised corrosion on the other hand is not easy to predict or control because it is often associated with occluded area of the material. Types of localised corrosion (Figure 2.9) include: crevice corrosion, pitting corrosion, selective dissolution of active metal (dezincification, graphitization), co-joint action of corrosion and mechanical factors (erosion-corrosion, fretting, hydrogen cracking, stress corrosion cracking and cavitation damage (43).

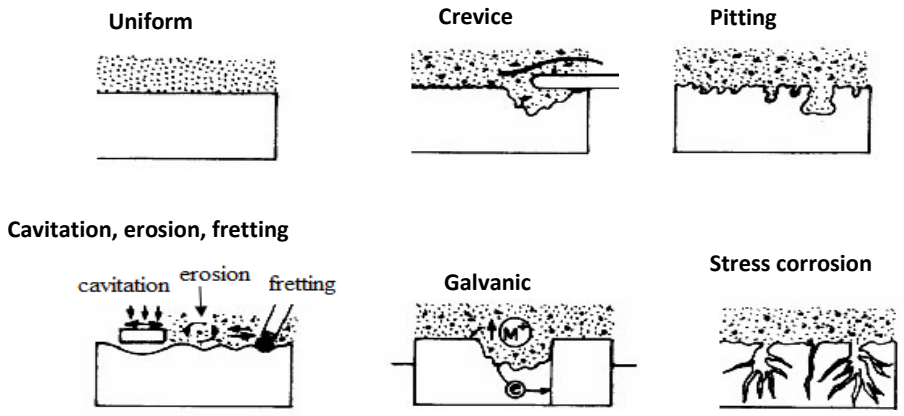

Figure 2.9: Types of corrosion (53)

2.2.1 Pitting Corrosion

Corrosion resistant alloys (CRAs) are resistant to general corrosion due to the passive film formed on their surface from reaction between them and the corroding environments like oxygen and water (17). The breakdown of passive film formed on corrosion resistance alloys leads to a localised material degradation (54). Figure 2.10 shows a typical breakdown of passive film that led to corrosion pit. It is also of importance to say that pitting occurs at preferred sites where there is secondary phase especially MnS. Near the precipitate site is a zone that is deficient of chromium and hence the passive film is weak. The breaking down of the passive film occurs at a particular temperature referred to as Critical Pitting Temperature (CPT). Critical Pitting Temperature (CPT) is the lowest temperature below which pitting will not occur under a specific test condition.

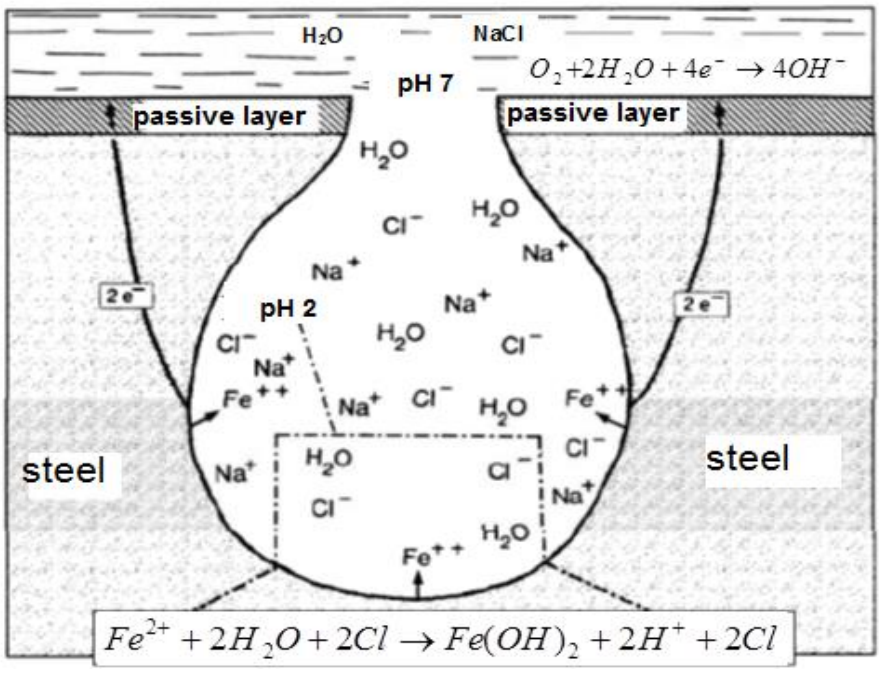

Figure 2.10: A typical corrosion pits showing the hydrolysed bottom with depleted oxygen (55)

The major drawback to CRAs is localized corrosion in form of pits and crevices. Pitting corrosion of stainless steels is dependent on the composition of the alloy represented by Pitting Resistance Equivalent Number (PRE_N), passive film characteristics, temperature, bulk solution composition (pH and anion contents) and geometry of the joint (crevices) (56, 57). Pitting resistance equivalent number is often represented by the amount of the corrosion resistant alloying elements in a given alloy (%Cr +3.3%Mo +16%N). The major alloying elements that contribute to this number are: Chromium, Molybdenum and Nitrogen (58). The ability of a CRA to resist corrosion, especially localized corrosion, is also a function of the resistance of the passive film formed on its surface. The passive film's stability is dependent on its composition, thickness and structure, Figure 2.11 (59). The passive film on stainless steels has its own composition different from the composition of the substrate alloy. Such composition is, however, dependent on the substrate's composition as well as the corrosion environment (60). It is well reported in the literature that the ultrathin passive film is highly enriched in chromium (60, 61). The ratio between the chromium contents of the substrate and the oxide (chromium enrichment factor) is defined as a parameter. Molybdenum helps in increasing the chromium content of the oxide while nickel has been reported to be either absent or have very negligibly presence in the oxide film. However, it is said that the nickel is enriched just below the oxide film (59, 61).

Interestingly, the chromium content of the passive film increases with passivating potentials (59, 61). The pitting behaviour of stainless steels is reported (59, 61) to be dependent on the chloride ion concentration of the environment as well as the PRE_N

of the alloy. It also reported (57) that the passive film breakdown usually occurs on a localised site commonly an inclusion of manganese sulphide. The pit is also believed to first initiate and then propagate. The mechanism of pit initiation and propagation is said to be different from each other. Initiation of pits is said to be by absorption/migration of aggressive ions on the passive film. Some schools of thought also believe it could be by mechanical disruption of the passive film. Pit propagation on the other hand is believed to be by metal dissolution, salt layer formation or it could be by mass transfer.

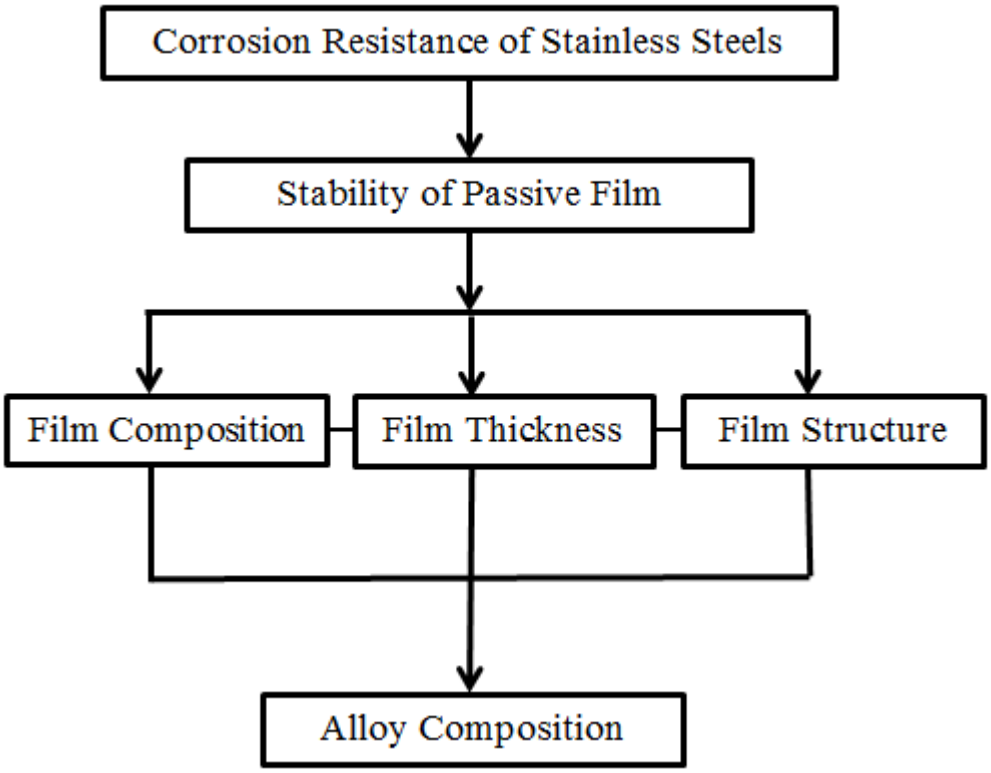

Figure 2.11: Relationship between corrosion resistance of stainless steels and passive film properties (59)

2.2.2 Crevice corrosion

Crevice corrosion (Figure 2.12) is geometry dependent and it is associated with stagnant solution at micro environment level. This makes it different from pitting which is not dependent on the material geometry. Crevice corrosion occurs in shielded or occluded area such as gasket, washers, fastener heads etc. The crevice is oxygen deficient and thus an electrochemical cell is set up between it and the surface closer to the bulk solution environment. Because of the low oxygen level of the crevice it thus acts as the anode while the external surface acts as the cathode. Because of the large difference between the cathodic and the anodic areas, the anodic dissolution rate is thus very high.

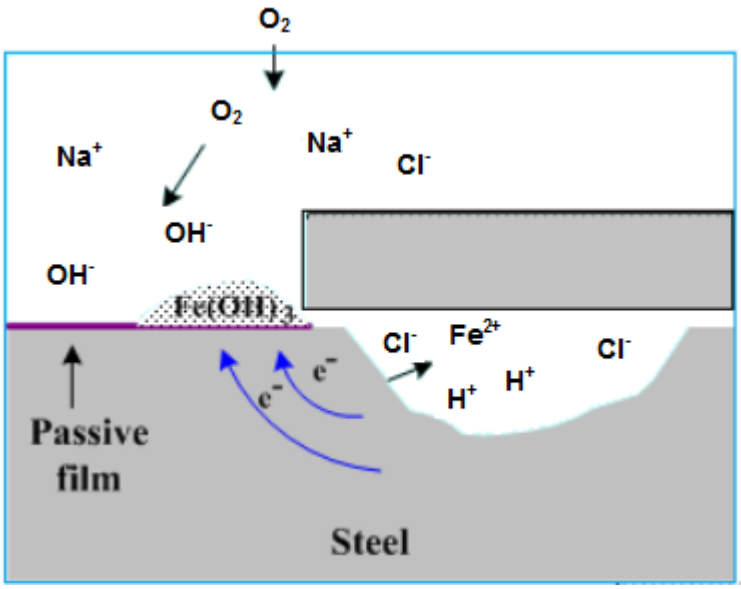

Figure 2.12: Schematics of crevice corrosion of steel in NaCl environment

2.3 Corrosivity and Passivity

Passive films protect the surface of a passive alloy when they react with their environment. They have limited ionic and electronic conductivities (62) and hence slow down the rate of reaction between the metal and its environment. The formation

of passive film happens spontaneously. Passive film has been studied to comprise of an outer layer of the n-type and an inner layer of p-type semiconductors (62). The outer and the inner layers have also been reported to comprise of iron oxide/hydroxide and chromium oxide respectively (Figure 2.13). For a passive film to be stable, a layer of hydroxide should be on the inner oxide layer. It is not also uncommon to see the oxides of molybdenum in association with the chromium oxide. Despite the fact that the passive film is resistant to general corrosion, it can be susceptible to localized corrosion in form of crevices and pitting. It should be stated that, despite the abundant literature on the subject of passivity breakdown, there is yet no agreement on their formation, composition and the breakdown mechanism.

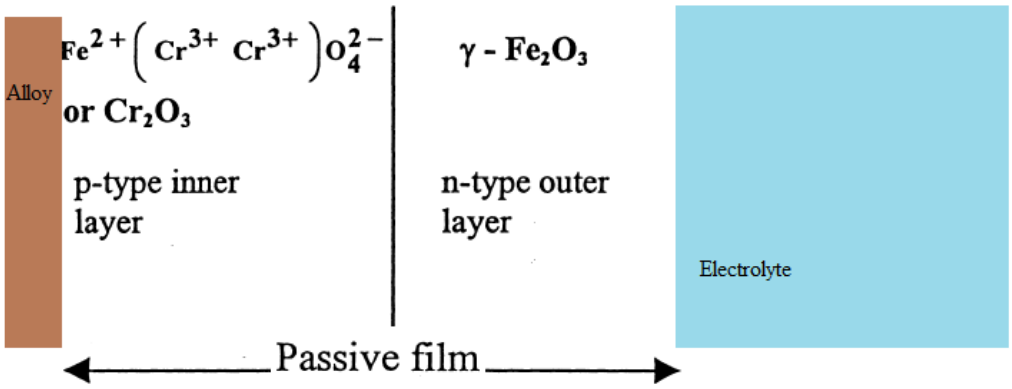

Figure 2.13: Inner and outer layers of a passive film adapted from Hakiki *et al.* (63)

One method used to study the electrochemical corrosion behaviour of passive alloy is the polarisation curves. An alloy that corrodes normally in an environment may exhibit passivation in the same environment at higher potentials when passive film/oxide is generated on its surface. This is mostly common for the corrosion resistant alloys. However, if the potential is raised to a certain limit the passive oxide may breakdown leading to a severe localized corrosion.

2.4 Polarization Curves for Passive Alloys

Typical polarization curves to study the behaviour of passive alloys are shown in Figures 2.14 and 2.15. Figure 2.14 is a typical potentiodynamic curve (no reverse scan) while Figure 2.15 is a typical cyclic polarisation curve (41).

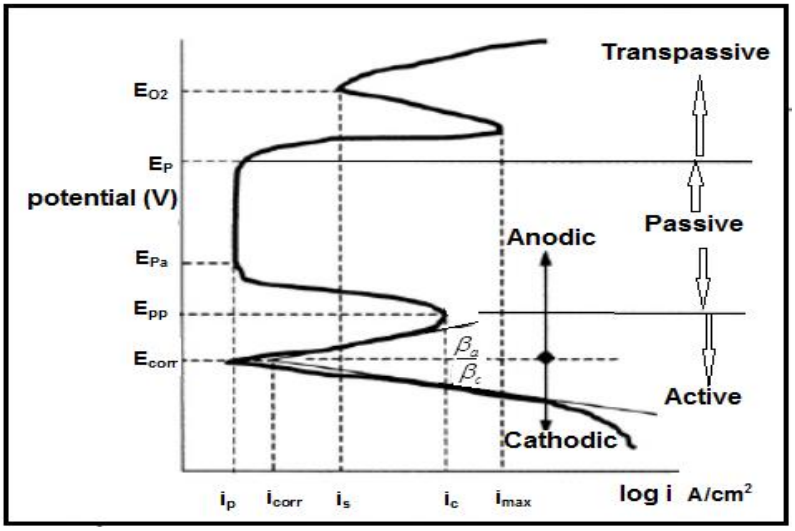

Figure 2.14: Polarisation scan, no reverse scan (41)

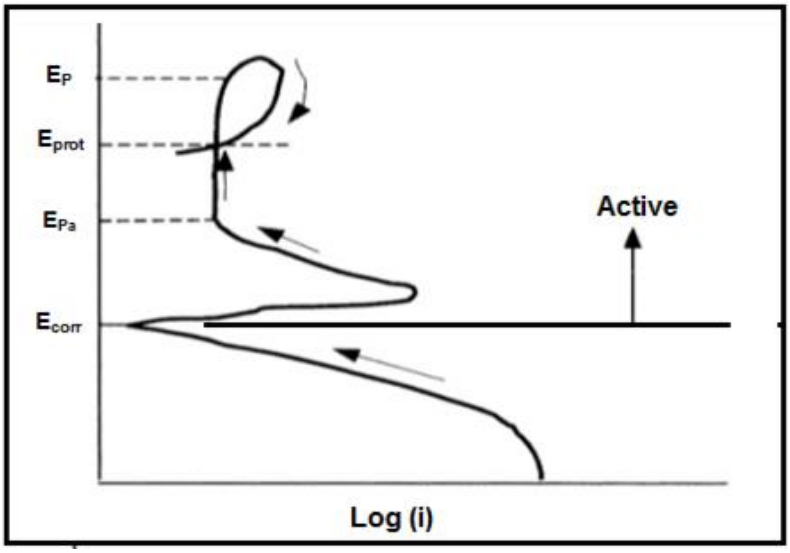

Figure 2.15: Schematic polarisation curves of a passive alloy with a reverse scan (41)

The corrosion potential at open circuit is represented by E_{corr}. At this point, the sum of the cathodic and anodic reaction rates on the working electrode is zero. As a result the current density measured is approximately zero. When the potential is scanned in the positive direction, the dissolution rate increases up to the primary passivation potential point (E_{pp}) and then begin to decrease until the passivation potential (E_{pa}) is attained. Once the passivation potential (E_{pa}) is attained, increase in potential has little or no effect on the current density.

The current density at the primary passivation potential is referred to as the critical current density (i_c). Critical current density is the active current density at the passivation potential. Current density at the passivation potential E_{pa} is the passive current density i_p. This current is constant over a range of potential until the breakdown potential (E_b) where the current density suddenly increases as a result of localised breakdown of passivity, oxygen evolution or transpassive dissolution of the passive film. An aggressive ion such as chloride if present in the electrolyte helps in the dissolution of the passive film and hence brings down the breakdown potentials. On the reverse scan, the potential at which the backward loop crosses the forward loop is the protection potential (E_{prot}). If this potential falls below the corrosion potential, pit will propagate but if it is above the corrosion potential the alloy is immune against pit propagation in such environment (64).

2.5 Repassivation of Passive Film Damaged by Mechanical Disruption in a Corrosive Environment

The corrosion resistance of alloys with passive film protection can be negatively affected by the solid particle impact (34). However, if the passive film can regenerate

fast, the alloy will remain corrosion resistant. The total amount of material loss by the impact of erodent and that of corrosive medium is a function of the behaviour of the passive film. As a matter of fact, the generation rate of fresh metal surface and the repassivation rate of the alloy are two important factors that determine the erosion-corrosion resistant of such alloys (32, 65). The oxide is assumed to first nucleate and initially grow according to the *surface coverage model* (66). According to this model, passivating film covering a unit area is entirely removed (by the erodent/tip of the tribometer). Furthermore, metal oxidation on such area is assumed to occur exclusively on the bare metal/alloy surface leading to lateral growth of an oxide. After the entire area has been covered by the passivating film, growth of the film then follows the *growth model* (66). Film growth model assumes that an anodic oxide grows uniformly on the initial oxide formed. The growth rate in this case is determined by the high field conduction.

The film growth mechanism has been found by experiments to follow either the logarithm or inverse logarithm law represented by equations 2-30 and 2-31 respectively.

$$L = A + B\ln t \qquad 2\text{-}30$$

$$\frac{1}{L} = C - D\ln t \qquad 2\text{-}31$$

L is the film thickness

t (s) is the time taken for the film to grow to thickness L (mm)

A, B, C, and D are constants.

It has also been argued that repassivation and the initial growth of damaged film is controlled by ion migration in a high electric field obeying inverse logarithm law at the passive potential (67). In order to explain both logarithm and inverse logarithm laws, several models have been developed over the years. Some of the models are given in the next section.

2.5.1 Mott-Cabrera Model

Mott and Cabrera proposed a model in 1948 based on the initial work of Mott a year earlier. These authors assumed the following:

1. That the film growth is as a result of the movement of metal cation from the bulk alloy to the film/solution interface.
2. That the penetration of the metal cation into the film oxide is assisted by a high electric field strength that exists within the film.
3. That the field strength is constant throughout the film thickness.
4. That the reaction rate for film formation is controlled by the rate of emission of the cation into the film at the metal/film interface.

From these assumptions a rate law with the following expression in equation 2-32 was proposed for passive film growth

$$dL/dt = N\Omega V \exp[(-W + \frac{qa\phi_f}{2L})/kT] \qquad 2\text{-}32$$

Where,

N is the number of mobile ions per unit surface area

Ω is the molecular volume per cation (cm^3/mol)

V is the vibration frequency (Hz)

W is the activation energy for the rate determining step (J)

q is the charge on the cation (Coulomb)

a is the jump distance (mm)

kT is the thermal energy (J)

Solution to this equation using integration by part gives an inverse logarithm rate law (68).

2.5.2 Sato and Cohen Model

Sato and Cohen related the external current to the applied potentials and the charge accumulated in the film oxide by the equation (2-33)

$$i = k'\exp(mV_{app} - Q_{T/n} \qquad \text{2-33}$$

i is the external current (Ampere)

V_{app} is the applied potential (Volts)

$Q_{T/n}$ is the charge accumulated in the film (Coulumb)

K, m, and n are parameters

Sato and Notoya later proposed that under potentiostatic conditions the integration of equation 2-33 will result in a logarithm law (68).

2.5.3 Fehner and Mott Model

Ferner and Mott modifield the Mott-Cabrera model by making the following assumptions:

1. That anion diffusion is responsible for film growth.
2. That the rate of reaction is determined by the emission of anion from the environment into the film at the film/environment interface.
3. That the field strength in the film is independent on the film thickness.
4. That the activation energy of the reaction increases linearly with the film thickness.

These assumptions also yielded another logarithm law (68).

2.6 Film-Free Surface and Repassivation

Depassivation and repassivation of a passive surface can be studied by several methods of which erosion-corrosion is one. A typical scratch electrode method for studying the repassivation mechanism of a passive oxide is shown in Figure 2.16.

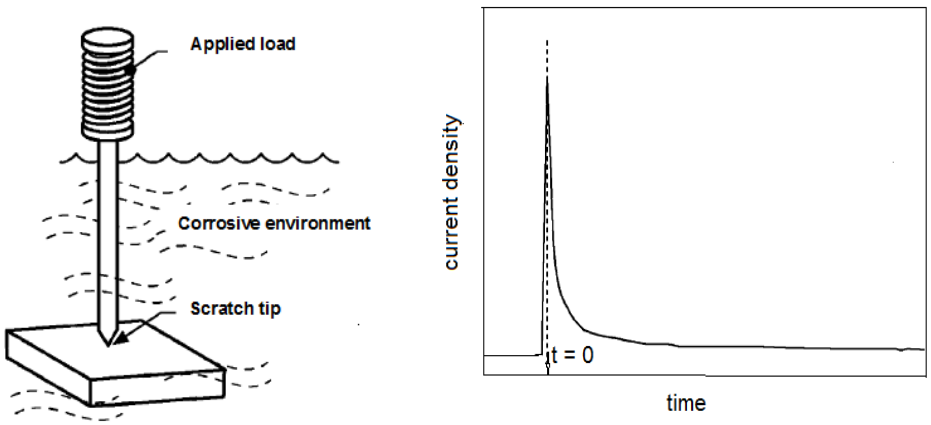

Figure 2.16: Scratch electrode method of studying repassivation kinetics (69)

One method that is adopted to study the repassivation behaviour of passive film is the use of current transients. A model of the form $i(t) = At^{-n}$ is often adopted (65, 70, 71). Where i(t) is the anodic current density consumed in rebuilding of

passive film on a film-free surface at time, t. A is a constant and n is the repassivation index.

The plot of logarithm of current density against the logarithm of time based on the relation:

$$i(t) = At^{-n} \qquad 2\text{-}34$$

will give a relationship of the form shown in Figure 2.17. The slope of the linear portion of the graph is determined as the repassivation index, n. The repassivation index, n, is an indirect measure of the rate of formation of the passive film on the film-free metal surface. The higher the value of n the faster the repassivation process and vice-versa (65, 70).

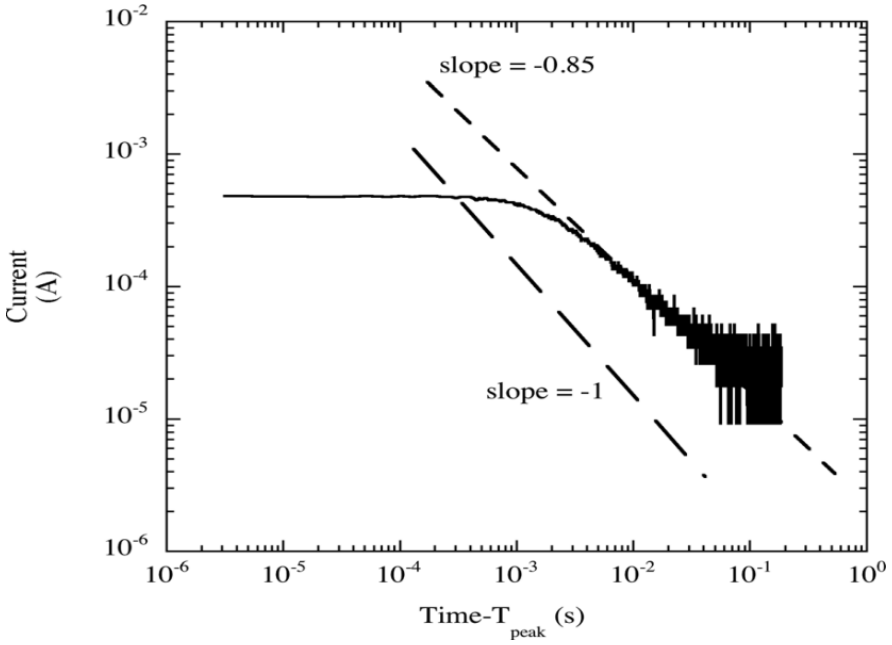

Figure 2.17: A typical example of a log current versus log time for UNS S30403 in 0.9 M NO_3- solution after a scratch test (72)

The flat part in Figure 2.17 represents the portion where the depassivated surface is still under a lateral growth as explained under the *coverage model.* Within this

portion, it is assumed that the depassivated surface is still not completely covered (under coverage mechanism) (66) or that the rate of repassivation and that of metal dissolution are still at equilibrium (71).

2.7 Corrosion in CO_2-Saturated Oilfield Environments

Corrosion of carbon steel in CO_2-containing environment is a very complex phenomenon and still requires further clarification (73). At different segments of the oil well, CO_2 corrosion follows different mechanisms because of changing conditions (74). However, there are two common features of the CO_2 corrosion mechanism:

(a) intense cathodic evolution of H_2 gas and (b) formation of carbonate film at the anode. CO_2 corrosion occurs in stages and may be described thus:

1. Dissolution of CO_2 in the liquid phase

2. The diffusion of the electrochemical active species to the metal surface

3. Reduction of the species at the metal surface

4. The transportation of the reaction products back into the bulk solution (75).

$$CO_{2(g)} => CO_{2(liq)} \quad 2\text{-}35$$

The cathodic reaction is thus represented

$$2H_2CO_3 + 2e^- => H_2 + 2HCO_3^- \quad 2\text{-}36$$

$$2HCO_3^- + 2e^- => H_2 + 2CO_3^{2-} \quad 2\text{-}37$$

$$2H^+ + 2e^- => H_2 \quad 2\text{-}38$$

At the anode

$$Fe^{o} => Fe^{2+} + 2e^{-} \quad \text{2-39}$$

Overall

$$CO_2 + H_2O + Fe^{o} => FeCO_3 + H_2 \quad \text{2-40}$$

CO_2 corrosion is one of the most encountered material degradation problems in an oil and gas installation. This is because CO_2 is often encountered in the production fluid as a result of exploitation of deeper wells and also due to the injection of CO_2 for secondary oil recovery (75). However, for CO_2 to be corrosive it would be dissolved in an aqueous phase. The corrosiveness of CO_2 is also of no significance especially at low temperatures (73). However, it becomes a problem when it dissolves (CO_2 is very soluble in this liquid) in a aqueous phase such as brine, water and even hydrocarbons (76). The association of CO_2 in the aqueous phase give carbonic acid which further dissociates to form bicarbonate and carbonate ions (77).

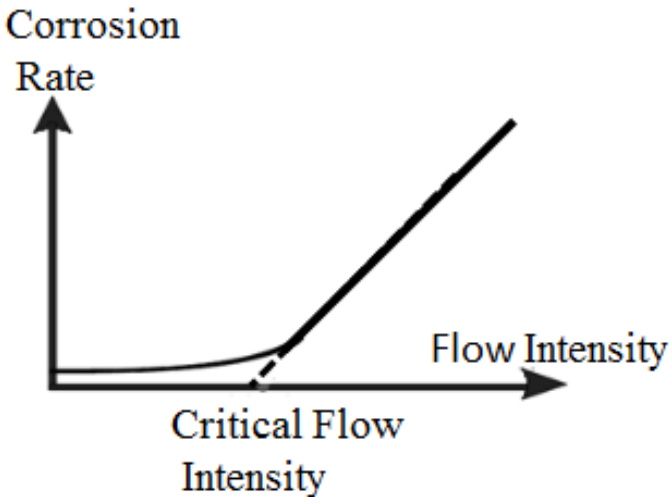

Figure 2.18: Effect of flow on CO_2 corrosion (78)

As earlier explained, CO_2 corrosion thrives in the presence of a liquid phase and it is also affected by the fluid flow (73). Also, it is generally believed that the high

flow rate enhances the CO_2 corrosion by helping in the removal of more Fe^{2+} ion thereby increasing corrosion rate (78). Equally, the near wall turbulent flow for instance either prevents the formation of the protective scale or removes it when it has been formed (73).

The major influencing factors that affect CO_2 corrosion are: its partial pressure (Figure 2.19), temperature and the pH of the bulk electrolyte, fluid flow (Figure 2.18) and the materials composition and microstructure (Figure 2.20)(79).

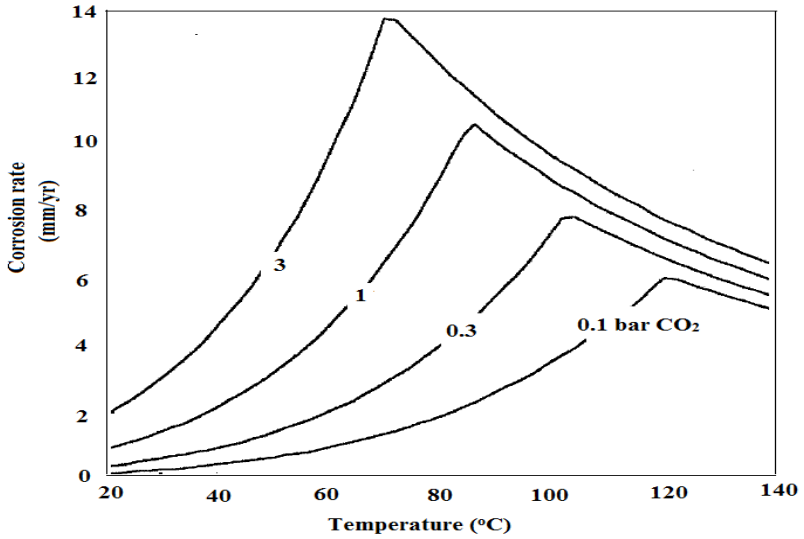

Figure 2.19: Effect of CO_2 partial pressure and temperature on CO_2 corrosion (73)

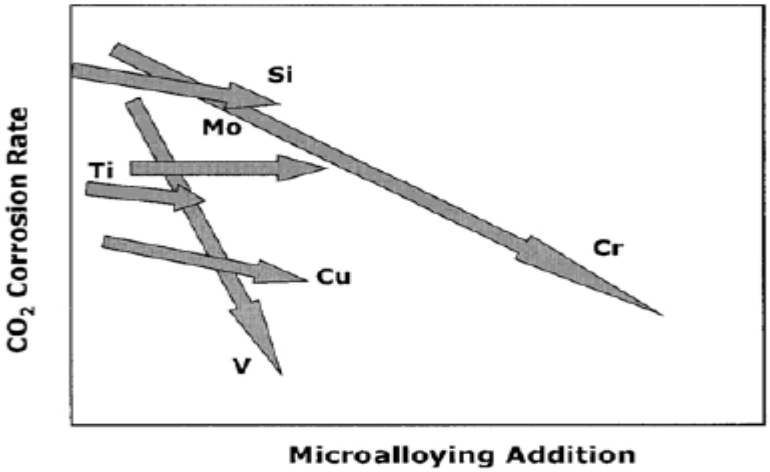

Figure 2.20: Schematic diagram showing the influence of alloying elements on CO_2 corrosion rate (78)

Furthermore, CO_2 corrosion behaviour of carbon steels can be classified into general corrosion that occurs below 60^oC, deep pitting and ring worm that occurs at about 100^oC and corrosion resistance as a result of formation of $FeCO_3$ film that occurs above 150^oC. At about 100^oC, carbon steels and low alloy steels have the highest susceptibility to CO_2 corrosion. The corrosion behaviour of steels greatly depends on the behaviour and characteristics of the $FeCO_3$ film which is the corrosion product of the environment (80). In addition, $FeCO_3$ film precipitation and stability is also dependent on temperature (80). At temperature below 70^oC the film is unstable and dissolves into the bulk solution but as the temperature increases the solubility decreases and reaches optimum at about 150^oC. Lower temperature stability of the oxide film is only possible when the pH is increased (Alkaline). Additionally, It is also reported that the protectiveness of the oxide film is a function of the substrate's microstructures (80). In carbon steels, it is reported that a ferrite – pearlite microstructure has better adherence than a bainitic or a martensitic microstructure (78).

Moreover, as reported by Schmitt and Hörstemeier (78), the rate of CO_2 corrosion is said to increase with increase in CO_2 partial pressure. Also, the rate of CO_2 corrosion of carbon steel depends on the alloying elements of the substrate. Of all the alloying elements, chromium seems to be the most influential alloying element on corrosion of the materials. Generally, the higher the chromium content of the substrate the lower the CO_2 corrosion rate of the low alloyed carbon steels (78). Also, as being mentioned above, the only condition where the $FeCO_3$ film can be protective at lower temperature is when the pH of the solution is high. This means that higher pH reduces CO_2 corrosion rate by influencing the formation of $FeCO_3$

precipitate. The rate of CO_2 corrosion is also dependent on the bulk solution composition in that the higher the concentration of the ions (such as Na^+,Ca^{2+}, Mg^{2+} and other cations) the greater the saturation of the solution and the higher the propensity for precipitation of the oxide film. Also, when more precipitates are formed the corrosion rate is reduced. Furthermore, other parameters that affect CO_2 corrosion include O_2 and H_2S concentrations.

Higher oxygen concentration enhances CO_2 corrosion rate by forming iron oxide which is not protective. The effect of H_2S is somehow complex in that it helps in formation of film with better adherence but also assists in anodic dissolution by the adsorption of sulphur on the substrate. Also, higher H_2S concentration implies lower pH and hence higher corrosion rate (78). The presence of acetic acid can also help in promoting CO_2 corrosion. It is also reported that acetic acid produces hydrogen ion for cathodic reduction and can as well be reduced directly at the cathode thereby increasing cathodic current and hence the overall corrosion rate. The major types of damage associated with CO_2 corrosion are pitting, mesa attack and flow induced localised corrosion (73).

2.8 Marine Corrosion

Marine environments, especially seawater, are corrosive due to the high chloride content and the activities of microbial organisms (81, 82). The marine water is very useful for many industrial processes such as desalination and oilfield water injection. However, the major limitation to its usage is its corrosiveness. Seawater is a solution comprising so many solids/ solutes among which are chlorides. The major constituents of seawater are: Na^+,K^+,Mg^{2+},Ca^{2+},Sr^{2+},Cl^-,Br^-,F^-,HCO_3^-,SO_4^{2-},$B(OH)_3$.

The properties of seawater is remarkable and quite often the properties vary with locations (16). Seawater is unique in such that some basic properties are common to it regardless of the location. Such properties include: high chloride concentration, high electrical conductivity, high pH (above 8.0), and presence of bio fouling. Seawater is also specified in terms of salinity which is the number of solute (g) in one kg of the seawater. Salinity is closely related to chloride ion concentration and also to the seawater conductivity. The conductivity of seawater is generally between 32 Siemen/meter and 35 Siemen/metre which is also a measure of its salinity (16).

It is noteworthy that chlorinated seawater is more corrosive than a natural sea because of the increase in potential experienced in such environment. Also, bio fouling activities in natural seawater is detrimental to the passivity of stainless steels because of the cathodic reaction involving oxygen reduction (81).

2.8.1 Materials Used in Marine Environments

Materials selection for marine applications is based on the performance as well as the cost of the materials. The initial cost of procurement and the maintenance costs are usually considered alongside the properties of such material (39).

Materials commonly used ranges from cast iron, mild steel, aluminium bronze, stainless steels, nickel and copper based materials. The other major limitation to the choice of these materials is the flow rate of seawater. Materials for marine applications must be able to withstand relatively high flow rate as such can enhance material degradation. Cast iron, mild steels and copper based alloys for instance are not resistant to erosion-corrosion. Nickel based alloys and high alloy stainless steels can combat high flow rate but are limited by economy (39).

2.8.2 Microbial Influence on Marine Corrosion

Microorganisms are abound in natural seawater and they greatly influence the rate of material degradation (83). Their metabolic activities can change both physical and chemical behaviour of a locality along a pipeline (83). Sulfur reducing bacteria (SRB) are believed to accelerate corrosion by consuming the cathodic hydrogen and also help in formation of ferrous sulphides (83). The corrosion behaviour of steels in natural seawater is greatly modified by the activities of microbiological lives which help in accelerating cathodic reactions (81).

2.9 Erosion

The subject of erosion-corrosion is best explained by first looking at pure erosion mechanism. Erosion has been defined as the mechanical removal of materials from a target by the cutting action of particles moving at a high velocity (84). Erosion is considered to be different from corrosion which is the chemical and/or electrochemical removal of materials from the material surface. Erosion is mostly encountered in oil and gas industries, coal turbine; hydraulic turbines, coal hydrogenation industries and rocket engines (84-86). Most erosion problems found in oil and gas industries are as a result of produced sand moving with the hydrocarbons at high velocity and drilling mud that enters and flow through the pipe wall at high pressure as a result of leakages or cracks and loose connections.

Transportation of hydrocarbons through flow lines involves the flow of liquid, gas and sand. The kind of flow that emanates from such multiphase process lead to erosion-corrosion (87). The solid phase and the liquid-gaseous phase hit the wall of

the pipe repeatedly; this results in the erosion of such walls. If such materials are ductile, erosion occurs by displacement and cutting causing detachment of materials of such surfaces. Brittle materials on the other hand erode by interaction and propagation of cracks (84). Ian Finnie (88), proposed the first erosion model for ductile materials. His model is the basis for which subsequent models were developed.

The Finnie model (88) accurately predicted ductile material erosion at low impact angles. It however, failed to predict erosion at high impact angles. Bitter's model (89, 90) on the other hand proposed both deformation wear and cutting wear. He was able to predict high impact angle erosion. The Finnie and Bitter mechanisms of erosion damage are the basis for other models that were later developed to predict erosion rate.

2.9.1 Factors that Affect Erosion

Three fundamental areas to be considered when discussing erosion include the role of solid particles (erodent); the role of the target material and the nature of the fluid carrying the erodent. Erodent characteristics include its size, shape, mass and concentration. Materials target properties to be considered include the hardness, fracture toughness, ductility, surface roughness and microstructure. Fluid characteristics mostly considered are viscosity, temperature and density. Flow characteristics which include the velocity of flow, impact angle of the erodent, flow trajectory and particle interaction are also fundamental to the study of erosion.

The major causes of erosion are cavitation, liquid impingement and solid particle impingement. Cavitation and impingement (solid and liquid) result in fatigue and

abrasion that eventually lead to material loss from the target. This material loss is a function of many variables that can be classified into the slurry variable and the target materials variables (30). Jordan (91), streamlines these variables into materials properties (ductility and brittleness), angle of impact and velocity of the particles. A ductile material behaves differently under the action of erosion to a brittle material. The mode of material removal in ductile materials by scraping or cutting of the target wall during impact while brittle materials first crack and then chip off the target (91). In addition, for ductile materials, higher erosion rate is recorded at lower impact angle (usually getting to the peak between 15 ^{o} and 40^{o}) as compared to brittle materials where the erosion reaches the peak at 90^{o} impact angle as shown in Figure 2.21. Wood (30), reported that the failure of ductile surface is related to accumulated plastic strain which is induced by cyclic plastic deformation from successive impact. For a brittle material, the particle is removed by intersection of cracks which radiates from the point of impact of eroding particle.

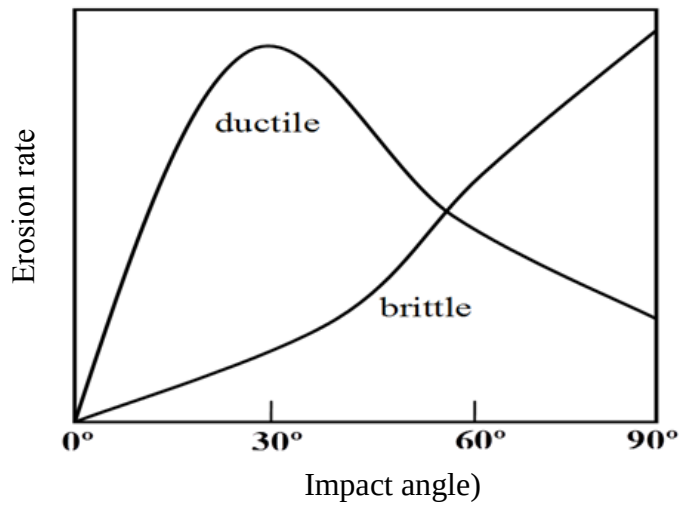

Figure 2.21: Relationship between erosion rate and impact angles for ductile and brittle materials (84)

It has, however, been reported that the hardness of the target material is of little significance when considering the erosion rate of metallic materials (91). It was also reported that as the particle size increases erosion rate increases up to a maximum limit. The relationship between the particle hardness and the erosion rate for steel material is such that erosion rate increases with particle hardness.

2.9.2 Erosion Models

Several models have been developed to predict erosion. The earliest of such models was developed by Finnie (84, 88). One limitation to most of the erosion models is that full documentation, assumptions and limitations are not often stated (92).

2.9.2.1 Finnie's Erosion Model

The mechanistic model developed by Finnie (84) states that wear by erodent is dependent on the motion by the entrained particles as well as the interaction between the particle and the target material. Finnie's model assumed that the entrained particle obeys the law of motion. The volume of material removed from the target during wear is also said to be dependent on the swept area by the erodent. The simple models described in equations 2-41 and 2-42 were able to predict erosion at low angle of impact but failed to predict materials removal at high angle especially 90^{o}.

$$V_r = \frac{mv^2}{p\Psi K}\left(\sin\alpha - \frac{6}{k}\sin^2\alpha\right) \qquad \text{if} \quad \tan\alpha \le \frac{K}{6} \qquad \text{2-41}$$

$$V_r = \frac{mv^2}{p\Psi K}\left(\frac{K\cos^2\alpha}{6}\right) \qquad \text{if } \tan\alpha \ge \frac{K}{6} \qquad \text{2-42}$$

V_r is the volume of materials removed (m^3), m is the mass of the erodent (g), v is the velocity of the erodent (m/s) , K is the ratio of the vertical force component on the particle face to the horizontal force component, p is the plastic flow stress (Pa) ,ψ is the ratio of the depth of contact to the depth of cut, α is the angle of impact (^{o}).

2.9.2.2 Bitter's Erosion Model

Unlike Finnie, Bitter (89, 90) proposed two types of wear mechanism. The cutting mechanism in which the erodent cuts the target during its motion. The second mechanism is the deformation mechanism that occurs by impingement. The impingement is said to cause materials to be broken away from the target material. Bitter model also considered the properties of both the target and the erodent. Energy balance is used to describe how the energy is distributed during collision between the erodent and the target material (equation 2-43). Cutting wear mechanism is represented by equation 2-44 and 2-45. While Finnie related material strength to the energy absorbed during cutting, Bitter's model correlated energy absorbed to the integrated product of the stress-strain curve.

$$W_D = \frac{1}{2}\frac{m(\sin\alpha - U_P)^2}{\gamma} \qquad 2\text{-}43$$

$$W_{c1} = 2mC_1\left(\frac{v\sin\alpha - U_p^2}{\sqrt{v\sin\alpha}}\right)\left[v\cos\alpha - C_1\frac{v\sin\alpha - U_p^2}{\sqrt{v\sin\alpha}}\rho 1\right] \qquad 2\text{-}44$$

$$W_{C2} = \frac{1}{2}\left[\frac{mv^2\cos^2\alpha - k_1(\sin\alpha - U_p)^{3/2}}{\rho 1}\right] \qquad 2\text{-}45$$

W_D is the total deformation wear (cm^3)

C_1 is a constant that depends on density and elastic load unit

W_{c1} is the cutting wear unit when $v \neq 0$ (cm^3)

W_{c2} is the cutting wear unit loss when v=0 (cm^3)

α is the impact angle (^{o})

ρ is the energy needed to scratch out a unit volume from the surface (gf cm/cm^3)

U_p is the maximum particle velocity at which collision is purely elastic (cm/s)

γ is the deformation wear factor (gf cm/cm^3)

k1 is a constant based on mechanical properties

2.9.2.3 Hutchings' Erosion Model

The Hutchings (93) model takes into account both low and high angles of impact. The model assumed that the indentation caused by the erodent forms a rim of plastically deformed region around the indentation. The region becomes work-hardened after several cycles of indentation and thereby detached as wear debris. Work done by the erodent as it comes to rest on the target material is said to be equal its initial kinetic energy. Hutchings expressed the velocity exponent as 2 and the impact angle as Θ. Material removal from the target is said to occur after the accumulated plastic strain has attained a certain value or attain a certain cycle of fatigue. Hutchings also introduced a critical strain to failure factor (2-47). Equation 2-46 presents a low angle wear model where cutting action is predominant. Equation 2-47 and 2-48 present higher impact angles. While equation 2-47 expresses wear as a result of accumulated plastic strain equation 2-48 sees wear as a form of low cycle fatigue.

$$E_m = \frac{K_1 \rho_m v^n}{H_s} \alpha \qquad 2\text{-}46$$

$$E_m = \frac{K_2 \rho_m \rho_s^{1/2} v^3}{\varepsilon_c^2 H_s^{3/2}} \alpha \qquad 2\text{-}47$$

$$\varepsilon = \frac{2^{3/2} v^{1/2}}{5\Pi r_p} \left(\frac{3H_s}{2\rho_s} \right)^{1/4} \qquad 2\text{-}48$$

H_s is the hardness of the target materials (GPa)

K_1 and K_2 are the fraction of materials displaced from the indentation as debris

ρ_m is the density of the target material (g/m^3)

ρ_s is the density of the spherical erodent (g/cm^3)

α is the mean plastic strain rate (S^{-1})

r_p is the radius of the spherical erodent (m)

E_m is the ratio of mass of the material removed over the mass of erodent striking the surface.

2.9.2.4 Hashish's Erosion Model

The deficiencies in Finnie erosion model were addressed by Hashish (94). Higher velocities exponent of values greater than 2, erodent shape and density were taken into consideration. The Hashish model introduced a constant value C_k to take account for the materials flow stress, particle density and shape factor. He also incorporated wear deformation from Bitter's model (94) .

$$E = \frac{14}{\pi} \frac{\rho_m}{\rho_p} \left(\frac{v \sin\alpha - v_c}{C_k} \right)^{2.5} \cot\alpha \qquad 2\text{-}49$$

$$C_k = \sqrt{\frac{3\sigma_s R_f^{3/5}}{\rho_p}} = \frac{V_k}{R_f^{1.2}} \qquad 2\text{-}50$$

E is the ratio of mass of material removed to the mass (g) of abrasive particle

C_k is the modified characteristic velocity that combines the characteristics of both the erodent and the target materials.

2.9.3 API Guidelines for Erosion in the Oilfield

Erosion problems become a serious issue as a result of the ageing oilfield assets. In such situations, operators are not often disposed to using sand screen so as not to reduce production rate (95, 96). To avoid the reduction in production, operators tend to manage sand production by redesigning the facilities.

Since most erosion models are applicable in specific erosive conditions (97) and most often the erosion models might not predict the rate accurately, operators of oilfield are subject to guidelines. One of such guidelines is the American Petroleum Institute Recommendation Practice 14E (API-RP-14E).

According to API-RP-14E, the highest velocity that is allowed for the prevention of erosion in pipelines is given by the expression

$$V_e = \frac{c}{\sqrt{\rho}} \qquad 2\text{-}51$$

V_e = maximum allowable erosion velocity in ft/secs ρ = density (Ib/cuft)

C= an empirical constant (C factor)

However, this equation is not generally ideal for situations where corrosion and erosion are involved because it assumed sand and corrosion free situation for the C

factor (98). However, much other research work has been carried out to factor in the effects of sand and corrosion so that a close to ideal equation of erosion velocity can be attained. According to Salama (98), for a fluid that is free of sand and not corrosive provided there is no pressure drop.

$$V = \frac{400}{\sqrt{\rho m}} \qquad 2\text{-}52$$

Where V is the maximum fluid velocity in ft/sec, ρ_m is the density of the fluid at the flowing temperature and pressure. For fluid where erosion due to sand is prevalent;

$$V = \frac{D\sqrt{\rho m}}{20\sqrt{W}} \qquad 2\text{-}53$$

Where W is the sand flow rate in kg/day, and D is the internal diameter of the pipe.

For multiphase flow Salama (98), added the term that accounts for mixture density and velocity as well as a geometry dependent constant.

$$ER = \frac{1}{S_m}\frac{WV_m^2 d_p}{D^2 \rho_m} \qquad 2\text{-}54$$

where ER is erosion penetration rate, mm/yr; W is sand production rate, kg/day; V_m is fluid mixture velocity, m/s; dp is sand size, micron; D is pipe diameter, mm; ρ_m is fluid mixture density, kg/m^3 and S_m is geometry-dependent constant. Shiraz *et al.* (99) also develop a model to be used for a wider range of operations conditions where geometry type, materials, fluid properties, sand properties (size, shape and density) are considered. The model is thus represented:

$$h = F_M F_s F_p F_{r/D} \frac{WV_L^{1.73}}{(\frac{D}{D_O})^2} \qquad 2\text{-}55$$

where h is penetration rate (m/s), F_M is empirical constant that accounts for material hardness; F_S is empirical sand sharpness factor; F_P is penetration factor for steel (based on 1″ pipe diameter) m/kg; $F_{r/D}$ is penetration factor for elbow radius; W is sand production rate, kg/s; V_L is the characteristic particle impact velocity, m/s; D is pipe diameter (inch); D_0 is reference of 1 inch pipe diameter.

To account for the addition of inhibitors Ramachandran *et al*. (100) added another factor, F_i and came up with the expression below.

$$h = F_i F_M F_s F_p F_{r/D} \frac{W V_L^{1.73}}{(\frac{D}{D_O})^2} \qquad 2\text{-}56$$

2.10 Erosion-Corrosion

Flow-induced corrosion occurs when alloys are exposed to flowing corrosive fluids. The rate of material degradation becomes aggravated by the motion of the flowing fluid (101). When solid particles are entrained within the flowing fluid, the rate of material loss becomes worse. Erosion-corrosion is the term used to describe the flow induced corrosion when solid particle are entrained within the flowing corrosive medium. Erosion-corrosion may also be described as corrosion that is enhanced by erosion and vice versa (101). It is the mechanism of erosion and corrosion taking place simultaneously. Erosion-corrosion is both mechanical and chemical process. It involves wear loss as a result of mechanical abrasion of the protective oxide film and loss due to corrosion action. The protective film is worn by the impacting shear stress of the moving fluid/solid (101). Furthermore, during erosion-corrosion the protective films can be swept away by moving water and solid particles exposing the metal to more corrosion (101). The impact of erosion-

corrosion is mostly significant at sections of a pipe where there is a change in geometry (elbow, bend, orifices etc).

Also, erosion-corrosion takes place when flow is turbulent (101, 102). The solid particles within the turbulent fluid often destroy films/oxide that is formed by corrosion mechanism to allow more corrosion to take place. This form of material loss is aggravated when there is solid suspension in the flowing liquid or gas (103). Such solids cause the erosion while the fluid will be responsible for the material loss by chemical reaction. The material loss by each process when treated separately is not as high as when the two work hand in hand (33). It is worth mentioning that carbon dioxide saturated brine is a common environment in the oil and gas production. For aged well where optimum oil recovery is a challenge, CO_2 is pumped into the well to help in increasing oil and gas recovery (104). Added to this is the problem of sand entrainment that is also unavoidable in the produced fluid. Moreover, sand is produced from rocks as a result of shear or tensile failure during exploitation (105).When oil, gas, water, carbon dioxide and sand are altogether being transported through the pipeline system, and corrosion and erosion are two serious problems the oil and gas industries have to face.

2.10.1 Factors Affecting Erosion-Corrosion

2.10.1.1 Materials

Factors that affect erosion-corrosion can be classified as material and environmental factors (101). According to Roberge (101), materials with different oxides formations behave differently under erosion-corrosion. For instance, oxides can either be thick and porous, thin and compact and thin and invisible. The type of

oxide formed is also a function of the alloying system of the material. Generally, it is reported that the higher the content of the alloying elements especially chromium, molybdenum and copper, the lower the materials loss due to erosion-corrosion (101). Also, apart from the composition of the alloy, other parameters to be considered are the grain boundary, crystal structure and surface conditions.

2.10.1.2 Environmental

The environmental influence on erosion-corrosion can be viewed from the pH, oxygen content, temperature of the environment and other erosivity factors of which the fluid flow and sand condition are part (101). If all other factors are assumed constant, the rate of erosion-corrosion is considered to be dependent on flow rate of the fluid and the solid particles. In liquid-solid flow, the erosion-corrosion rate can thus be written:

$$R = CV^n \qquad (106) \qquad 2\text{-}57$$

Where,

V = Flow velocity (m/s)

The value of n ranges from 1 to 3

When n is close to 1 corrosion is the rate controlling step and when n is close to 3 erosion is the rate controlling step (106).

Other factors that are subsets of the fluid flow are the surface shear stress, turbulence intensity and mass transfer coefficients. The impact of fluid flow exerts pressure on the film formed by corrosion activity. It is the measure of this pressure

that is referred to as the shear stress. For flow induced corrosion, the surface shear stress must exceed the force binding the oxide film to the base material (101).

The effect of temperature on erosion-corrosion of materials can also be viewed from the fact that temperature influences the behaviour of oxidation and reaction processes. However, in general, the effect of temperature on flow induced corrosion is such that it increases the rate of material loss up to a peak, about 135^{o}C for carbon and low alloy steel, and then the rate begins to decline (101).

2.10.2 Hydrodynamic Aspects of Erosion-Corrosion

The study of erosion-corrosion involves fluid flow. Moreover, the effect of near wall turbulent flow on the corrosion of target material can be studied by looking at the mass transfer of the electrochemically active species to the corrosion site or the mass transfer of the corrosion product away from the corrosion site. Another very important parameter to be considered is the wall shear stress which according to Efird (107), is the force in the flowing fluid at the wall of the target materials. This force must be greater than the force binding the oxide film to the wall of the target for it to dislodge the film. Both the mass transfer and wall shear stress phenomenon occur within the diffusion boundary layer (Figure 2.22) of the hydrodynamic boundary layer (101, 107). Wall shear stress and mass transfer coefficient are related by the formula

$$K_d = 17.24 \left(\frac{\tau_w}{\rho}\right) SC^{2/3} \qquad 2\text{-}58$$

Where,

K_d is the mass transfer coefficient (m/s)

τ_w is the wall shear stress (N/m^2)

ρ is the fluid density (Kg/m^3)

Sc is the Schmidt number

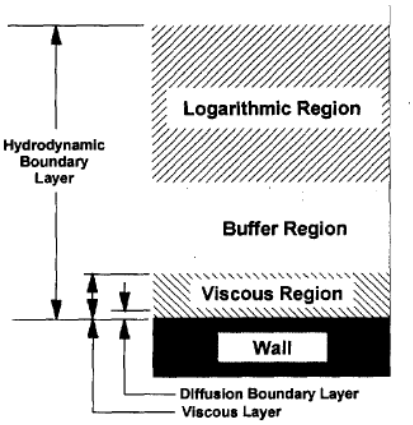

Figure 2.22: Structure of the hydrodynamic boundary layer (107)

The diameter of a pipeline carrying the corrosive medium affects the velocity boundary layer and the diffusion boundary layer. For fluid flowing under the same velocity, the larger the pipe diameter, the thicker the velocity boundary layer . As a result of this the velocity gradient and the wall shear stress is lower for such pipes. Generally in stagnant medium, corrosion rate is low and decreases parabolically with time due to the formation and growth of corrosion protective film. At lower velocity the corrosion mechanism transits to flow accelerated mode. The film formed on the metal surface dissolves due to the action of the moving medium. When the flow velocity is increased to a certain critical level, the protective film is continuously damaged and removed. At this critical velocity the material loss is predominantly by cavitation erosion and droplet impact (101).

Erosion-corrosion may be classified into impingement corrosion and turbulence corrosion. While impingement corrosion occurs in multiphase flow, turbulence corrosion occurs when there is a sudden change in geometry of a pipe leading to high turbulent flow. The motion of the corrosion medium in relation to the corroding metal has a great influence on the rate of corrosion metal. This occurs mostly when the rate is mass-transfer controlled or by impingement of entrained solid (108). Corrosion rate may be increased when the electrochemical active species are transported to the fluid/metal interface. Conversely, the rate of corrosion may be reduced when the aggressive ions are transported away or when inhibitor is transported to the fluid/metal interface (101).

2.10.2.1 Impingement Jet Flow Profile

Among the several methods of studying erosion-corrosion is the jet impingement method. The flow conditions under the impingement condition are easily defined. Such flow profile is shown in Figure 2.23.

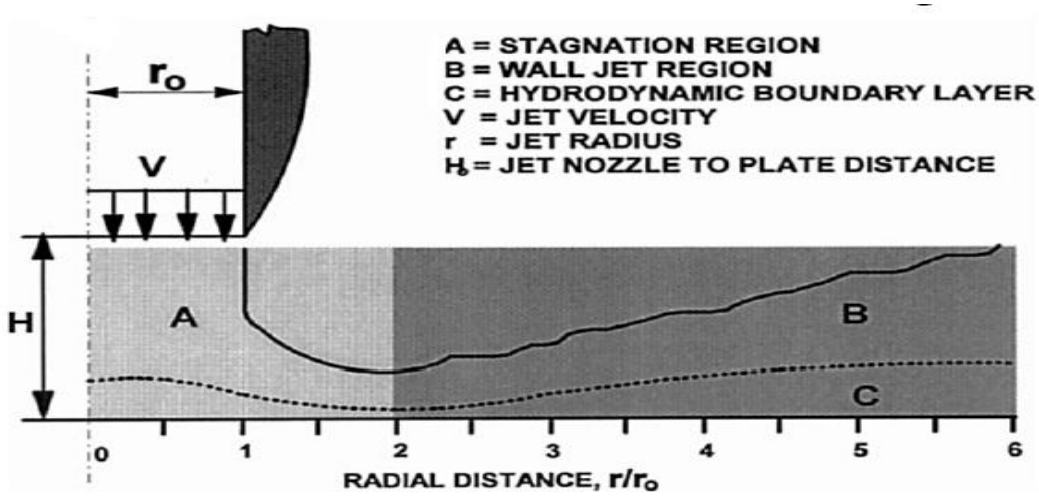

Figure 2.23: The jet impingement flow profile (107)

The flow regime can be characterised into three zones. Zone A is the centre of the stream which is near to the stagnation zone. Flow within this zone is laminar near the surface. Velocity of flow changes from axial to radial and become intense moving out of this zone. The increase in velocity thinned the laminar boundary layer as one moves into zone B. Zone B is the region of high turbulence with high velocity gradient and therefore high shear stress. This is the area most affected by flow-induced corrosion when sand is not entrained within the flow (107, 108).

2.10.3 Material Loss in Erosion-Corrosion

The total mass loss in erosion-corrosion is represented by

$$K = K_{CO} + K_{eo} + \Delta K_c + \Delta K_e \quad (109) \qquad 2\text{-}59$$

Where K is the total rate of weight loss, K_{co} is the corrosion rate in the absence of erosion, K_{eo} is the erosion rate in the absence of corrosion and ΔK_c is change in corrosion rate in the presence of erosion and ΔK_e is the change in erosion rate in the presence of corrosion.

Material loss by erosion and corrosion can be studied separately and the interaction between the two can also be evaluated (33). Watson *et al*. (33), when reporting an experimental result put the total material loss as a result of erosion-corrosion as T [expressed in volume loss (mm^3) per exposed area (mm^2) per unit time (hour)], materials loss due to corrosion alone as C_o (mm/yr), material loss due to wear as W_o [expressed in volume loss (mm^3) per exposed area (mm^2) per unit time (hour)] and came up with an expression for the total weight loss due to erosion-corrosion thus:

$$T = \frac{\Delta M_{wocath} TF}{SA_{wocath} D \Delta h_{wocath}} \quad (2\text{-}60)$$

Material loss due to erosion without corrosion

$$W_o = \frac{\Delta M_{cath} TF}{SA_{cath} D \Delta h_{cath}} \quad (2\text{-}61)$$

Subscript: Cath-means with cathodic protection***;*** Wocath-means without cathodic protection

ΔM= mass loss (g)

SA= surface area (cm^2)

D = density (g/cm^3)

Δh =time of exposure (hours)

Time Factor (TF) = factor to convert time from hour to year ($8.76x10^3$)

The value of i_{corr} from (2-62) can be used to convert the degradation due to corrosion into penetration rates (mm/yr) using equation (2-63)

$$i_{corr} = \frac{\beta_a \beta_c}{2.303(\beta_a + \beta_c) R_p} \quad (2\text{-}62)$$

$$C_o = \frac{i_{corr} CRCF(EW)}{D} \quad (2\text{-}63)$$

Where β_a and β_c are the Tafel anodic and cathodic slopes, Rp is the polarisation resistance and C_o is the penetration rate (mm/yr). D is density (g/cm^3), CRCF is the corrosion rate conversion factor when Faraday's law is used to convert corrosion current to penetration rate (mm/yr) and also includes a time factor to convert from hour to year = $3.27x10^{-3}$ ($\frac{mm\ g}{\mu A\ cm\ yr}$) (110).

i_{corr} (equation 2-63) is expressed in µA/cm^2

EW= equivalent weight

2.10.3.1 Synergism

Synergy has been described as the interaction between erosion and corrosion. Wood and Speyer (111), when commenting on this phenomenon described it as a difficult parameter to determine. They, however, said that it can be calculated with the formula:

$$T = E + C + S \quad 2\text{-}64$$

Where S is the synergy, T, the total material loss, E, the total material loss by erosion alone and C material loss by corrosion alone. Stack *et al*. (109) in their submission believed that synergism of erosion-corrosion and additive of erosion-corrosion can be distinguished from each other. According to their formula

$$K = K_{CO} + K_{eo} + \Delta K_c + \Delta K_e \quad 2\text{-}65$$

The effect becomes additive when the term ΔKe in equation 2-59 is taken off. That is, the term erosion rate in the presence of corrosion is taken off the equation. Meng *et al*. (112) however described synergy as how corrosion assists erosion and additive as how erosion assists corrosion. They came up with the following formula:

the total material loss $T = S + W_o + C_o$ 2-66

Where S has two components

$$S = s' + s'' \quad 2\text{-}67$$

Where s' is the increase in erosion due to corrosion (synergy) and s'' is the increase in corrosion due to erosion (additive).

Hu and Neville (113) also described the total weight loss (TWL) as a result of erosion corrosion thus:

$$TWL = E' + C' + dE_c + dC_e \quad \text{2-68}$$

where E' is the pure erosion component, C'is the corrosion rate under static condition, dEc is the change in erosion rate due to corrosion and dCe the change in corrosion due to erosion. The authors went further to describe the term C'+ dC_e as being equal to C in Eq. 2-64, which is the total material loss by corrosion.

2.11 The Submerged Impinging Jet Rig

The submerged impinging jet (SIJ) rig is one of the various experimental rigs used to study erosion and erosion-corrosion in the laboratory (27, 43, 113, 114). The SIJ is built with a reservoir of 50/70 litres where the electrolyte and the erodent are stored. The mixture of sand and electrolyte is passed through a two-nozzle arrangement and the jet impinges onto the samples from predetermined stand-off distance and at an angle. The advantage of the rig is that both the stand-off distance and the angle of impingement can varied. Electrochemical measurements can also be made by placing the reference and counter electrodes near the nozzles and connecting them to the working electrode. This rig and its mode of operation are further discussed in Chapter 4.

Chapter 3. Literature Review II – Duplex Stainless Steels

3.1 Duplex Stainless Steels

Stainless steels, a prominent member of ferrous alloys with great importance, evolved almost a century ago (115). Since its development, stainless steel has revolutionized the materials world. Their importance is due to the versatility and numerous applications they are used for (116). Duplex stainless steels, one special member of the larger stainless steel family developed about 25years ago, are usually used in many industrial environments. These alloys can be broadly classified into lean duplex, standard duplex and super duplex stainless steels (116).

According to Lo *et al*. (116) and Hussain and Hussain (117), duplex stainless steels are used in the oil and gas industries to withstand corrosion- a major problem that causes failure of pipelines. They are used in the down hole pipes and wellheads, flow lines, umbilical, process piping vessels, mechanical parts, high pressure system and heat exchangers (118). They also find applications in pulp and paper plants (58), chloride containing process fluids, ammonium carbonate solutions, mining and minerals processing industries, fertilizer plants and in numerous other chemical industries (119). Furthermore, duplex stainless steels combine the properties of both austenitic and ferritic classes of stainless steel because of the near balance of austenite and ferrite phases present in its microstructure (120). The properties they offer range from high corrosion resistance in corrosive environments containing chloride ions, very high pitting resistance, good sulphide stress corrosion, good

mechanical strength and ductility, abrasion resistance, erosion resistance and a very good weldability (117).

3.1.1 Metallurgy of Duplex Stainless Steels

During the solidification of duplex stainless steels, ferrite phase first nucleates and solidifies out of the liquid alloy before the diffusion of austenite out of the ferrite matrix. The temperature at which nucleation and growth of austenite from ferrite starts depend on the chemical composition of the duplex steel. Proper cooling rate must be selected to avoid the precipitation of the deleterious phases (sigma, chi, alpha prime) (15). These precipitate phases even at a very low percentage affect the toughness and corrosion properties of duplex steels considerably. Although these deleterious phases can be taken into solid solution by solution annealing and quenching. It is, however, difficult to fit large casting parts into most furnaces. Nevertheless the best microstructure of these alloys is achieved under solution treated conditions.

The solution annealing process is applied to duplex stainless steel after the hot forming operation. This operation is intended to dissolve the intermetallic phases present. The annealing temperature is also a function of the chemical composition of the alloy. However, it ranges from about 1000^{o}C to 1100 ^{o}C from the lean type to the super duplex type. This is the treatment that can actually eliminate the third phases and also help in the balance between ferrite and austenite (120). A near balance of austenite/ferrite ratio gives duplex stainless steels the best combination of properties. The importance of the ferrite–austenite balance is that it helps the alloy to combine the properties of both phases fairly well. For instance, austenite has good weldability

and high toughness while ferrite is susceptible to welding failures but exhibit higher resistance to stress corrosion cracking.

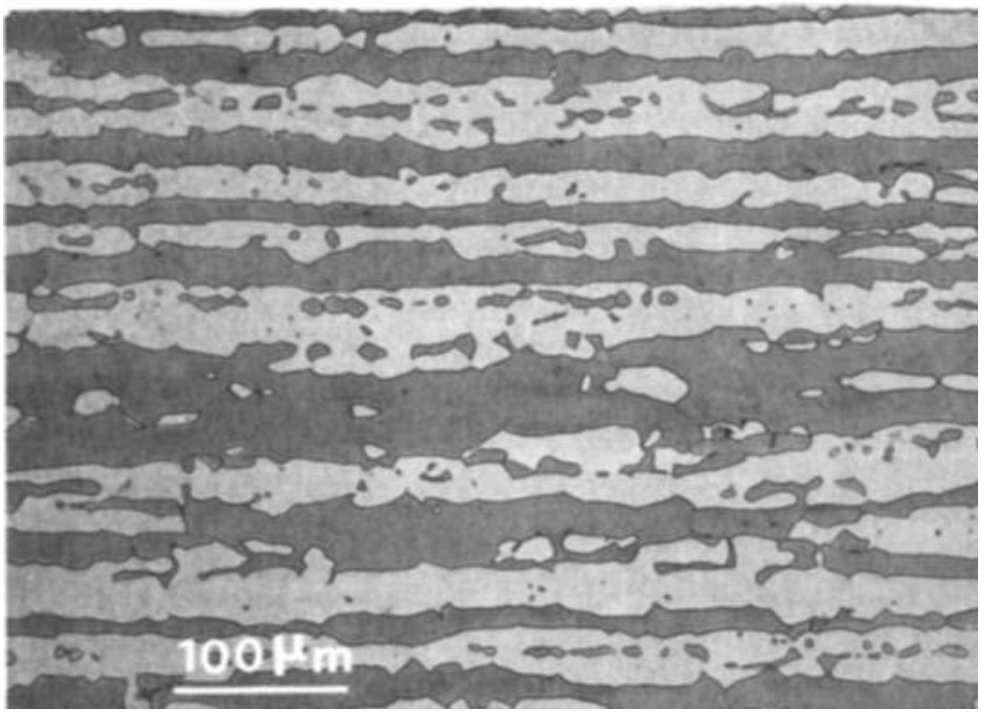

Figure 3.1: Optical micrograph of a typical duplex stainless steel in longitudinal section (121)

3.1.2 Standard Duplex and Super Duplex Stainless Steels

Of all the classes of duplex stainless steels, the most widely used and with highest production tonnage is the standard duplex (UNS S31803/S32205) also referred to as 2205 (115). This alloy started gaining recognitions for gas pipeline long ago. The standard duplex has chromium content of approximately 22%, nickel content of about 5% to 6%, 0.16% nitrogen and about 3% molybdenum. Nitrogen was introduced into the alloying system to increase the austenite reformation during welding thereby reducing higher ferrite and invariably lowers the formation of precipitates which reduces corrosion resistance. The alloy has strength double the conventional austenitic stainless (304 and 316) because of the high strength of ferrite

phase present. Its corrosion resistance is also higher than the conventional austenitic types. These alloys have a Pitting Resistance Equivalent Number (PRE_N) greater than 30 but less than 40 which makes it resistant in chloride environments. One beauty of this alloy is its ability to retain is properties in the as welded condition (15).

The super duplex types are generally known for their high Pitting Resistance Equivalent number (PRE_N) in the excess of 40. They are of 25% Chromium by weight with high molybdenum, reasonable tungsten and nitrogen additions of up to 0.27%. They have better resistance to chloride environment than the standard duplex types but definitely more expensive. One problem with this class is the intergranular corrosion due to the carbide precipitate resulting from the high alloying system.

Table 3-1: Some standard and super duplex stainless steel grades

	Grade	UNS	Cr	Ni	Mo	Cu	W	N	PRE_N
Standard Duplex	2205	S31803	22.5	5	3.2			0.17	36
	Ferralium 255	S32550	26	5.5	3	1.7		0.17	39
	Uranus 47N	S32550	25	6.5	3			0.18	38
Super Duplex	SAF2507	S32750	25	7	4			0.27	43
	Zeron 100	S32760	25	7	3.5	0.5	0.6	0.25	42

3.1.3 Lean Duplex Stainless Steels

The lean duplex stainless steel has lower nickel and molybdenum and relatively lower chromium contents. The lower nickel and molybdenum contents makes it a less expensive alternative to the standard duplex (UNS S32205) and the super duplex (UNS S32570) while the lower chromium contents reduces its susceptibility to sigma formation-sigma phase is mostly formed by thermal ageing, radiation and during the

slow cooling after welding (116, 122). This phase is characterised by high hardness and invariably reduces the toughness of the duplex stainless steel. It is basically a Fe-Cr-Ni-Mo intermetallic compound that is greatly influenced by Cr and Mo diffusion (116, 122). Because this phase is rich in the basic elements that help in corrosion resistance, it deprives the neighbouring matrix of these elements and hence exposes the near neighbour matrix to corrosion.

The low nickel content of lean duplex stainless steels is compensated for by the addition of manganese and nitrogen. Manganese not only acts as an austenitizer but also help to increase nitrogen solubility (19). Nitrogen itself is a very effective austenitizer and structural stabilizer (123, 124). Nitrogen also helps in phase reformation of austenite in the heat affected zone (HAZ) after welding, thereby reduces intergranular corrosion. It is unarguable that the corrosion resistance of this family is not comparable to the standard and super duplex types. Nevertheless, it competes favourably well and less expensive than the 300 series austenitic stainless steels and also serves as economic alternatives to the standard and super duplex types in some environments. The recent developments in duplex stainless steel involve reducing the alloying elements, especially nickel whose market price has been fluctuating and replace part of it with manganese with the steel still having good quality at reduced price (15). Reported studies (14, 16, 17) have shown that LDX2101 (a lean duplex alloy) has better corrosion resistance than 304L. According to Olson *et al*. (17) and Zhang *et al.* (14), LDX2101 has an improved pitting and crevice corrosion resistance which is superior to that of 304L and similar to 316L. Most work on the lean duplex steel has not considered at the behaviour of these alloys in varying environments.

3.1.3.1 Types of Lean Duplex Stainless Steels

Types of lean duplex stainless steels available are the LDX2101 (UNS S32101) or 1.4162, AL2003 (UNS S2003), Uranus 35N (UNS S32304) and more recently LDX2404 (UNS S82441). Of these types, LDX2101 has the highest manganese content of 5% and the lowest nickel content of 1.5%. The molybdenum content is also low (0.5%) but not as low as that of UNS S32304 with Mo content of 0.25%. S32003 with a fairly low Ni content of 3.5% has a relatively lower Mn of below 2% but with high Mo of 1.75%. UNS S32304 with the highest Ni content of 4.4% and Mn of the same range with 2003 has the lowest Mo content of 0.25%. LDX2404 is a new entrance into the lean duplex family. It has a PRE_N very close to UNS S32205 but the nickel and molybdenum contents are lower than that of UNS S32205. This alloy has been developed as an economic alternative to UNS S32205. The lean duplex stainless steels can be distinguished from one another by the differences in their Ni, Mn and Mo contents. All members of this class contain Cr contents ranging from 21.5, 21.0, 23 and 24% for LDX2101, UN S32003, UN S2304 and LDX2404 respectively. Table below describes the composition of these alloys (125).

Table 3-2: Types of lean duplex stainless steels (118)

	ASTM /UNS	C	Mn	Si	P	S	Cr	Ni	Mo	Cu	N	PRE_N
SAF 2304	S32304	0.03	≤1.0	≤1.0	≤0.03	<0.002	23.0	4.4	0.25	0.25	0.11	25
LDX2101	S32101	0.04	5.0	≤1.0	≤0.04	≤0.03	21.5	1.5	0.5	0.5	0.22	26
AL2003	S32003	0.03	≤2.0	≤1.0	≤0.04	≤0.02	21.0	3.5	1.75	-	0.17	30
LDX2404	S82441	0.02	3.0	0.33	0.021	0.001	24.0	3.6	1.6	0.37	0.27	34

3.1.3.2 Mechanical Properties of Lean Duplex Stainless Steels

All members of the lean duplex have similar mechanical properties. The yield strength for all exceeds 450 MPa and the ultimate tensile strength exceeds 620 MPa. They are all ductile with percentage elongation exceeding 25 % (118). The lean duplex steels are tougher than the ferritic and have better corrosion resistance than the austenitic types. Apart from their corrosion resistance, the strength of lean duplex stainless steels is another attractive property especially when compared to austenitic types. Thinner gauges are possible with the use of lean duplex stainless steels which reduce material usage and safe both weight and cost (7).

3.1.4 Materials Used in CO_2 Corrosion and Erosion-Corrosion Conditions

Oil itself is not a corrosive material (except if it contains organic acid) but most substances that flow with it - chlorides; carbon dioxide, hydrogen sulphide and oxygen- are the corroding agents. The component of a well head fluid for instance comprises of chlorides, carbon dioxide, hydrogen sulphide, oxygen, bicarbonates, sulphates, and some elemental ions. Some of these contaminants find their ways into the system by the action of the operators. For instance, hydrochloric, formic and hydrofluoric acids are pumped in to improve formation permeability, concentrated brine is also used for formation pressure (126). From oil and gas production through the refinery to the downstream sector, many channels (flow lines and pipelines) are used to transport oil and gas with the corroding agents. The most used material for this channels is plane carbon steel (X65) (7, 8). This is because it expensive as compared to other alloy steels and stainless steels and can be used with varieties of

inhibitors (8). However, plain carbon steels have shortcomings due to their susceptibility to corrosion. Moreover, most aging oil wells and deep-water/offshore wells produce highly corrosive substances along with the crude oil and gases. These kinds of wells cannot afford to rely on the carbon steels as the pipeline materials. So, the current trend is to use either low alloy steels or stainless steels. Nevertheless, it must also be mentioned that the use of inhibitors with carbon steels is also a very common practice in most oil and gas production (127). However, in some circumstances, inhibitor addition may not be reliable. More so, inhibitors can also have some negative environmental impact. The initial cost of procuring stainless steels might seem too high for the operators of oil and gas field. However, looking at the long time effects and the capital expenditure (CAPEX) versus the operation expenditure (OPEX) balance, it might be reasonable to choose them especially for the more aggressive environments.

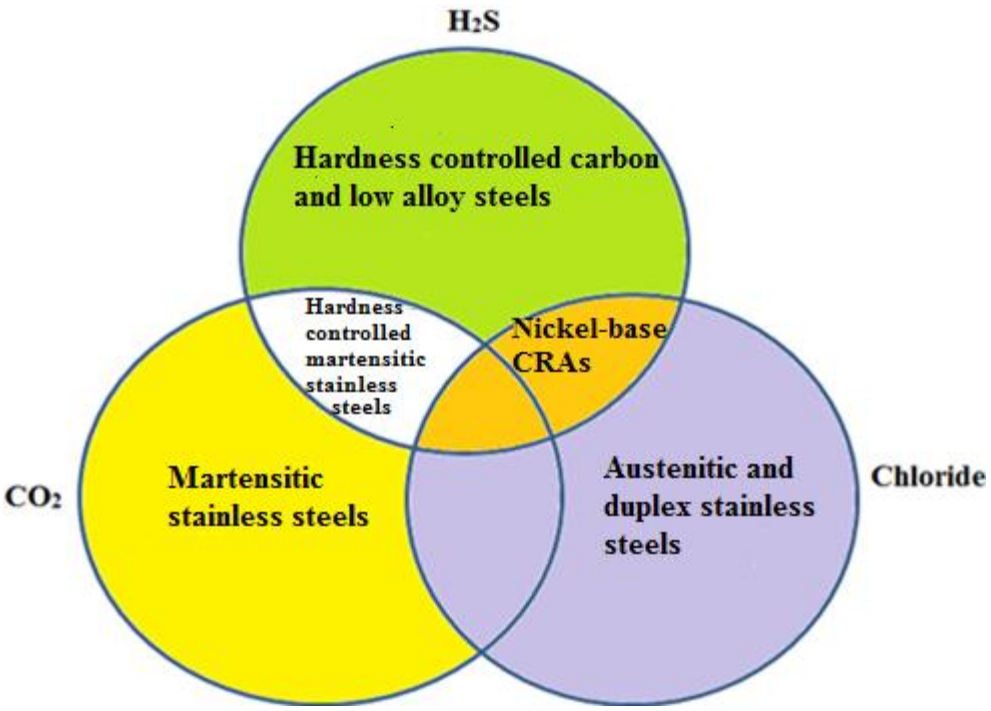

Figure 3.2: Materials used in different corrosion regimes (128)

In sweet environments according to Fu *et al*. (127), Ueda and Takabe (129), API L80 13%Cr (Martensitic) steel is the most widely used (Figure 3.2). This alloy is said to be of high corrosion resistance in sweet environments. However, due to the cost of procurement some oil and gas production companies still prefer to use the less expensive X65 with the help of inhibition especially for low production and for wells that will be operated for a short period (127). Others go for low chromium (less than 2%Cr) steels because it is a better alternative to 13% Cr with regard to stress corrosion cracking and cost (129). Roche (7), reported that the majority of materials employed for pipelines are carbon steels but stainless steels especially duplex stainless UNS S31803 (UNS S32205), and 13% Cr martensitic steels are used for flow lines, short pipelines and for longer ones when inhibition is not effective (high velocity and temperature) or difficult to inject in far and deep offshore. Pendley (128), reported that for CO_2 environments with low levels of H_2S, carbon steel (with proper inhibition) and low alloy steel may be considered when the partial pressure of CO_2 is low. 13% Cr martensitic stainless steel will be effective for CO_2 environments when the temperature is not more than 150^oC, 300 series austenitic stainless steels for environment with the combination of high level CO_2 and chloride. However, for sweet environments with high CO_2, high chloride and relatively high temperatures in the excess of 250^o C duplex stainless steels will be a better candidate.

However, more often, sand and oil are mined together especially in mature oil wells, deep water wells and in sand-oil systems. It is essential to have materials which can withstand both the aggressive corrosion environments and the erosive damage by the sand particles. Jones and Llewellyn (130), reported that carbon steels

have the least resistance to erosion-corrosion; 316L stainless steels have better corrosion resistance than carbon steels but also show inferior erosion-corrosion when compared to the duplex stainless steels. However, most often the cost of the 22Cr duplex stainless steel make the oil and gas industries go for the less expensive but not very effective 13Cr (8).

The most applied materials for CO_2 erosion-corrosion resistance are carbon steels (with inhibition), 13Cr, super martensitic stainless steels and the duplex stainless steels.

3.1.4.1 Application of Lean Duplex Stainless Steels in Oil and Gas Industries

Lean duplex stainless steels are popular in construction and building industries for the fabrication of containers and vessels (118). The application in building construction is mainly due to its ease of fabrication, high strength and aesthetics. Applications of lean duplex stainless steels in the oilfield are due to their corrosion resistance capabilities, better yield strength and attractive economy as compared to the 304 and 316 family. Lean duplex stainless steels also became popular due to the high cost of standard and super duplex stainless steels, the unreliability of martensitic stainless steels in slightly sour environments (129), and weak resistance of martensitic stainless steels to sea water (14). Presently, the lean duplex stainless steels find applications in flow lines that connect well heads with production units, flexible pipes (carcass), umbilical tubing, water injection lines, for construction of transport vehicles and topside oil and gas installations such as heat exchangers, separation units, cable trays etc (12).

3.2 Corrosion Properties of Duplex Stainless Steels

The alloying elements in the duplex steel play important roles in their corrosion properties. Chromium, molybdenum, nickel and nitrogen are the principal elements that determine the corrosion resistance of these alloys. The carbon content also has to be extremely low to avoid carbide precipitation (131). These alloying elements can be classified as ferrite formers (Mo and Cr) and the austenite stabilizers (Ni and N). Chromium increases the general corrosion resistance of duplex steels while molybdenum enhances the resistance to pitting. These two elements are mainly taken into the ferrite phase while nickel and nitrogen are partitioned into the austenite phase. Nitrogen particularly is an essential member of these alloying elements because it performs so many functions such as: structural stability, pitting resistance, austenite former and reformer and inhibiting the formation of the precipitate phases – nickel is also a powerful austenite former (131). Chromium and molybdenum are helpful in passivation and repassivation while copper (58, 132) (when present) is an alloying element that raises the erosion-corrosion resistance of most duplex stainless steels. Sulphur is a deleterious element that combines with most oxide to form precipitates that eventually act as sites for pitting (15).

The major parameter used to rank the localized corrosion behaviour of the duplex stainless steels is the Pitting Resistance Equivalent Number (PRE_N). This number is denoted by %Cr +3.3%Mo +16%N or sometimes %Cr +3.3%Mo +16%N+1.65%W. PRE_N indicates resistance to pitting and chloride induced corrosion and can be used to classify the duplex family (15). The lean duplex stainless steels have PRE_N greater than 20 but lower than 30, standard duplex have PRE_N greater than 30 but lower than

40 while super duplex have PRE_N greater than 40. It invariably means that super duplex stainless steels have higher resistance to pitting and stress corrosion cracking as compared to the other two members (58).

One major problem with the highly alloyed duplex stainless steels is the formation of the third phase (precipitate phase). This is essentially due to the high chromium, molybdenum and nitrogen. Moreover, molybdenum and chromium are generally comfortable to form carbide precipitate when the heat treatment is not properly done. These precipitates are richer in the said elements and thereby render the surrounding matrix deficient in chromium and molybdenum hence the matrix is exposed to corrosion (120). Formation of the precipitates is not high in the lean duplex (2101 and 2304) because of the lower alloying system essentially near zero molybdenum.

Another major corrosion problem of duplex stainless steels is the Hydrogen Induced Stress Corrosion (HISC). This occurs mostly on the ferrite phase. So, duplex stainless steels perform better in environment of high CO_2 partial pressure in the presence of chloride and relatively high temperature with a very low H_2S partial pressure (128, 133). They are the perfect alloys for chloride environments because of their high resistance to pitting and SCC. The nitrogen enhanced duplex stainless steels are also very resistant to intergranular corrosion essentially due to the ability to reform austenite even after welding (131). Getting the proper corrosion resistance involves proper alloying during melting and making sure the alloy is properly heat treated and also ensuring proper welding procedure during fabrication. Annealing temperature can change the volume fraction of both ferrite and austenite. It can also

lead to precipitation of the deleterious phases which affect the corrosion behaviour of these alloys (134).

Little attention has been given to CO_2 corrosion of duplex stainless steels as that given to carbon steels, low alloy steels and martensitic stainless steels (135). The corrosion resistance of stainless steels rests on its ability to repassivate in the corroding medium. The major problem of high CO_2 dissolution is local corrosion (mesa attack and pitting). Duplex stainless steels are selected for environments of high CO_2 partial pressure in the excess of 0.02 MPa and temperature tending to 200-250^oC. This is because the plain carbon steels become ineffective at pressure higher than 0.02 MPa and temperature higher than 150 ^oC. Also, 13%Cr steels are limited to environments with extremely low H_2S concentration and temperature lower than 180^oC with little or no chloride concentrations. Duplex stainless become the candidate where there is high CO_2 partial pressure, relatively high temperature, high chloride and reasonable H_2S partial pressure (16, 128).

3.3 Erosion-Corrosion of Duplex Stainless Steels

Duplex stainless steels are designed for applications in aggressive oilfield and marine environments where both corrosion resistance and mechanical properties of austenitic stainless steels would be inadequate (23). The standard duplex and super duplex has been reported to exhibit good wear-corrosion resistance due to the high hardness and the ability of the austenite phase to work-harden. In the same investigation, it was reported that the erosion-corrosion behaviour of the duplex stainless steels can be related to the volume fraction of the austenite phase and the flow rate of the slurry (128). Researchers in this field have also attributed the high

erosion-corrosion resistance of duplex stainless steels to their ability to repair the breakdown oxide after the liquid-solid impingement (27, 117, 130).

The erosion-corrosion resistance of super duplex stainless steel UNS S32760 has been reported to be better than that of a superaustenitic stainless steel when tested under marine conditions (112). Meng *et al.* (112) also reported that pure erosion contributed the highest damage to the total materials loss. Bargmann *et al*. (136) also made the same observation when they studied the erosion-corrosion of a super austenitic stainless steel. It was reported that pure corrosion contributed only about 1% of the total material loss while the highest damage was by erosion. Neville *et al.*(27) compared the erosion-corrosion resistance of UNS S32205, UNS S31603 and a carbon-manganese steel and found the duplex stainless to be the best among the three alloys. These authors also showed that the material removal is predominately by erosion when the passive film becomes ineffective under the highly erosive liquid-solid impingement (Figure 3.3).

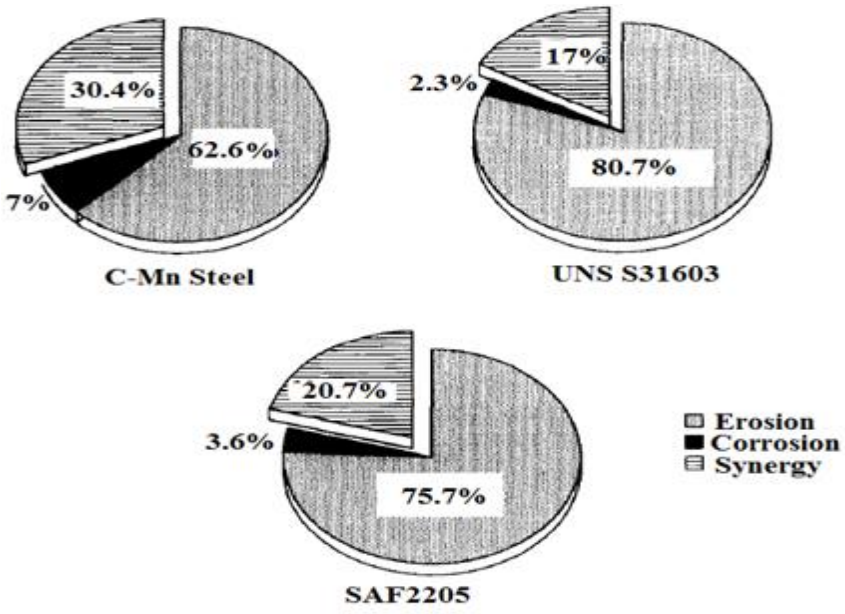

Figure 3.3: Breakdown of total weight loss under erosion-corrosion at 50^{o}C (27)

In another development, it was reported that the extent to which the passivating film can assist in preventing erosion-corrosion is limited though it was agreed that it has the ability (117). Oh *et al*. (137) investigated the corrosion-wear behaviour of biomedical materials for implant in simulated human body fluid and reported that a high molybdenum and high nitrogen austenitic stainless steel could be a substitute to the conventional materials for implants in frictional environments. This, the authors reported, was because the material exhibited comparable erosion-corrosion resistance to the conventional materials due to its ability to passivate. Conventional austenitic stainless steel with high nickel content are believed to cause allergy in human bodies when used as implants (118). Generally, high manganese and low nickel duplex stainless steel are believed to possess better corrosive wear primarily because of the similarity of the austenitic phase with the Hadfield manganese steels (116).

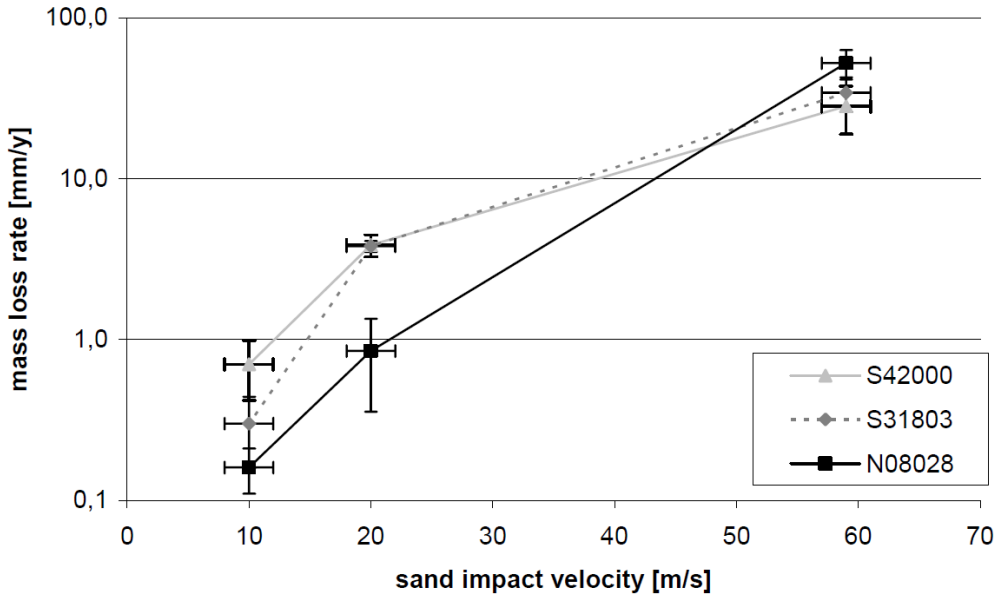

Figure 3.4: Effect of alloying on erosion-corrosion (138)

The effect of PRE_N on the erosion-corrosion of some stainless steels (martensitic (S42000), duplex (S31803) and superaustenic stainless steels (N08028) was investigated by Haberl *et al.* (138). The outcome of the investigation showed that at a low impact velocity, lower than 20m/s, in multiphase slurry, the erosion-corrosion resistance of the alloys depend on the PRE_N. However, at higher impacting velocity between 20 and 60m/s, the effect of PRE_N on the erosion-corrosion of the materials becomes insignificant. The results showed that the martensitic stainless (S42000) steel with PRE_N of 12.2 shows similar erosion-corrosion behaviour with the duplex stainless steel (S31803) with PRE_N 36 and the superaustenitic stainless steel (N08028) with PRE_N of 42 (Figure 3.4). It was reported that at higher impact velocity, the material loss is predominantly mechanical (independent of PRE_N) but that at the lower impact velocity, both corrosion and erosion interplay (138).

3.4 Corrosion and Erosion-Corrosion Resistance of Lean Duplex Stainless Steels

There is no doubt that much research have been carried out to study the corrosion resistance of lean duplex stainless steels. The pitting corrosion resistance and the critical pitting temperature have been found to be better than the standard austenitic types (18). Lean duplex stainless steel, UNS S32101 has been reported to have very good resistance to stress corrosion cracking (139). This alloy is said to have the best combination of strength and corrosion resistance among the lean duplex stainless steels (12). UNS S32101 has also been reported to be a good substitute for the 300 series austenitic stainless steels for corrosion and structural applications (139).

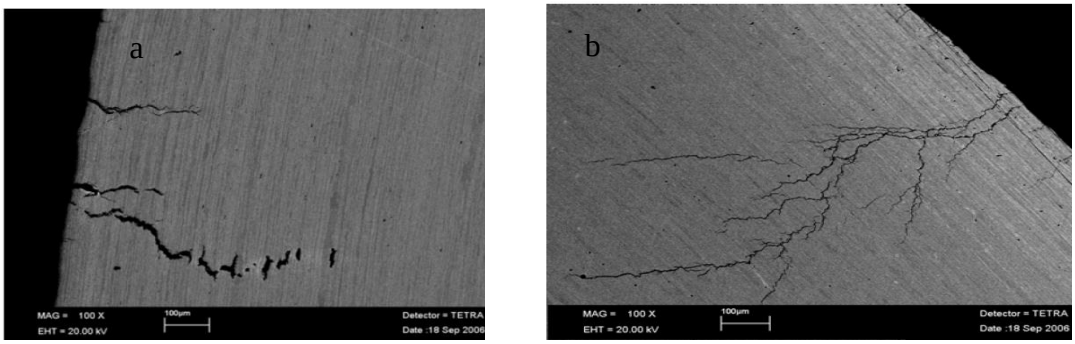

Figure 3.5 : SEM images representatives of crack propagations in (a) UNS S32101and (b) UNS S32205 after stress corrosion cracking tests in 45% $MgCl_2$, 150^oC for 24 hours (139)

Surprisingly, the Stress Corrosion Cracking (SCC) resistance of UNS S32101 lean duplex stainless steel under constant strain loading has been reported to be similar to that of standard duplex stainless steels Figure, 3.5 (139). Localised corrosion resistance of UNS S32101 has also been reported to be better than UNS S30403 (140). The pitting behaviour of this alloy also compares favourably well with UNS S31603 (140). Wei *et al.*(14) studied the mechanical and corrosion properties of a lean duplex steel which has similar chemical composition to UNS S32101, in a chloride medium. These authors found the critical pitting temperature of the lean duplex stainless steel to be higher than that of UNS S30403 austenitic stainless steel. In another development, the suitability of UNS S32101 as a substitute alloy for UNS S31603 in the carcass of an unbounded flexible pipe was carried out (12). It was reported that the UNS S32101 with higher strength, better corrosion properties and lower cost is a favourite candidate for such application. However, despite the above literature on corrosion resistance of UNS S32101 and the abundant literatures (25-31, 111, 112, 117, 130, 137, 141-143) on of erosion-corrosion of other passive alloys,

there is limited information (136) on the erosion-corrosion behaviour of lean duplex stainless steels.

3.5 Repassivation Kinetics of the Passive Film Formed on Lean Duplex Stainless Steel

Passive alloys are protected from corrosion by the thin layer of passive oxide formed on their surface. Under mechanical wear however, this passive oxide could be removed or thinned and this would increase the corrosion susceptibility of the alloy. The passive film removed, nevertheless tries to repassivate by the oxidation of the exposed bear metal/alloy. In the course of repassivation, an anodic current flows which can be measured in a potentiostatic experiment. The measured anodic current is usually used to study the repassivation kinetics of the passive film (144). Several authors have proposed different models to discuss passive film growth (68, 145, 146). Burstein and Davenport (147), Jemmely et al. (66) modelled current transients for tribological actions using film growth kinetics and ohmic resistance of the solution. All the authors assumed that

1. All the current measured is used in the film formation
2. Film growth follows the high field conduction mechanism.

The same mechanism in tribo-corrosion (scratch or rubbing method) is also applicable to solid particle impact. During solid particle impact, the passive film is removed. However, if the passive film can regenerate fast, the alloy will remain corrosion resistant. The total amount of material loss by the impact of erodent and that of corrosive medium is a function of the behaviour of the passive film. The

generation rate of fresh metal surface and the repassivation rate of the alloy are two important factors that determine the erosion-corrosion resistance of such alloys. Erosion can also be detrimental to the pitting resistance of alloys especially if the repassivation rate is low. The erodent generates rough surfaces which easily trigger pitting. Therefore, an alloy with lower repassivation rate is likely to be more susceptible to pitting than alloys with a high repassivation rate. It then means that the study of the ability of passive film to regenerate after depassivation is very important (32, 65)

Much work has been done on the study of the repassivation kinetics of damaged passive film on stainless steels. Several models have also been developed to describe passive film growth (66, 147, 148). One agreement by most authors in this field is that the passive film and their repassivation kinetics are functions of the alloy chemistry (Figure 3.6), applied potentials, pH and chloride ion concentration of the environment (70, 149, 150). According to Lee (70), an increase in chromium content increases the repassivation rate of an Fe-Cr alloy (Figure 3.6).

According to this report, an addition of nitrogen and molybdenum also raises the repassivation rate (Figure 3.6). Hoshimoto *et al*.(151) and Lee (70) examined the repassivation kinetics of some stainless steels with molybdenum additions in a chloride-containing solution using abrading method. Silicon carbide (SiC) disc was used to abrade the working electrode while immersed in the electrolyte to acquire current transients. The conclusion of these authors is that molybdenum-containing alloy repassivates faster than the other alloy without molybdenum.

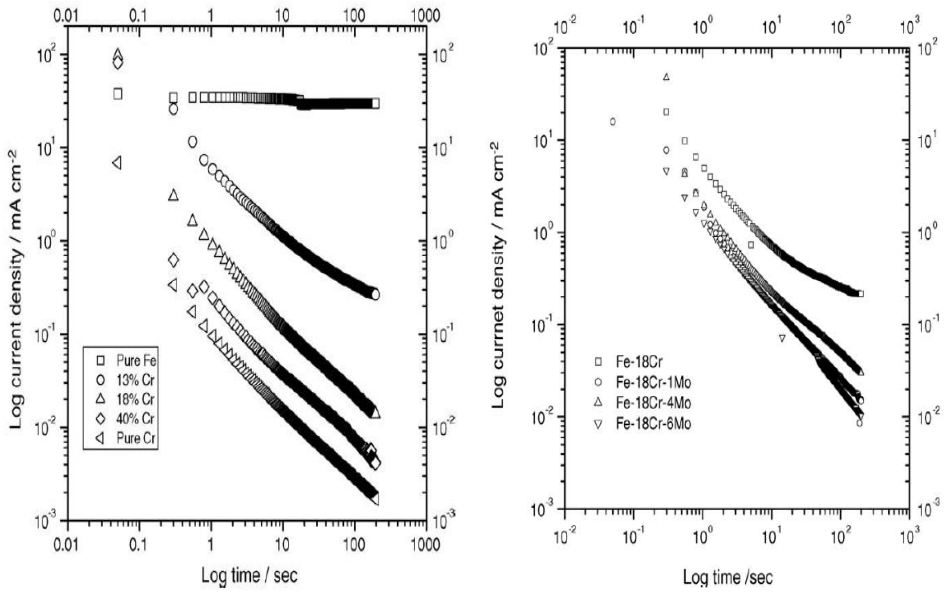

Figure 3.6: Effects of alloying elements on repassivation kinetics of austenitic stainless steels (a) chromium (b) molybdenum (70)

Manganese is believed to have a detrimental effect on the general corrosion of stainless steels because of MnS inclusions. However, according to Toor *et al*. (152), the effect of Mn on pitting corrosion resistance of Fe-Cr-Mn alloys is still controversial. The effect of Mn on repassivation kinetics is still rarely studied. Toor *et al*. (152) while studying the repassivation behaviour of two nonstandard high manganese, low nickel stainless steel alloys and austenitic stainless steel 304 in deaerated 0.5M NaCl solution came up with the following conclusions: that repassivation kinetics of high Mn stainless steels are similar to the austenitic and ferritic stainless steels but that repassivation rate decreases with increase in Mn content. Yamamoto *et al.* (153) studied the repassivation behaviour of three stainless steels (304, 316L and 312L) in 0.9 M NaCl solution. These authors found out that indentation not only ruptured the passive film but also that the indentation might introduce stress, dislocation and probably a change in the microstructure. These

authors also align with the fact that the effect of plastic deformation caused by indentation on the pitting behaviour of the substrate alloy is complex. Data available in literature is very inconsistent. Some researchers believe that plastic deformation by cold rolling increases the pitting potential of stainless steels (154), while others argue that the pitting potential is shifted to a more active direction by plastic deformation (155). Yamamoto and co-workers (153) align with the former argument saying the pitting potential is not shifted in the cathodic direction because the stress is compressive.

3.6 Passive Film Chemistry and their Breakdown

There is no doubt that the composition of the passive film on stainless steels is influenced by alloy constituents (156, 157), composition of the environment, chemical stability of the passive film (156, 158) and diffusivity of the alloying elements through the film. It has been argued that pure Cr_2O_3 should give the best protection against breakdown of passive film (158, 159). However other impurities as well as lower valance ions often lead to point defects and thereby increase mobility of the deleterious species such as Cl^- ion through the passive film to the reactive substrate of the alloy.

Many investigations have been carried out on the passive film characteristics of the standard and highly alloyed austenitic stainless steels (156, 157) and highly alloyed duplex stainless steels (157). However, there are few studies on the subject of passivity of lean duplex stainless steels (160). The lean duplex stainless steels UNS S32101 with 5wt% Mn is an alloy of interest due to the negative effect of Mn, in form of MnS inclusions. MnS inclusions have been shown to be present on the

surface of such alloys affecting the pitting behaviour (161). Mn is said to form the detrimental MnS in alloys with high sulphur content although modern metallurgy has made it possible to produce ultra-low sulphur steels. Mn is an active element like Fe and could also be dissolved from the passive film (162, 163) leaving the passive film porous. It should however be noted that Mn could contribute positively to the properties of stainless steels. For instance, Mn is said to enhance the solubility of nitrogen. This means that with addition of Mn into a low sulphur steel and with high solubility of N_2, there will be low nitride formation during welding of such steels (160).

Much research has been directed towards the study of passive films formed in seawater, HCl, HNO_3 ,$FeCl_2$ and artificial saliva (157, 158, 162). However, there is little information on the passive film formed in CO_2-saturated environment and the nature of oxidation of Mn in the passive film formed on austenite and ferrite phases in duplex stainless steels. Recently, Frediksson *et al*. (160) reported that Mn is present in the passive film of both 316L and UNS S32101 but that the Mn was enriched in 316L. Their argument was that Mn is likely to be preferentially oxidized and absorbed into the passive film formed on the austenite phase more than the dual (ferrite+austenite) phase of the lean duplex UNS S32101. Anselmo and co-worker (163) also reported that a synergy existed between CO_2 and chloride ion on the breakdown of passive film formed on 13Cr stainless steel. The breakdown potential for the alloy was found to be more positive in aerated seawater than a CO_2-saturated solution with the same chloride concentration and at higher chloride concentration. However, this reversed at lower chloride concentration. The nature of interaction between CO_2 and chloride ion is still not well understood.

3.7 Relationships between Subsurface Morphology and Erosion-Corrosion

It has been argued by many authors that current modelling approach has not been able to predict accurately the total material loss by the synergistic effect of both erosion and corrosion primarily because of the complexity of the interaction. Despite the abundant attempt to predict erosion-corrosion, few researchers have considered the effects of the sub-surface morphology and crystallography of the layer of the bulk alloy just below the passive film, Figure 3.7 (35, 36).

It is on record that this thin layer of the modified part of the bulk alloy have received better attention under tribo-corrosion and tribo-bio-corrosion in form of sliding wear and micro abrasion-corrosion. Attempts have, however, been made in the past to modify the surface and sub-surface morphologies of alloys to increase their erosion-corrosion resistance (164, 165).

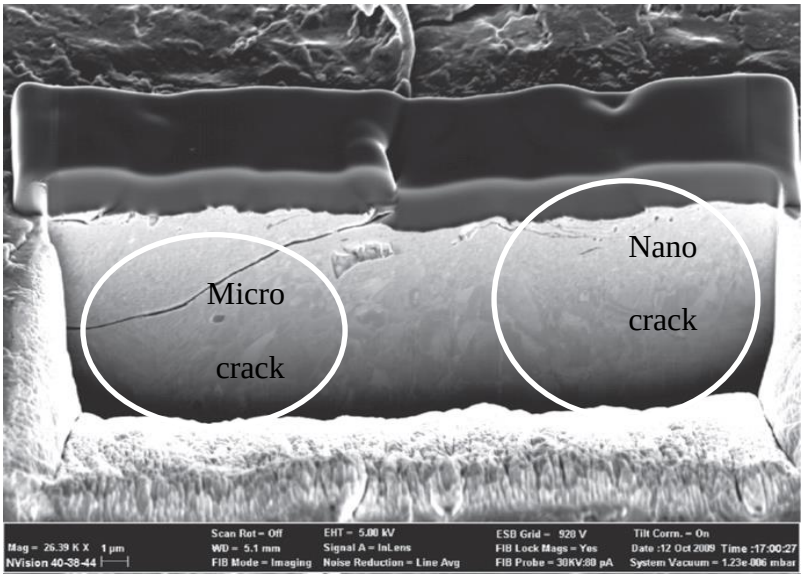

Figure 3.7: FIB cross-section of UNS S31603 stainless steel after erosion-corrosion for 1 hour in 3.5 % NaCl showing micro and nano-cracks beneath the impacted lip (35)

One way such modification could be achieved is to increase surface/subsurface hardness by strain hardening. If the strain is large enough, features below the impinged surface could undergo crystallographic and microstructural modifications as well as grain refinement. Buscher and Fischer (166) reported a multilayer structure consisting of an outer nano-crystal layer, a stuctureless layer at the middle and a layer consisting of stacking fault and ε-martensite below the structureless layer on a CoCrMo after tribo-corrosion of all metal hip joint. Bidiville *et al*. (167) also found the same nano-crystal structure on the outer layer of a 316L stainless steel after tribo-corrosion in sulphuric acid. These authors also reported a strain-induced martensite layer below the surface of the nano-crystal.

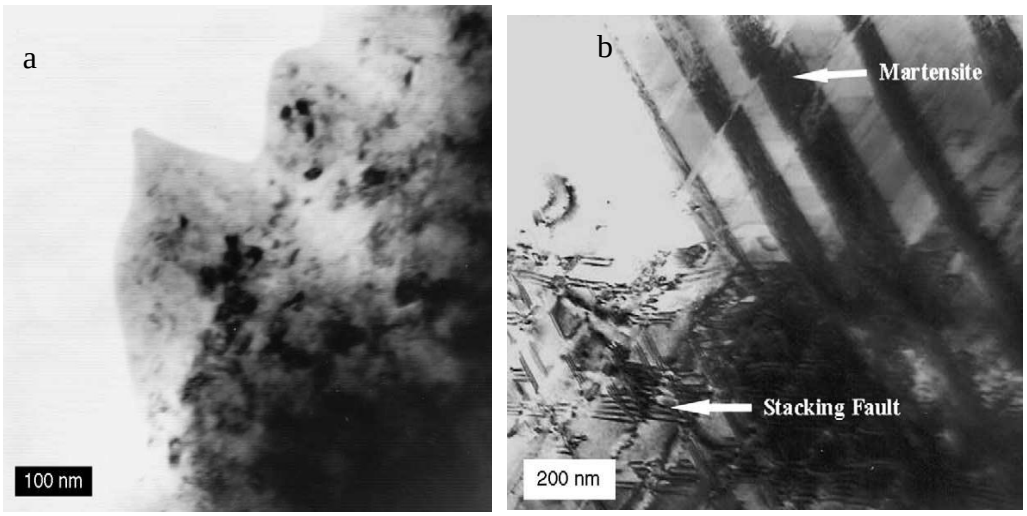

Figure 3.8: A low carbon CoCrMo disc rubbed by a pin with a load of 5N for 30 hours (a) top layer (less than 1µm) showing nano crystalline structure (b) stacking fault and martensite needles about 30 µm below the worn surface (166)

Sub-surface modification by solid particle erosion was also studied by Ives and Ruff (168) and Edington and Wright (169, 170) confirming that solid particle erosion resulted in build-up of dislocation density and grain refinement below the surface of

alloys that have undergone solid particle erosion. Mohammed and Luo (28) recently studied the effects of cold work on erosion-corrosion of 304 austenitic stainless steel by cold rolling the alloy to specific sample thickness. They reported a decrease in the erosion-corrosion rate of the alloy with an increase in the cold working up to 5% thickness reduction.

The use of SEM has been extensive in understanding the surface morphology of the deformed alloy under erosion-corrosion. However, as a result of the high resolution involved in understanding the structure and composition of the surface beneath the deformed surface of alloys, the use of SEM for such is limited (35). However, Electron Backscattered Diffraction (EBSD), Transmission Electron Microscope (TEM) and Focused Ion Beam (FIB) are gaining popularity in the study of sub-surface morphology of deformed alloys in transverse sections (35, 36). Recently Rajahram and his co-workers (35, 36) used the FIB and TEM to characterise the sub-surface morphology of UNS S31603. They found that the evolution of crystallography and martensitic transformation (Figure 3.9) below the surface contributed to the erosion-corrosion synergy. This also corroborates the work of Lu and his co-workers (Figure 3.9b) (171) on the corrosive wear behaviour of stainless steels in sulphuric acid medium using a modified pin-on-ring tester.

However, lean duplex stainless steel alloys have not been considered for evaluation by these authors. Additionally, none of the aforementioned tests was carried out in a simulated CO_2-saturated oilfield environment and the use of the Submerged Impinging Jet (SIJ) to study the subsurface transformation of alloys under erosion-corrosion has not yet been considered.

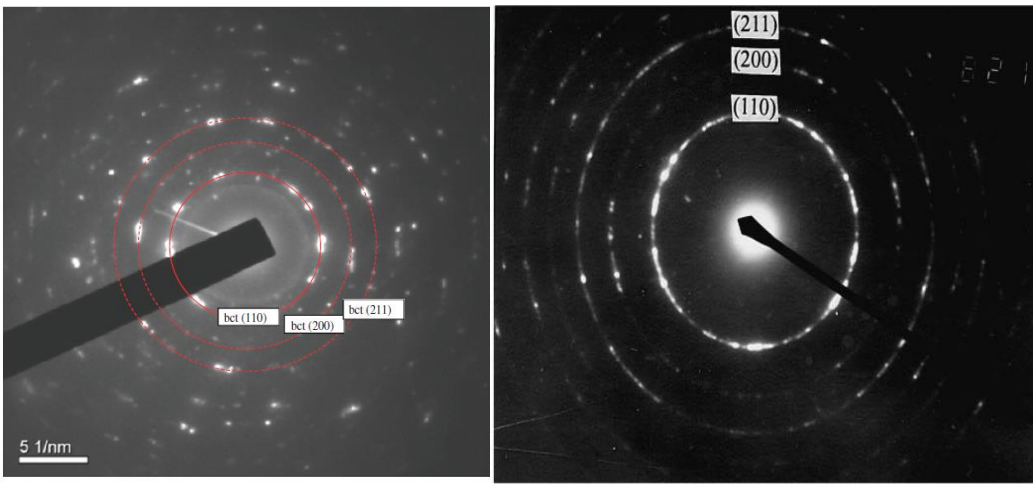

Figure 3.9: Selected Area Electron Diffraction (SAED) of austenitic stainless steel showing the transformation from FCC to BCT crystal structure (a) erosion-corrosion at 7 m/s in a 3.5% NaCl slurry (35) (b) tribo-corrosion (pin-on-ring) in sulfuric acid (171)

3.8 Summary of Literature Review

Lean duplex stainless steels are among the new alloys employed for pipeline applications in the oilfield environments. However, despite the abundant literature on the subject of erosion-corrosion of other passive alloys and the localized corrosion behaviour of these alloys, there is limited information on the erosion-corrosion behaviour of lean duplex stainless steels. Bargmann (55, 136) reported that lean duplex stainless steel (UNS S32101) performance under erosion-corrosion conditions is comparable with highly alloyed austenitic stainless UNS S31254.

Efforts have been made in the past to study passive films formed on passive alloys in aerated seawater, HCl, HNO_3 ,$FeCl_2$ and artificial saliva (157, 158, 162, 172). However, since stainless steels are also widely used in sweet oilfield environments, information on the passive film formed in CO_2-saturated environment is of interest to the operators of the oilfield. Moreover, the nature of interaction

between CO_2 and the chloride ion on the behaviour of the passive film is still not well understood.

The influence of the sub-surface modifications on tribo-corrosion behaviour of stainless steels has received more attention under sliding wear and micro abrasion-corrosion conditions. In the past, attention has always been on austenitic stainless steels and cobalt-chromium alloys for applications in bio-tribo-corrosion and acidic environments. Rajahram (35) reported a change in subsurface morphology and microstructure of UNS S31603 austenitic stainless steel after erosion-corrosion at 7 m/s in aerated conditions. Neither of the aforementioned tests was carried out in a simulated CO_2-satuarted oilfield environment nor did they consider the lean duplex stainless alloy. Surprisingly also, UNS S30403 with a better work-hardening characteristic than UNS S31603 was not considered for evaluation under the erosion-corrosion conditions. Additionally, the use of the Submerged Impingement Jet (SIJ) to study the subsurface transformation of alloys under erosion-corrosion has not yet been considered.

Much work has been done on the study of the repassivation kinetics of damaged passive films on stainless steels. Previous methods that have been used extensively for the study of repassivation kinetics of passive films include: abrading electrode technique (70), scratching electrode technique (161, 173), cavitation technique (65) as well as micro and nano indentations (153, 174-177). Single impact by sand and glass beads has also been considered for austenitic stainless steels (31, 178). However, none of these previously-reported experiments have been carried out in a CO_2-saturated oilfield environment. Additionally, the repassivation behaviour of lean duplex stainless steel UNS S32101 has not been considered for evaluation in CO_2-

saturated oilfield conditions. Finally, the use of the Submerged Impinging Jet (SIJ) for such investigation has not yet been considered.

Chapter 4. Methodology

4.1 Introduction and Chapter Overview

The focus of this research is to extend the knowledge on the subject of corrosion and erosion-corrosion behaviour of lean duplex stainless steels in static and flow-induced (erosion-corrosion) oilfield environments. As a result, several methods have been adopted to achieve the objectives set out for this study. For the static corrosion conditions, the breakdown potentials of six alloys were determined. Passive film chemistry of two lean duplex alloys UNS S32101 and UNS S32304 was also determined after exposure to the environments at the open circuit potential for twenty four hours. These two lean duplex alloys were chosen because of the difference in their manganese additions as well as their close pitting resistance equivalent number (PRE_N).

Under flow-induced corrosion conditions, four alloys were considered. Erosion-corrosion behaviour of these alloys was studied in a submerged impinging jet (SIJ) rig in aerated and in CO_2-saturated conditions at 15 m/s impinging velocity. Two of the alloys, UNS S32101 and UNS S30403 representing lean duplex and standard austenitic stainless steel families, were later selected for an in-depth study. Repassivation kinetics of the passive film formed on these alloys was studied in CO_2-saturated oilfield conditions. A higher velocity of 24 m/s was also used to study the erosion-corrosion behaviour of these alloys in a CO_2-saturated oilfield brine.

4.2 Stainless Steel Alloys Used for this Study

Six different stainless steel alloys were used for the static corrosion evaluation in the initial stages. These comprise standard austenitic stainless steels (UNS S30403, UNS S31603), lean duplex stainless steels (UNS S32101, UNS S32304 and UNS S82441) and a standard duplex stainless steel (UNS S32205). The number of the alloys was later reduced to four (UNS S30403, UNS S32101, UNS S32304, UNS S32205) for erosion-corrosion conditions. The four alloys were chosen to have representations of each class of the alloys. Two grades of lean duplex stainless steels were chosen because of the interest of this research on such alloys. Passive film chemistry of the two lean duplex alloys (UNS S32101 and UNS S32304) was also studied in static corrosion conditions. In the later stage of this research, the alloys were eventually streamlined to two (UNS S30403, UNS S32101) as discussed in the later chapters. The properties of all the six stainless steel alloys are shown in Table 4-1.

Table 4-1: Properties of alloys used for the research (Data sheet from Outokumpu Research Foundation, Avesta, Sweden)

ASTM/ UNS	Type	Cr	Ni	Mo	Cu	Mn	N	*PRE_{N16}	Tensile Strength (N/mm^2)	Yield Strength (N/mm^2)	Micro hardness $(HV)_{500g}$
S30403	Austenitic	18.2	8.15	0.39	0.33	1.61	0.07	20.6	635	328	170
S31603	Austenitic	16.82	10.49	2.52	0.33	1.7	0.043	25.8	651	351	192
S32101	Lean duplex	21.26	1.6	0.24	0.26	4.81	0.232	25.7	784	596	260
S32304	Lean duplex	23	4.8	0.3	0.25	1.0	0.10	25.5	745	450	257
S82441	Lean duplex	24.11	3.59	1.6	0.37	2.85	0.269	33.7	802	644	275
S32205	Duplex	22.43	5.73	3.15	0.24	1.4	0.18	35.7	841	657	278

*PRE_N (pitting resistance equivalent number) is calculated from the formula

%Cr +3.3%Mo +16%N (18)

4.3 Brine Used for the Research

Two different brines were considered for this research. 3.5% NaCl solution in aerated conditions and synthetic oilfield brine (CO_2-saturated) with the composition shown in Table 4-2. The oilfield brine is chosen because it has an equivalent total dissolved solid (TDS) with 3.5% NaCl. The oilfield brine is simulated from a produced fluid taken from an offshore facility in the North sea (179).

Table 4-2: Oilfield brine adopted for the research (TDS 34,418 ppm)

Salts	mg/L
NaCl (Sodium Chloride)	24090
KCl (Potassium Chloride)	706
$CaCl_2.2H_2O$ (Calcium Chloride Di-hydrate)	1387
$MgCl_2$ (Magnesium Chloride)	4360
$BaCl_2.2H_2O$ (Barium Chloride Di-hydrate)	16
$SrCl_2.6H_2O$ (Strontium Chloride Hexa-hydrate)	33
Na_2SO_4 (Sodium Sulphate)	3522
$NaHCO_3$ (Sodium Bicarbonate)	304

4.4 Experimental Methods for Static Corrosion

4.4.1 Breakdown Potential Determination

All the stainless steel samples were cut from flat plates (3 mm thick) into square sections of 20 x 20 mm. An electrical wire was soldered to one face of each specimen and then mounted into epoxy resin. The specimens were then ground to a surface finish of 600 grit (P1200) using silicon carbide paper. They were then

polished with 15 μm diamond paste. All samples were degreased with acetone and then washed with distilled water before being dried in air. After these steps, the interface between the sample and the resin was sealed with silicone rubber and left to cure overnight. Electrochemical tests were performed using EG&G, 263A potentiostat/galvanostat. Anodic polarisation tests were conducted for all the alloys in a three-electrode electrochemical set up using an Ag/AgCl reference electrode and a platinum counter electrode (Figure 4.1).

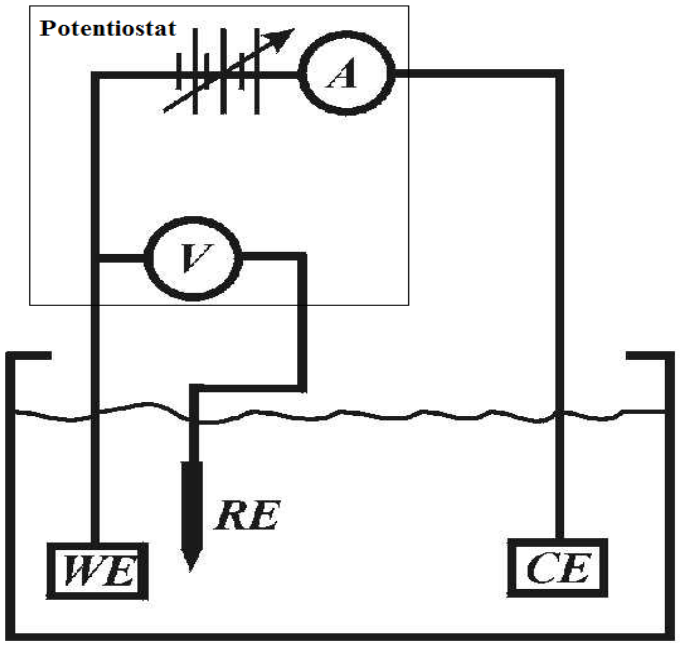

Figure 4.1: 3-electrode cell used for electrochemical measurement

The potential was scanned from the corrosion potential at a scan rate of 0.167 mV/s up to a point when the current density reached 500 μA/cm^2 and then reversed in accordance with ASTM G5 and G61. The oilfield brine was initially sparged with CO_2 gas for 8 hours and stored in an air tight container. Before each experiment, the oilfield brine was also sparged for one hour resulting in a pH of approximately 5.0

and the oxygen level was reduced to less than 50 ppb. Moreover, CO_2 was continuously fed into the solution throughout the duration of the experiment. The breakdown potential (potential at the point where current density is approximately 10 $\mu A/cm^2$ (140, 180)) was determined for all the alloys at temperatures of 20°C and 50°C. A schematic diagram of how the breakdown potential was determined is shown in Figure 4.2

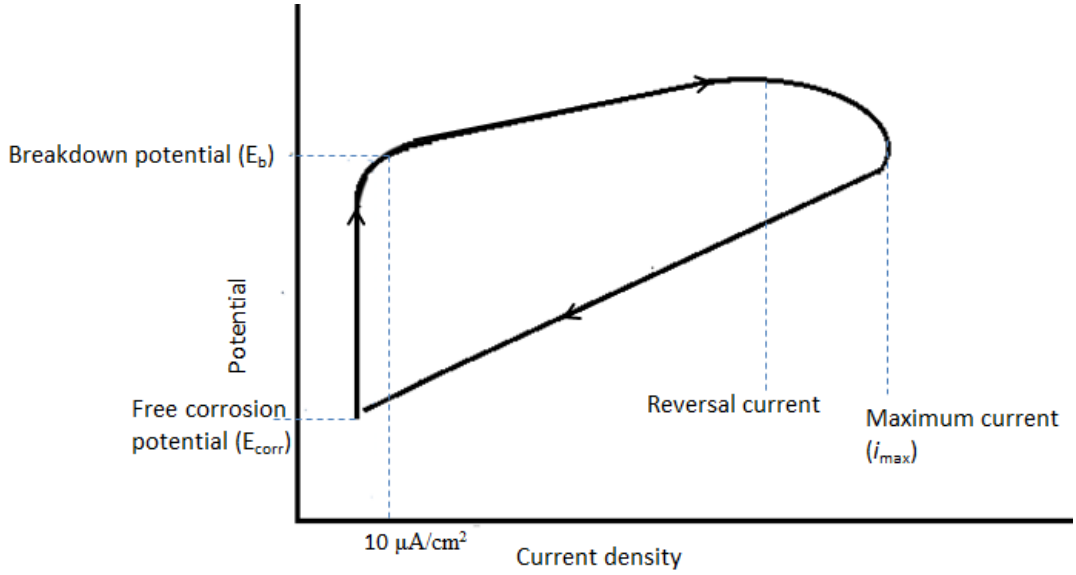

Figure 4.2: Schematic diagram of how the breakdown potential was determined

4.4.2 Open Circuit Potential (OCP) and Passive Film Chemistry

Lean duplex stainless steel alloys UNS S32101 and UNS S32304 were used for this investigation. The stainless steel samples were cut from flat plates (3 mm thick) into a square shape of 5 mm x 5 mm (to be able to fit into the XPS VG Escalab sample holder). An electrical wire was glued to one face of each specimen using a conductive epoxy and then mounted into epoxy resin. The specimens were then metallographically ground to a surface finish with 600 grit (P1200) SiC paper and

then polished with 15 μm diamond paste. All samples were degreased with acetone and then washed with distilled water before being dried in air.

Cathodic polarisation tests were performed to strip the native oxide formed in air using an EG&G, 263A potentiostat/galvanostat and a three-electrode electrochemical set up consisting of an Ag/AgCl reference electrode and a platinum counter electrode. The potential was stepped to -0.85V relative to the reference electrode for 30 minutes in order to strip the native oxide (60, 181). The sample was then allowed to repassivate in the absence of applied potential at 50^{o}C for 24 hours.

4.5 Experimental Methods for Flow-Induced Corrosion

4.5.1 Pure Erosion and Erosion-Corrosion Determination

A jet impingement rig with a re-circulating system is adopted. A mixture of sand and fluid is passed through a two-nozzle arrangement with a diameter of 4 mm. The jet impinges onto the samples from a 5 mm stand-off distance at an angle of 90^{o} (Figure 4.3-4.4).

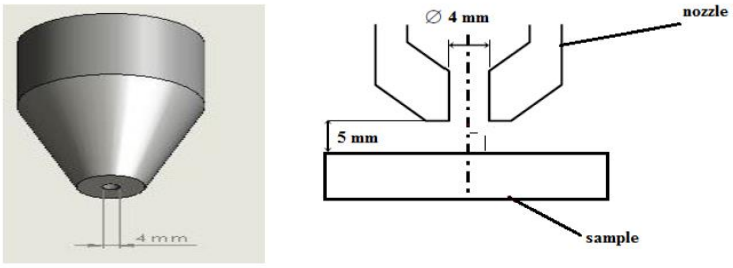

Figure 4.3: Exit nozzle diameter and the stand-off distance

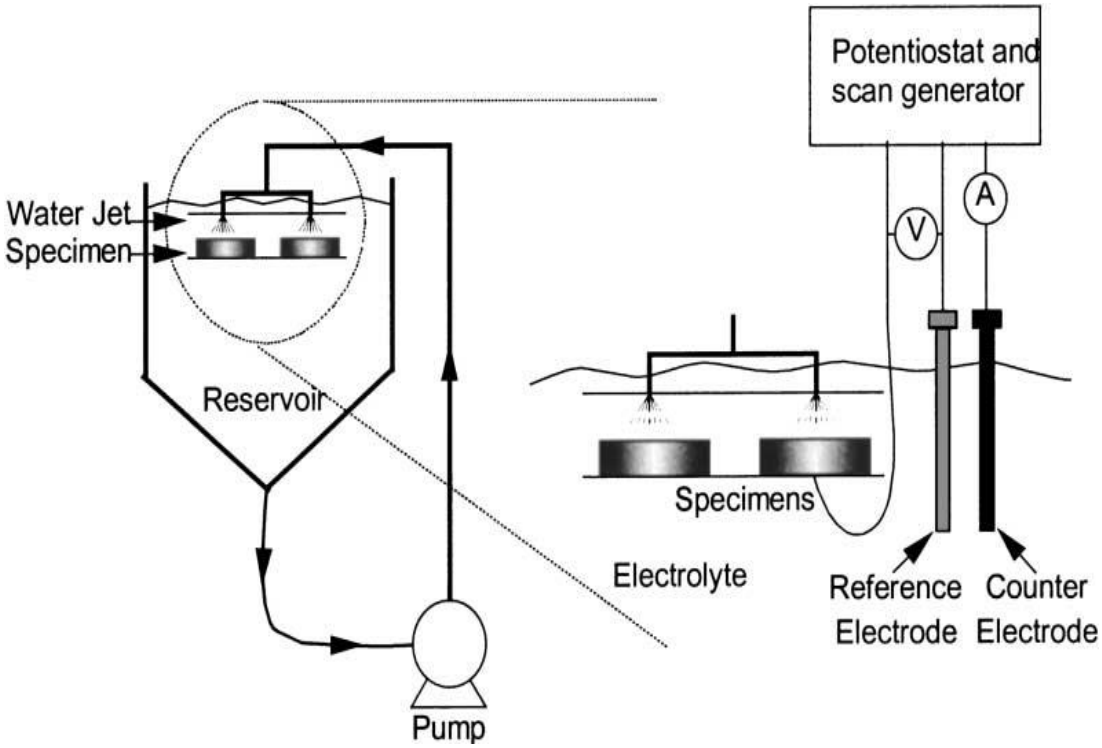

Figure 4.4: The submerged impinging jet (SIJ) rig

Electrochemical methods were used in conjunction with weight loss analysis to isolate the contribution due to corrosion and erosion. Anodic polarisation tests were conducted to measure the changes in corrosion rate under impingement conditions. Anodic and cathodic polarisation tests were performed on different coupons to avoid using a surface that has previously undergone cathodic polarisation. The potential of the working electrode was shifted 10 mV negative to the open circuit potential and then polarised at 0.167 mV/s in positive direction for the anodic branch. For the cathodic branch the potential was shifted 10 mV positive to the open circuit potential and then polarised at 0.167 mV/s in the negative direction. The corrosion current density was determined from the Tafel plot as the intersection between the extrapolated anodic and cathodic branches of the potential scan (51). Due to the nature of the polarisation curves (mixed reaction), the linear fits of the Tafel slope

was taken between 100 mV to 150 mV away from the open circuit potential. The corrosion current obtained from the Tafel extrapolation was used to calculate the corrosion rate.

A check on these values (i_{corr} obtained from the Tafel plot) was done using the linear polarisation method and Stern-Geary coefficient (B) of 26 mV. Linear polarisation scan was conducted for the alloys to obtain the polarisation resistance, R_p

. An external DC potential signal of ± 20 mV was applied to the alloys under impingement conditions and the current flowing in the external circuit was measured. The polarisation resistance (R_p) was calculated as the slope of the linear correlation between the applied potential and the measured current.

$$R_p = \frac{\Delta E}{\Delta i}$$

The corrosion current density was then calculated thus:

$$i_{corr} = \frac{B}{R_p}$$

Tafel coefficient of 120 mV/decade was chosen for both β_a and β_c. This is because the actual value of the slope is difficult to obtain from the nature of the Tafel plots. Theories of both Tafel extrapolations of linear polarisation have been discussed in Chapter 2, Sections 2.1.5 and 2.1.6.

In order to isolate the erosion component of the damage, the change in weight was measured in a nitrogen purged impinging jet. Water was sparged for 12 hours with nitrogen gas (N_2) to de-aerate the environment. Nitrogen gas was also bubbled into the tap water throughout the duration of the experiment. A 3.5% NaCl in aerated

condition and a CO_2-saturated oilfield environment were used to study the erosion-corrosion and total weight loss. 500 mg/l silica sand with shape and size distribution shown in Figures 4.5-4.6 operating at 15 m/s and a temperature of 50^{o}C was employed for impingement.

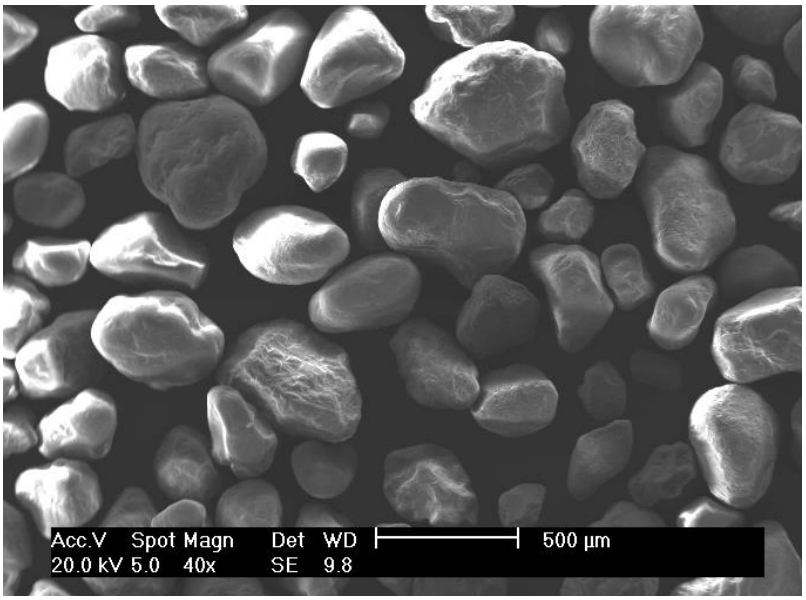

Figure 4.5: SEM images of HST60 silica sand particles used in the jet impingement

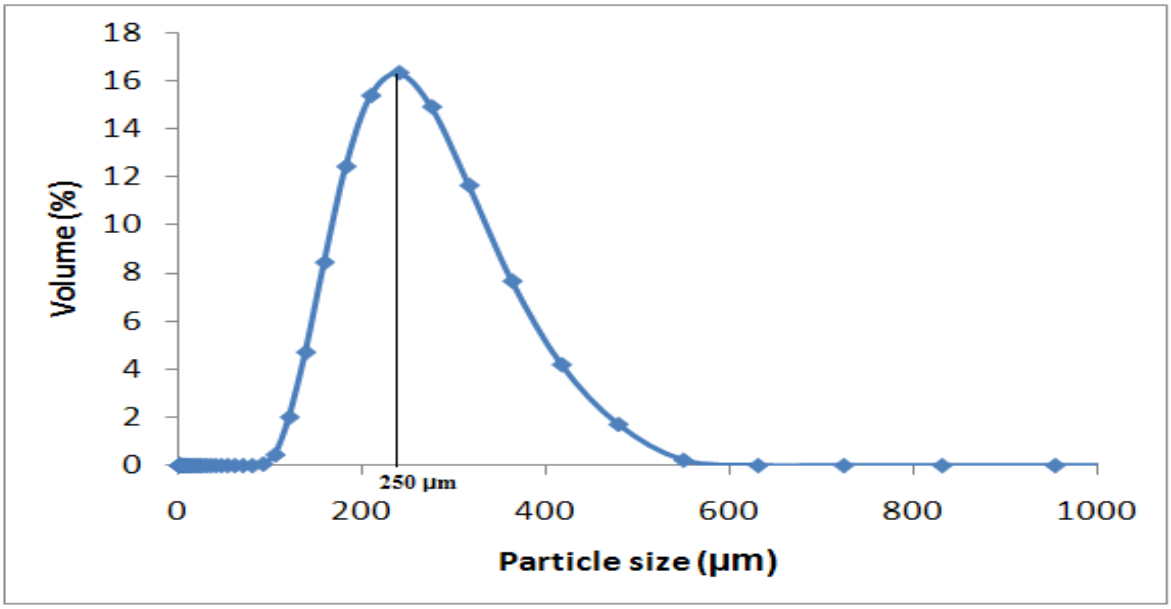

Figure 4.6: Sand particle distribution of the silica sand used in the jet impingement tests

Further tests were carried out for UNS S32101 and UNS S30403 at higher impinging velocity of 24 m/s in a CO_2-saturated oilfield. Pure erosion was determined at 50^{o}C as well as 20^{o}C. The total weight loss tests were conducted for 4 hours (adapted from ASTM G75-95 and ASTM G76-06) and each test was conducted at least in triplicate. The specimens were weighed before and after the experiments to determine the weight loss.

4.5.2 Repassivation Kinetics of the Passive Film Formed on UNS S32101 and UNS S30403 in a CO_2-Saturated Oilfield after Erosion-Corrosion

In order to study the repassivation behaviour of passive film, the passive film is disrupted by sand particle impingement. A new oxide film then grows on the alloy by the oxidation of the bare metal surface. Different methods have been used in the past to achieve this. Included in the methods are abrasion methods (70), scratching electrode methods (152), cavitation methods (65), indentation methods (174) and electrochemical reduction of the oxide film by cathodic polarisation (71). In this research, however, the passive film is removed by sand particle impingement using a submerged impinging jet in order to study the repassivation kinetics.

A potentiostatic polarisation method was adopted to obtain current transients under the sand impingement (Figures 4.3, 4.4 and 4.7).

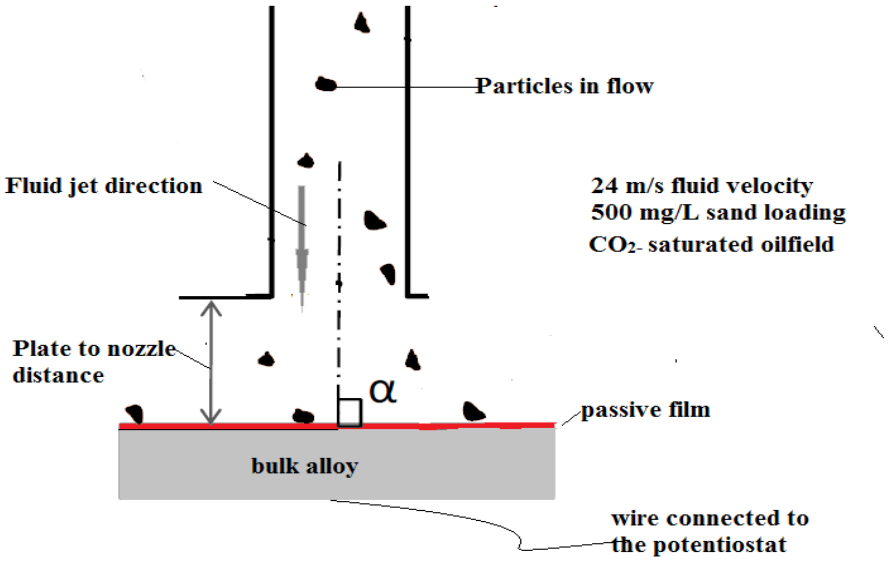

Figure 4.7: Schematic diagram of the fluid jet direction and the entrained particles

Two alloys UNS S30403 and UNS S32101 were tested. Prior to the potentiostatic test, the OCP was allowed to settle for 1 hour. The potential was then stepped to -850 mV Ag/AgCl for 30 minutes to strip the native oxide. This is done to ensure the same starting passive film formed on the alloys. A constant potential of -200 mV vs Ag/AgCl was then applied for 150 minutes. This potential was chosen as it lies within the passive region of both alloys. The passive film was allowed to passivate for the first 30 minutes and then the pump was switched ON for 1 hour. This was to allow the slurry to impinge on the sample surface thereby depassivating the passive film. The pump was switched OFF after 1 hour to allow the passive film to repassivate for another 1 hour. A velocity of 24 m/s and sand loading of 500 mg/L was employed for the impingement. This condition was chosen to simulate severe erosion conditions in order to ensure that the passive film is damaged prior to its repassivation. The experiment was conducted at temperatures of 20 and 50^{o}C. The

frequency of acquisition of data was 20 Hz and assuming all sand particles hit the sample surface, the frequency of sand impact was calculated to be 7.5 KHz.

All the experiments were conducted in CO_2-saturated oilfield brine with composition shown in Table 4-2.

4.6 Calibration of the Submerged Impinging Jet Rig

For any laboratory experiment to be acceptable, operating conditions of the experiment should be repeatable. However, this always poses challenges as the conditions are most often difficult to reproduce. To take account of the variance in the operating conditions, the equipment used in this study was regularly calibrated. For a submerged impinging (SIJ) rig, the pump frequency is calibrated to give the average velocity at which the fluid/ particle exit the nozzle. At the same time, when sand is involved, there could be non-uniform mixing of the sand in the reservoir; sand may also be entrapped within the pipe network. There is also the issue of inter-particle collisions and sweeping action of the liquid jet that should be accounted for. It has been reported (182, 183) that not all the sand particles added to the reservoir impact the surface of the sample.

4.6.1 Velocity Calibration

The energy required to drive the impingement action is derived from a centrifugal pump. The pump in this case is driven by an electric motor that is controlled by its frequency. In order to determine the exit velocity of the fluid coming out of the nozzle, the flow data from the pump is used. If the frequency of the pump is known, the flow rate data of the nozzle exit (nozzle size is known) is

then calculated. This is done by collection a certain amount of fluid exiting the nozzle at a time interval. Various frequencies may be used from which the flow rates are measured. The flow rate is then converted to nozzle exit velocity using the cross sectional area of the nozzle exit.

4.6.2 Sand Concentration Calibration

Sand concentration is defined as the ratio of the weight of the sand particle to the weight of the fluid solution in the reservoir. However, the specific sand concentration exiting the nozzle is not always equal to the amount of sand in the reservoir as earlier explained. To estimate the specific sand concentration exiting the nozzle, a specific amount of slurry is taken through the nozzle exit. The sand particles within the fluid are then filtered, dried and weighed. This is used to determine the specific amount of sand exiting the nozzle.

4.6.3 Calculation of Sand Flux and Impact Frequency at 50 Hz

During the calibration of the pump, a flow rate of 0.0003 m^3/s was estimated for a frequency of 50 Hz. This translated to an impinging velocity of 24 m/s using the cross-sectional area (diameter 4 mm, Figure 4.3) of the nozzle. A specific sand loading of 500 mg/L (500,000 mg/m^3) was also estimated from the calibration at 50 Hz.

The sand particle flux = flow rate (m^3/s) X specific sand loading (mg/m^3)

= 0.0003 m^3/s X 500,000 mg/m^3

The sand particle flux at 50 Hz = 150 mg/s = 0.00015 kg/s

Recall from Figure 4.6 that the average diameter of the HTS60 silica sand (assumed spherical) is 250 µm. Density of silica sand is 2650 kg/m^3.

Therefore, mass of one grain of sand = density (2650 kg/m^3) X volume (8.18 X10^{-12} m^3) = 2 X 10^{-8} kg

$$\text{Impact frequency} = \frac{particle\ flux\ (\frac{kg}{s})}{mass\ of\ one\ grain\ of\ sand\ (kg)} \qquad (184)$$

$$= \frac{0.00015\ (\frac{kg}{s})}{0.00000002\ (kg)}$$

= 7500 impacts/ seconds = 7.5 kHz

4.7 Surface Analysis Equipment Used in this Research

4.7.1 Scanning Electron Microscope (SEM)

Evo MA Series Scanning Electron Microscope from Carl Zeiss Microscopy LCC was used for the electron microscopy. The SEM available at the University of Leeds uses a variable pressure and a resolution ranging from 3-20 nm.

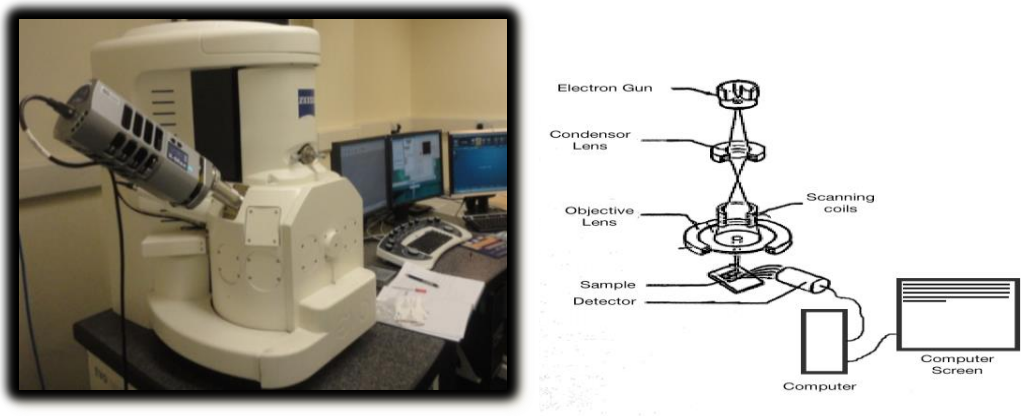

Figure 4.8: (a) Evo MA Series Scanning Electron Microscope (Carl Zeiss Microscopy GmbH, Jena, Germany) available at the University of Leeds (185) (b) Schematic image of a typical SEM

The total magnification obtainable in the SEM is between < 7-1,000,000. The accelerating voltage used was 20 kV while the working distance used was between 9-10 mm

4.7.2 Focused Ion Beam (FIB)

The Focused Ion Beam (FIB) was used to prepare the sample for Transmission Electron Microscopy. The Focused Ion Beam (FIB) images acquisition and the Transmission Electron Microscope (TEM) samples preparation were carried out using the FEI Nova 200 Nano Lab High Resolution Field Emission Gun Scanning Electron Microscope (FEGSEM) with precise Focused Ion Beam (FIB). This instrument which can etch and deposit materials precisely is available at the University of Leeds. FIB uses a focused beam of ions usually gallium (Ga+) unlike the SEM that uses a beam of electrons. When the ion beam hits the sample surface, it sputters a small amount of materials that leaves the surface as either secondary ions (i^+ or i^-) or neutral atoms (n^0). The primary beam also produces secondary electrons (e^-). As the primary beam rasters on the sample surface, the signal from the sputtered ions or secondary electrons is collected to form an image.

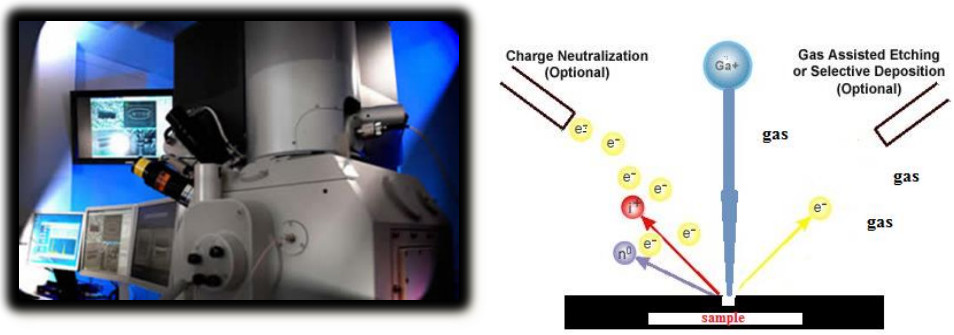

Figure 4.9: FEI Nova 200 Nano Lab (FEI Company, Hillsbrow Oregon, USA) available at the University of Leeds (185)(b) Schematic diagram of the mode of operation of FIB (186)

Before imaging the area of interest from the bulk, the sample is first coated with platinum to avoid ion implantation as well as damage to the surface. It is then tilted to an angle of 54^{o} in order to ensure a perpendicular alignment to the ion beam column. The location of interest is then milled out to a length of 20 µm and a breadth of 10 µm. For the TEM imaging and analysis, the milled lamella is attached to a surface; the signal from the sputtered ions or secondary electrons is collected to form an image pillar ominiprobe TEM grid where it is further thinned to the required dimension.

4.7.3 Transmission Electron Microscopy (TEM)

The Transmission Electron Microscope used is a FEI Tecnai TF FEGTEM Field Emission Gun TEM/STEM (FEI Company, Hillsbrow Oregon, USA). The instrument is fitted with HAADF detector and Oxford instrument INCA 350 EDX system and 80 mm X-max SDD detector and Gatan Orius SC600A CCD camera. Scanning transmission electron microscope operating at 30 kV and providing a resolution of 0.8 nm is adopted. Both dark field and bright field imaging techniques were employed to provide good contrasts. Selected Area Electron Diffraction (SAED) was employed to study the microstructure.

4.7.4 Selected Area Electron Diffraction (SAED) Method

A selected area electron diffraction (SAED) pattern is collected using parallel electron illumination. An aperture in the image plane is used to select the region of the specimen, giving site-selective diffraction analysis. SAED pattern of polycrystalline materials gives ring patterns which are made up of reflections from specific crystal plane with specific 2Θ values but a range of angular values. If,

however, the crystal size exceed that of the SAED aperture, only a spot diffraction pattern from a single crystal will be observed.

The diameter of the ring is measured using a calibrated digital image of the pattern in digital micrograph software (Gatan Inc). Measurements in the image are done in reciprocal space, and so the reciprocal of the value gives the real d-spacing value in nanometres. This value is then matched with the d-spacing in literature or predetermined value from the XRD.

4.7.5 X-ray Photoelectron Spectroscopy (XPS)

X-ray Photoelectron Spectroscopy (XPS), VG Escalab 250 available at the University of Leeds was used to analyse the passive film chemistry**.** The XPS is equipped with a high intensity monochromatic Al Kα source which can be focussed to a spot 120-600 μm in diameter on the sample. A high resolution XPS with a high signal to noise ratio is thus possible. This Escalab can map sample to obtain a 25 μm resolution. The instrument also has a high intensity UV source for Ultraviolet Photoelectron Spectroscopy (UPS), and a FEGSEM for SEM imaging and Scanning Auger Microscopy. Depth profiling by etching is made possible by a focussed argon ion miller. X-ray photo electron spectroscopy uses UHV surface technique. The instrument is able to identify elemental composition of the near surface of a solid up to 10 nm.

In this research, XPS analysis was conducted on the samples after passive film has been built on the surface for 24 hours. Sample was quickly transferred, after 24 hours, to a vacuum desiccator from which it was transferred to the XPS chamber. XPS analysis was carried out using a high intensity monochromatic Al Kα x-ray

source. The spot size was 500 µm with a power of 150 W. Detailed spectra of individual peaks were taken at energy of 20 eV. Detailed spectra had a Shirley background fitted to them and peaks were deconvoluted using Gaussian-Lorentzian fits (using CASAXPS software) (181). The XPS spectra were corrected for charge shifts by normalizing binding energies to that of the adventitious carbon 1s peak at 284.6 eV. A peak separation of 1.7 eV and an area ratio of 2:1 were used to fit the Cl 2p3/2–2p1/2 spectra (187). The full width at half maximum (FWHM) for Cl 2p3/2 and 2p1/2 were taken as 1.7 eV and 1.9 eV respectively (188).

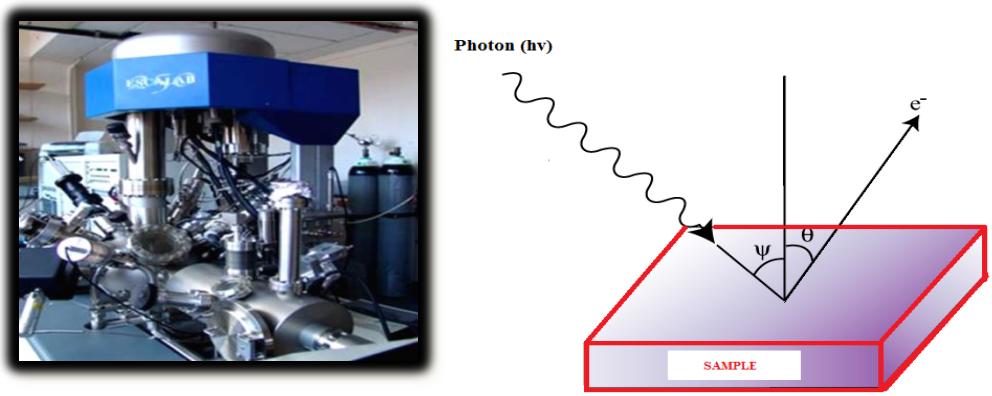

Figure 4.10: (a) X-ray Photoelectron Spectroscopy (XPS), VG Escalab 250N (Thermo VG Scientific, Wattham, MA, USA) available at the University of Leeds (185) (b) Basic principle of XPS

4.7.6 X-ray Diffraction (XRD)

An X-ray Diffractometer-Philip X'pert (Philips Analytical B.V., The Netherland) available at the University of Leeds was used to analyse the sub-surface properties of the alloys after erosion-corrosion. X-ray diffraction (XRD) uses X-rays to investigate and quantify the crystalline nature of materials by measuring the diffraction of X-rays from the planes of atoms within the material. It is sensitive to both the type and relative position of atoms in the material as well as the length scale over which the

crystalline order persists. It can, therefore, be used to measure the crystalline content of materials; identify the crystalline phases present (including the quantification of mixtures in favourable cases); determine the spacing between lattice planes and the length scales over which they persist; and to study preferential ordering and epitaxial growth of crystallites. In essence it probes length scales from approximately sub Angstroms to a few nm and is sensitive to ordering over tens of nanometres.

The X-rays are generated by a cathode ray tube. The rays are filtered to produce monochromatic radiation. They are then directed towards the target/crystal. When the rays interact with the solid, a constructive interference//diffraction is produced as long as the conditions for the Bragg's law is satisfied. Bragg's law relates the wavelength of the electromagnetic radiation to the diffraction angle and the lattice spacing in a crystal by the formula:

$$n\lambda = 2d\sin\theta \qquad 4\text{-}1$$

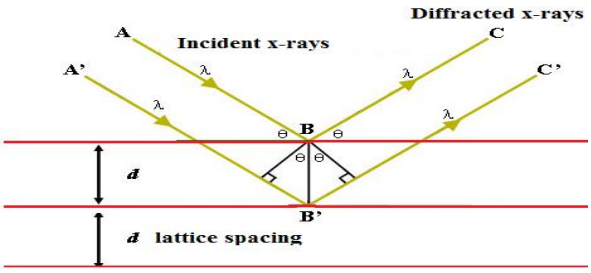

Figure 4.11: Bragg's law of reflection. The diffracted X-rays exhibit constructive interference when the distance between paths ABC and A'B'C' differs by an integer number of wavelengths (λ)(189)

When the sample or target is scanned through a range of 2θ angles, all the diffraction directions of the lattice is attained due to the random orientation of the material. The diffraction peaks are then converted to the d-spacing which allow the

mineral/crystal to be identified. This is because each mineral/crystal has a unique d-spacing. To achieve this, the d-spacing is generally compared with standard reference.

Chapter 5. Results of Static Corrosion Evaluation

5.1 Introduction and Chapter Overview

An overview of the tests conducted is presented in the flow chart shown in Figure 5.1

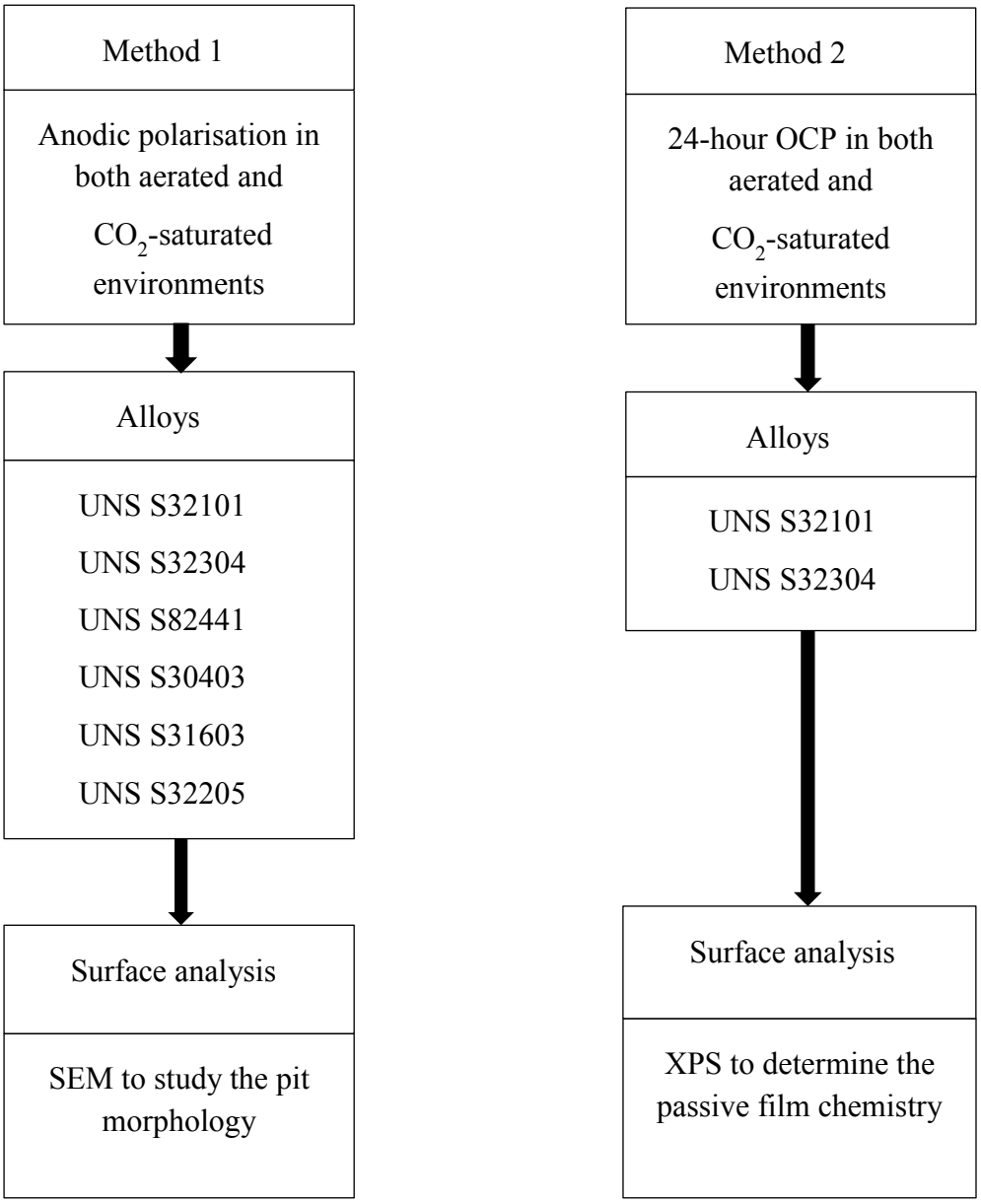

Figure 5.1: Roadmap for the experimental study

Efforts were made to evaluate the breakdown potential of six stainless steel alloys comprising of lean duplex stainless steels (UNS S32101, UNS S32304, and UNS S82441) standard austenitic stainless steels (UNS S30403, UNS S31603) and a standard duplex stainless steel (UNS S32205). Aerated 3.5% NaCl and CO_2-saturated oilfield environments were considered for the experiments. The chemistry of the passive film formed on two of the lean duplex alloys (UNS S32304 and UNS S32101) was later evaluated using X-ray Photoelectron Spectroscopy (XPS) method. Efforts were also made to relate the breakdown potentials with the amount of chloride ion intake into the passive film.

5.2 Breakdown Potential Evaluation

An example of the cyclic polarization curves for UNS S32101 in aerated 3.5% NaCl and a CO_2-saturated oilfield environment is shown in Figure 5.2. The breakdown potential is determined as the potential where current density attained a value 10 $\mu A/cm^2$ (140, 181). Breakdown potentials of all the alloys in both aerated 3.5% NaCl and CO_2 saturated brine at 20^oC and 50^oC are as shown in Figure 5.3. It is shown that the breakdown potentials are more negative in the CO_2-saturated environment compared to 3.5% NaCl for all the alloys tested.

Also, the breakdown potential is clearly shown to be highly dependent on temperature as expected. The breakdown potentials of the austenitic stainless steel, UNS S30403 and the lean duplex stainless steel, UNS S32101 are comparable in aerated 3.5% NaCl at both 20^0C and 50^0C. UNS S30403 and UNS S32101 at 20^oC in the aerated condition have breakdown potentials of 438 and 459 mV vs (Ag/AgCl) respectively. At the same temperature and in the CO_2-saturated oilfield environment,

UNS S30403 and UNS S32101 have breakdown potentials of 387 and 413 mV vs (Ag/Ag/Cl) respectively. Also, at 50^{o}C and in the aerated condition UNS S30403 and UNS S32101 have breakdown potentials of 280 mV and 295 mV vs (Ag/AgCl) respectively.

However, in the CO_2-saturated oilfield environment at 50^{0}C, UNS S30403 and UNS S32101 have breakdown potentials of 163 mV and 103 mV vs (Ag/AgCl) respectively.

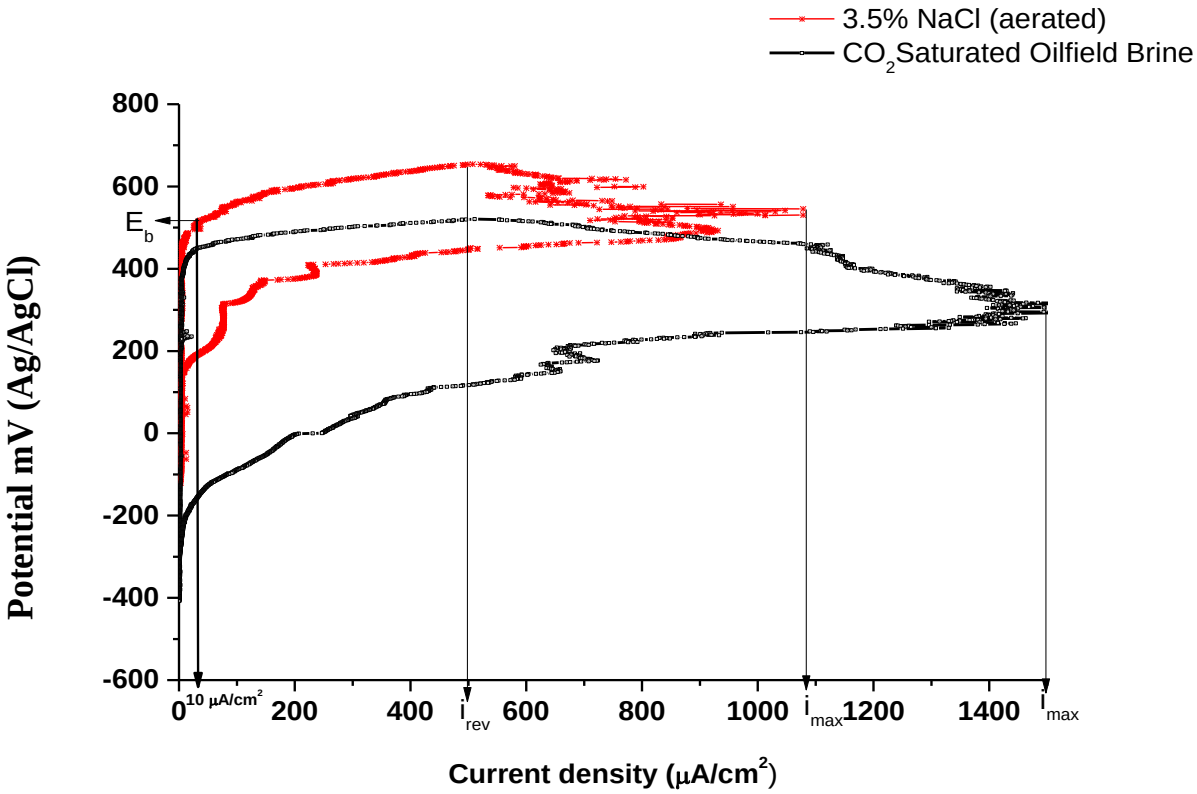

Figure 5.2: Cyclic polarization curves for UNS S32101 in aerated 3.5% NaCl and CO_2-saturated oilfield environments at 20^{o}C showing how the breakdown potential (E_b) is determined

Figure 5.3 also shows that the austenitic stainless steel UNS S31603 and lean duplex UNS S32304 exhibit close breakdown potentials in both environments at both 20^{o}C and 50^{o}C. UNS S31603 and UNS S32304 have breakdown potentials of 539

mV and 574 mV vs (Ag/AgCl) respectively in aerated 3.5% NaCl at 20°C. In the CO_2-saturated oilfield, at the same temperature, the breakdown potentials of UNS S31603 and UNS S32304 are 393 and 435 mV (Ag/AgCl) respectively. UNS S31603 and UNS S32304 have breakdown potentials of 335 mV, 215 mV and 335 mV, 229 mV (Ag/AgCl) respectively in aerated and CO_2-saturated oilfield and at 20 and 50°C respectively.

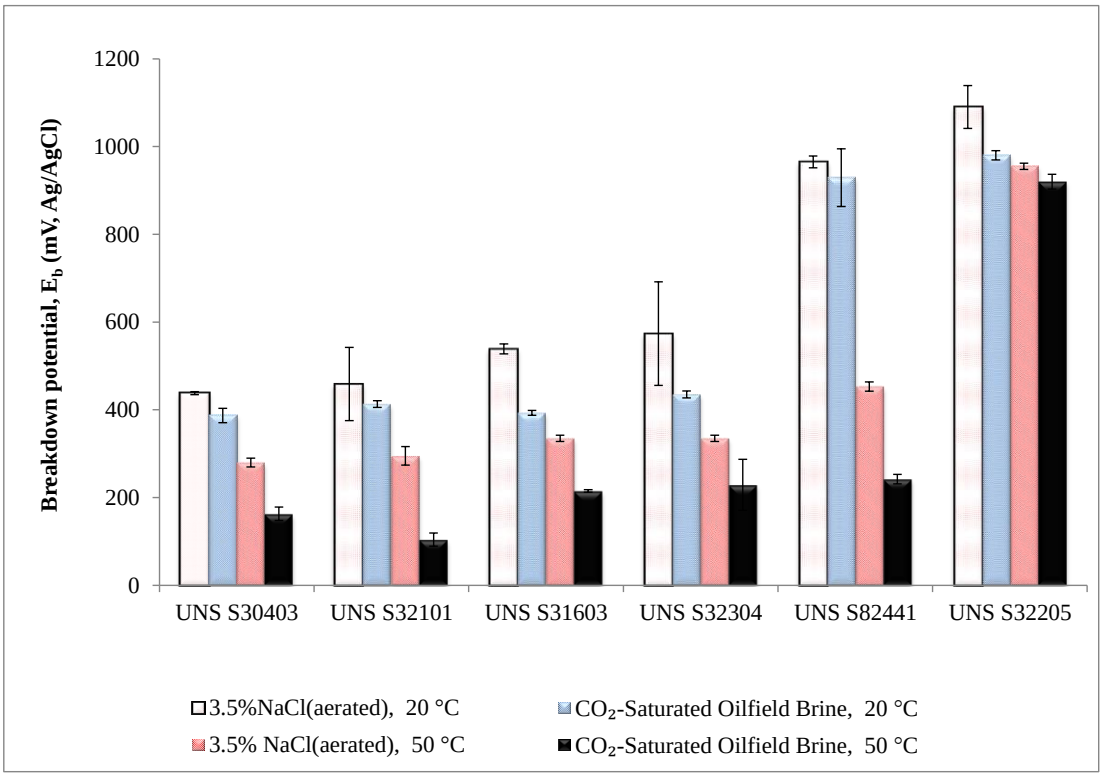

Figure 5.3: Breakdown potentials of lean duplex, standard duplex and austenitic stainless steels in aerated 3.5% NaCl and CO_2-saturated oilfield environment (Error bar is the spread of 3 data points)

The breakdown potential of the lean duplex stainless steel, UNS S82441 is lower than that of standard duplex stainless steel, UNS S32205 at both 20°C and 50°C. However, UNS S82441 exhibits very noble breakdown potentials of 965 mV and 929 mV (Ag/AgCl) in aerated and CO_2-saturated oilfield respectively at 20°C. These

potentials are comparable with that of the standard duplex stainless steel UNS S32205. UNS S32205 recorded breakdown potentials of 1090 mV and 980 mV in aerated and CO_2-saturated oilfield respectively at 20^{o}C.

5.3 Open Circuit Potential Behaviour of Lean Duplex Stainless Steels UNS S32101 and UNS S32304

Figure 5.4 illustrates the trend in the open circuit potential of the alloys at 50^{o}C in aerated 3.5% NaCl and CO_2-saturated environments. The figure shows that the alloys ennobled from corrosion potentials of -368 mV to -24 mV and -303 mV to -68 mV for UNS S32101 and UNS S32304 respectively after 24 hours exposure in the aerated environment at 50^{o}C.

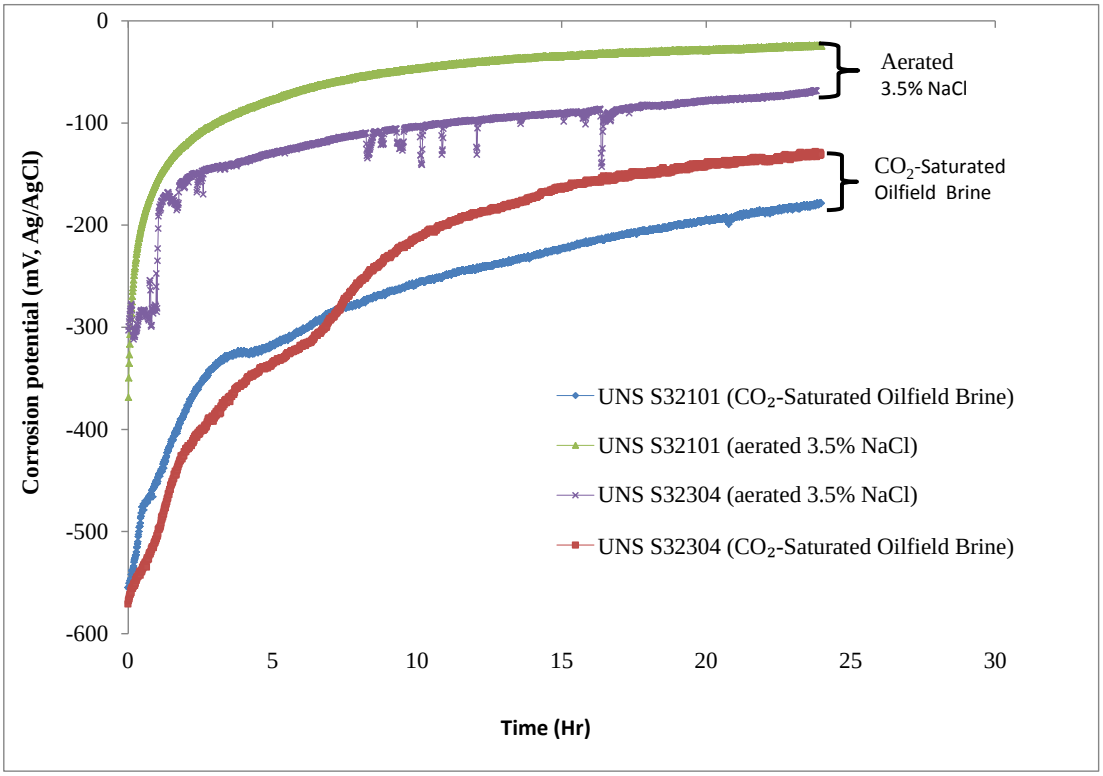

Figure 5.4: Open circuit potentials for UNS S32101 and UNS S32304 in 3.5% NaCl and CO_2-saturated oilfield environment

The open circuit potentials in a CO_2-saturated environment are -555 mV and -571 mV for UNS S32101 and UNS S32304 respectively. This is more negative than the values obtained in the aerated environment due to the acidic nature of the CO_2-saturated environment. The potentials also ennobled in CO_2-saturated environment stabilizing at approximately -179 mV and -131 mV (more negative than the aerated 3.5% NaCl) for UNS S32101 and UNS S32304 respectively after 24 hours exposure.

The following observations were also made:

- The open circuit potential values of the two alloys ennobled asymptotically with exposure time (Figure 5.4). However, the initial OCP after activation at -0.85 V is more positive in aerated 3.5% NaCl than CO_2-saturated oilfield.
- Also, the potentials of both alloys are more positive throughout in aerated 3.5% NaCl than the CO_2-saturated oilfield after 24 hours exposure.
- In aerated 3.5% NaCl, UNS S32101 has an initially more negative OCP than UNS S32304 as expected. However after 24 hours exposure UNS S32101 is more ennobled anodically in the aerated environment.
- In the CO_2-saturated environment UNS S32101 has a more positive OCP up to 8 hours (Figure 5.4). However, after the first 8 hours, UNS S32304 became more ennobled.

5.4 Localised Corrosion

UNS S32101 and UNS S30403 suffer severe localised attack in aerated 3.5% NaCl. The severity of the attack is higher for these two alloys in aerated 3.5% NaCl compared to the CO_2-saturated oilfield environment (Figures 5.5 and 5.6).

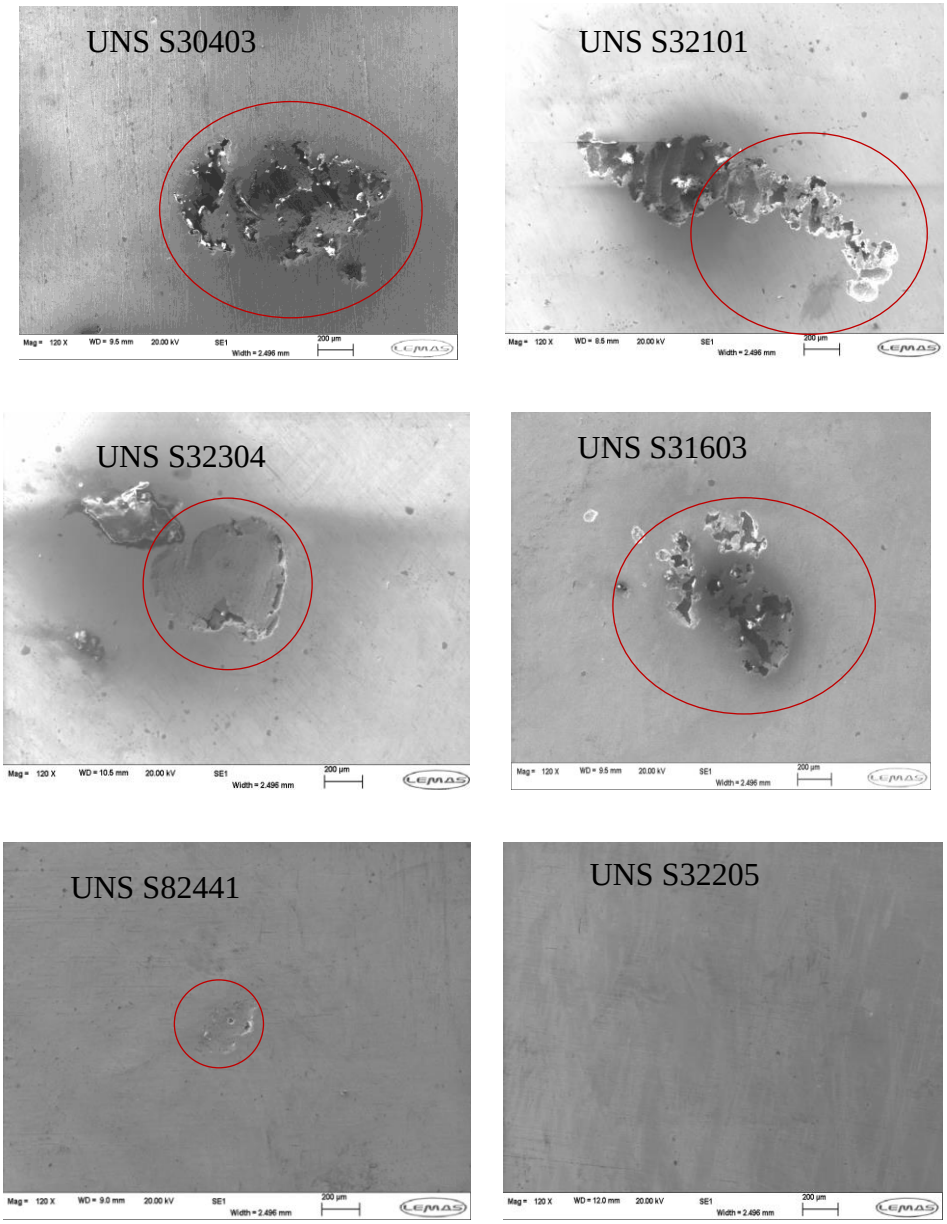

Figure 5.5: SEM images of the alloys showing lacy cover (circled) formed in aerated 3.5%NaCl (Scale bar = 200 µm)

UNS S31603 and UNS S32304 also suffer greater pitting damage in aerated 3.5% NaCl than CO_2-saturated oilfield environment. However, the severity of attack on these two alloys is mild compared to UNS S32101 and UNS S30403.

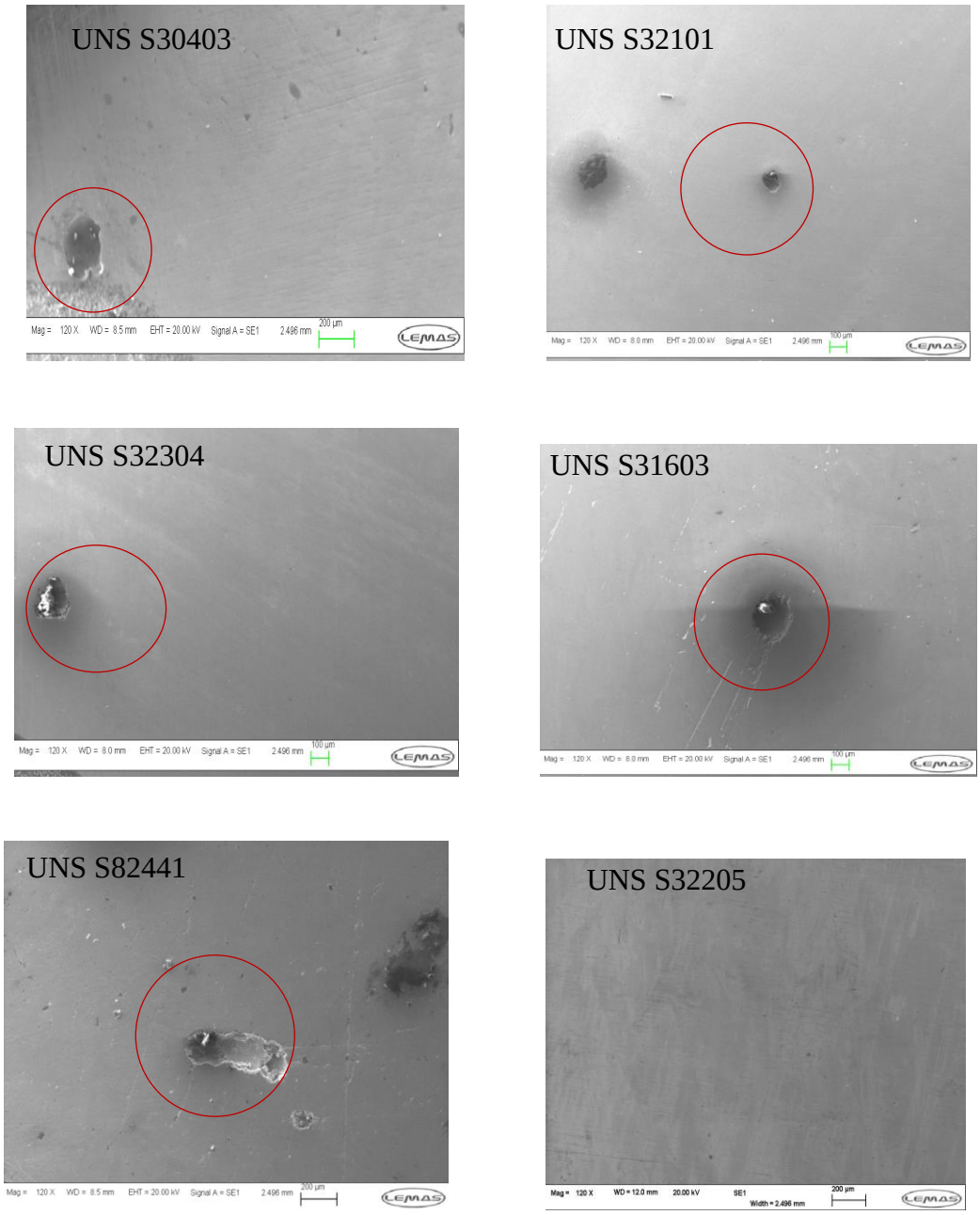

Figure 5.6: SEM images of the alloys showing open pits (circled) formed in CO_2 saturated oilfield environment (Scale bar = 200 µm)

Figure 5.5 shows that the pitting mode in aerated 3.5% NaCl at 50^0C is lacy in nature. At low magnification the standard duplex stainless steel UNS S32205 shows no feasible pits. UNS S82441 shows the highest resistance to pitting among the lean duplex stainless steels. The pitting mode in the CO_2-saturated oilfield environment

seems to be different from that of aerated 3.5% NaCl. The pits formed in the CO_2 environment are not covered and the sizes are smaller compared to those formed in aerated 3.5% NaCl (Figure 5.6).

5.5 X-ray Photoelectron Spectroscopy (XPS)

XPS was utilised in order to investigate the exact chemical composition of the surface passive film layer. Figures 5.7 and 5.8 demonstrate the survey spectra obtained for UNS S32304 and UNS S32101 stainless steels after initial 10 seconds of etching (to eliminate carbon contamination) of the surface. Figures 5.7 and 5.8 demonstrated a similar elemental presence in each case. It is interesting to note the presence of chloride ion within the passive film layer for samples immersed in aerated and CO_2-saturated oilfield environments.

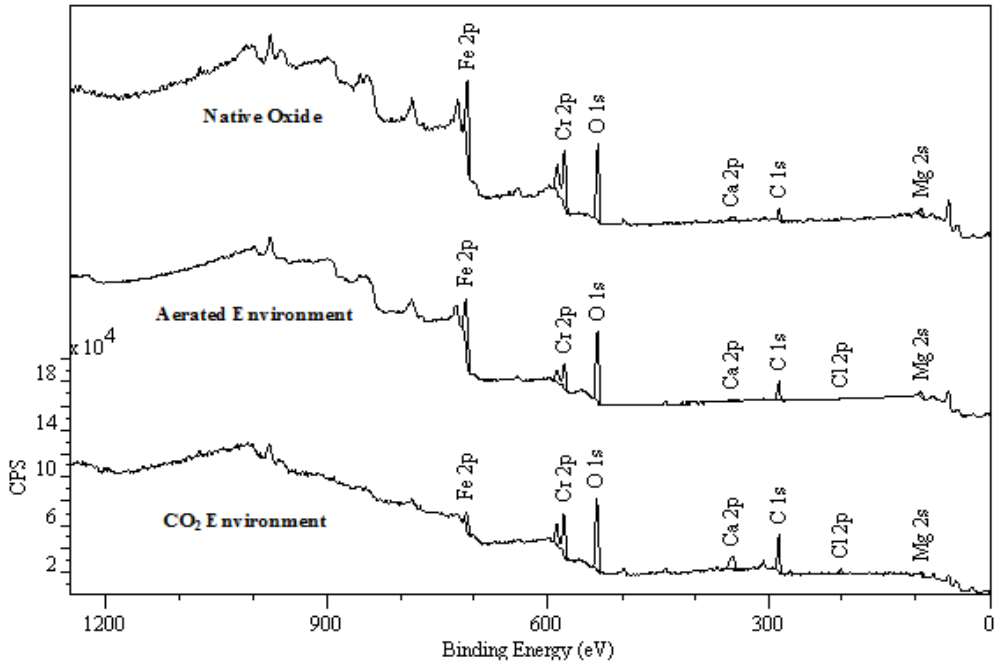

Figure 5.7: General XPS spectra surveys for the oxide layer formed on UNS S32304 stainless steel in aerated 3.5% NaCl and CO_2-saturated oilfield brine

Resolution of the Cl 2p spectra further showed the adsorption of chloride into the passive oxide layer (Figure 5.9). The chloride ion (Cl^-) was seen to be present in both the oxide layers formed in aqueous environments.

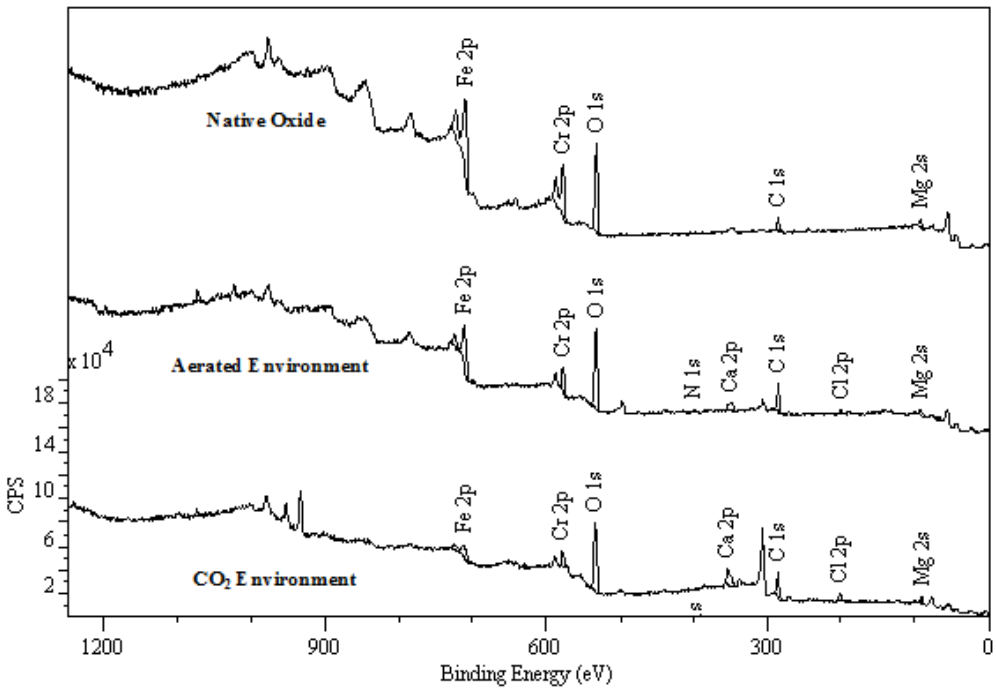

Figure 5.8: General XPS spectra surveys for the oxide layer formed on UNS2101 stainless steel in aerated 3.5% NaCl and CO_2-saturated oilfield brine

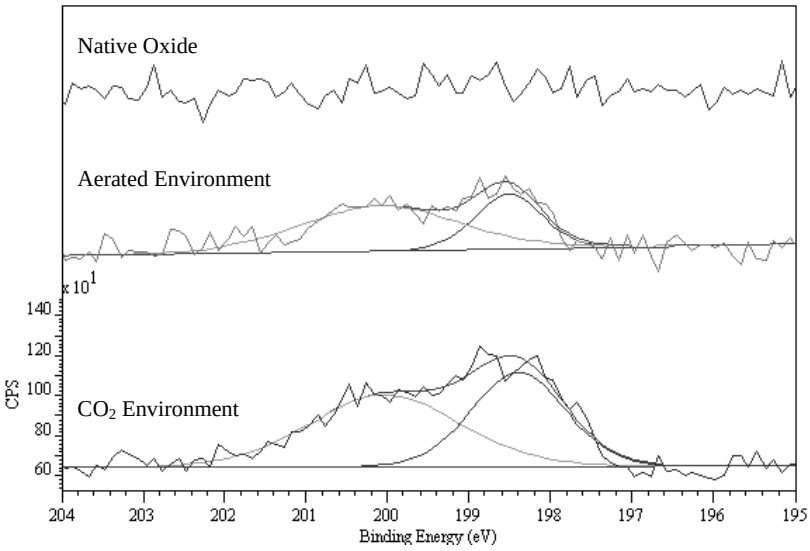

Figure 5.9: Resolution of the Cl 2p spectra for UNS S32101 stainless steel in aerated and CO_2 environment as well as the native oxide film

An increased amount of Cl^- was seen to be present in the oxide formed in the CO_2-environment compared to the aerated environment. Figures 5.10 and 5.11 show the quantification of atomic weight per cent of the chloride ion in the both aerated and the CO_2-saturated environments.

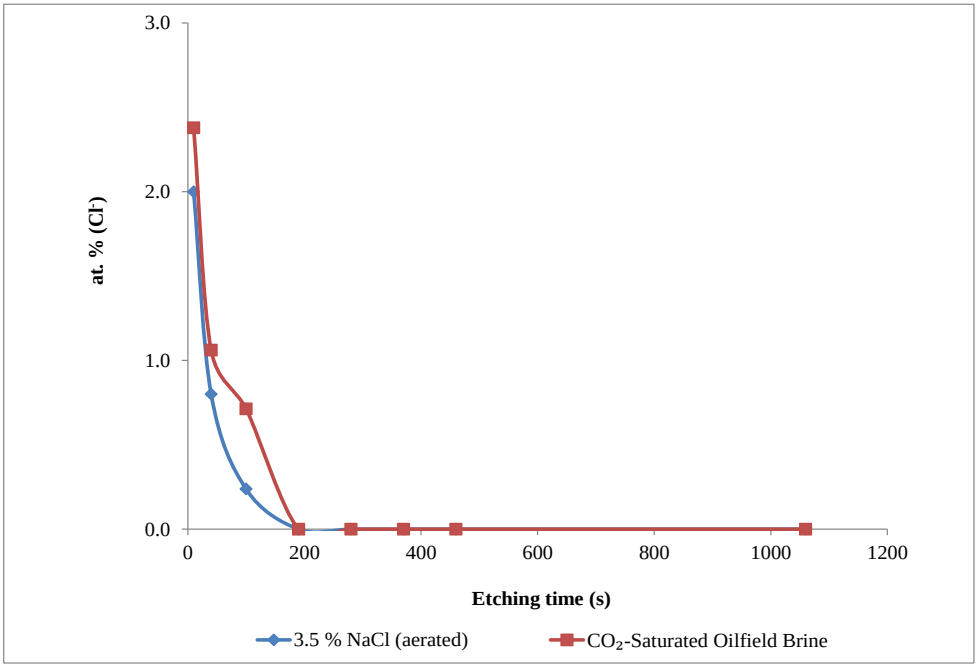

Figure 5.10: Chloride incorporated into the passive film formed on UNS S32101

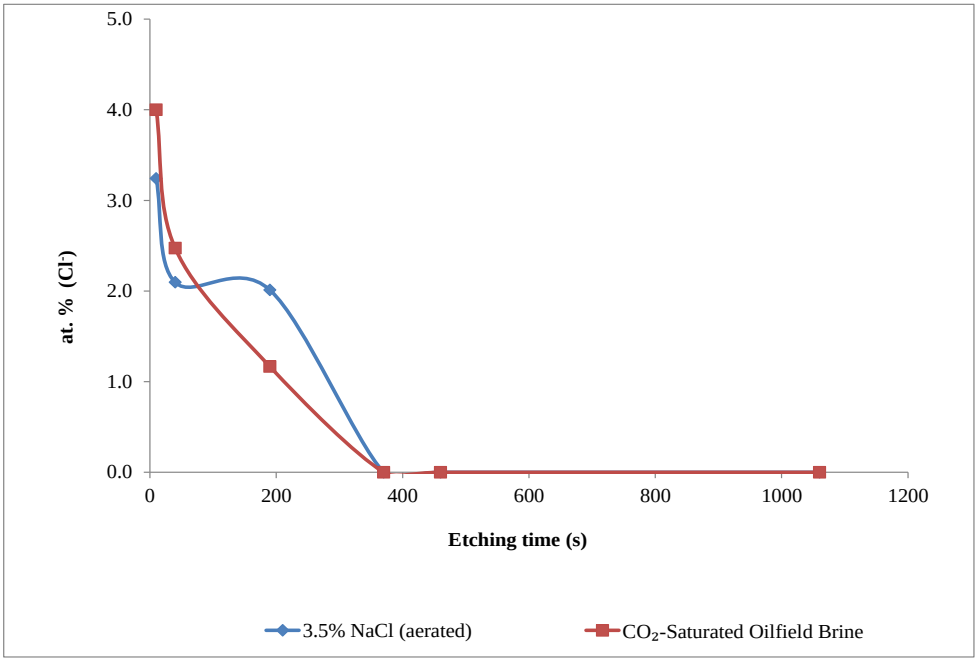

Figure 5.11: Chloride incorporated into the passive film formed on UNS S32304

Trace amounts of Mn were observed within the native oxide film formed in aerated condition for UNS S32101 stainless steel. There seems to be insignificant amount of Mn in the oxide formed in CO_2 environment. Figure 5.12 depicts the Mn 2p spectra for passive films formed on UNS S32101 stainless steel as well as the native oxide film. Peaks were seen to occur at 638.77eV, and 641.05eV representing the presence of elemental Mn and MnO within the oxide layer. Lower Mn peaks in the CO_2 environment compared to the aerated and native oxide is thought to be due to its acidic nature leading to higher dissolution of the active element (Mn) from the passive film into the solution. The same result was also reported for a nickel free manganese alloy in an alkaline medium (190).

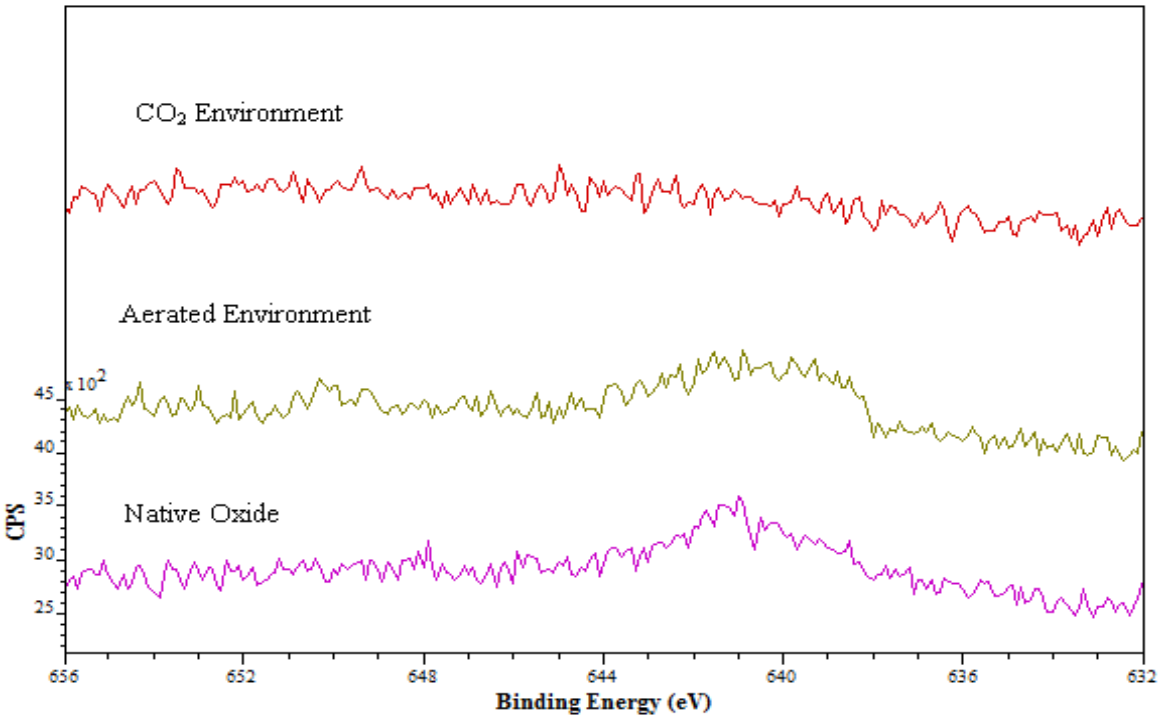

Figure 5.12: Resolution of the Mn 2p spectra obtained for UNS32101 stainless steel in aerated and CO_2 environments' as well as the native oxide film

5.6 Summary of Chapter 5

The breakdown potentials of all the alloys have been evaluated to be more negative in the CO_2-saturated oilfield than the aerated 3.5% NaCl.

The higher amount of chloride absorbed into the passive film formed in the CO_2-saturated oilfield is thought to be one reason, in addition to the lower pH, why the passive film breaks down at lower potential in this environment.

- It should be noted that the bulk solution in the aerated conditions has a higher chloride concentration of 21,000 mg/L compared to the 19,000 mg/L in the bulk solution of the CO_2-saturated environment. This however does not translate to the amount of chloride in the passive film.
- It is therefore thought that a synergy exists between the CO_2 and the chloride in bulk solution that helps in enhancing the intake of the latter into the passive film.

Another interesting result from this chapter is the fact that the Pitting Resistance Equivalent Number (PRE_N) does not seem to be a good parameter to rank the lean duplex and the austenitic stainless steels when they are considered together.

- This is because UNS S32101, UNS S31603 and UNS S32304 all have approximately equal PRE_N but UNS S32101 does not have equal resistance to pitting (as evaluated by the breakdown potential) to the other two alloys. Also, UNS S30403 with a PRE_N much lower than that of UNS S32101 has very comparable breakdown potential (even higher breakdown potential in the CO_2-saturated environment) with UNS S32101.

- A critical PRE_N of 35 is however proposed for higher temperature service (50^oC and above) in CO_2 and aerated environments used in this research.

All of these are addressed in the discussion section.

Chapter 6. Results of Flow-Induced Corrosion (Erosion-Corrosion)

6.1 Introduction and Chapter Overview

An overview of the tests is presented in the flow chart shown in Figure 6.1

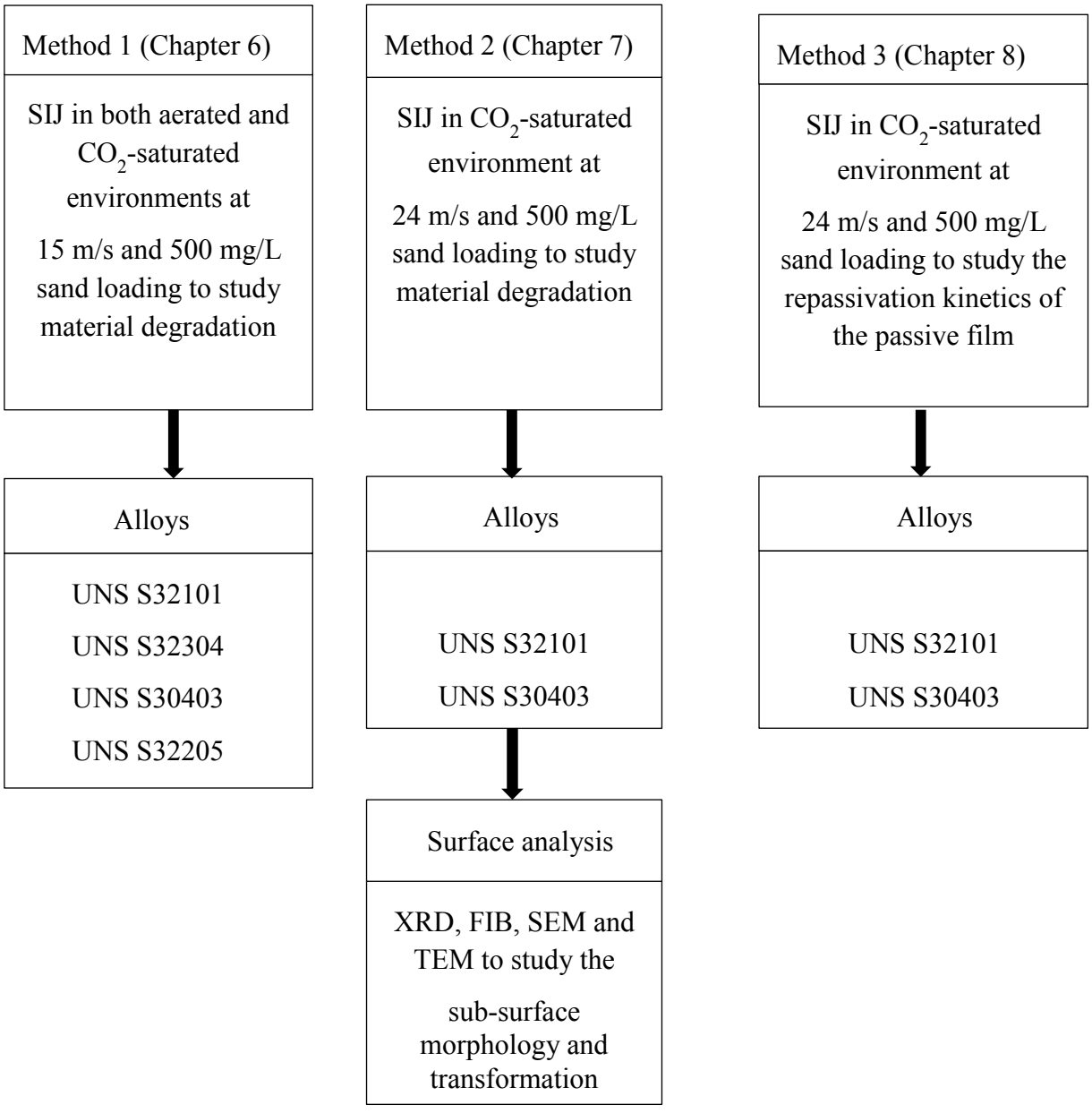

Figure 6.1. Roadmap for the experimental study

Alloys considered for evaluation included: UNS S32101, UNS S32304, UNS S30403 and UNS S32205. These alloys were studied under pure-erosion conditions (in a N_2 purged water) and erosion-corrosion conditions (aerated 3.5 % NaCl and CO_2-saturated oilfield brine) at 15 m/s and 500 mg/l sand loading. Higher impinging velocity of 24 m/s was also employed to study the material degradation and repassivation behaviour of the passive film formed on UNS S30403 and UNS S32101. These two alloys were chosen because UNS S32101 is being considered as an alternative alloy to the standard austenitic stainless steels in the oilfield. Efforts were made to relate the material degradation of these two alloys to both repassivation of the passive film and the sub-surface structure evolution under the high impinging velocity.

6.2 Results of Pure Erosion and Erosion-Corrosion

6.2.1 Weight Loss Measurement in Aerated 3.5% NaCl Solution

Material degradation in the form of mass loss for all the alloys tested is shown in Figures 6.2 and 6.3. Pure erosion loss (E) and the total weight loss are presented. Pure erosion after 4 hours of sand impingement at 20^{o}C shows that UNS S30403 has the highest material loss of (4.95 mg) and UNS S32304 the least material loss of (3.01 mg). UNS S32101 and UNS S32205 have material losses of 3.78 mg and 4.33 mg respectively. Figure 6.3 shows that pure erosion damage is higher at higher temperature for all alloys tested except the austenitic alloy. The increase in the erosion damage at higher temperature is thought to be as a result of many factors among which is lower viscosity (25, 26, 191-193) of the liquid at higher temperature. The dynamic viscosity of water at 20^{o}C (9.7720 X 10^{-4} kg/m.s) is almost double the

viscosity of water at 50°C (5.3185 X 10^{-4} kg/m.s). At higher temperature, the drag force on the sand particle is thus reduced thereby resulting in higher impact. It is thought that this higher impact would result in better response of the austenite phase to strain-hardening and thus higher hardness. This could be the reason while the UNS S30403 is showing good erosion resistance at the higher temperature. The higher material loss at higher temperature for all the alloys is also possible due to corrosion activity occurring at the higher temperature. Bearing in mind that oxygen is not completely eliminated from the nitrogen purged solution. Total weight loss of the alloys under erosion-corrosion conditions at 50°C shows that UNS S32205 has the lowest material loss of 6.78 mg while UNS S30403 with 8.20 mg suffered the highest degradation. UNS S32101 and UNS S32304 have material losses of 6.80 mg and 6.95 mg respectively.

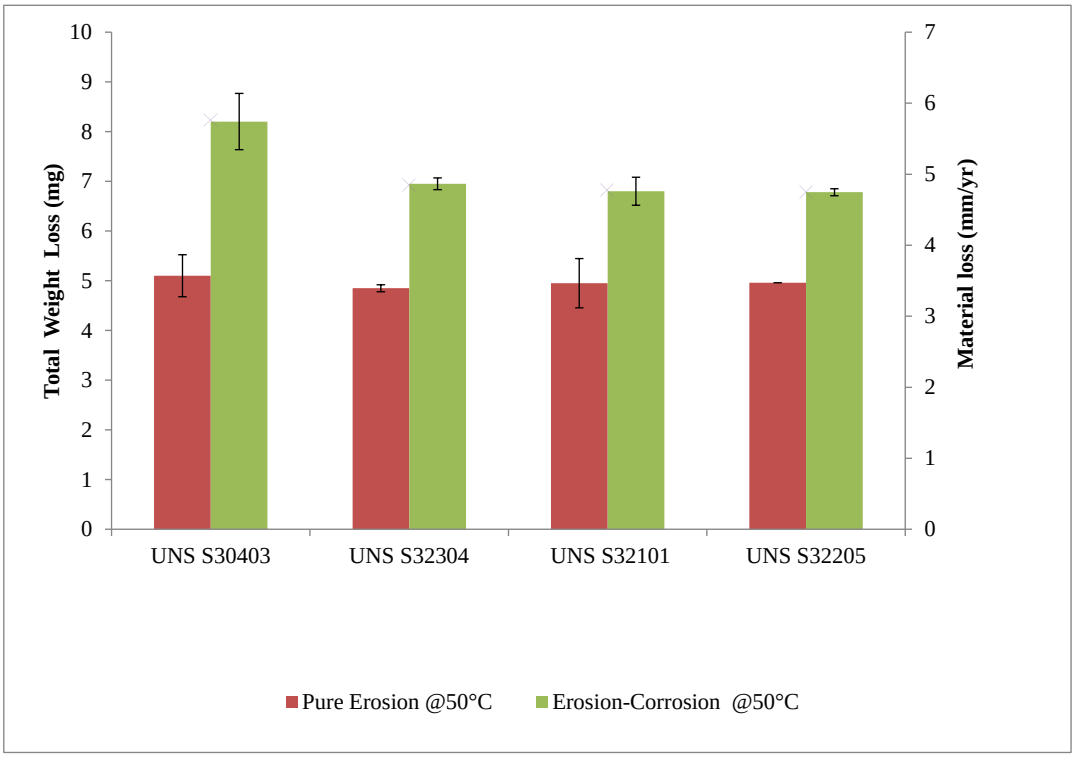

Figure 6.2. Pure erosion (in nitrogen purged water) and total weight loss (in aerated 3.5% NaCl) of the alloys at 50°C, 15 m/s and 500 mg/L sand loading (Error bar is the spread of 3 data points)

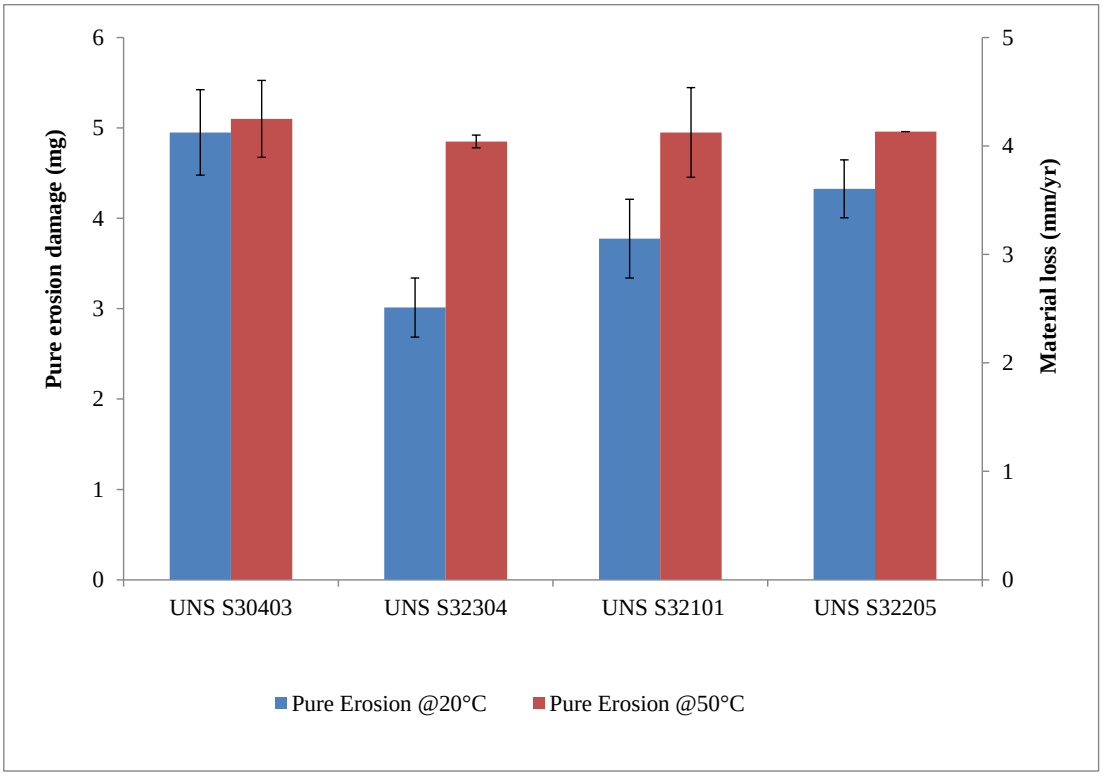

Figure 6.3: Pure erosion damage at 20°C and 50°C, 15 m/s and 500 mg/L sand loading in nitrogen purged water (Error bar is the spread of 3 data points)

6.2.2 Corrosion Current under Impinging Conditions

The *in-situ* current density derived from the Tafel plots (Figure 6.4-6.7) for all the alloys is shown in Figure 6.8. This was determined from the polarisation curve under impinging 3.5% NaCl solution and 500 mg/L sand particles at a velocity of 15 m/s. These values were checked by evaluating the polarisation resistance of the alloys and were found to correlate well. As earlier explained in section 4.5.1, chapter 4, the anodic and cathodic polarisation tests were performed differently before they were combined. Hence the nature of the curves in Figures 6.4-6.7.

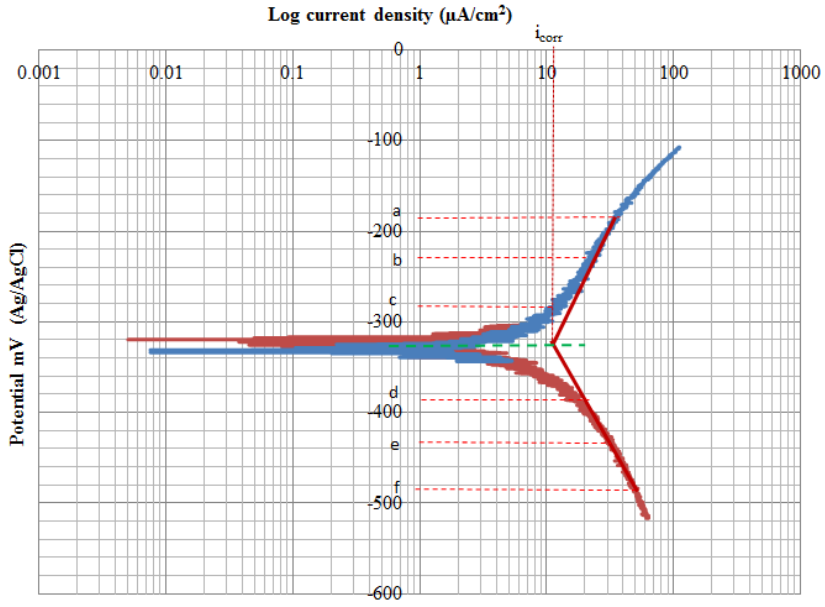

Figure 6.4: Tafel plot for UNS S32101 used to determine current density under erosion-corrosion conditions of 15 m/s and 500 mg/L sand loading in aerated 3.5% NaCl; a, b, c are points 150 mV, 100 mV and 50 mV respectively above OCP; d, e, f are points 50 mV, 100 mV and 150 mV respectively below OCP

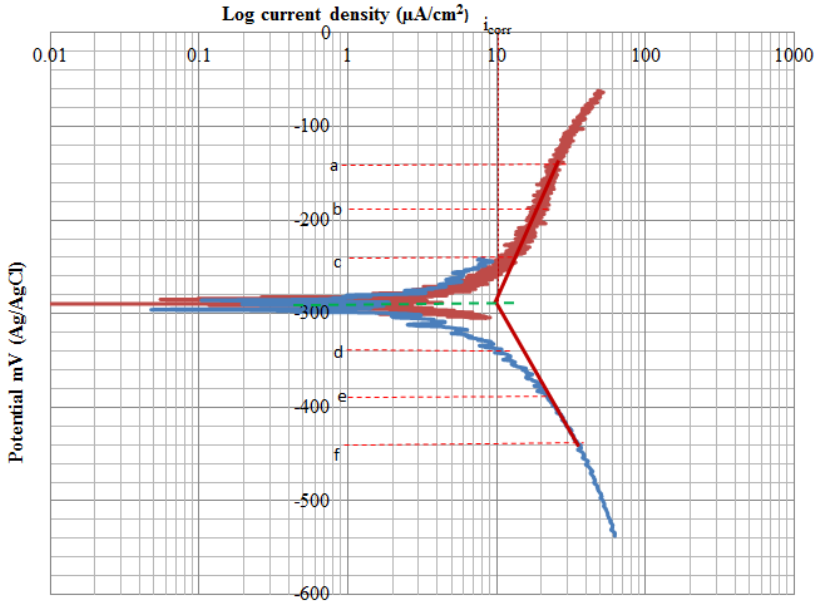

Figure 6.5 Tafel plot for UNS S32205 used to determine current density under erosion-corrosion conditions of 15 m/s and 500 mg/L sand loading in aerated 3.5% NaCl; a, b, c are points 150 mV, 100 mV and 50 mV respectively above OCP; d, e, f are points 50 mV, 100 mV and 150 mV respectively below OCP

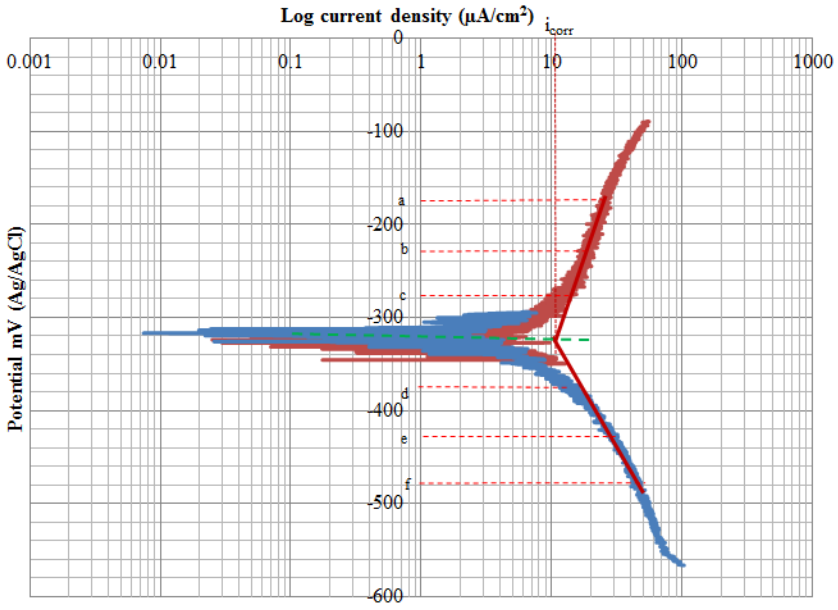

Figure 6.6: Tafel plot for UNS S32304 used to determine current density under erosion-corrosion conditions of 15 m/s and 500 mg/L sand loading in aerated 3.5% NaCl; a, b, c are points 150 mV, 100 mV and 50 mV respectively above OCP; d, e, f are points 50 mV, 100 mV and 150 mV respectively below OCP

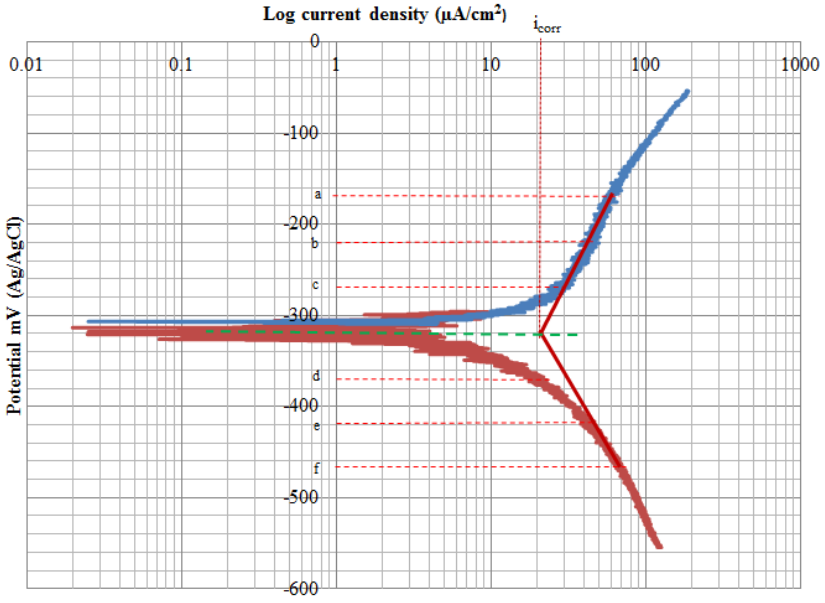

Figure 6.7: Tafel plot for UNS S30403 used to determine current density under erosion-corrosion conditions of 15 m/s and 500 mg/L sand loading in aerated 3.5% NaCl; a, b, c are points 150 mV, 100 mV and 50 mV respectively above OCP; d, e, f are points 50 mV, 100 mV and 150 mV respectively below OCP

This *in-situ* corrosion current density was used to calculate the mass loss due to erosion-enhanced corrosion (assuming a negligible material loss under static corrosion conditions). All the duplex stainless steels exhibited similar current density under the slurry impact. *In-situ* corrosion current densities of approximately 14, 13 and 12 µA/cm^2 were recorded for UNS S32101, UNS S32304 and UNS S32205 respectively. Austenitic stainless steel, UNS S30403 however recorded the highest corrosion current density of approximately 21 µA/cm^2.

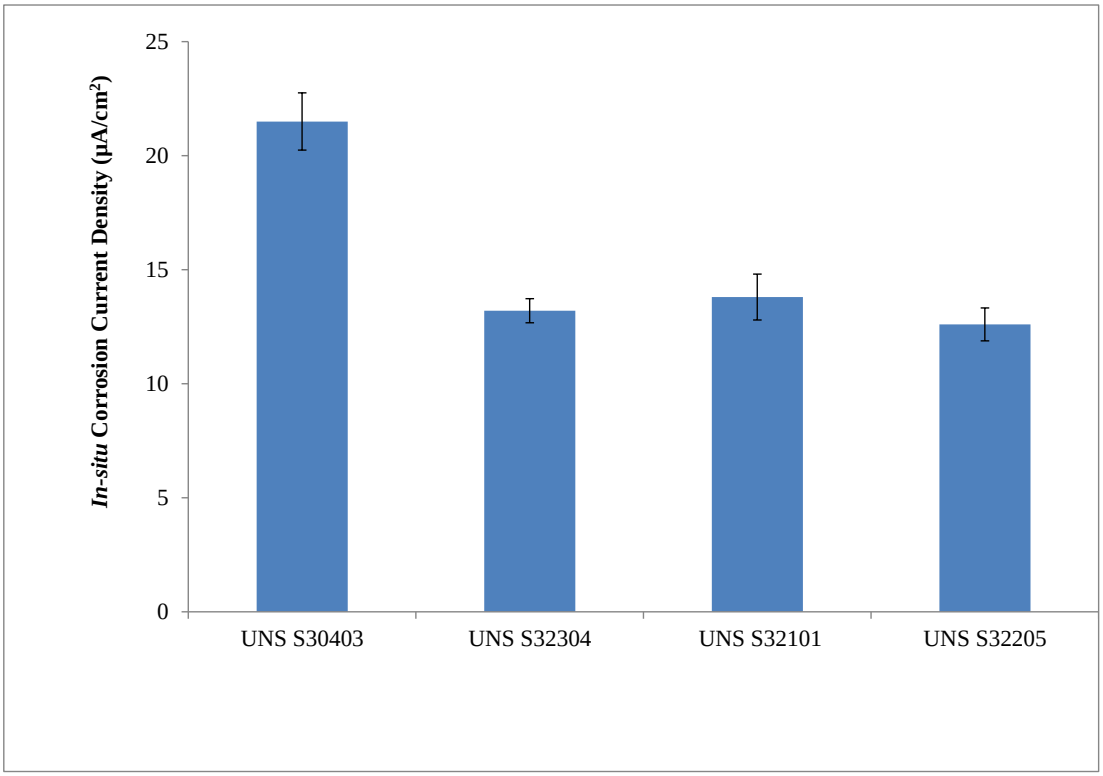

Figure 6.8: *In-situ* corrosion current density for the alloys in aerated 3.5% NaCl at 15 m/s and 500 mg/L sand loading (Error bar is the spread of 3 data points)

6.2.3 Synergy between Corrosion and Erosion

Material loss due to erosion-enhanced corrosion was derived from the *in-situ* corrosion according to the relationship:

$$Mass\ loss\ (g) = (C_o + dC_E)\ =\ dC_E\ = \frac{i_{corr}\ W\ A\ T}{nF}$$

i_{corr} is the corrosion current density in A/cm^2, W is the atomic weight in g/mol, A is the surface area of the specimen in cm^2, T is time in seconds, n is the number of ions , F is Faraday's constant, (96500 Coulombs/mole).

It has been reported (25, 28) that the static corrosion component (C_o) is negligible for passive alloys. It is therefore assumed that the total material degradation due to corrosion, *in-situ* corrosion ($C_o + dC_E$), in this study is equal to dC_E (erosion-enhanced corrosion). Therefore the formula for the total weight loss (TWL) could be represented thus:

$$TWL = E + dE_C + dC_E$$

Instead of

$$TWL = E + C_O + dE_C + dC_E$$

Where, TWL= total weight loss

E= pure erosion component

C_o= static corrosion component (in this case negligible)

dE_C = corrosion-assisted erosion (synergy)

dC_E = erosion-assisted corrosion (additive)

Figure 6.9 depicts the contribution of each component of the total weight loss. Corrosion-enhanced erosion is generally higher than erosion-enhanced corrosion (*in-situ* corrosion).

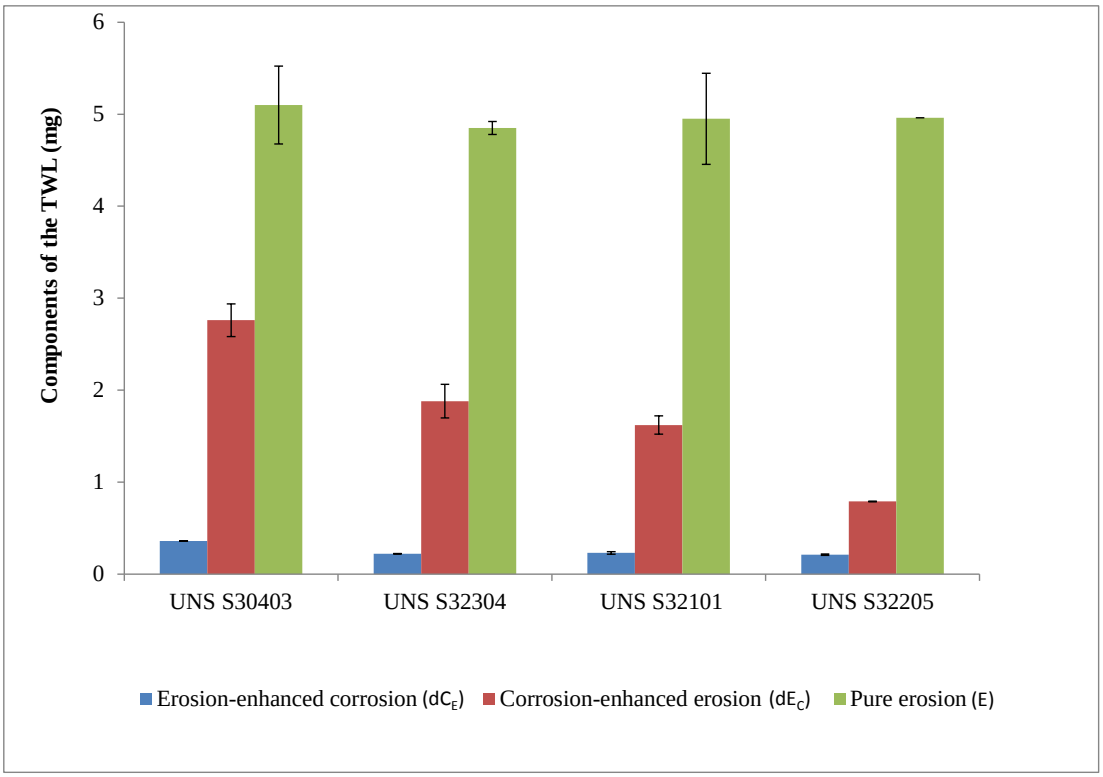

Figure 6.9: Components of the total weight loss for the alloys at 15 m/s and 500 mg/L sand loading and temperature of 50^{o}C (Erosion-corrosion in 3.5% NaCl; Pure erosion in nitrogen purged water) - (Error bar is the spread of 3 data points)

The mechanism of erosion-corrosion synergy is thoroughly explained and discussed in the discussion section in chapter 9. All the duplex stainless steels exhibit an equivalent material degradation due to erosion-enhanced corrosion (Figure 6.9). UNS S30403 seems to have the highest susceptibility to material degradation by erosion-enhanced corrosion.

The percentage contribution of each component of erosion-corrosion is shown in Figure 6.10. The contribution of corrosion-enhanced erosion is more than the contribution from erosion-enhanced corrosion. All the duplex stainless steels exhibit an equivalent percentage contribution due to erosion-enhanced corrosion (Figure 6.10).

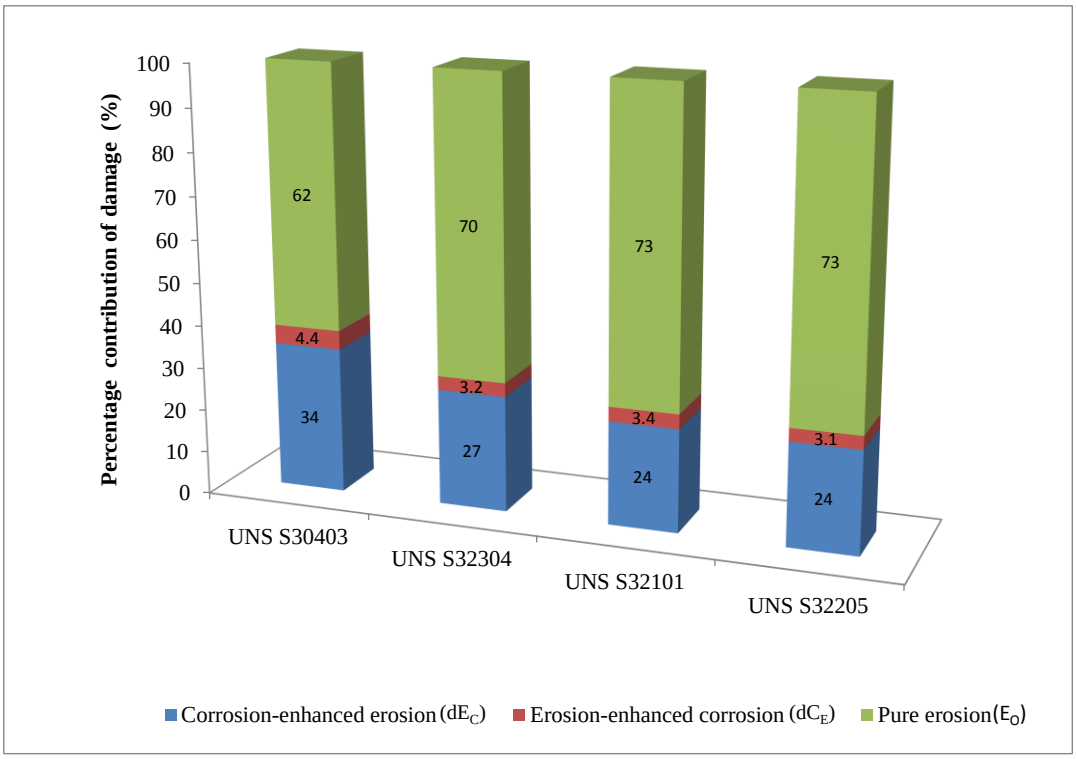

Figure 6.10: Percentage contribution of each component in erosion-corrosion conditions at 15 m/s and 500 mg/L sand loading in aerated 3.5% NaCl (Erosion-corrosion in 3.5% NaCl; Pure erosion in nitrogen purged water)- (Error bar is the spread of 3 data points)

The contribution due to erosion-enhanced corrosion is highest for UNS S30403. About 30% contribution due to the synergy between erosion and corrosion for the duplex stainless steel is lower than 39% contribution by same for the austenitic stainless steel. Material damage is predominantly by pure-erosion which contributed the highest percentage to the total damage. Also, despite the fact that the austenitic stainless steel UNS S30403 suffers higher materials loss due to pure-erosion and erosion-induced corrosion, the percentage contribution of erosion to the total damage for the alloy is lower than the duplex stainless steels.

6.3 Results of Erosion-Corrosion in a CO_2-Saturated Oilfield Environment at 15 m/s and 500 mg/L Sand Loading

6.3.1 Weight Loss Measurement in a CO_2-Saturated Oilfield Environment

Material degradation in the form of mass loss for UNS S30403, UNS S32101, UNS S32304 and UNS S32205 in a CO_2-saturated oilfield brine is shown in Figure 6.11.

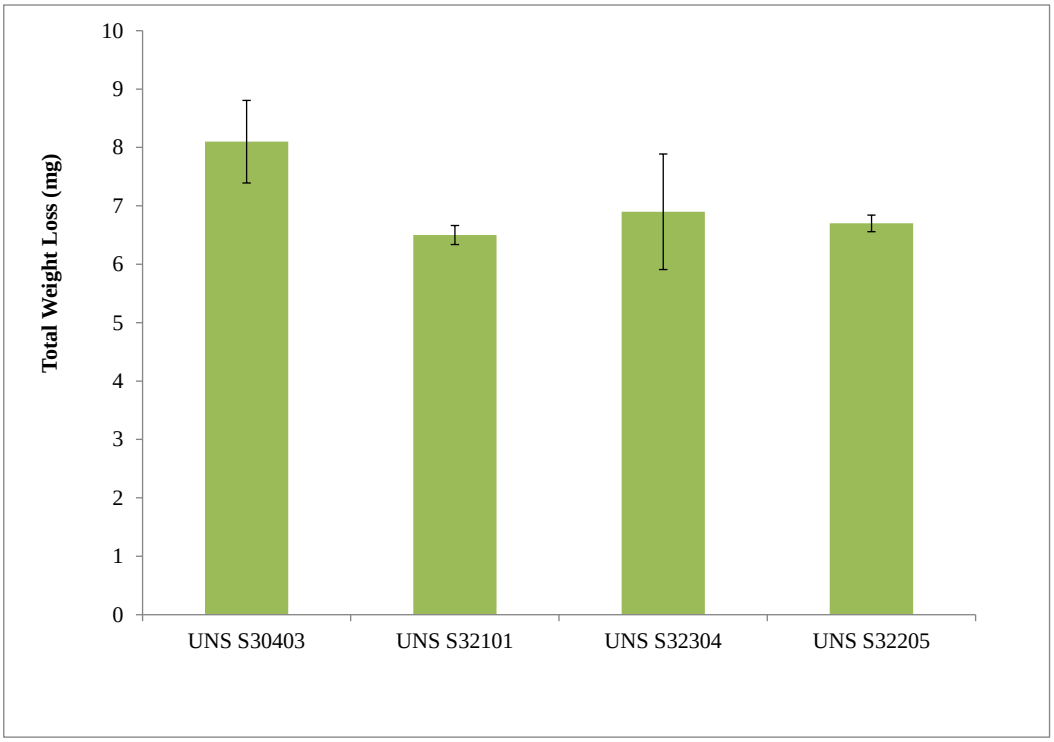

Figure 6.11: Weight loss measurement in a CO_2-saturated oilfield environment at 15 m/s and 500 mg/L sand loading (Error bar is the spread of 3 data points)

Total weight loss of the alloys under erosion-corrosion conditions at 50^{o}C shows the material loss of 6.50 mg, 8.10 mg, 6.90 mg and 6.70 mg for UNS S32101, UNS

S30403, UNS S32304 and UNS S32205 respectively. These values are comparable to 6.95 mg, 8.20 mg, 6.80 mg and 6.78 mg for UNS S32101, UNS S30403, UNS S32304 and UNS S32205 respectively obtained in aerated conditions. There seems to be very close relationship between the material loss under aerated and CO_2-saturated conditions. It seems the difference in the chemistry of the two corrosive media does not have significant influence on the material loss at the test conditions applied in this research.

6.3.2 Anodic Polarisation of the Alloys under Sand Impingement in a CO_2-Saturated Oilfield Environment

Anodic polarisation curves in Figure 6.12 indicate the alloys exhibit a lower range of passive region (almost active for UNS S30403) compared to the curves under static conditions. The current values are also several orders of magnitude higher than what is obtained in static conditions. Initial active corrosion behaviour is noticed as the potential is shifted in anodic direction (Figure 6.12). This is more pronounced in UNS S30403. One other important observation from the anodic polarisation (Figure 6.12) is the higher anodic current density obtained for UNS S30403 as compared to the duplex stainless steels. The lean duplex stainless steels showed comparable passive current density with the standard duplex stainless steel, UNS S32205. This supports our earlier observation for the alloys in aerated 3.5% NaCl slurry where UNS S30403 showed higher current density compared with the duplex alloys.

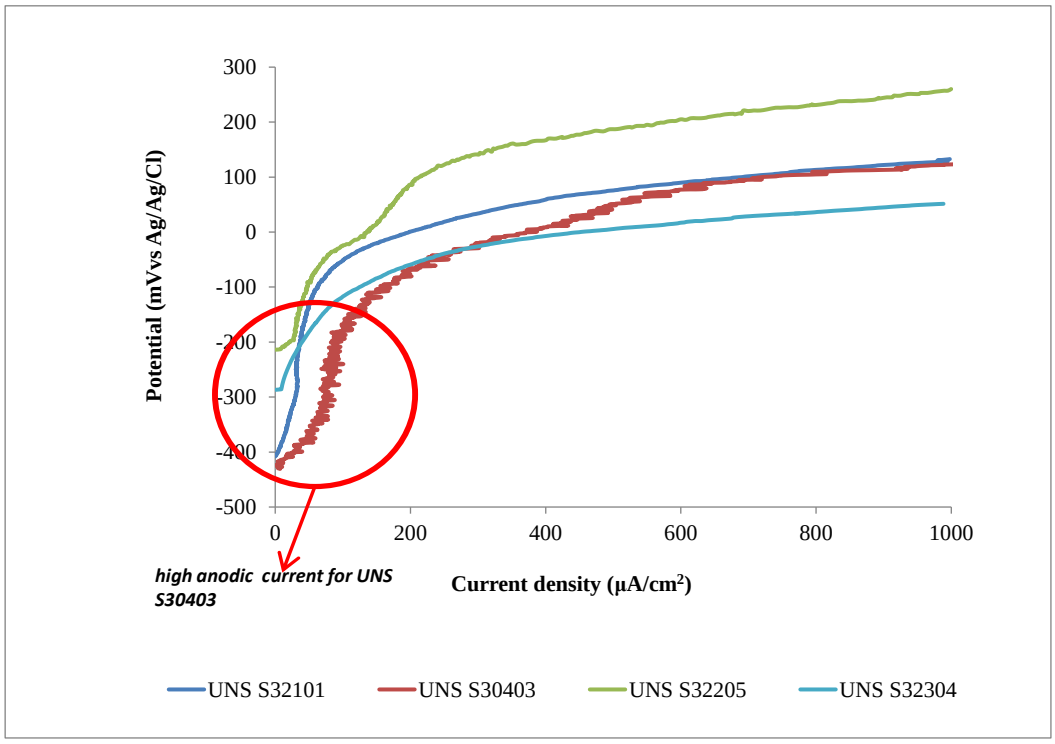

Figure 6.12: Anodic polarisation for the alloys at 15 m/s and 500 mg/L sand loading in a CO_2-saturated oilfield environment (Error bar is the spread of 3 data points)

6.4 Pure Erosion and Erosion-Corrosion of UNS S32101 and UNS S30403 at 24 m/s and 500 mg/L Sand Loading in CO_2-Saturated Oilfield Brine

Material degradation in the form of mass loss for the two alloys tested at 24 m/s with 500 mg/L sand is shown in Figure 6.13. Pure erosion damage (E) and the total weight loss are presented. Pure erosion after sand impingement shows that UNS S30403 has the highest material loss of 16.8 mg and UNS S32101 has a value of 14.7 mg. Total material loss under erosion-corrosion shows that UNS S32101 has a value of 17.2 mg while UNS S30403 has a value of 19.2 mg. These values were compared with the material loss under 15 m/s impinging velocity presented in section 6.3.1. It

was observed that the behaviour of the alloys still follow the same trend observed at 15 m/s impinging velocity. UNS S30403 still suffered higher degradation as result of pure erosion, *in-situ* corrosion and corrosion-enhanced erosion.

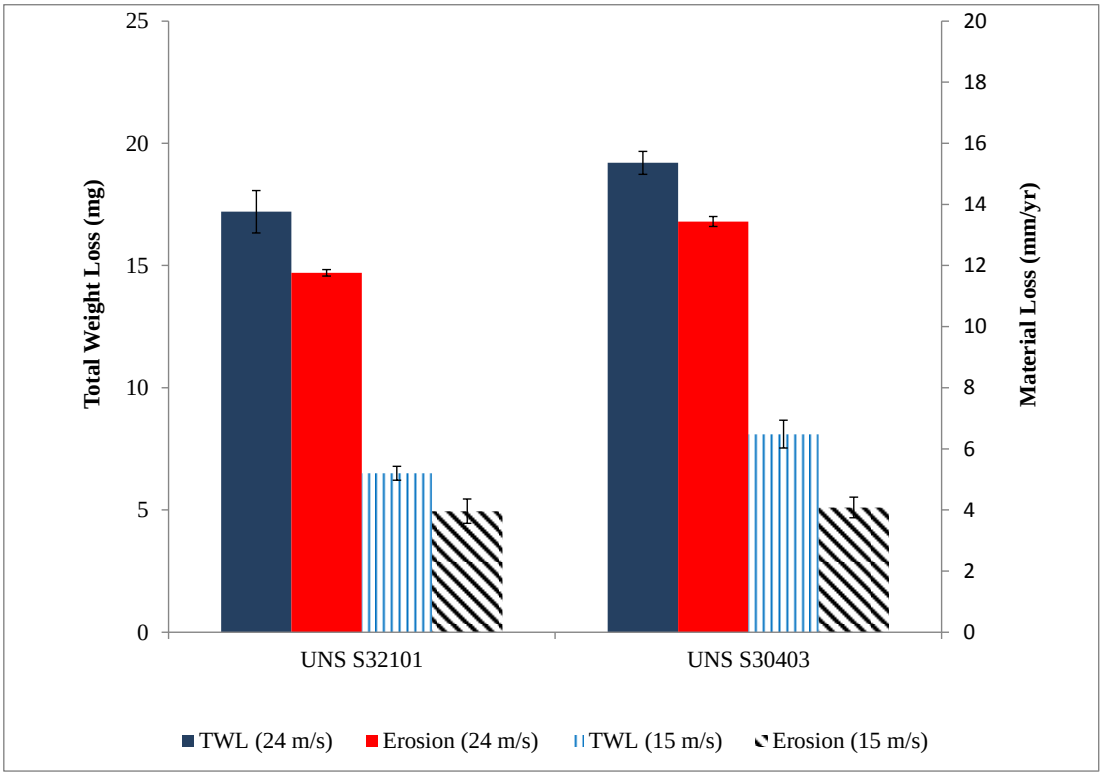

Figure 6.13: Material loss after 4 hours at 15 m/s and 24 m/s with 500 mg/L sand loading in CO_2 environment (Error bar is the spread of 3 data points)

6.4.1 *In-situ* Corrosion Current and the Synergy between Corrosion and Erosion under High Impingement Condition

Tafel plots used to determine the corrosion current density are shown in Figures 6-14-6.15. Corrosion current density evaluated by the extrapolation of the Tafel slope is shown in Figure 6.16. These values were checked by evaluating the polarisation resistance of the alloys and were found to correlate well.

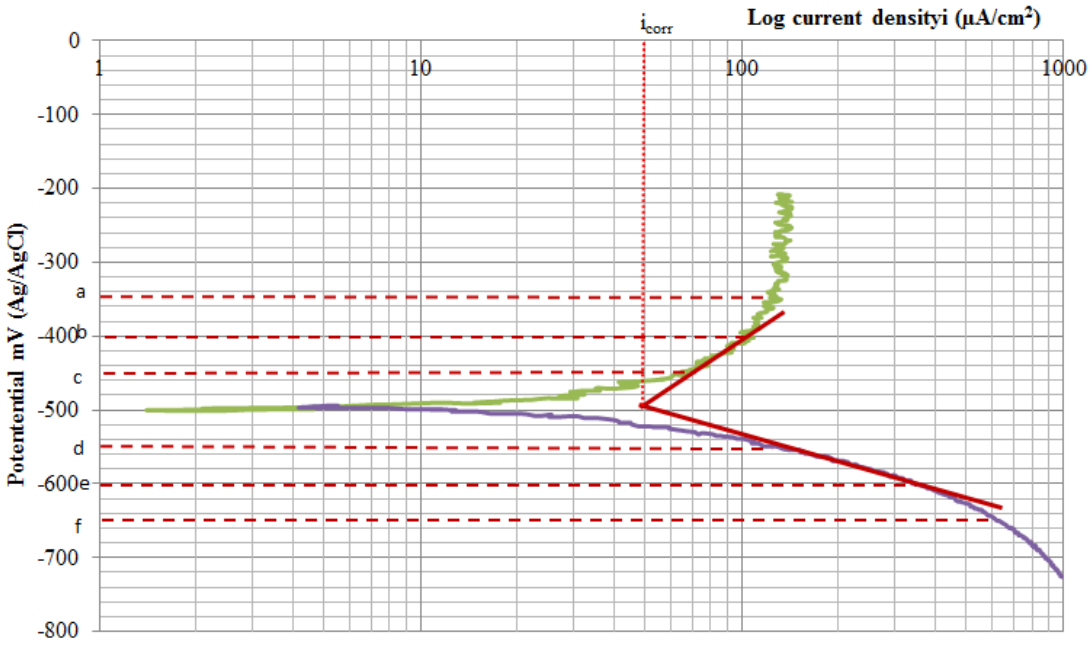

Figure 6.14: Tafel plot for UNS 32101 at 24 m/s and 500 mg/l sand loading in a CO_2-saturated oilfield; a, b, c are points 150 mV, 100 mV and 50 mV respectively above OCP; d, e, f are points 50 mV, 100 mV and 150 mV respectively below OCP

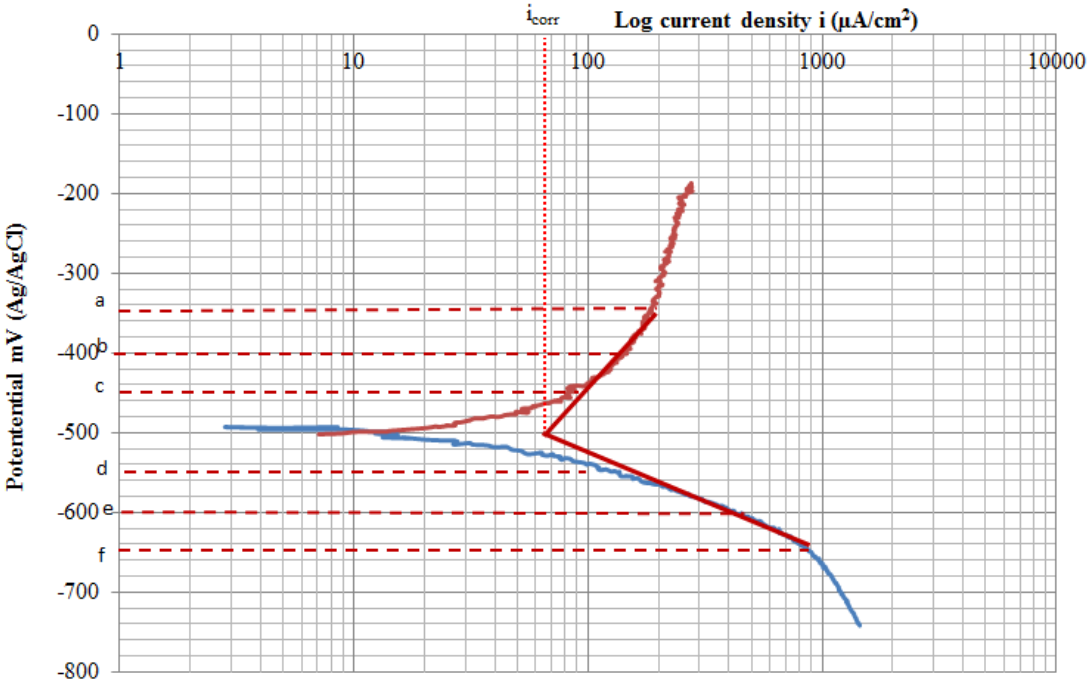

Figure 6.15: Tafel plot for UNS S30403 at 24 m/s and 500 mg/l sand loading in a CO_2-saturated oilfield; a, b, c are points 150 mV, 100 mV and 50 mV respectively above OCP; d, e, f are points 50 mV, 100 mV and 150 mV respectively below OCP

UNS S30403 and UNS S32101 show average *in-situ* corrosion current density of 50 µA/cm^2 and 65 µA/cm^2 respectively (Figure 6.16). Components of the total weight loss are shown in Figure 6.17.

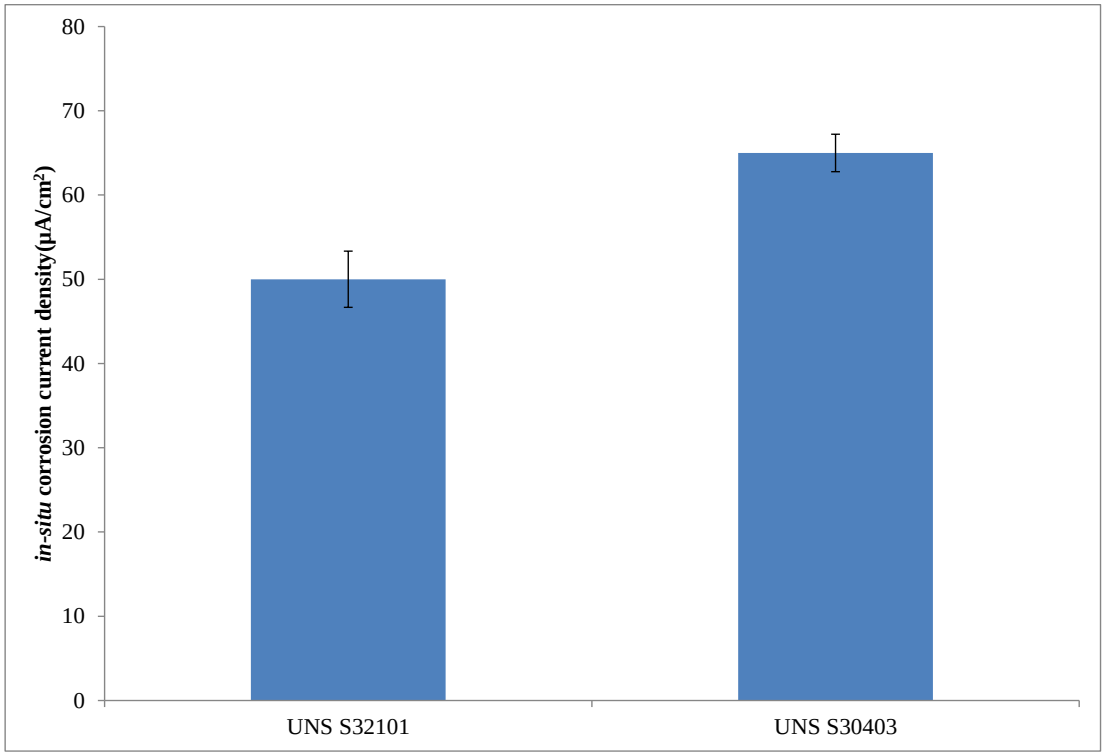

Figure 6.16: *In-situ* corrosion-current density for UNS S30403 and UNS S32101 at 24 m/s and 500 mg/L sand loading in a CO_2-saturated oilfield environment at 50^{o}C (Error bar is the spread of 3 data points)

The percentage contribution of erosion-enhanced corrosion and corrosion enhanced erosion is shown in Figure 6.18. The percentage contribution by corrosion-enhanced erosion is higher than the contribution by erosion-enhanced corrosion. The total contribution by both erosion-enhanced corrosion and corrosion enhanced erosion is less than 13%. This shows that at the high impinging condition pure erosion damage is more dominant contributing more than 86% of the total damage

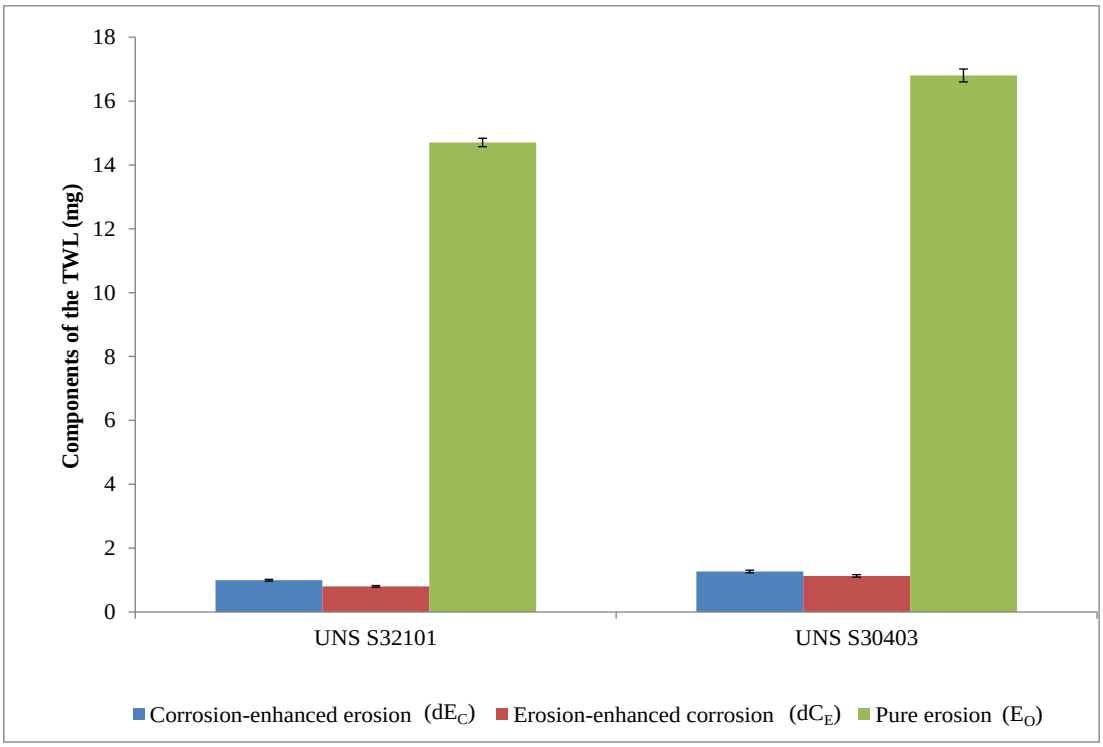

Figure 6.17: Components of the TWL for the alloys at 24 m/s and 500 mg/L sand loading in CO_2-saturated environment (Error bar is the spread of 3 data points)

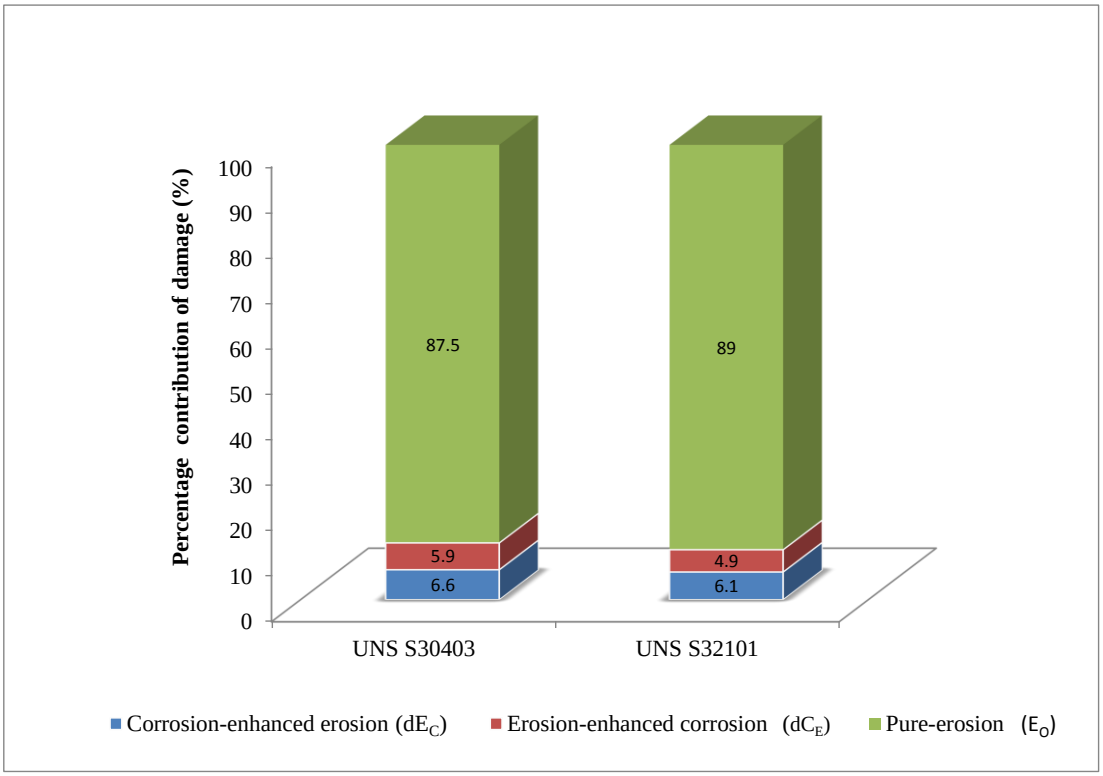

Figure 6.18: Percentage contribution of each component of the total weight loss at 24 m/s and 500 mg/L sand loading in CO_2-saturated environment

6.5 Summary of Chapter 6

UNS S32101, UNS S32304, UNS S30403 and UNS S32205 have been tested under pure erosion and erosion-corrosion conditions. Using sand particles of 500 mg/L and an impinging velocity of 15 m/s in a nitrogen purged environment, the lean duplex stainless steels performed better than the austenitic as well as the standard duplex stainless steel. When a corrosive medium is considered lean duplex alloys still show good resistance considering their chemistry compared to the standard duplex alloy. The standard austenitic stainless steels showed an inferior performance to the lean duplex alloys in the sand laden oilfield and aerated environments. UNS S30403 and UNS S32101 were considered at higher impinging velocity of 24 m/s and the same 500 mg/L sand concentration. The lean duplex alloy also outperforms the standard austenitic stainless steel when pure erosion and erosion-corrosion were considered.

The contribution of the synergy towards the total material degradation was found to be higher at 15 m/s velocity compared to the higher velocity of 24 m/s. Pure erosion seems to be the dominating material damage at the higher velocity contributing more than 86 % of the total degradation. Also, at 15 m/s and 24 m/s impinging velocities the lean duplex alloy, UNS S32101 showed a high resistance to erosion-enhanced corrosion and corrosion-enhanced erosion.

Chapter 7. Sub-Surface Properties of UNS S32101 and UNS S30403 after Erosion-Corrosion

7.1 Introduction and Chapter Overview

The total material loss during erosion-corrosion by solid particle impact can be described by the formula (113):

$$TWL = E_o + dE_C + C_o + dC_E \quad \textbf{7-1}$$

TWL= total weight loss

E_o= pure erosion component

C_o= static corrosion component (negligible for passive alloys)

dE_C = corrosion-enhanced erosion (synergy)

dC_E = erosion-enhanced corrosion (additive)

The terms corrosion-enhanced erosion (dE_C) and erosion-enhanced corrosion (dC_E) have been discussed to be dependent on several factors (35, 194, 195). Among these factors are the repassivation behaviour of the passive film (8, 143, 196, 197), the response of the work-hardened layer to both erosion and electrochemical dissolution (35-37, 141, 198), roughening of the surface by the erodent, galvanic coupling between the anodic (deformed layer) and the cathodic area (passive area) (143, 199, 200). It invariably means that the chemical and mechanical interaction within the surface of the alloy is at a scale which exceeds the thickness of the passive film layer. Despite the abundant models available for the prediction of erosion-corrosion, there is still an incomplete understanding of the physical erosion-corrosion

mechanism. This has hindered the accurate prediction of material degradation by erosion and erosion-corrosion.

The subject of erosion-corrosion synergism and antagonism has not been fully extended to the evolution of modified subsurface crystallography and microstructure (35, 36). The sub-surface and near-surface properties, which could be markedly different from the bulk alloy, have always been represented by the bulk properties. Figure 6.1 shows a simple schematic diagram describing the expected different layers in an alloy under entrained particle impacts. It was suggested that if the physical changes within the near-surface of the bulk alloy (just below the passive film) are understood; it could help in explaining some of the fundamental contributions to the material loss during erosion-corrosion (35-37).

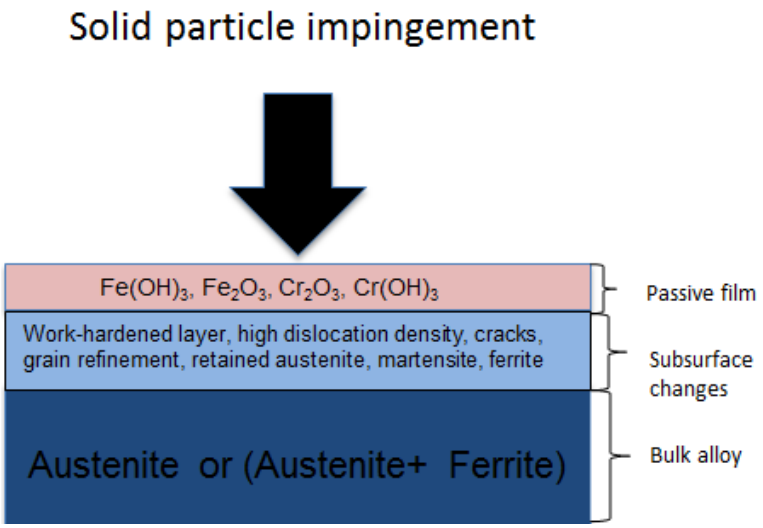

Figure 7.1: Schematic diagram of the proposed model diagram of the near surface of a work-hardenable alloy under solid particle impact

The first step towards the incorporation of the subsurface influence on the erosion-corrosion synergism was taken recently by Rajahram and his co-workers (35, 36). These authors proposed that erosion-corrosion synergism not only depends on

the surface properties but also on the modified sub-surface of the alloy. For metastable phase such as austenite, this becomes even more important as this phase could transform to a more stable strain-induced martensitic phase if it is heavily strained. The austenite phase is known to have low stacking fault energy (171, 201, 202) and it is prone to strain-induced martensitic transformation. Apart from this, alloys under such heavy solid particle impact could develop fatigue cracks, work-hardened layers, high dislocation densities and grain refinement within the sub-surface (194, 203, 204). All these factors would modify both the corrosion and erosion resistance properties of the affected region and subsequently this could affect the synergy between corrosion and erosion. Moreover, when a dual phase alloy comprising ferrite and austenite, such as the duplex stainless steels, is considered, the erosion-corrosion behaviour becomes even more complex. This is because, ferrite is known to be strain rate sensitive and austenite is a metastable phase (121, 205). Therefore, each phase responds differently to the imposed stress under the impinging conditions. To the best of our knowledge, the influence of strain-induced martensite and the other subsurface properties on erosion-corrosion has not been extended to the duplex stainless steels especially the lean duplex stainless steels.

7.2 Hardness Profile and the SEM Images of the Damaged Surface

Figure 7.2 shows the micro-hardness profile of the cross-section of the alloys after erosion-corrosion. There is a general increase in hardness within the centre (near the stagnation zone) of the specimen. The increase in hardness is very pronounced in the austenitic stainless steel compared to the duplex alloys. This is

thought to be as a result of the better response of the fully austenitic phase in UNS S30403 to strain-hardening. SEM images of the alloys taken at three different zones are also shown in Figures 7.3 and 7.4. Region 1 with heavy indentation corresponds to the region close to the stagnation zone where heavy impact resulted in indentation and a pronounced enhancement in hardness. Region 2 showing ploughing and cutting mechanism represents the region between the transition and the wall jet zones. Region 3 represents the region close to the wall jet zone. The wear mechanism around this region is cutting and ploughing as shown in Figures 7.3 and 7.4.

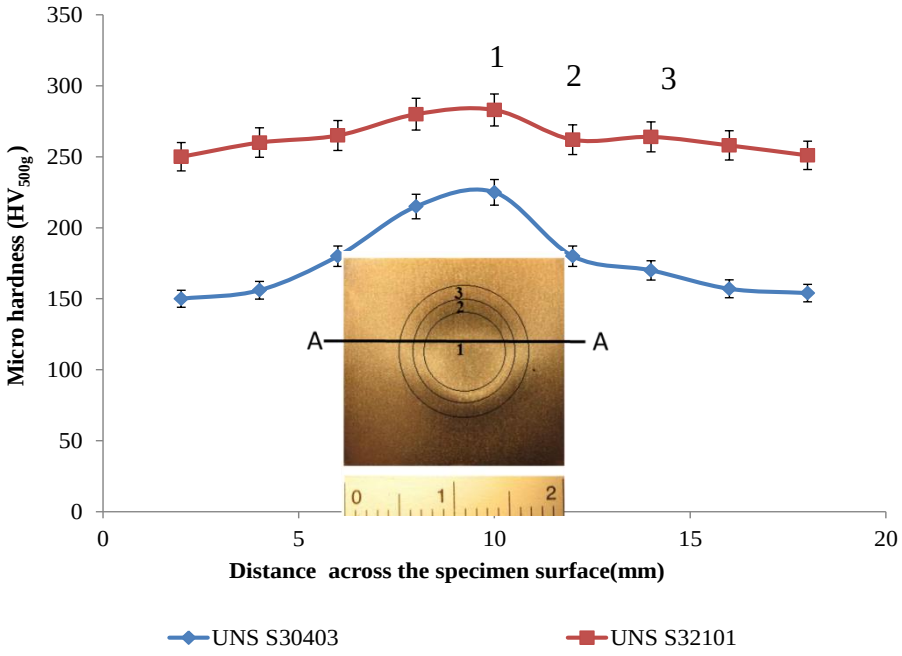

Figure 7.2: Micro-hardness profile of the cross-section (A-A) of alloys after erosion-corrosion by sand in a CO_2-saturated oilfield environment at 24 m/s and 500 mg/L sand loading (Error bar is the spread of 3 data points)

The enhancement of hardness begins to flatten out at the edge of the stagnation zone. There is virtually no improvement in hardness within region 3 which is close to the wall jet zone. Heavy indentation leads to grain refinement and work-hardening within the stagnation zone. Decrease in grain size would lead to increase in grain

boundaries. These multiple grain boundaries become barriers to the movement of dislocations. The portion of the bulk alloy under this heavy impact is thus strengthened and the hardness increases compared to the other parts.

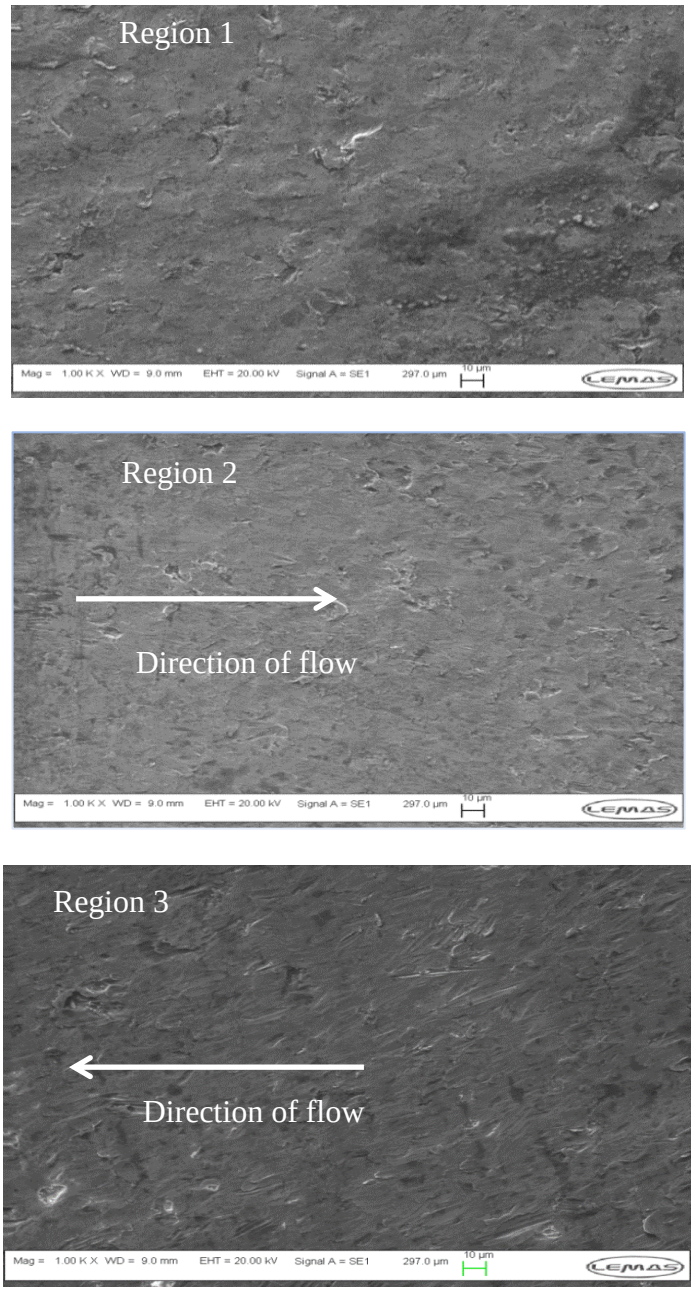

Figure 7.3: SEM images of UNS S32101 after erosion-corrosion at 24 m/s and 500 mg/L sand loading (1, stagnation zone, 2 transition zone, 3, wall jet zone) (Scale bar = 10 µm)

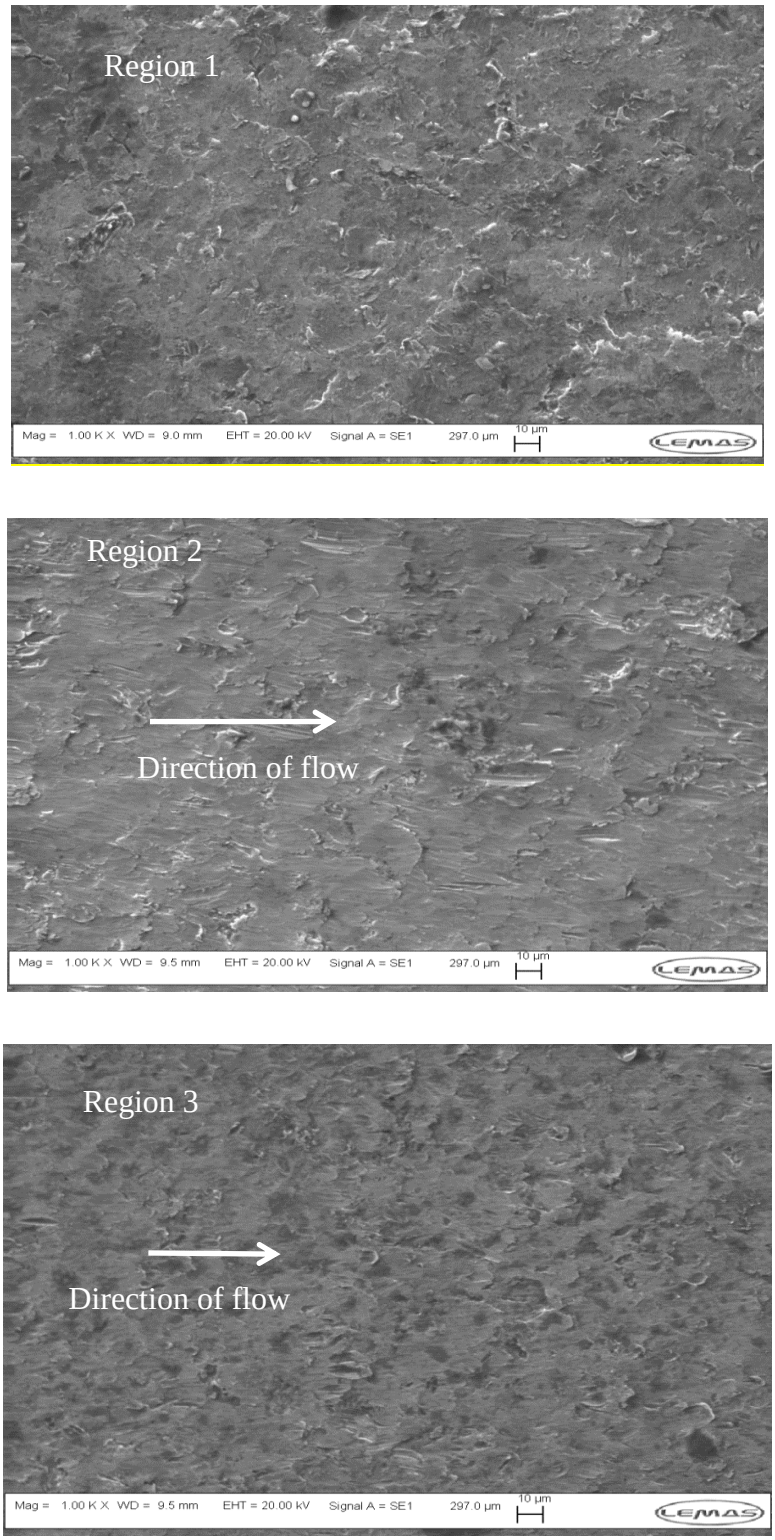

Figure 7.4: SEM images of UNS S30403 after erosion-corrosion at 24 m/s a500 mg/L sand loading. (1, stagnation zone, 2 transition zone, 3, wall jet zone) (Scale bar = 10 µm)

7.3 X-ray Diffraction (XRD) Pattern of the Damaged Surface

The XRD spectra for UNS S30403 and UNS S32101 are shown in Figures 7.5 and 7.6. Large strain resulting from the impact was able to cause plastic deformation beneath the passive film. Phase transformation from the face centred cubic (FCC) to the body centred-tetragonal (BCT) martensite also occurred as a result of the repeated impacts. As shown in Figure 7.6, all the austenite peaks (A) in the polished samples of UNS S30403 have been drastically reduced and the few strain-induced martensite peaks (M) as a result of grinding and polishing have increased after the work-hardening. A new martensite peak can also be seen to have emerged at about $2\Theta = 65^{o}$.

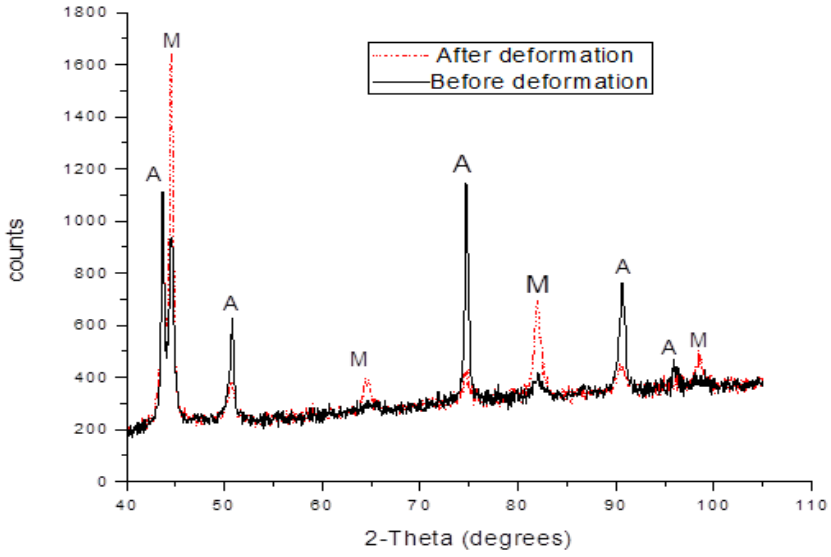

Figure 7.5: XRD pattern of UNS S30403 before and after erosion-corrosion at 24 m/s and 500 mg/L sand loading

For the UNS S32101 lean duplex in Figure 7.6, assuming all the initial BCC peaks before the sand impact are for ferrite, it was expected that after work-

hardening there will be a reduction in ferrite volume fraction as a result of the strain rate sensitivity of ferrite as compared to austenite. This can be seen from Figure 7.6 as the volume fraction of martensite+ferrite seems to be very close to the initial ferrite peaks. Addition of martensite to the volume fraction does not seem to match the rate at which ferrite is removed from the dual (martensite+ferrite) phase. There is however a general reduction in the austenite peaks confirming a transformation to strain-induced martensite in this alloy.

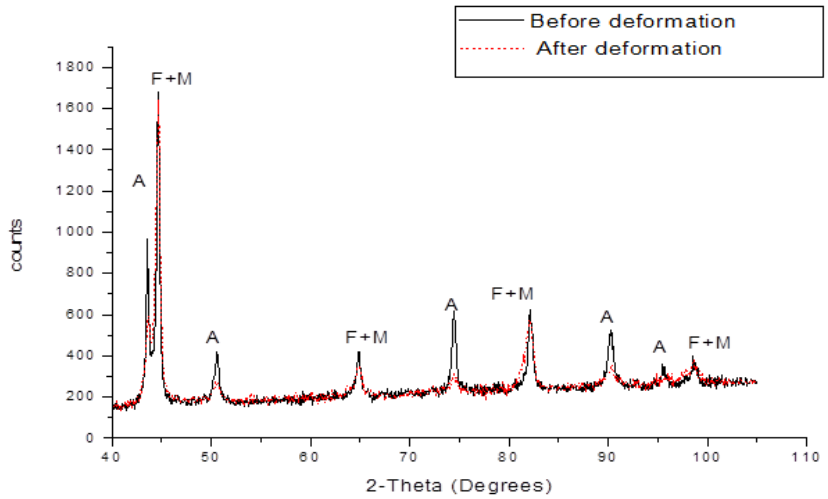

Figure 7.6: XRD pattern of UNS S32101 before and after erosion-corrosion corrosion at 24 m/s and 500 mg/L sand loading

7.4 Focused Ion Beam (FIB) and SEM Images of UNS S30403 after Erosion-Corrosion

Focused Ion Beam (FIB) was used to study the sub-surface wear morphology and crystallographic changes due to erosion-corrosion. After the materials have been subjected to a CO_2-saturated environment with 500 mg/L sand and a velocity of 24 m/s, samples were taken for FIB preparation. Two samples were prepared from each

coupon with one sample taken from the heavily deformed centre (stagnation zone) and the other taken from the edge (near the wall jet zone) of the sample. Figure 7.7A shows the SEM image of the heavily deformed stagnation zone. Figure 7.7B shows how the sample was milled out with the ion beam. The sample prepared for both FIB and TEM is shown in Figure 7.7C. Figure 7.7D shows the image with SEM prior to observation in the TEM.

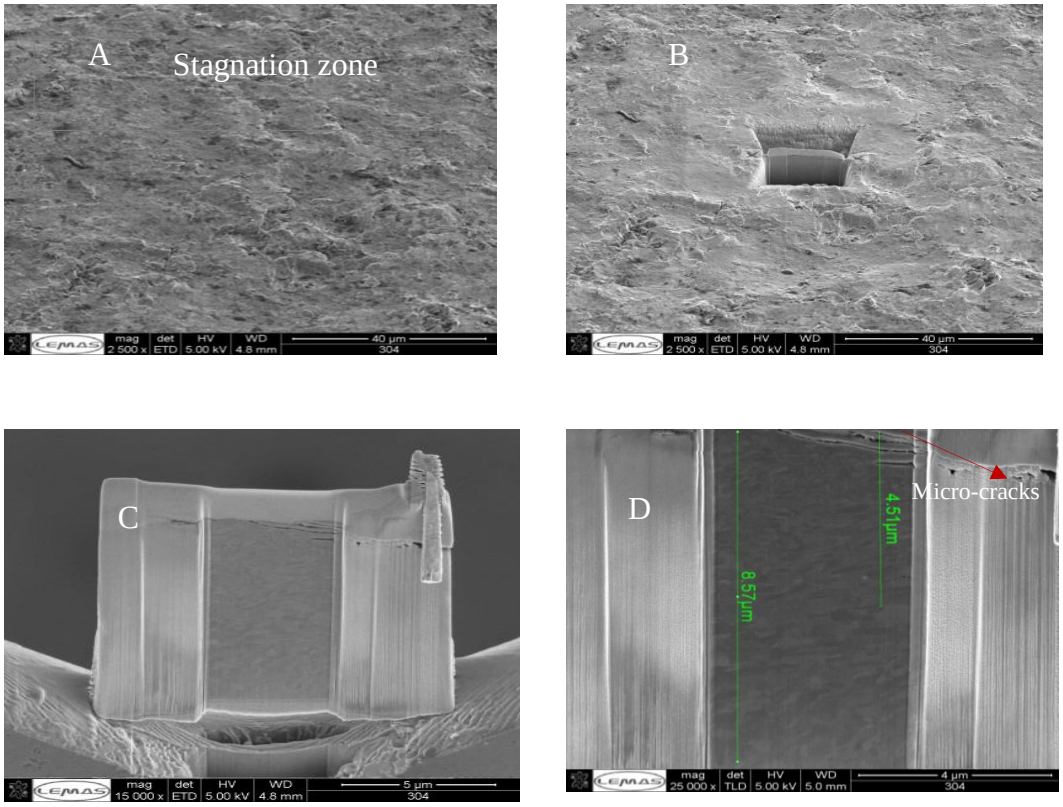

Figure 7.7: FIB images of UNS S30403 taken from a point near the stagnation zone of the coupon subjected to 500 mg/L sand at 24 m/s in a CO_2-saturated oilfield environment

Sub-surface micro cracks are observed near the surface of the deformed sample. A close look at the subsurface of the alloy shows two distinct regions. The near surface region within the top 4 µm shows grains with smaller sizes compared with the bulk. It is expected that with the high multiple impact from the sand, a nano-grain

layer (not seen here) will be formed at the topmost layer with the micro grains formed beneath this. Since the work-hardened layer would transmit most of the energy to the bulk grains; micro grains and deformation layer is expected below the topmost layer.

Outside the heavily deformed area (Figure 7.8D), the extent of subsurface cracking is less compared to the observations made in Figure 7.7D.

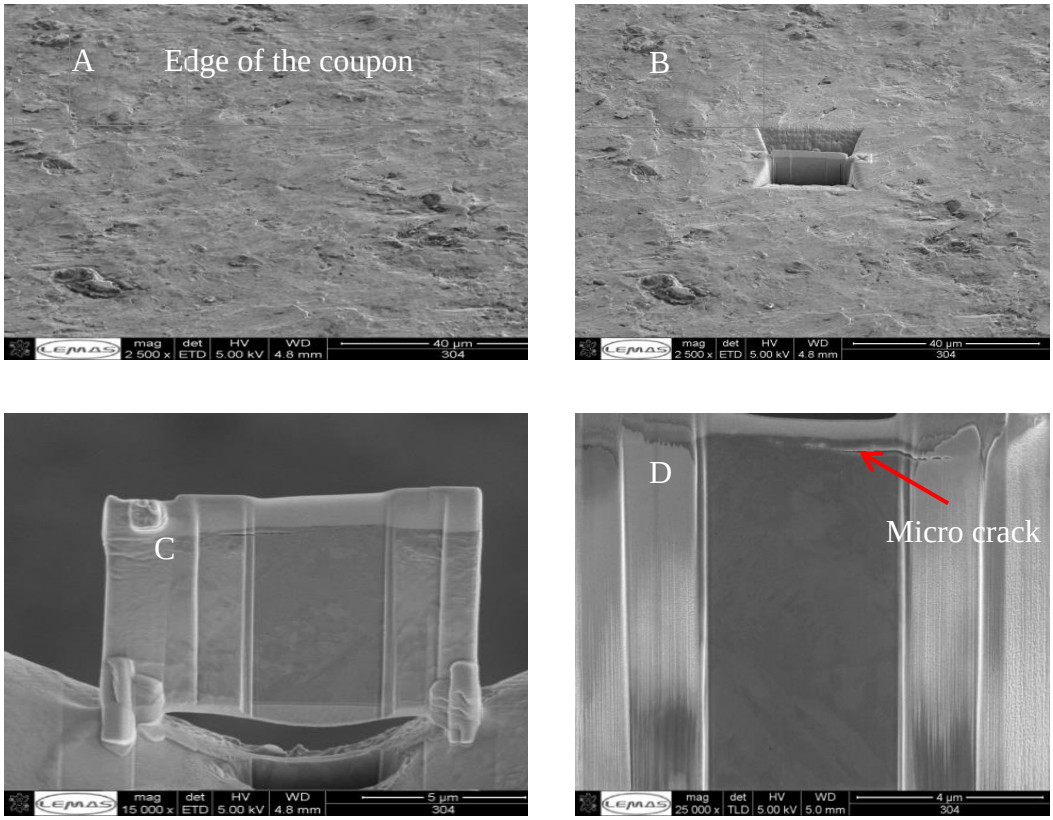

Figure 7.8: FIB images of UNS S30403 taken from the edge of the coupon (near the wall jet zone) subjected to 500 mg/L sand at 24 m/s in a CO_2-saturated oilfield environment

Also, the changes in the grain sizes observed previously in the case of the stagnation zone are not really visible within this region. Probably, twin formation could be

possible here as a result of the shear pattern. However, this could not be resolved with the SEM.

7.5 Focused Ion Beam (FIB) and SEM Images of UNS S32101 after Erosion-Corrosion

The same procedure in Figure 7.7A was repeated for UNS S32101. Figure 7.9A shows the SEM image of the heavily deformed stagnation zone. Figure 7.9B shows how the sample was milled out with the ion beam. The milled sample has a thickness of approximately 80 nm and a length of about 2µm.

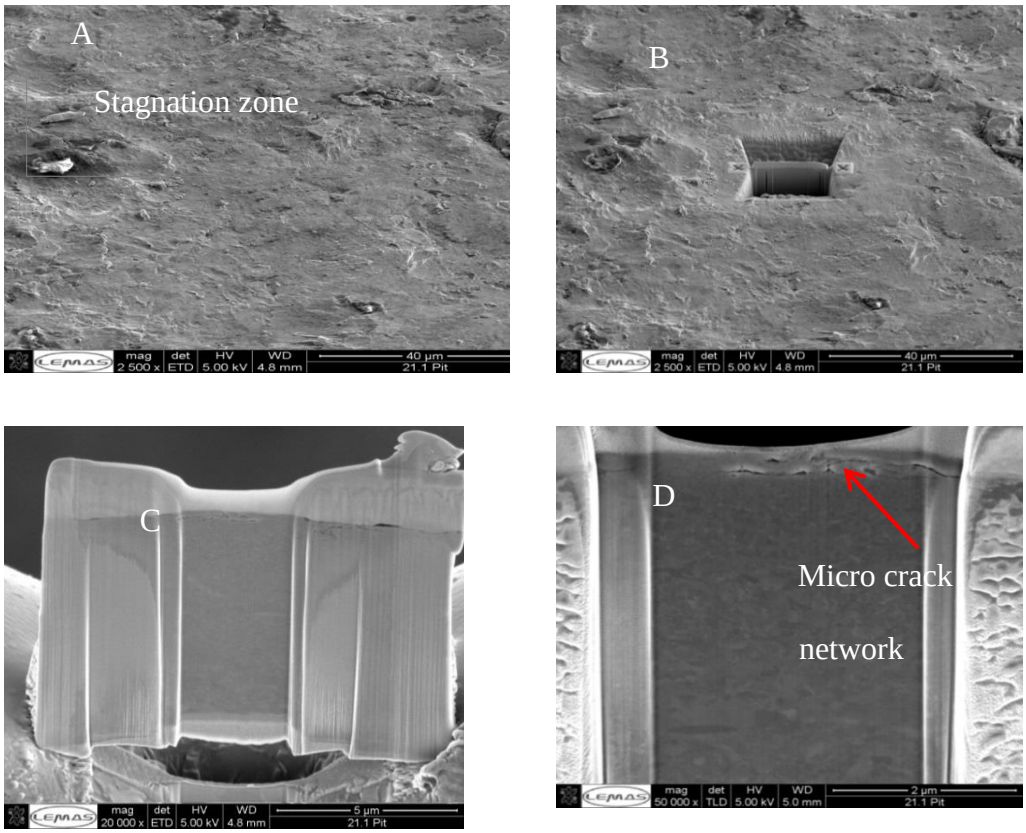

Figure 7.9: FIB images of UNS S32101 from the stagnation zone of the coupon subjected to 500 mg/L sand at 24 m/s in a CO_2-saturated oilfield environment

The sample prepared for both FIB and TEM is shown in Figure 7.9 C. Figure 7.9 D shows the imaged sample with the FIB in the SEM mode.

Micro cracks were observed near the surface of the sample taken from the stagnation zone. No evidence of subsurface cracking was seen from surface cross-sections taken from the edge of the coupon (7.10D).

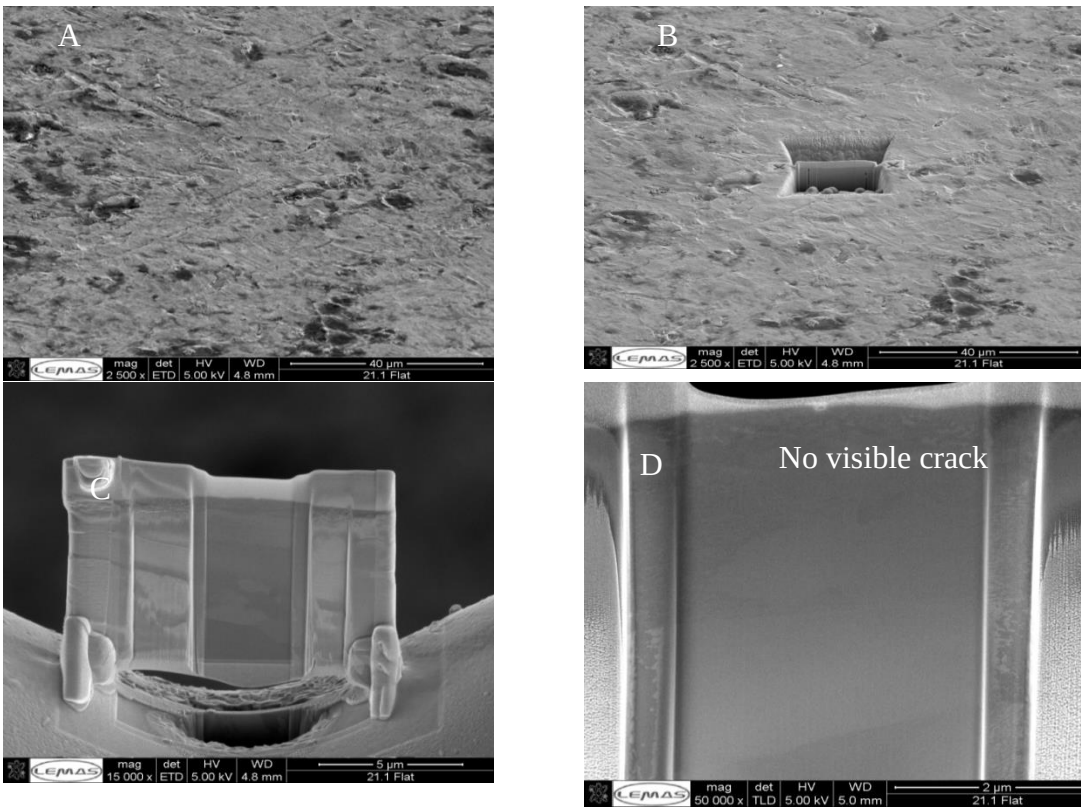

Figure 7.10: FIB images of UNS S32101 from the edge (near the wall jet zone) of the coupon subjected to 500 mg/L sand at 24 m/s in a CO_2-saturated oilfield environment

This is quite different from the UNS S30403 where subsurface cracking coupling could be observed within this zone. There is also a visible change in grain sizes from the near surface to the bulk of the coupon especially for the coupon taken within the stagnation zone (Figure 7.9 D). This is not really visible in the cross-section taken from the edge of the sample (Figure 7.10D). As discussed earlier, the high multiple

impact from the sand has the potential to modify the crystallographic structure near the surface of an alloy via a strain induced mechanism. Energy would be transmitted from the work-hardened layer to the bulk leading to a preferential re-crystallisation of the alloy within a few micro-meters of the top surface.

7.6 Bright Field TEM Images of UNS S30403

Transmission Electron Microscopy (TEM) bright field images of the sample taken within the stagnation zone and the edge of the coupon are shown in Figure 7.11 and 7.12 respectively.

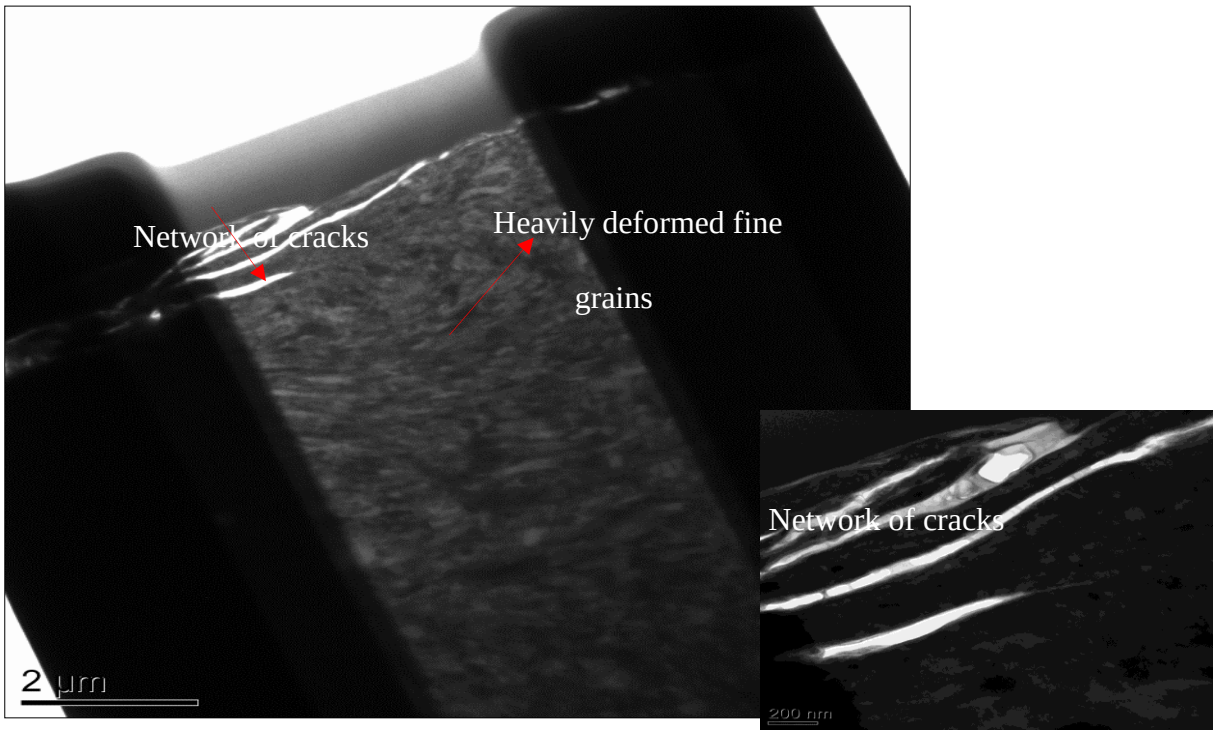

Figure: 7.11: TEM bright field images of UNS S30403 taken from the stagnation zone of the alloy subjected to 500 mg/L sand at 24 m/s in a CO_2-saturated oilfield environment

Fatigue-cracks could be seen below the extruded lips. Within the crack network and just below the deformed surface is a layer of nano-grains that extended up to

about 100 nm. Below this is the heavily deformed and disoriented micro grain as a result of the induced strain (Figure 7.11). This is very obvious within the stagnation zone. Fewer cracks were observed within the sample taken at the edge of the coupon (Figure 7.12).

The heavily deformed grains are not observed at this region. However, there seems to be twin formation (Fig. 7.12) a few distances below the surface. This is probably due to the shearing of the grains resulting from the low angle shear impact near the wall jet zone. As we know that the impact within this region is at low angle which could lead to shear stresses.

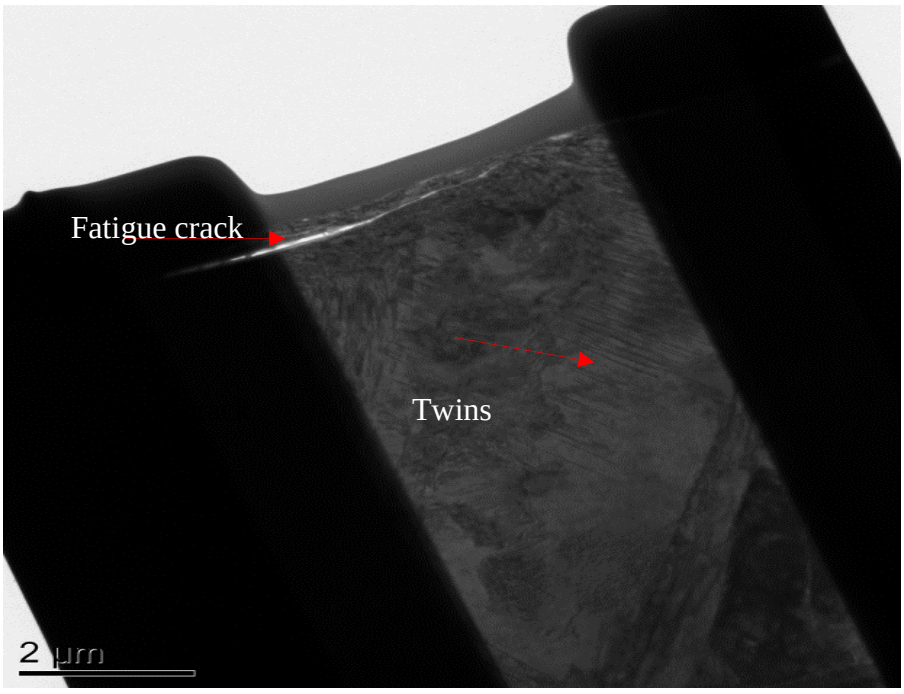

Figure 7.12: TEM bright field images of UNS S30403 taken from the edge of the coupon of the alloy subjected to 500 mg/L sand at 24 m/s in a CO_2-saturated oilfield environment

Crack formation is indicative of brittle behaviour which is possible in a ductile material as a result of work-hardening of the top layer. The multiple sand impacts at a very high strain rate could increase the yield strength of the subsurface of the alloy.

Higher yield strength increases the risk of fatigue crack. The crack could also be due to the localised stress built up by the impurity (sand and oxide) embedded as a result of the repeated folding of lips.

7.6.1 Phase Transformation from Austenite (FCC) to Martensite (BCT)

Figure 7.13 shows the Selected Area Electron Diffraction (SAED) pattern obtained in the deformed region. The continuous diffraction rings shows that the grains are nano-sized and have random crystallographic orientations (206).

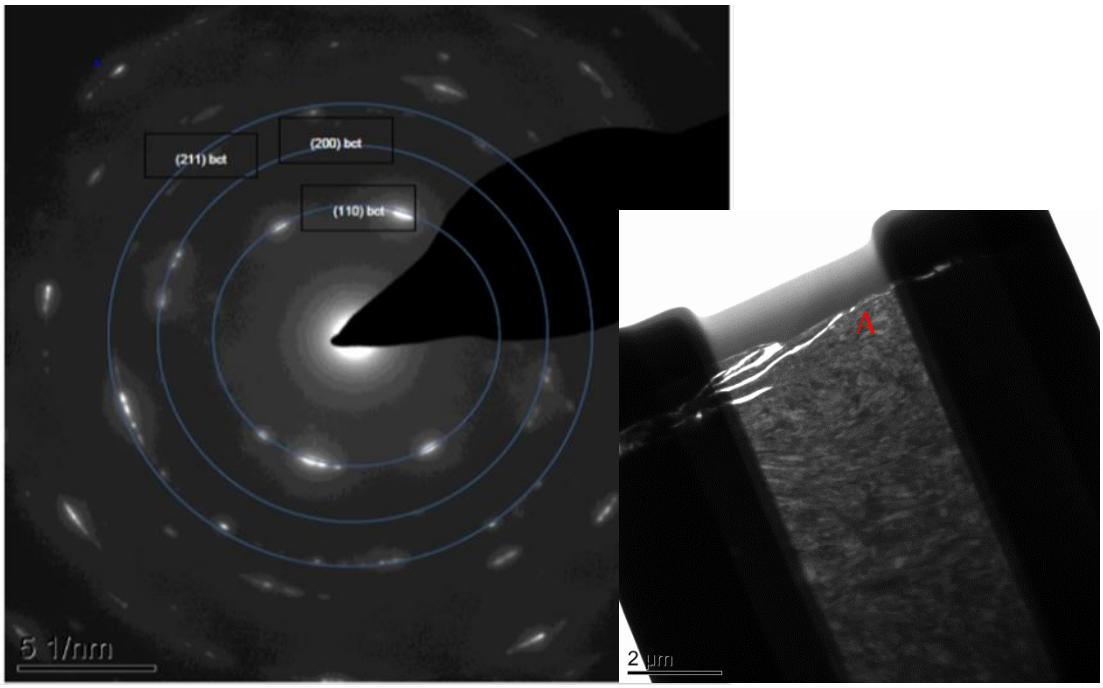

Figure 7.13: Selected area electron diffraction (SAED) pattern of point A taken from the stagnation zone of UNS S30403 after erosion-corrosion at 24 m/s and 500 mg/L sand loading showing the BCT rings confirming the transformation from FCC to BCT

These rings that could be indexed to Body Centre Tetragonal (BCT) crystal structure within the Face-Centred Cubic (FCC) austenitic phase. The BCT rings have indices (110), (200) and (211). This is transformation from the face centre cubic

austenite as a result of the large strain induced by the impact. Such impact has been reported (35, 36) to cause increase in dislocation density and eventually the strain-induced transformation as observed in this case. The same martensitic transformation was reported in Figures 7.5 and 7.6 using the X-ray diffraction. Similar results have also been reported by Rajahram *et al*. (35, 36).

7.7 Bright Field TEM Images of UNS S32101

Transmission Electron Microscopy (TEM) bright field images of the sample taken within the stagnation zone and the edge of the coupon are shown in Figure 7.14 and 7.15 respectively.

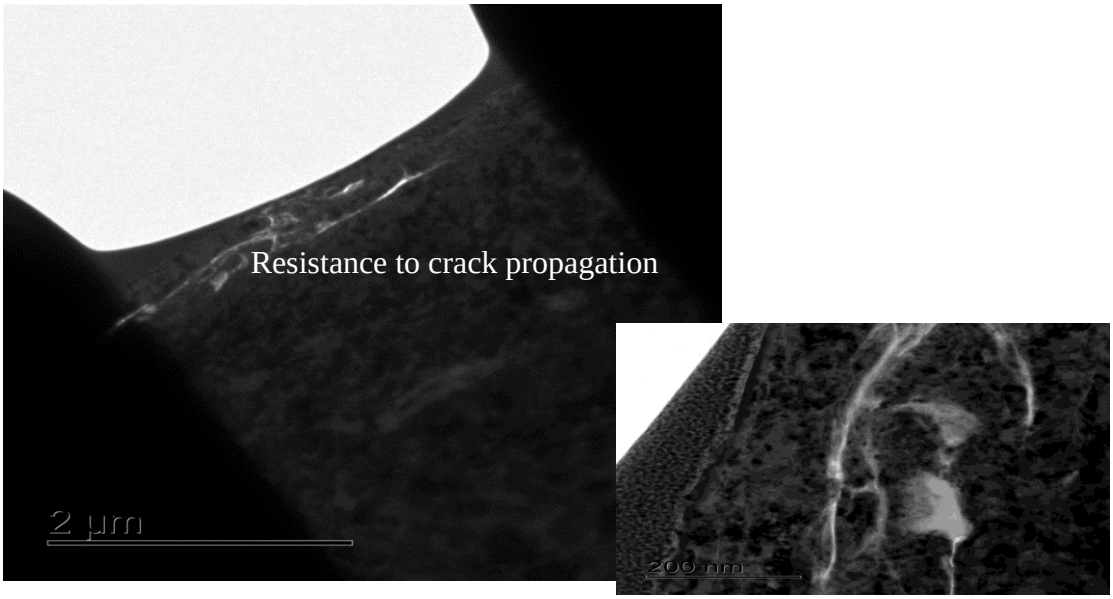

Figure 7.14: TEM bright field images of UNS S32101 taken from the stagnation zone of the alloy subjected to 500 mg/L sand at 24 m/s in a CO_2-saturated oilfield environment

Crack propagation could also be seen below the extruded lips (Figure 7.14). The extent of these cracks is not as severe as what was seen in UNS S30403. No visible crack is noticed within the subsurface close to the edge of the coupon (Figure 7.15).

The heavily deformed grains noticed within the stagnation zone are not also observed at the edge of the coupon.

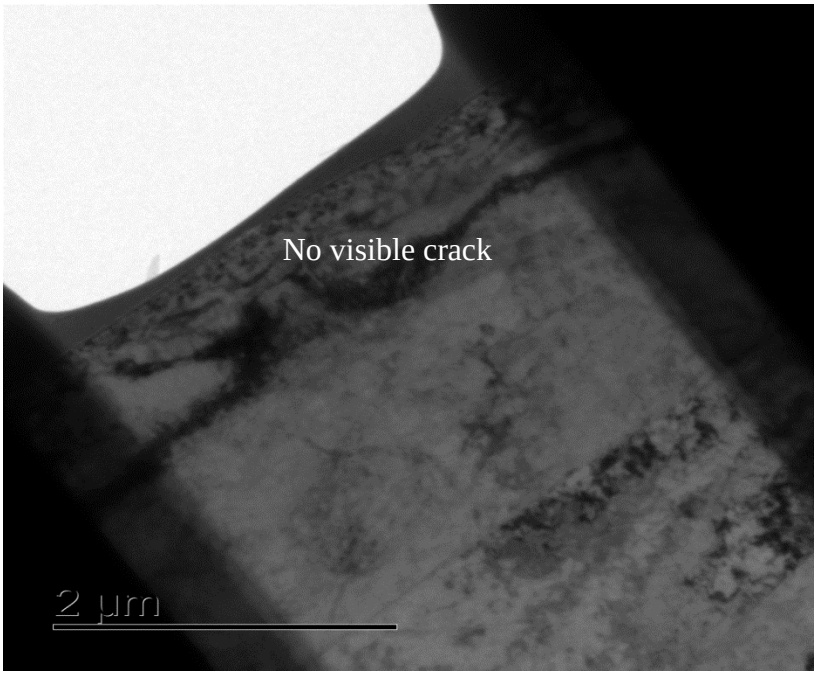

Figure 7.15: TEM bright field images of UNS S32101 taken from the edge of the coupon subjected to 500 mg/L sand at 24 m/s in a CO_2-saturated oilfield environment

7.8 Summary of Chapter 7

Micro-hardness results in Figure 7.2 show that hardness within the subsurface (within a few micro metres below the passive film) of the heavily deformed stagnation zone is increased. It was also observed, by the X-ray diffraction patterns in Figures 7.5 and 7.6 that the metastable FCC austenite transformed to a more stable strain-induced BCT martensite after erosion-corrosion. This was supported by the Selected Area Electron Diffraction obtained with the TEM. Transmission electron microscopy image showed fatigue cracks and grain refinement within the subsurface of the alloys after erosion-corrosion at 24 m/s and 500 mg/L sand loading. All of

these results show that apart from surface wear and corrosion, sub-surface morphology and crystallography changes also occurred.

Erosion-corrosion is a complex phenomenon with varying contributory factors. In this chapter effort has been made to elucidate the fact that microstructural and crystallographic changes occur near the surface (below the passive film layer) of workhardenable alloys. The contribution of such changes to erosion-corrosion will be discussed in chapter 9 of this thesis.

Chapter 8. Repassivation Kinetics of the Passive Film Formed on UNS S32101 and UNS S30403 in a CO_2-Saturated Oilfield Environment Containing Sand

8.1 Introduction and Chapter Overview:

The generation rate of fresh metal surface and the repassivation rate of the alloy are two important factors that determine the erosion-corrosion resistance of such alloys (33, 207-209). Erosion can also be detrimental to the pitting resistance of alloys especially if the repassivation rate is low (32, 34). The erodent generates rough surfaces which easily trigger pitting. Therefore, an alloy with lower repassivation rate is likely to be more susceptible to pitting than alloy with high repassivation rate. It then means that the study of the ability of passive film to regenerate after depassivation is very important to the study of erosion-corrosion and pitting of passive alloys (32, 65, 210)

Previous methods that have been used extensively for the study of repassivation kinetics of passive films including: abrading electrode technique (70), scratching electrode technique (152, 173), cavitation technique (65) as well as micro and nano indentations (153, 174-177). Single impact by sand and glass beads has also been considered for austenitic stainless steels (31, 178). To the best of the author's knowledge, however, none of the experiments has been carried out in a CO_2-saturated oilfield environment. Additionally, the repassivation behaviour of lean duplex stainless steel UNS S32101 has not been considered for evaluation, whether

in CO_2-saturated oilfield or any other environment. It is also of interest to study the repassivation behaviour of fully austenitic stainless steel and compare this with the lean duplex stainless steel of similar corrosion resistance. Two alloys that have been in contention for application in the oilfield are the lean duplex stainless steel UNS S32101 and austenitic stainless steel UNS S30403 as both alloys exhibit similar corrosion resistance.

8.2 Theory behind the Repassivation Kinetic Method Used in this Research

When the passive film on an alloy is depassivated by abrasion, rubbing, scratching, cavitation, indentation or sand impact, the damaged passive layer tends to re-oxidize. The process of re-oxidizing leads to electron loss on the exposed bare metal and hence a charge transfer occurs. The charge transfer reaction could either result in dissolution of metal ion or formation of solid oxide. Reformation of the passive film thus requires an anodic charge which can be measured in electrochemical experiment (66).

Models that describe repassivation kinetics are already discussed in Chapter 2, Section 2.5. Two general models described are *surface coverage model* and *film growth model*. These two models are based on the assumption that only solid oxide is formed during repassivation and that no metal dissolution occurs (66). In the coverage model current stays constant up to a time when a monolayer oxide is formed and then decreases sharply. This stage of the film growth is not well understood (66). The film growth model which is based on the high field conduction has been argued to describe well the film growth kinetics of the anodically polarized

metals (146). It has also been argued that the difference between using the combined model and the simpler growth model is insignificant (66). In view of this and based on the fact that there is high uncertainty in using only the lateral growth model, the combined model is considered for this research. Determination of the repassivation index is however based on the film growth model. Figure 8.1 shows a numerical simulation of passivation transients that combines both lateral growth and uniform growth models.

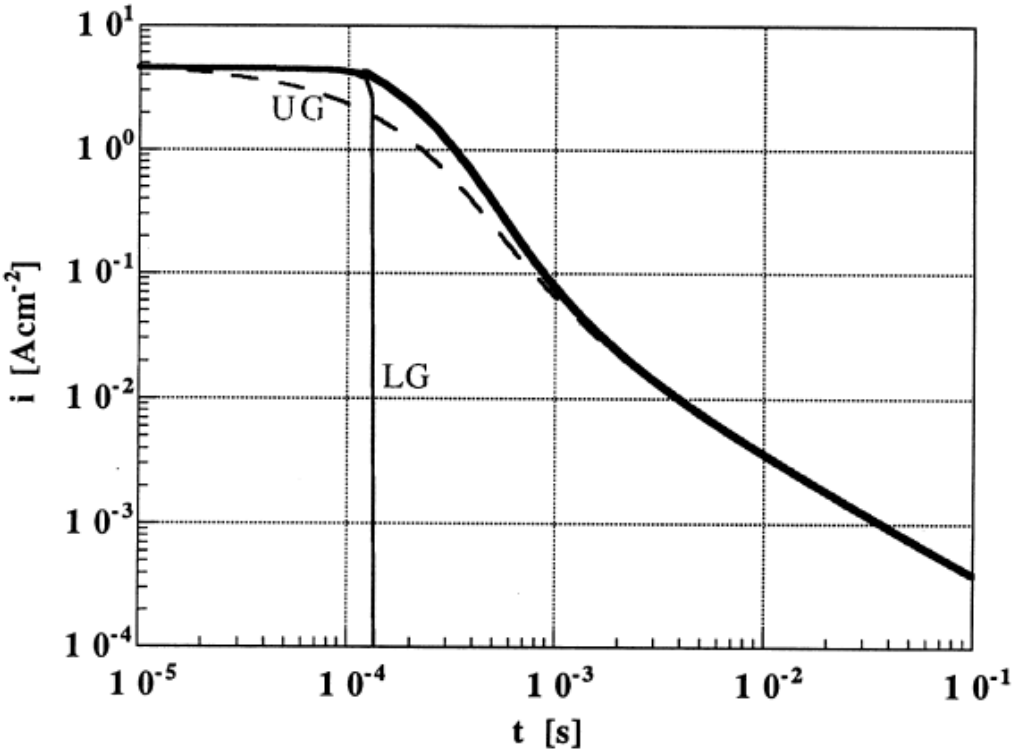

Figure 8.1: Numerical simulation of passivation transients obtained by combining lateral growth (LG) and uniform growth (UG) models. The bold line is the combined model (66)

8.3 Assumptions, Particle Flux and Particle Frequency

This research adopted multiple sand impacts to study repassivation mechanisms, hence a need to estimate the particle flux/frequency. An estimate of a single impact

frequency will be based on assumptions that are not practically possible based on the high sand concentration/sand flux exiting the nozzle. Inter-particle collisions, post impact rebound/collisions are some of the possible effects that need to be considered (193, 211, 212). However, if it is assumed that the particles travel at the free stream velocity, using the average diameter of the silica sand (assumed spherical) as shown in Figure 4.5, Chapter 4 as 250 µm with density of 2650 kg/m^3, then, the frequency of a single sand particle impact can be calculated assuming there are no inter-particle collisions as shown in Section 4.6.3, Chapter 4. From the analysis a value of 7.5 KHz was obtained (Table 8-1). High impact frequency has also been reported by other authors. A value of 200 KHz has been reported (213) for a velocity of 7 m/s and 10,000 mg/L sand loading in a slurry pot. Liebhard and Levy (184) also reported a value up to 25 KHz for particles at impact speed of between 20 to 60 m/s. Summary of the calculation done in chapter 4 is shown in Table 8-1.

Table 8-1: Data from the SIJ calibration

A	Frequency of the pump	50 Hz
B	Impinging velocity at 50Hz	24 m/s
C	Flow rate of the fluid at 50Hz	0.0003 m^3/s
D	Specific sand loading (exiting the nozzle)	500,000 mg/m^3
E	***Particle flux*** (C X D)	150 mg/s (0.15 x 10^{-3} Kg/s)
F	Mass of one sand grain (density X volume)	2 X 10^{-8} Kg
G	Sand ***particle frequency*** (E/F) (no inter-particle collision)	7.5 KHz

8.4 Current Noise during Erosion-Corrosion

Figures 8.2 and 8.3 show the current-time response for UNS S30403 and UNS S32101 before, during and after the sand impingement at 20°C and 50°C respectively. Current-time response for the first 30 minutes after activation at -0.85 V shows the decay of current at the test potential (-0.2 $V_{Ag/AgCl}$) and temperatures of 20 and 50°C. The test potential falls within the passive region of both alloys from the anodic polarisation results in Chapter 5.

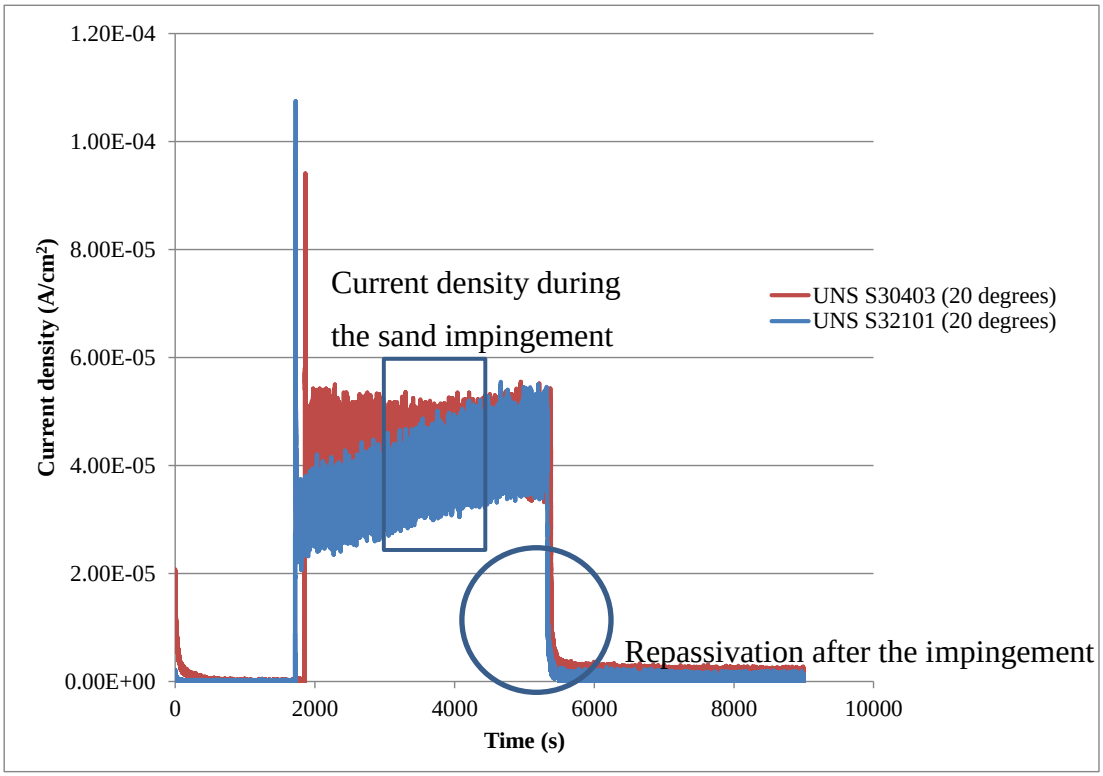

Figure 8.2: Current-time variation at constant potential (-0.2 $V_{Ag/AgCl}$) for 2.5 hours with 1 hour of sand impingement at 20°C in a CO_2-saturated oilfield environment at 24 m/s and 500 mg/L sand loading

At either temperature, UNS S32101 shows lower current density for the first 30 minutes compared with UNS S30403. Impingement with 500 mg/L sand resulted in

an increase in current density as result of higher metal dissolution rate occurring during impingement (26) (Figures 8.2 and 8.3). Current density resulting from one hour impingement is on average 80 µA/cm^2 and 60 µA/cm^2 at 50^{o}C for UNS S30403 and UNS S32101 respectively (Figure 8.3). Average current densities of 50 µA/cm^2 and 35 µA/cm^2 were recorded at 20^{o}C for UNS S30403 and UNS S32101 respectively (Figure 8.2).

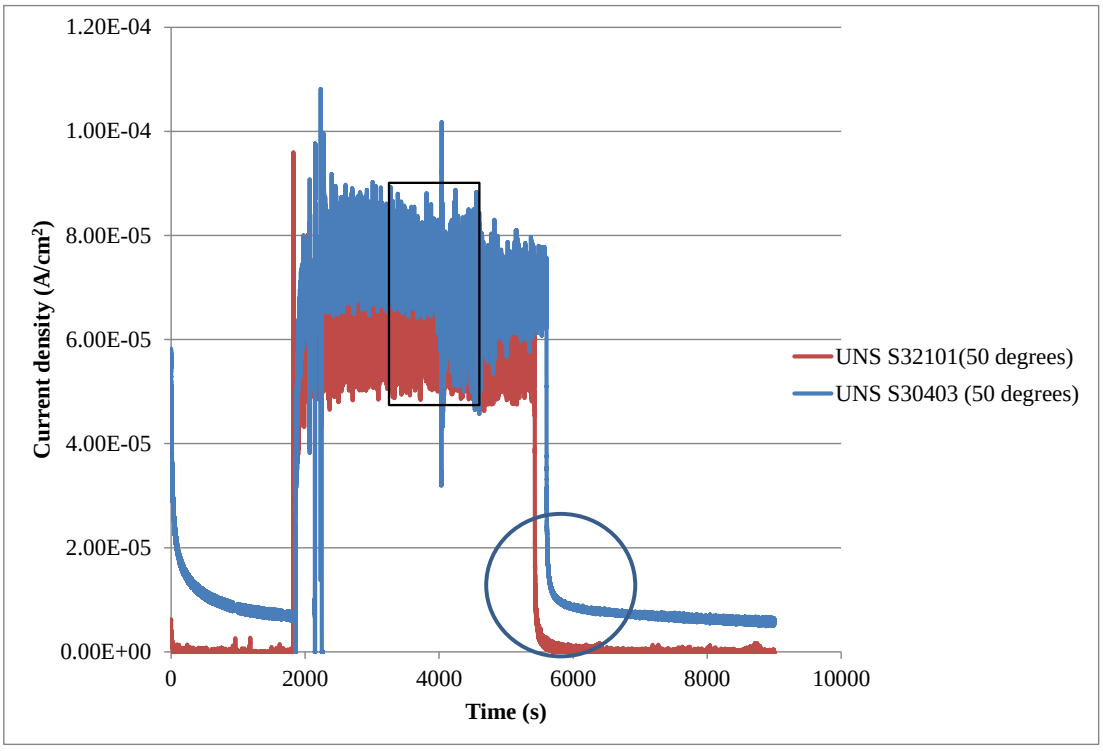

Figure 8.3: Current-time variation at constant potential (-0.2 $V_{Ag/AgCl}$) for 2.5 hours with 1 hour of sand impingement at 50^{o}C in a CO_2-saturated oilfield environment at 24 m/s and 500 mg/L sand loading

Higher current density recorded at higher temperature is a result of higher thermodynamic driving force which makes corrosion to occur at a higher rate during depassivation by sand impact (26). As the passive film is depassivated by the erodent, charge transfer occurs at a higher rate at elevated temperature. Another possibility for a higher current density at the elevated temperature as reported by Hu

and Neville (26) is the change in the fluid viscosity. Higher number of impacts and hence higher damage (as earlier discussed in chapter 6) to the passive film would result in higher charge transfer rate.

The current rise during the impingement was maintained throughout the duration of the impingement. This is believed to be as a result of the multiple sand impacts and the higher sand flux/impact frequency employed in this research. The surface of the alloy (especially near the stagnation zone) is thus under active depassivation/dissolution (25) with few intervals of repassivation. Depassivation-repassivation of the passive film is highly likely outside the stagnation zone (Figures 8.4 and 8.5) (25).

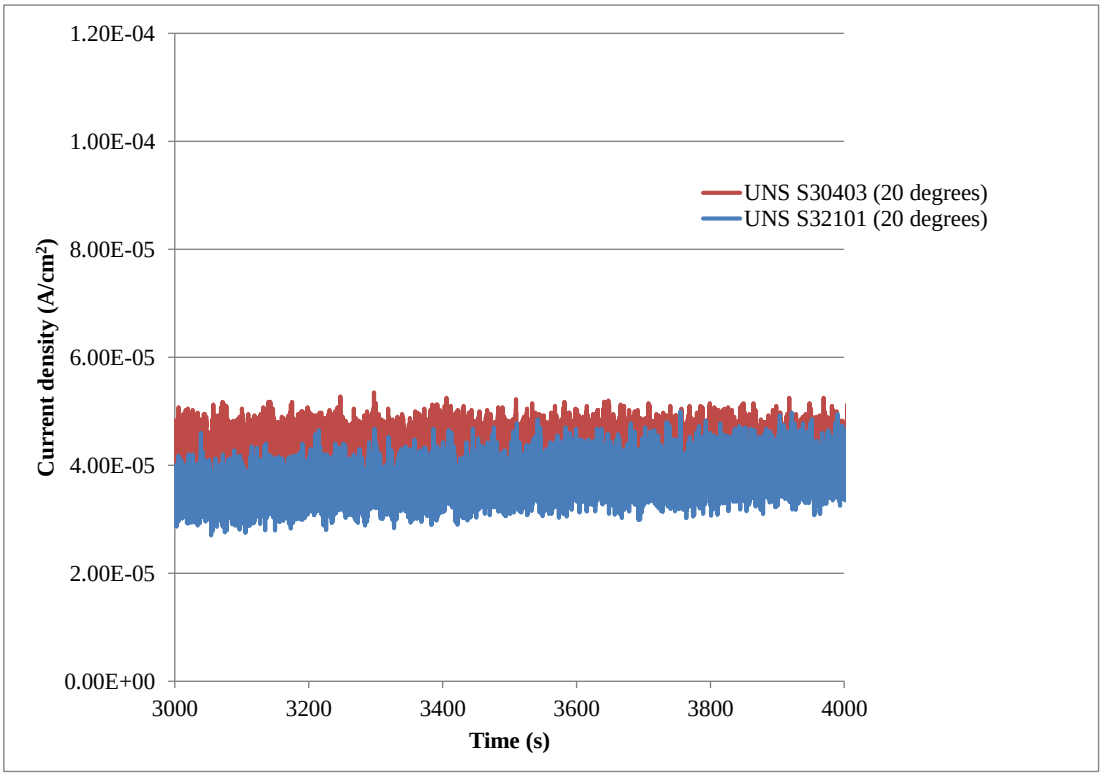

Figure 8.4: Average maximum current density (*in-situ* corrosion current density) for both alloys at 20°C in a CO_2-saturated oilfield environment at 24 m/s and 500 mg/L sand loading.

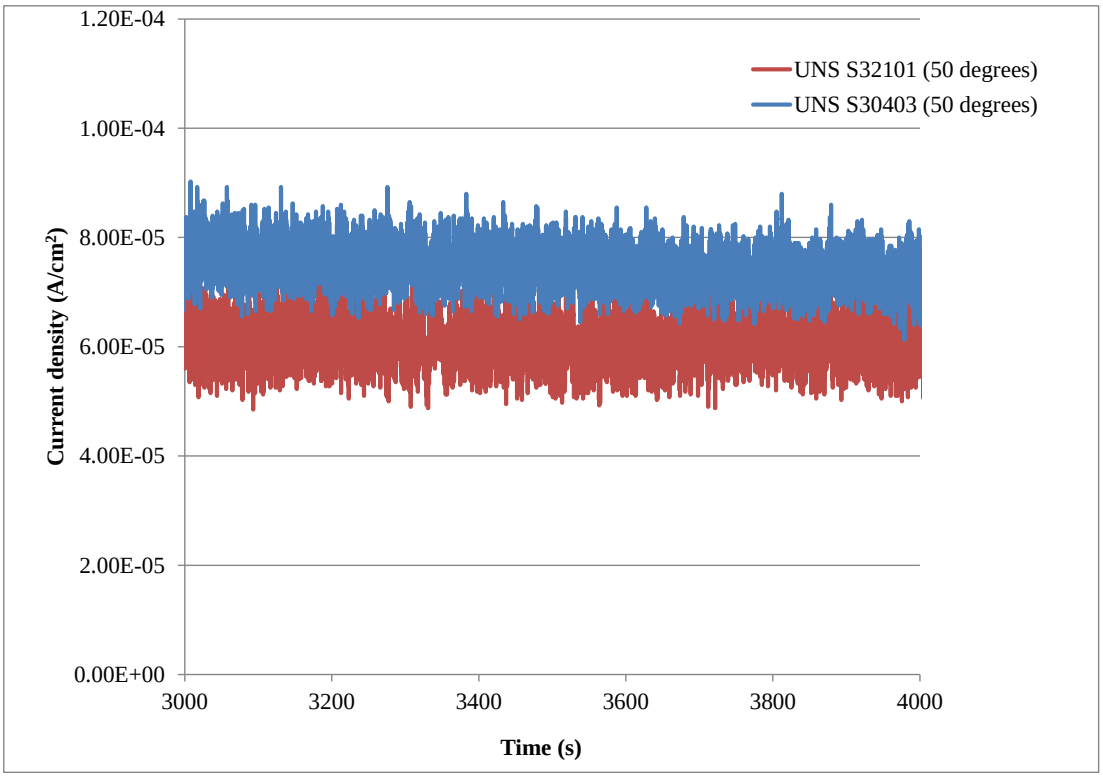

Figure 8.5: Average maximum current density (*in-situ* corrosion current density) for both alloys at 50°C in a CO_2-saturated oilfield environment at 24 m/s and 500 mg/L sand loading

It is noticed that the current noise is more pronounced at higher temperature of 50°C compared with 20°C (Figures 8.4 and 8.5). Average current fluctuation of 10 µA/cm^2 (Figure 8.4) and 15-20 µA/cm^2 (Figure 8.5) are seen at 20°C and 50°C respectively. Reasons for this have been explained above to include higher thermodynamic force and lower viscosity of the fluid at the higher temperature.

Typical current decay for 120 seconds after stopping the impingement at 20°C and 50°C respectively are shown in Figures 8.6 and 8.7.

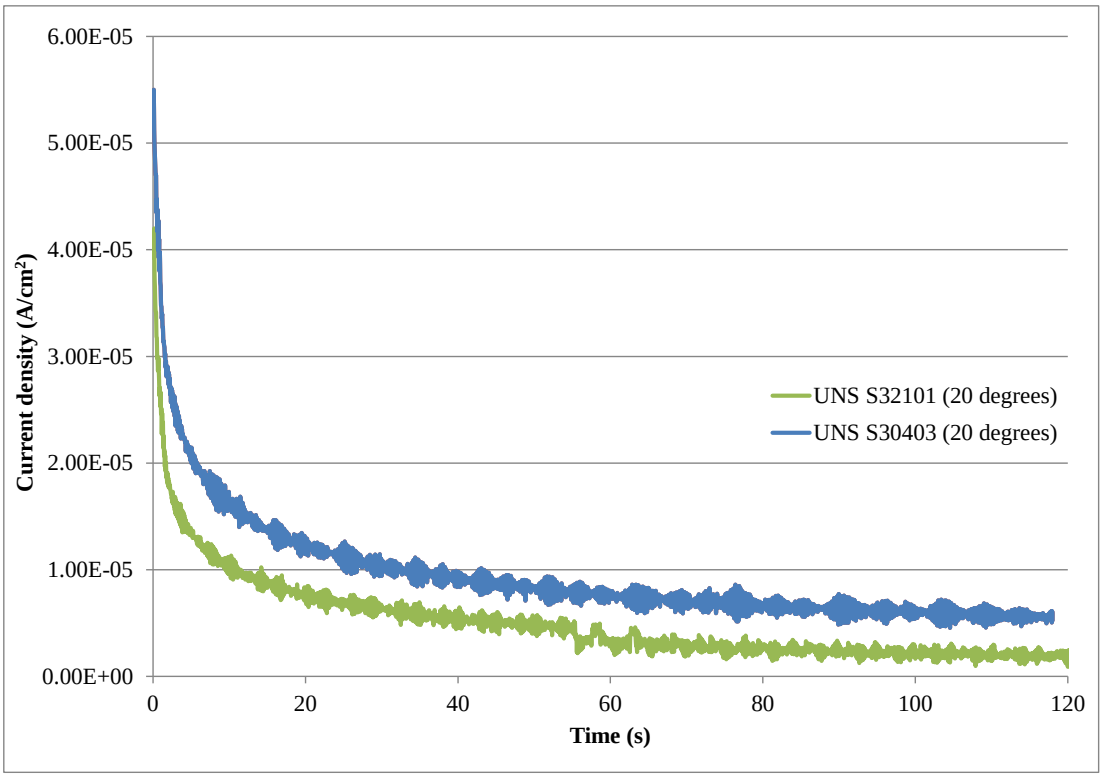

Figure 8.6: Current decay for 120 seconds during repassivation after 1 hour of sand impingement at 24 m/s, 500 mg/L sand loading and temperature of 20°C

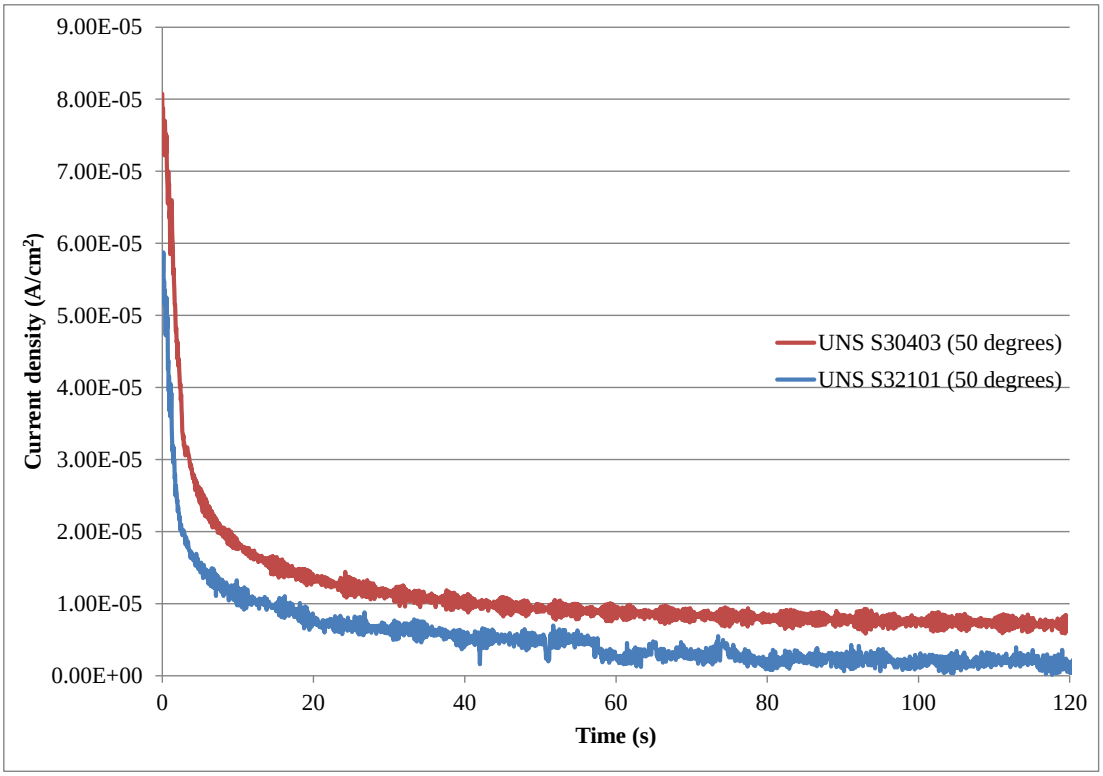

Figure 8.7: Current decay for 120 seconds during repassivation after 1 hour of sand impingement at 24 m/s, 500 mg/L sand loading and temperature of 50°C.

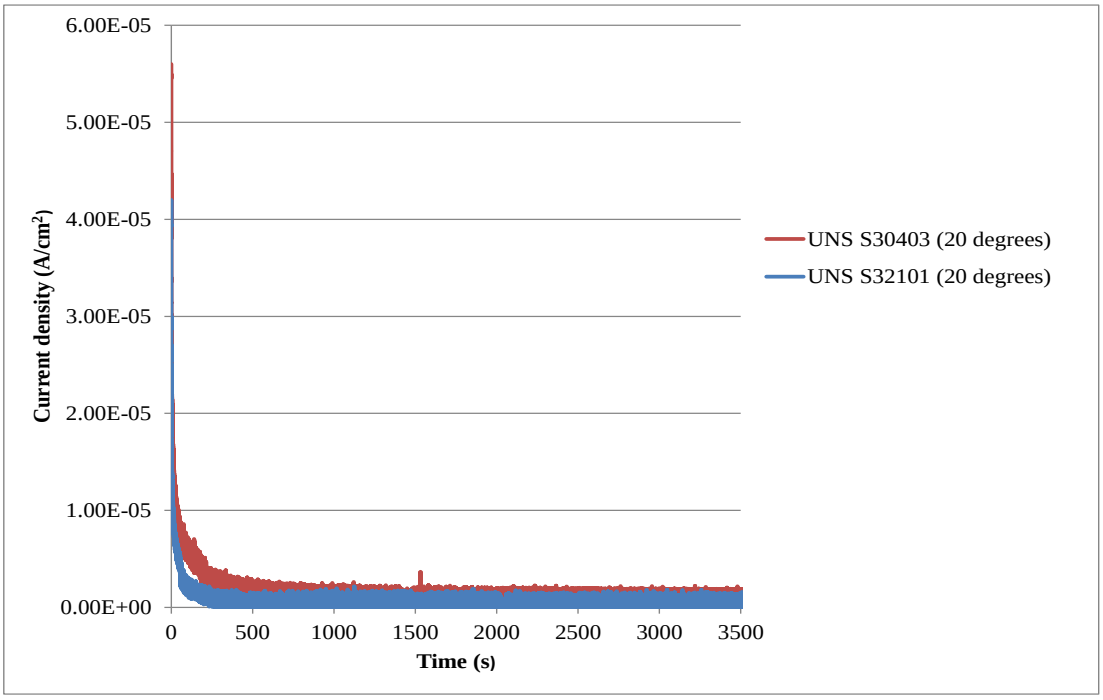

Figure 8.8 **:** Current decay for 1 hour during repassivation after sand impingement at 24 m/s, 500 mg/L sand loading and temperature of 20^{o}C

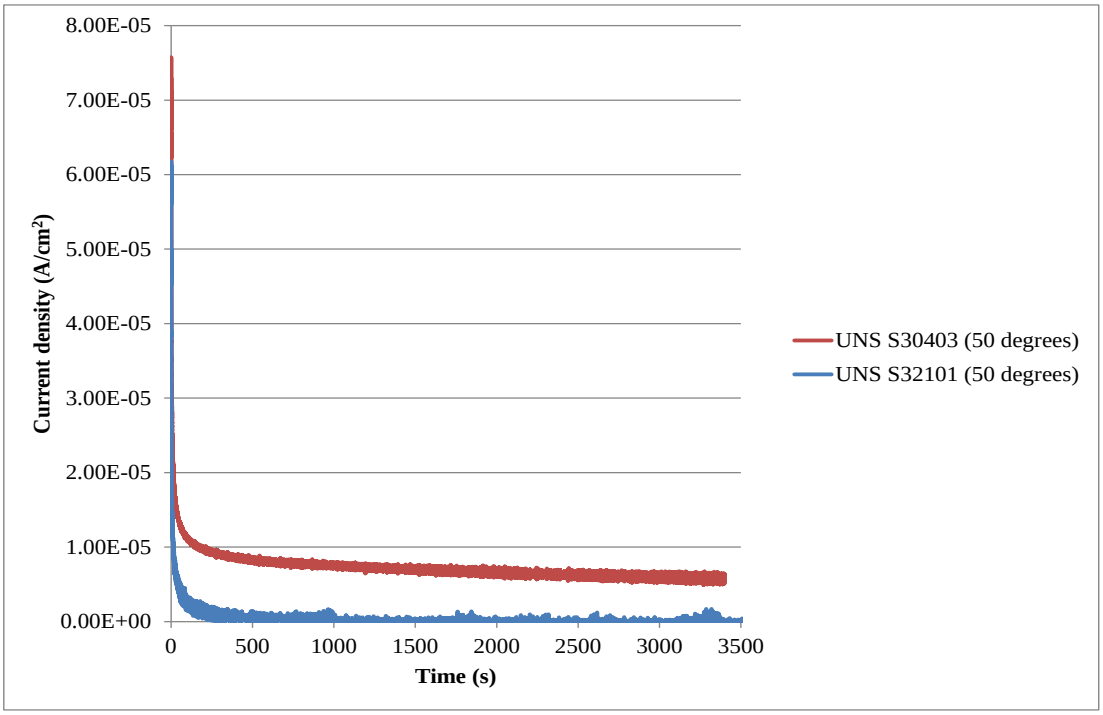

Figure 8.9: Current decay for 1 hour during repassivation after sand impingement at 24 m/s, 500 mg/L sand loading and temperature of 50^{o}C

The current decay at both temperatures show that UNS S32101 recorded a lower current density than UNS S30403. The nature of the current decay also shows that at both temperatures UNS S32101 is repassivating faster than UNS S30403. Figures 8.8 and 8.9 show that a stable current density was maintained for 1 hour after the initial current decay.

8.5 Repassivation Index Determination

The repassivation kinetics can be described by the empirical formula, $i\,(t) = At^{-n}$ (65, 70, 71, 214) explained in Chapter 2 Section 2.6. The anodic current density consumed during the repassivation of the damaged passive film is represented as $i\,(t)$. The repassivation index (n) has been found to be constant for a particular environment-alloy system. The parameter, n can be deduced from the slope of the linear portion of above equation in a logarithm scale:

$$\log i = logA - nlogt \qquad 8\text{-}1$$

Figures 8.10-8.13 show how the power plot was fitted to the plots in Figure 8.6-8.7 to determine the values of (n). Figures 8.14 and 8.15 show samples of the plots in logarithm scale of current against time for the first 120 seconds after the impingement was stopped. It has been argued that the straight portion of the logarithm graph represents the portion of the graph where the passive film growth is by high field conduction (uniform growth) (66, 69). The breakdown of the values of repassivation index, *n* is show in Table 8.2.

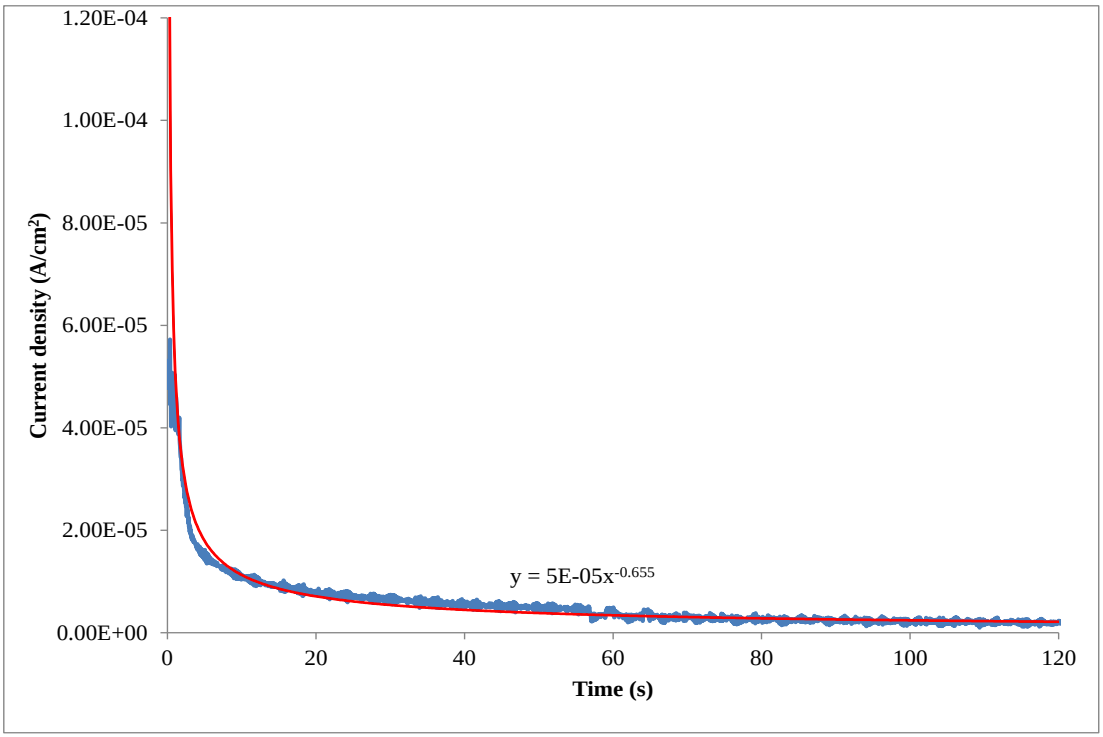

Figure 8.10: Fitted power plot on the current decay for UNS S32101 after sand impingement at 24 m/s, 500 mg/L sand loading and temperature of 20°C. Current decay taken for the first 120 seconds after the impingement stopped

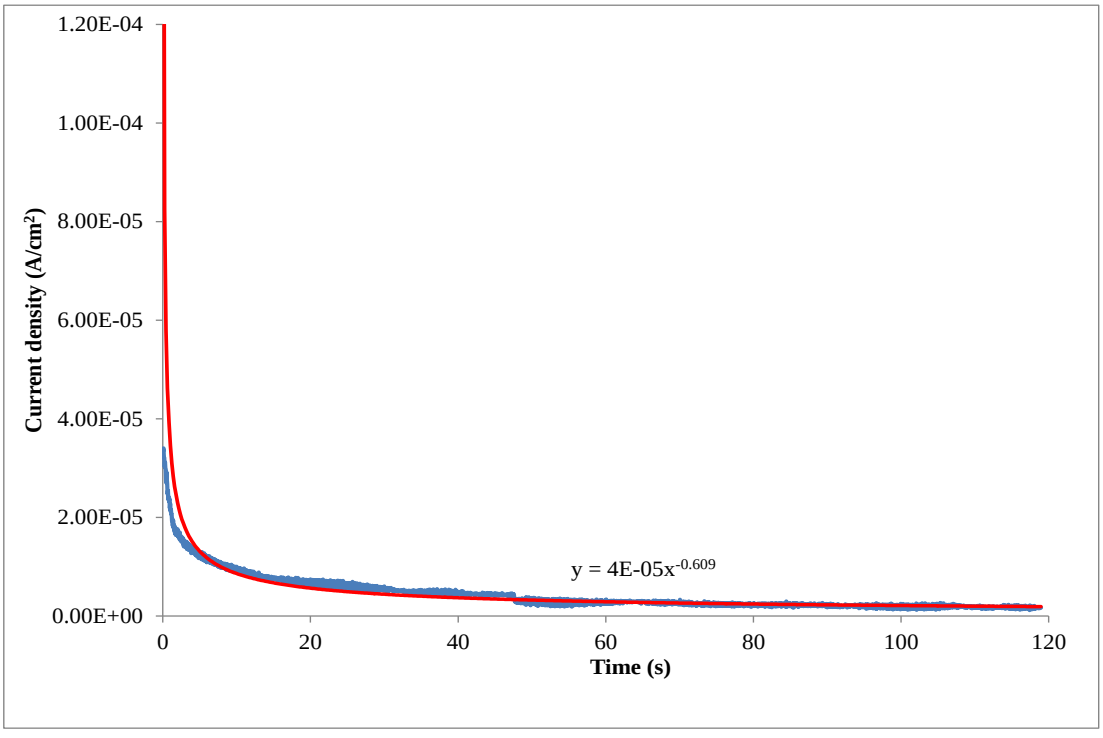

Figure 8.11: Fitted power plot on the current decay for UNS S32101 after sand impingement at 24 m/s, 500 mg/L sand loading and temperature of 50°C. Current decay taken for the first 120 seconds after the impingement stopped

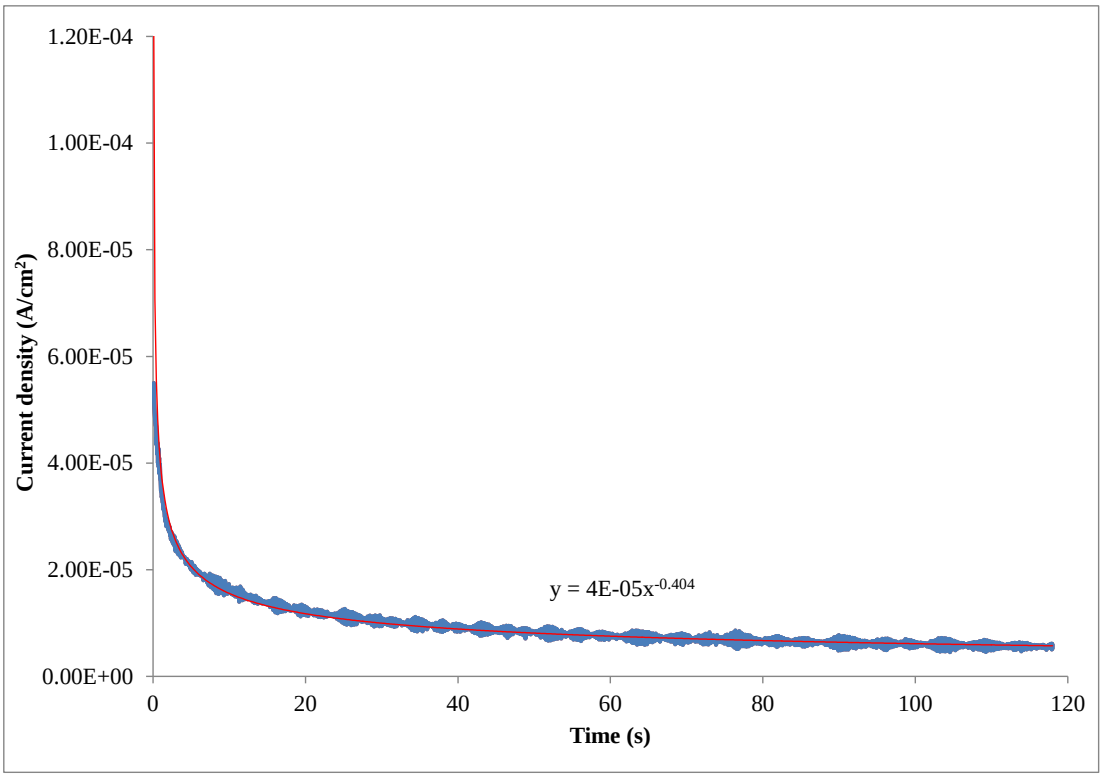

Figure 8.12: Fitted power plot on the current decay for UNS S30403 after sand impingement at 24 m/s, 500 mg/L sand loading and temperature of 20°C. Current decay taken for the first 120 seconds after the impingement stopped

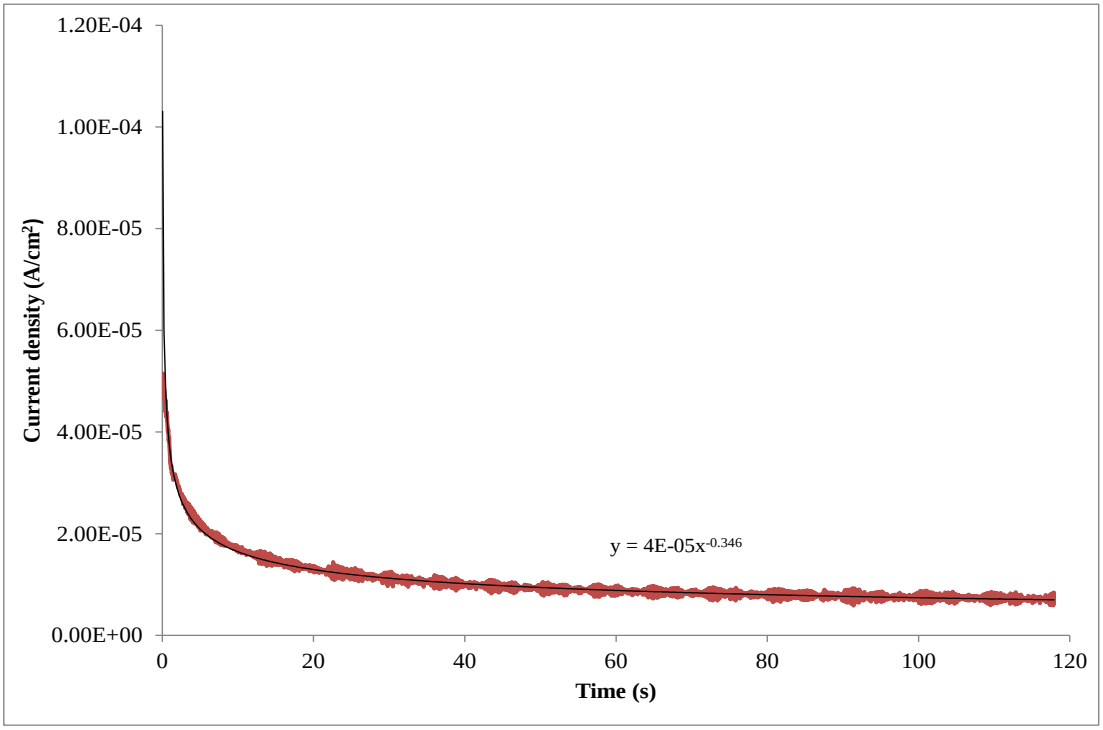

Figure 8.13: Fitted power plot on the current decay for UNS S30403 after sand impingement at 24 m/s, 500 mg/L sand loading and temperature of 50°C. Current decay taken for the first 120 seconds after the impingement stopped

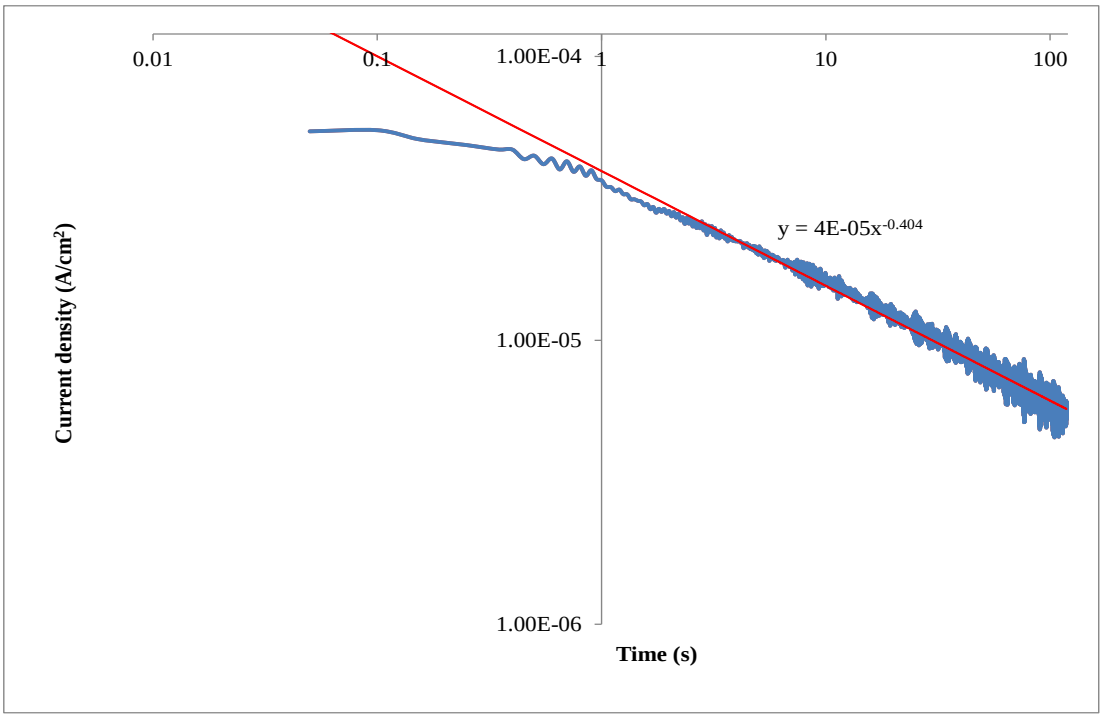

Figure 8.14: Log-log plot for the current decay during the repassivation of UNS S30403 at 20°C (Repassivation index determined from the straight part when growth is controlled by the high field conduction)

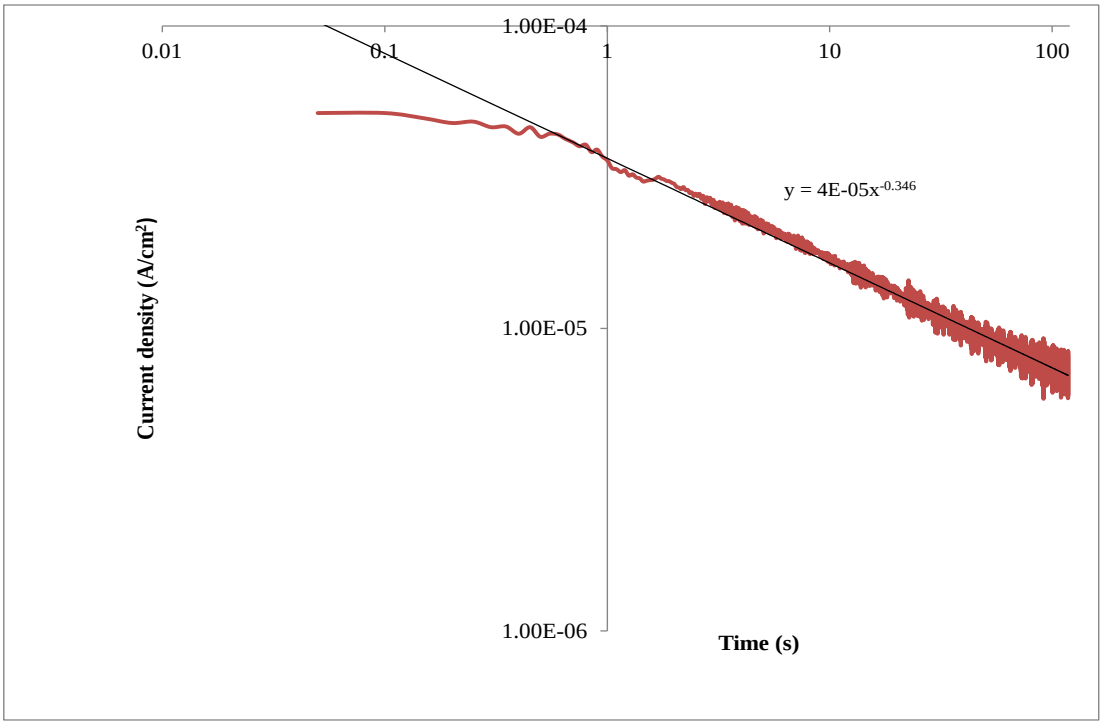

Figure 8.15: Log-log plot for the current decay during the repassivation of UNS S30403 at 50°C (Repassivation index determined from the straight part when growth is controlled by the high field conduction)

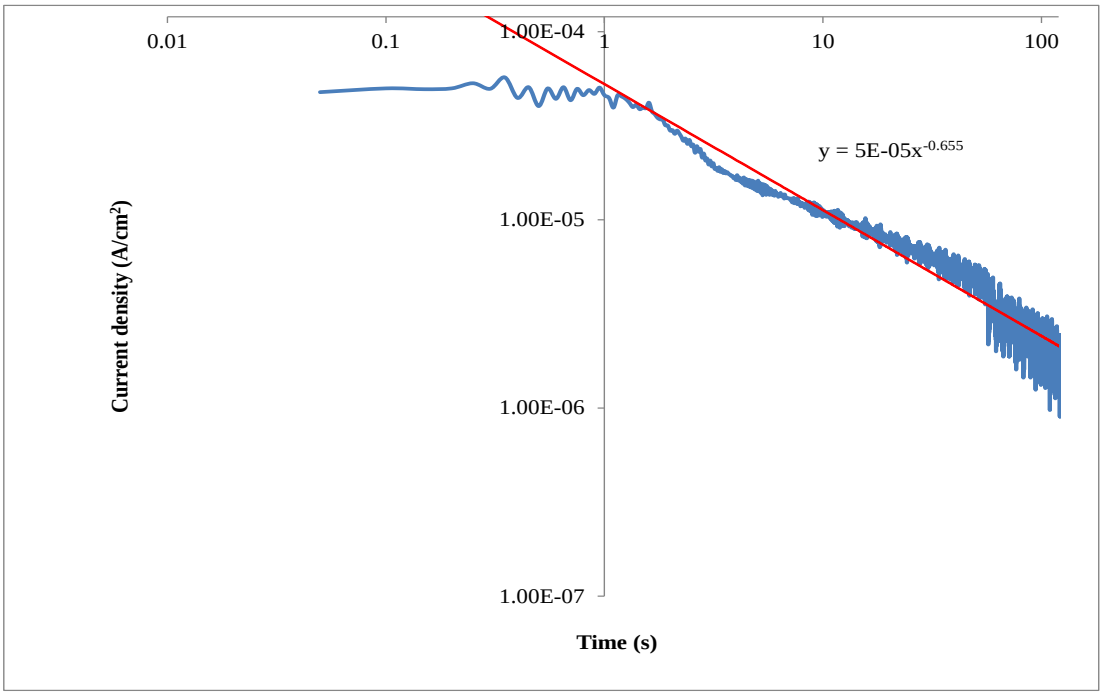

Figure 8.16: Log-log plot for the current decay during the repassivation of UNS S32101 at 20°C (Repassivation index determined from the straight part when growth is controlled by the high field conduction)

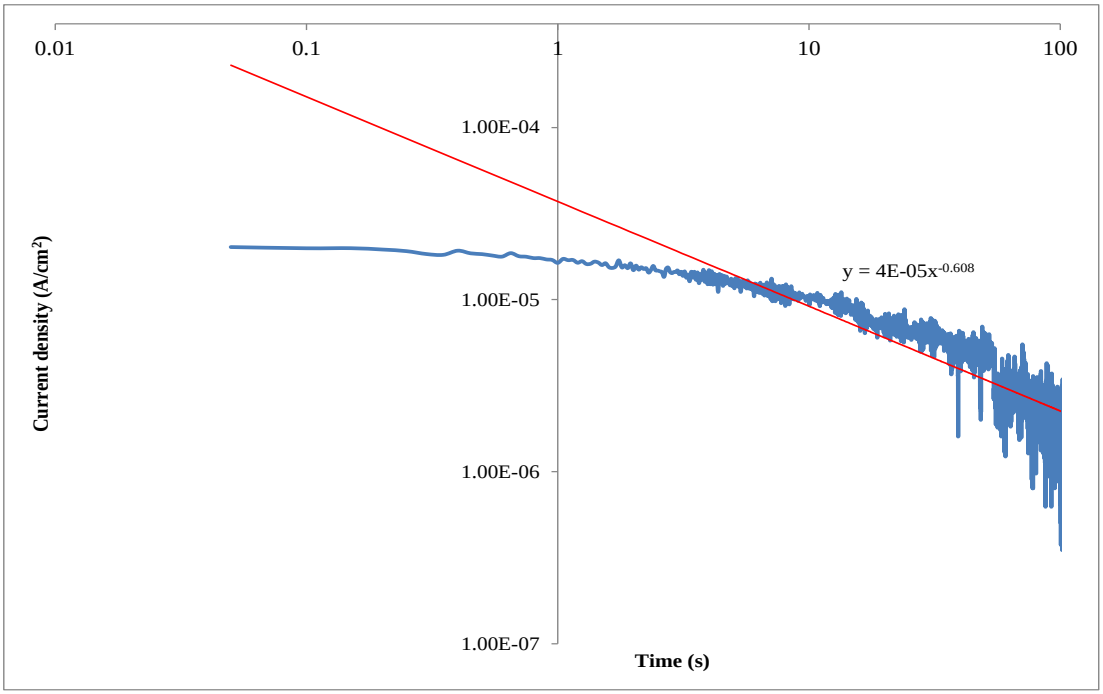

Figure 8.17:Log-log plot for the current decay during the repassivation of UNS S32101 at 50°C (Repassivation index determined from the straight part when growth is controlled by the high field conduction)

It has also been argued that '*n*' depends on the passive potential, temperature amongst other parameters. Also, when *n*=1, it indicates a very compact and highly protective film and when *n*=0.5, the film is said to be porous (71, 215) Analysis in Table 8-2 shows the values of '*n*' as 0.59 and 0.31 for UNS S32101 and UNS S30403 respectively at 50^{o}C. This indicates that the passive film formed on UNS S32101 is more protective than the film formed on UNS S30403 after the prior impingement at 50^{o}C.

The values of '*n*' increases with a decrease in temperature as expected. Values of 0.68 and 0.45 were recorded for UNS S32101 and UNS S30403 respectively at 20^{o}C. This shows that the rate of repassivation is higher at lower temperature. The values of '*n*' are also generally lower for UNS S30403 compared to UNS S32101. This suggests that the passive film formed on UNS S32101 is more compact than the passive film formed on UNS S30403. Also, the passive film on UNS S32101 repassivates faster than the passive film formed on UNS S30403. This could be one reason why UNS S32101 has a better erosion-corrosion resistance (lower in-situ-corrosion) than UNS S30403.

Deductions that can be made from Table 8-2 is that the passive film formed on UNS S2101 repassivates faster (after impingement) than the film formed on UNS S30403 at either 50^{o}C or 20^{o}C. It can therefore be concluded that UNS S32101 would be more resistant to erosion-enhanced corrosion than UNS S30403. Also, it can be said that the response of the alloys to erosion-enhanced corrosion would be better at lower (20^{o}C) than higher temperature (50^{o}C) because repassivation rate is faster at the lower temperature.

Table 8-2: Values of n taken over two different experiments

	UNS S32101			UNS S30403		
	1	2	Average	1	2	average
50^{o}C	0.608	0.568	0.588	0.346	0.279	0.312
20^{o}C	0.699	0.655	0.677	0.491	0.404	0.448

8.6 Summary of Chapter 8

Repassivation behaviour of UNS S32101 and UNS S30403 has been studied using a recirculating jet impingement rig. Higher values of repassivation index were recorded at lower temperature for both alloys. This suggests that the passive film is more compact and the rate of repassivation is faster at the lower temperature. Results from this chapter also show that the repassivation index is higher for UNS S32101 than UNS S30403 at both higher and lower temperatures. This suggests that the passive film formed on UNS S32101 is more compact than the passive film formed on UNS S30403. Also, the passive film on UNS S32101 repassivates faster than the passive film formed on UNS S30403.

Higher current density was observed at 50^{o}C compared to 20^{o}C for both alloys. Also, UNS S30403 also recorded higher current density at both 20 and 50^{o}C. The higher current density recorded for UNS S30403 compared with UNS S32101 is most likely due to the less effective passive film as well as the evolution of less corrosion resistant sub-surface (martensite, high density dislocation, fatigue cracks) which are more pronounced in this alloy than UNS S32101. Also, current density of the repassivated surface after 1 hour erosion-corrosion at 50^{o}C shows almost zero value for UNS S32101 and about 8 μA/cm^{2} for UNS S30403(Figure 8.9). This also

confirms that the passive film on UNS S32101 is more protective than the passive film formed on UNS S30403.

The behaviour of passive film on both alloys could be related to their erosion-corrosion behaviour reported in Chapter 6. UNS S32101 with faster repassivation rate showed better erosion-corrosion resistance than UNS S30403 under the same conditions used in this chapter.

Chapter 9. Discussion

9.1 Behaviour of the Alloys in Static Corrosion Conditions

9.1.1 Aerated and CO_2-Saturated Environments

The main objective of this research, as stated in section 1.2, is to improve the understanding of the corrosion mechanisms and metallurgical aspects of lean duplex stainless steels. The lean duplex stainless steels were also compared with austenitic stainless steels and a standard duplex stainless steel. All the alloys were tested and compared under static conditions in aerated and CO_2-saturated oilfield environments. The breakdown potential was used as a basis to determine the resistance of the alloys to localised corrosion. A more positive breakdown potential was observed in the aerated 3.5% NaCl compared with CO_2-saturated environment. The same trend was also observed when UNS S32101 and UNS S32304 were left for 24 hours at the open circuit potential. A more positive potential was observed in the aerated 3.5% NaCl than CO_2-saturated oilfield. The more positive breakdown potentials and OCP in aerated conditions is thought to be due to the higher oxygen available for the formation of a compact passive oxide. It is generally believed that the oxide film formed in CO_2-saturated environment is thinner and weaker than that formed in an aerated environment because of the deficiency of oxygen in the environment (163).

It appears that a relationship exists between CO_2 and the amount of chloride ion adsorbed into the passive film of the alloys. XPS spectra surveys in Figures 5.7-5.8 (section 5.5) established the adsorption /incorporation of Cl^- ion in the passive film

formed in both aerated and CO_2-saturated environments. Possibility of chloride ion adsorption and incorporation in the passive film formed on passive alloys has also been reported (60, 216-218). It was also established (Figures 5.9-5.11) that a greater amounts of chloride ions are incorporated into the near surface of the passive film formed in CO_2-saturated oilfield (despite the lower concentration of chloride in the bulk CO_2-saturated environment compared to 3.5% NaCl). This could also be one of the reasons why the breakdown potential and the OCP are more negative in this environment compared to 3.5% NaCl solution.

Moreover, Anselmo *et al.* (163) found the same synergistic effect between CO_2 and chloride concentration as shown in Table 9-1. A martensitic stainless steel was left at OCP in both environments for 4 hours. In each case the chloride concentration was varied from 20000 ppm to 80000 ppm. It was found that the OCP was nearly constant with increasing chloride concentration in the aerated environment. However a significant decrease in OCP was recorded in the CO_2-saturated environment.

Table 9-1: Synergy between CO_2 and chloride in CO_2-saturated seawater at 25^oC (163)

Chloride concentration(ppm)	E_{oc} (mV) X SCE	
	Aerated solution	CO_2-saturated solution
20000	-222	-490
40000	-219	-505
80000	-220	-520

The same authors also recorded a more negative pitting potential in CO_2-saturated environment compared with aerated environment at higher chloride concentration of 40000 ppm to 80000 ppm and the converse was the case at lower

chloride concentration of between 20000 ppm and 30000 ppm. It is thought that the findings from this research are in total agreement with these authors' if we consider the OCP. However, while these authors recorded lower pitting potentials in the CO_2-saturated oilfield brine at higher chloride concentrations (40000 ppm-8000 ppm), findings from this research shows that the same occurred at a much lower chloride concentration (19000 ppm for the CO_2-saturated oilfield brine used in this research). It should also be emphasised that the chloride concentration in the CO_2-saturated oilfield brine (19000 ppm) was lower than that of the aerated 3.5% NaCl (21000 ppm).

UNS S30403 and UNS S32101 showed comparable breakdown potentials in both environments. Although UNS S32101 and UNS S30403 have PRE_N of 25.7 and 20.6 respectively, both alloys showed comparable pitting resistance. One reason that could be responsible for this is that higher nickel content of the bulk UNS S30403 may result in a higher enrichment, of nickel (56, 190, 219) at the interface between the bulk alloy and the passive film.

The lean duplex alloy UNS S32101 on the other hand has higher chromium but lower nickel addition in the bulk. This could make the layer below the passive film have less nickel enrichment though the passive film will be highly enriched in chromium compared to the UNS S30403. Both the chemistry of the near surface of the bulk alloy and that of the passive film are important to the resistance of alloys to pit formation (190). Elsener *et al.* (190, 220) reported nickel enrichment at the interface between the bulk and the passive film formed on UNS S30400 and UNS S31803 after exposure to an alkaline medium for 24 hours. A modified model based on the work of these authors reported in (190) is shown in Figure 9.1.

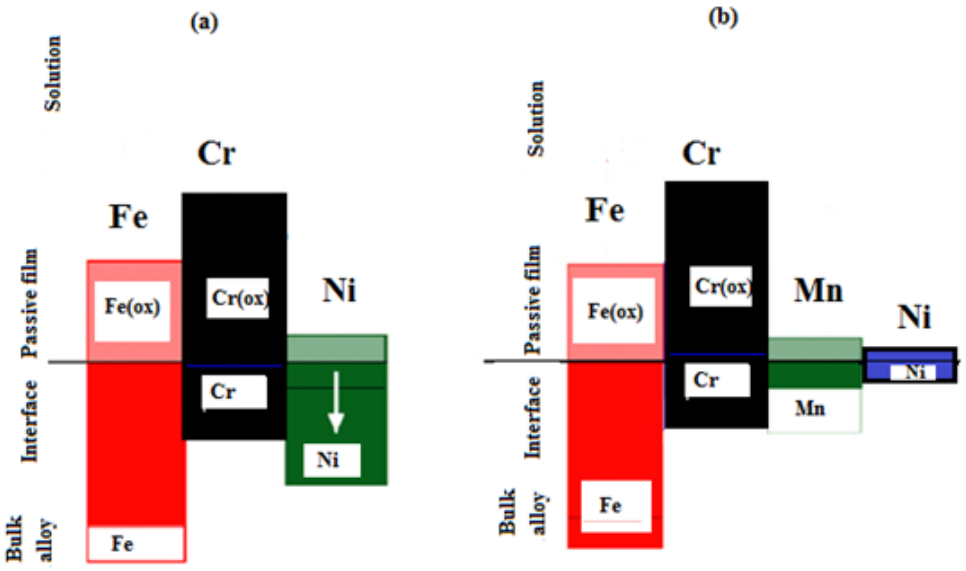

Figure 9.1: Model of the dissolution and film formation on (a) UNS S30403 and (b) UNS S32101 showing enrichment of Ni at the metal-oxide interface of UNS S30403, adapted from Elsener *et al*.(190)

It should, however, be noted that several factors determine the breakdown of passivity as well as the initiation of pits. Among these factors are the environment and the chemistry of the passive film as well as the chemistry of the layer of the bulk alloy just below the passive film (190). Lean duplex stainless steel UNS S32304 and austenitic stainless steel UNS S31603 have similar PRE_N of approximately 26 and both alloys have very low manganese alloying. This could be a justification for their close performance. However, it should be emphasized that UNS S31603 with approximately 2.5 % Mo and 11% Nickel is heavily alloyed compared to lean duplex UNS S32304. The lower breakdown potential of UNS S32101 (despite its high PRE_N) as compared to UNS S32304 and UNS S31603 could either be due to the nickel deficiency at the metal-oxide interface or dissolution of manganese from the passive film as explained earlier.

9.1.2 Mode of Pit Propagation in Aerated and CO_2-Saturated Oilfield Environments

The corrosion pits formed on the alloys in aerated environments have lacy covers (Figure 5.5, section 5.4) while those formed in CO_2-saturated environments are open (Figure 5.6, section 5.4).

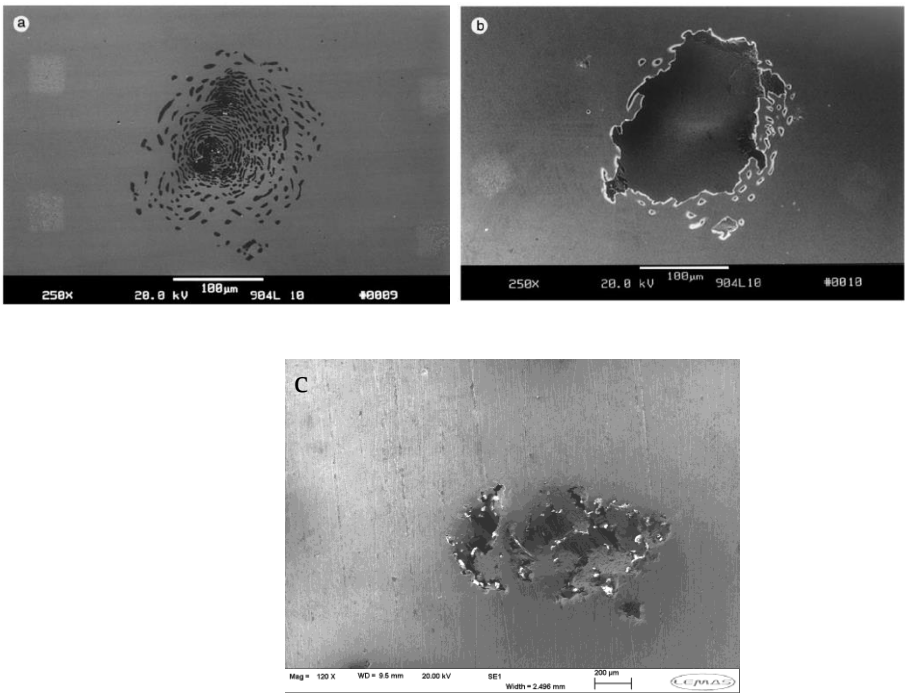

Figure 9.2: Lacy cover formation reported by Ernst and Newman (a. cover; b. interior) (221, 222); c. lacy cover formed on UNS S30403 in aerated 3.5 % NaCl (Figure 5.5, section 5.4)

The lacy cover (222) is formed in stainless steels as a result of local concentration within the pit and repassivation near the edge of the pit. Repassivation is more likely near the edge of the pit in aerated environment compared with the CO_2-environmenrt because of higher dissolved oxygen and lower Cl^- ion adsorbed as found in the research. Hence the lacy cover forms in such an environment. Pit severity was however, more pronounced in the aerated environment although the

passive film did not breakdown easily compared with the CO_2-environment. As soon as the stable pit was formed, local concentration within the pit led to active dissolution which eventually broke through the passive film (221). The passive film cover became cathodic with respect to the hydrolysed pit bottom, hence the severity of the pit in the aerated environment.

However, for the CO_2-saturated environment, an early distruption of the lacy cover seems to hinder the pit growth. It is reported (223) that when the pit cover is lost the anolyte in the pit is diluted, hence, the metal dissolution is retarded. This could be the reason that the severity of the damage in this environment is lower than what is observed in the aerated environment.

9.1.3 Effect of Manganese on Passive Film Breakdown

The behaviour of UNS S32101 with a relatively high manganese content compared to UNS S32304 and UNS S30403 in the CO_2-saturated oilfield environment was also very interesting. CO_2 dissolves in water to form carbonic acid. The environment becomes acidified and dissolves the active elements (163, 190), in this case, iron and manganese. Observations from the XPS analysis in section 5.5 showed that greater manganese was dissolved into the acidic (CO_2-saturated) environment. These reactions would make the oxide film that was formed in CO_2 environment less compact than the film formed in aerated environment. UNS S30403 and UNS S32304 with lower manganese in the bulk alloy, and thus less Mn in the film, consequently behaved better than UNS S32101 in the CO_2-saturated environment. Also, observation from the OCP curves in Figure 5.4 (section 5.3) showed that after about 8 hours of exposure in the CO_2 environment, UNS S32101

began to show a drop in the OCP compared with UNS S32304. This is most likely due to the fact that the CO_2-saturated environment was acidic and led to the dissolution of Fe and Mn, in the passive film formed on UNS S32101. It is thought that the dissolution of Mn from the passive film became severe after the 8^{th} hour and thus the passive film became porous and hence the OCP became more negative compared with UNS S32304.

9.1.4 Pitting Resistance Equivalent Number (PRE_N) and the Breakdown Potentials

Plots of breakdown potentials against the Pitting Resistance Equivalent Number (PRE_N), as shown in Figures 9.3 and 9.4, display a general trend that the PRE_N being higher increases the breakdown potential at 20^oC as expected. Adding more alloying elements of Cr, Mo and N should increase the metal resistance to localised breakdown of passive film. However, the trend was not followed when UNS S30403 (PRE_N 20.6) was compared with UNS S32101 (PRE_N 26) as well as when UNS S32101 is compared with UNS S31603 and UNS S32304 (all having PRE_N 26). This deviation from the usual increase in breakdown potential with an increase in PRE_N was thought to be due to Mn enrichment in the passive oxide of UNS S32101 compared to UNS S30403, UNS S31603 and UNS S32304 as earlier explained.

The relationship between breakdown potential and PRE_N was also interesting at 50^oC (Figure 9.4). For very large differences in PRE_N virtually no difference in the breakdown potential (E_b) was measured. It is only for the alloy with the highest PRE_N of 35 that a significant increase in E_b was measured. A critical PRE_N of 35 seems to exist for higher temperature (50^oC) service. It was also observed that an

alloy with a PRE_N of 20.6 has a more positive breakdown potential than an alloy with a PRE_N of 26 in the CO_2-saturated oilfield environment.

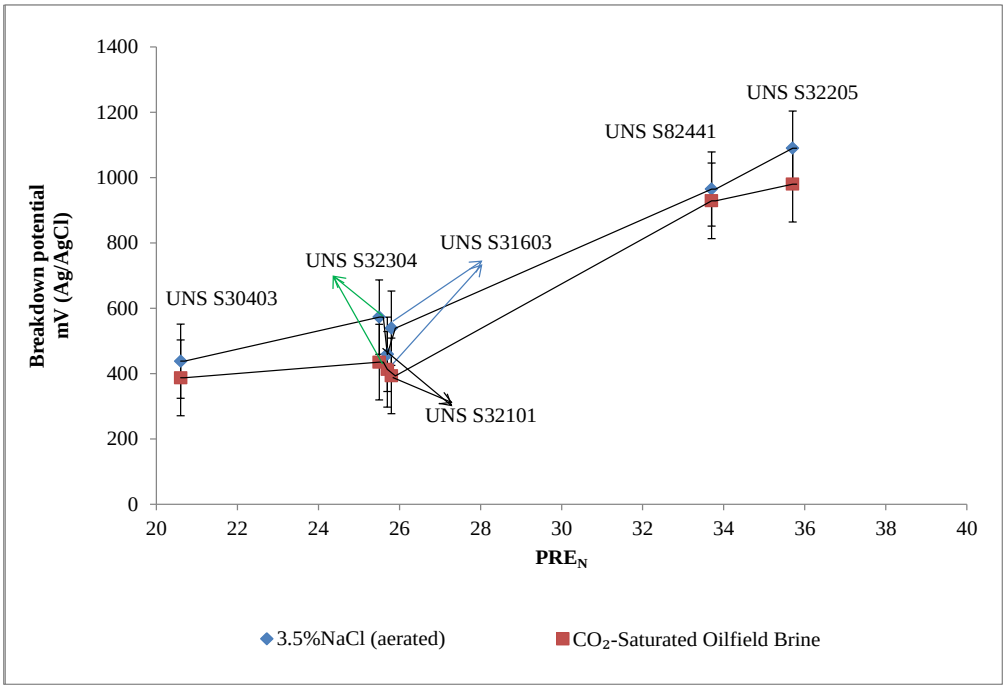

Figure 9.3: Relationship between breakdown potentials and PRE_N at 20°C (Error bar is the spread of 3 data points)

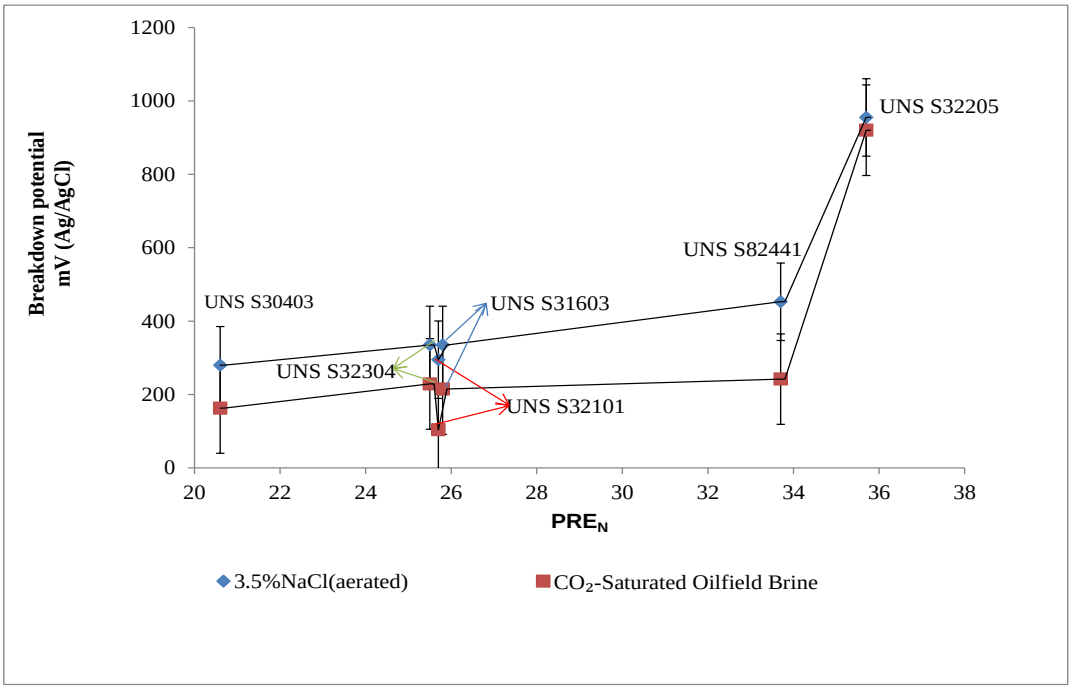

Figure 9.4: Relationship between breakdown potentials and PRE_N at 50°C (Error bar is the spread of 3 data points)

9.2 Influence of the Subsurface Crystallography and Microstructure on Erosion-Corrosion Behaviour of UNS S32101 and UNS S30403 in CO_2-Saturated Oilfield Environment

The Lean duplex stainless steels exhibited reasonably high resistance to pure erosion and erosion-corrosion. These alloys showed better resistance to both erosion and erosion-corrosion when compared with the standard austenitic stainless steel, UNS S30403. Surprisingly, erosion and erosion-corrosion behaviour of the lean duplex alloys is high when their chemistry is compared to UNS S32205.

Further tests were carried out to study the influence of the subsurface morphology of UNS S32101 and UNS S30403 on their erosion-corrosion behaviour. For instance, work-hardening of the layer of the bulk alloy just below the passive film has been reported to influence the synergy between erosion and corrosion. It has been reported (141) that the work-hardened layer is weakened by exposure to the corrosive medium and thus enhances erosion under corrosion conditions. The sub-surface of the UNS S30403 being more work-hardened than the duplex stainless steels is expected to be prone to erosion which is enhanced by corrosion (dissolution and weakening of the work-hardened layer). On the other hand, erosion-enhanced corrosion is dependent on the passive behaviour of the alloy as well as the phase transformation and changes in the crystallographic orientation as a result of the plastic deformation beneath the passive film. It has been argued that the plastic deformation could result in grain refinement which would help in reducing anodic dissolution. However, other activities such as phase transformation, crack formation,

highly stressed grains, sand embedment favour a higher rate of anodic dissolution. Dislocations have also been reported to help in passive film rupture (69) that could lead to higher anodic dissolution.

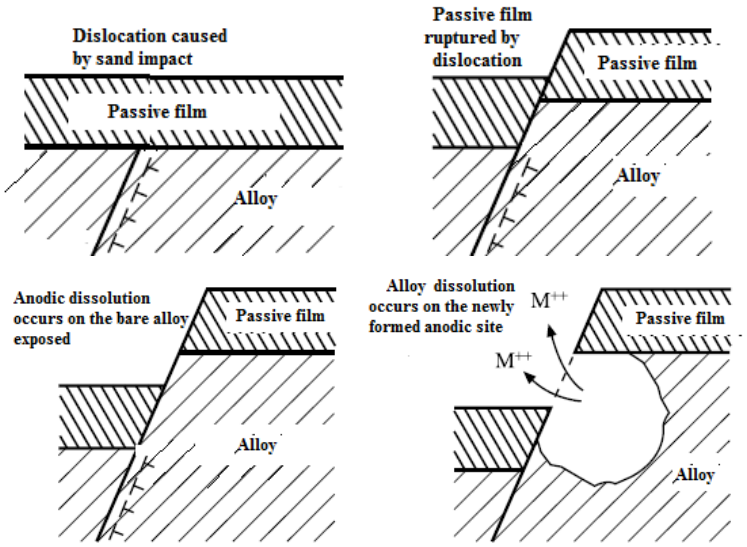

Figure 9.5: Anodic dissolution caused by rupturing of passive film as a result of dislocation (69)

The X-ray Diffraction (XRD) pattern and the Selected Area Electron Diffraction (SAED) pattern in chapter 7 showed strain-induced martensitic transformation within the subsurface of both UNS S32101 and UNS S30403. The austenitic stainless steel responded better to strain-induced transformation from the XRD and hardness results. The Focused Ion Beam and Transmission Electron Images showed crack propagations and heavily deformed grains within the stagnation region on the tested coupon. It is no doubt that these findings could contribute to the synergy between erosion and corrosion. UNS S30403 that showed a higher network of crack propagation (Figure 9.6a), supposedly higher volume fraction of strain-induced martensite within the subsurface suffered higher damage under erosion-corrosion conditions.

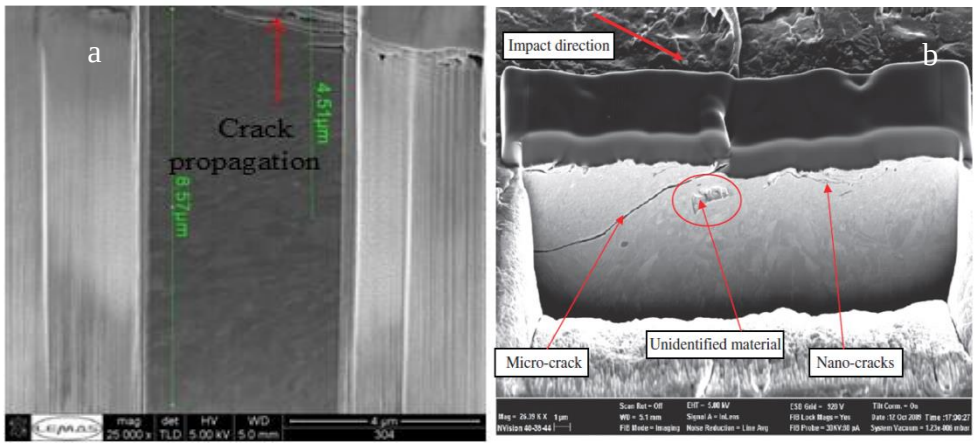

Figure 9.6: FIB images showing subsurface cracks after erosion-corrosion in (a) UNS S30403 used in this research and (b) UNS S31603 reported by Rajahram *et al.* (35)

Body-centred tetragonal (BCT) martensite was highly stressed and hence would be more susceptible to anodic dissolution compared to the FCC (austenitic) phase. Wood *et al*. (37) in their argument stated that such strain-induced martensitic site increases the chance of pit formation and becomes the site for preferential anodic dissolution.

Also, micro cracks are stress risers that could enhance the susceptibility of an alloy to wear and corrosion loss. It is not surprising then that UNS S30403 is more susceptible to both erosion and erosion-corrosion. The mechanisms explained above are thought to have reasonable influence on erosion-corrosion damage apart from the depassivation-repassivation mechanism.

Another possible factor responsible for higher material loss due to wear-enhanced corrosion of UNS S30403 is thought to be that the austenite phase is softer than the duplex phase. There is a higher likelihood of sand embedment (169, 170) within the near surface of the austenite phase which could turn this area into a

composite (metal-sand-oxide) with high stress concentration and inferior corrosion and erosion resistance compared to the duplex phase. Brown *et al*. (224) stated also that the subsurface embedded particles are able to accelerate void nucleation and thus provide paths of weakness for crack growth and platelet flaking.

9.2.1 Synergy between Erosion and Corrosion

9.2.1.1 Corrosion-enhanced Erosion (dE_c)

Corrosion is said to assist erosion by roughening the top layer of an alloy and exposing this layer to impact (141, 199). Many researchers (143, 199, 200) in the field have also discussed some mechanism of corrosion-enhanced erosion to include preferential corrosion in an alloy or composite which exposes the secondary phase to higher impact and hence higher material loss. The work-hardened layer is also thinned by dissolution (the passive layer is damaged by impact and hence the work-hardened layer is exposed) and becomes weakened. Anodic dissolution has been reported to weaken the hardness of a material (225). The weak work hardened layer is thus prone to higher erosion. Corrosion-enhanced erosion could also be accelerated through the subsurface cracks when the corrosive medium increases the crack initiation sites (35, 195, 226). There could also be a propagation of micro-cracks by debonding at the crack tips (195).

9.2.1.2 Erosion-enhanced Corrosion (dC_e)

Erosion-enhanced corrosion on the other hand has been widely reported on the passive behaviour of the alloys. However, contribution by the changes beneath the passive film (sub-surface of the bulk alloy) is also a possibility. Phase transformation, grain refinement, dislocation density and twin formation induced by

the impacting slurry on the near surface of the alloys could also contribute to the material loss by erosion-enhanced corrosion (194, 203). Figures 6.10 and 6.18 depict the percentage contribution of erosion-enhanced corrosion (*in-situ* corrosion) and corrosion-enhanced erosion. Deformation of the alloys by impacting slurry led to changes in the crystallographic orientation of the grains as well as phase transformation. The metastable austenite phase was transformed to strain-induced martensite (α-martensite), as shown by X-ray diffraction (XRD) in Figures 7.5 and 7.6 as well as the SAED in Figure 7.13, sections 7.6.1. An increase in corrosion activities is, therefore, a possibility as a result of the higher stored strain energy(227) (227) and strain-induced martensite formation near the surface of the alloys. The martensite phase is highy stressed and this would lead to it being selectively dissolved (203, 204) in preference to the austenitic phase. This could be one reason why the fully austenitic stainless steel had greater material loss under erosion-enhanced corrosion compared to the duplex stainless steels.

One other reason could be that because the austenite phase is softer than the duplex phase, there is a likelihood of higher sand embedment (35, 169, 170) within the near surface of the austenite phase which could turn this area into a composite (metal-sand-oxide) of inferior corrosion resistance compared to the duplex phase.

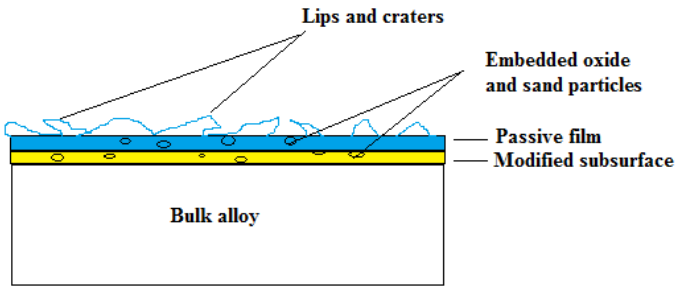

Figure 9.7: Schematic diagram of sand and oxide embedded within the subsurface of an alloy under sand impingement

Another possibility is the repassivation behaviour (which depends on the near-surface chemistry of the bulk alloy) of the passive film formed on the stainless steel in assisting in erosion- corrosion behaviour (8, 228). The rate of repassivation of the damaged passive film on the duplex stainless steel would be faster than the film formed on the austenitic stainless steel because of their higher chromium contents and the duplex structure. This could also assist in the lower material loss of the duplex stainless steels under erosion-corrosion conditions.

9.3 Erosion-Corrosion Behaviour of the Duplex Stainless Steels and Partitioning of Cr and Mo into the Ferrite Phase

All the duplex stainless steels have similar resistance to erosion-assisted corrosion (*in-situ* corrosion). *In-situ* corrosion current measured under aerated slurry (Figure 6.8, section 6.2.2) and the anodic current density measured in the CO_2-saturated oilfield (Figure 6.12, section 6.3.2) support this view. It is, however, known that the standard duplex stainless steel UNS S32205 has a higher resistance to pitting corrosion (PRE_N 36) compared with the lean duplex stainless steels. UNS S32101 and UNS S32304 have PRE_N of approximately 26. However, *in-situ* corrosion recorded in aerated 3.5% NaCl and 500 mg/L sand shows that UNS S32205, UNS S32101 and UNS S32304 have *in-situ* corrosion current density of 12, 14, 13 $\mu A/cm^2$ respectively.

In the CO_2-saturated oilfield, similar anodic current densities are recorded for the lean duplex and the standard duplex stainless steel as seen from the anodic polarisation in Fig. 6.12. This behaviour could be attributed to the similarity in the ferrite phase of all the duplex stainless steels. Ferrite phase in both lean and standard

duplex alloys are sensitive to strain rate. Despite the higher Cr and Mo contents of UNS S32205, the erosion-corrosion and *in-situ* current density is very similar to UNS S32101 and UNS S32304. It is thought that at the high strain rate conditions, ferrite (Mo and Cr are partitioned into ferrite phase (131)) is highly eroded compared to the austenite phase- (Ni, Mn, N) are partitioned into the austenite phase). It has been reported (121, 205) that erosion propagate faster in ferrite phase and that ferrite is more susceptible to anodic dissolution (205).

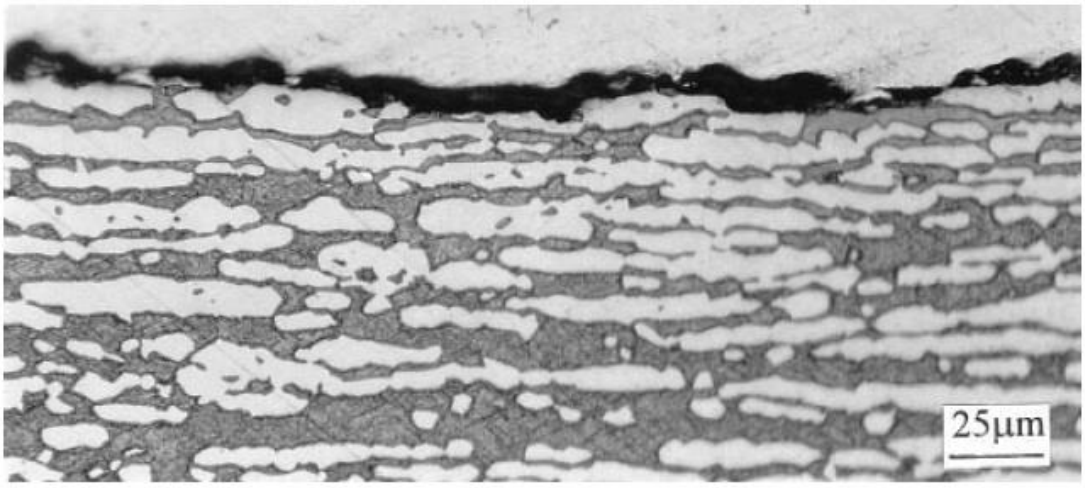

Figure 9.8: Cross section of a super duplex stainless steel UNS S32760 after being eroded for 4 hours- Dark phase (ferrite) more eroded than the white phase (austenite) (205)

Recall that the major contributors to PRE_N are Cr and Mo (% Cr +3.3 % Mo +16% N). Since these two alloying elements are partitioned into the ferrite phase, they are thus lost by mechanical erosion. Hence, higher pitting resistance equivalent number of the bulk alloy will not necessarily be a good indicator of higher resistance to erosion-enhanced corrosion for duplex stainless steels at the higher velocities used in this research. Effect of PRE_N on erosion-corrosion of stainless steels has also been reported to be insignificant at velocity above 20 m/s (138).

XRD pattern of the lean duplex stainless steel in Fig. 7.6 shows that the ferrite phase is highly eroded. Therefore, the duplex stainless steels are left with higher volume fraction of the retained and transformed austenite near the surface during erosion and erosion-corrosion conditions. It is thought that the retained and transformed austenite phases in both lean and standard duplex stainless steel alloys showed similar resistance to erosion-enhanced corrosion.

9.4 Influence of the Passive Film Behaviour on Erosion-Corrosion Behaviour of UNS S32101 and UNS S30403 in CO_2-Saturated Oilfield Brine

The repassivation behaviour of the passive film has also been reported to have influence on the erosion-corrosion behaviour of passive alloys (8, 197, 228). The faster the rate of repassivation of the damaged passive film on the steel the better the erosion-corrosion resistance of such alloy. Results obtained for the repassivation index in chapter 8 support this submission. The lean duplex stainless steel, UNS S32101 has been established to have higher values of repassivation index than UNS S30403 austenitic stainless steel. Higher repassivation index (value of 'n', in equation 8.1, Chapter 8) has been reported to be related to a higher rate of repassivation (71). Higher chromium in the bulk alloy of UNS S32101 (and invariably the passive film) is thought to assist in the repassivation kinetics of the passive film formed on UNS S32101. Since material loss due to erosion-corrosion has been earlier reported (8, 197, 228) to depend on the rate at which the passive film can heal, we could thus relate the higher material loss of UNS S30403 to its lower repassivation rate. Lower repassivation rates were also recorded at the higher

temperatures. The same trends were observed by Rincon *et al.*(8) when studying the repassivation behaviour of 13Cr and 22Cr stainless steels by scratch electrode method in a CO_2-saturated oilfield (Figure 9.9a). Higher repassivation rate is said to suggest higher corrosion component in erosion-corrosion (8).

Comparisons were made among the three alloys (13Cr, Super-13Cr and 22Cr duplex). The duplex stainless steel with the highest rate of repassivation was found to exhibit the lowest erosion-corrosion damage (Figure 9.9b). This supports the findings from this research where UNS S32101 with a higher repassivation rate has a better erosion-corrosion resistance than UNS S30403 with lower repassivation rate.

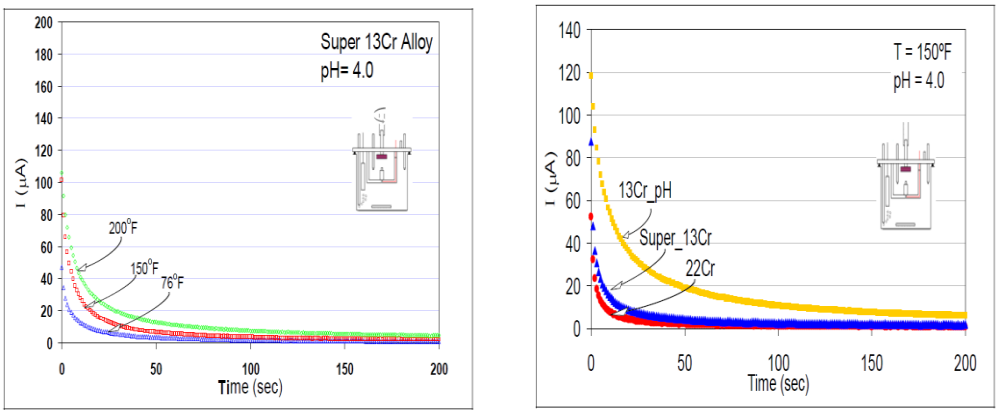

Figure 9.9: Repassivation rate of stainless steels in CO_2-saturated oilfield,(a) effect of temperature, (b) effect of alloying (8)

9.5 *In-situ* Corrosion Current under the Impinging Conditions.

Higher current density recorded at higher temperature (Figure 9.10) has been argued to be as a result of higher thermodynamic driving force which makes corrosion to occur at a higher rate during depassivation by sand impact (26). As the passive film is depassivated by the erodent, charge transfer occurs at a higher rate at elevated temperature. Another possibility for a higher current density at the elevated

temperature as reported by Hu and Neville (26) is the change in the fluid viscosity and hence impacts at higher temperature.

However the difference in the current evolution of UNS S30403 and UNS S32101 (Figure 9.10) under the impinging conditions at both 20°C and 50°C could be seen from two viewpoints. The higher current density for UNS S30403 compared with UNS S32101 is most likely due to the less effective passive film on UNS S30403. It has been reported (8, 197) that the repasivation behaviour of alloys assist in their erosion-corrosion resistance. It has also been found from this research that UNS S32101 repassivates faster than UNS S30403 from the results presented in Chapter 8.

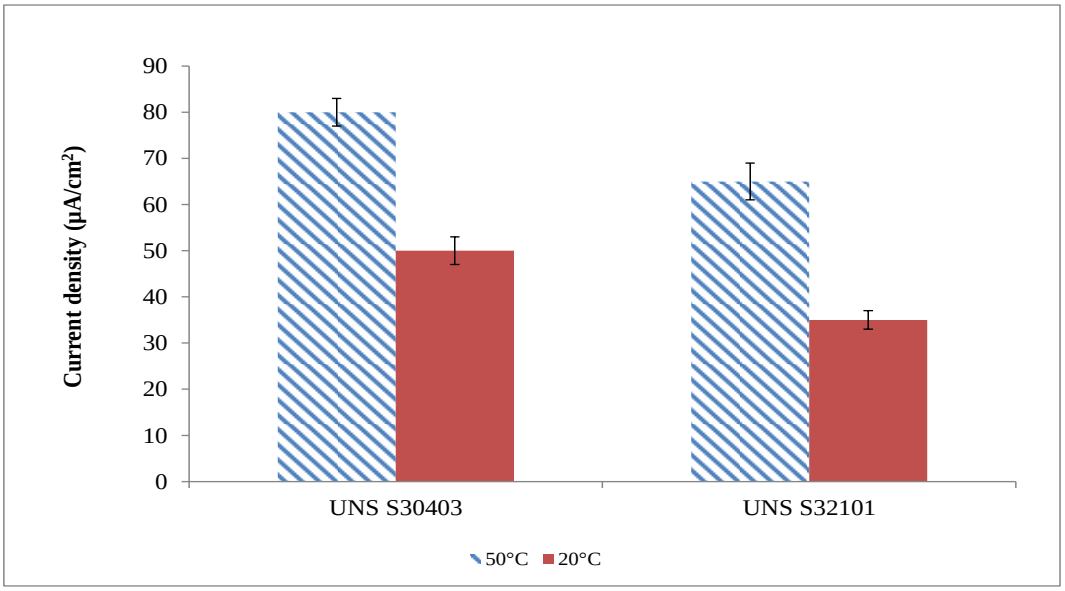

Figure 9.10: Maximum corrosion current density recorded for the alloys at 24 m/s and 500 mg/L sand loading in a CO_2-saturated oilfield (Error bar is the spread of 3 data points)

Another line of argument is the evolution of less corrosion resistant sub-surface morphology (strain-induced martensite, high dislocation density, fatigue cracks, galvanic coupling) which are more pronounced in UNS S30403 than UNS S32101.

Results from Chapter 7 of this thesis showed that these sub-surface changes are more pronounced in UNS S30403 compared with UNS S32101. Strain-induced martensite for instance has been reported to exhibit less corrosion resistance than the austenite phase (203, 204). Dislocation densities have also been reported to increase the activities of electrons and hence promotes higher corrosion rates (227, 229).

9.6 Proposed Damage Mechanism under Severe Erosion-Corrosion Conditions

The jet impingement provides a mixed wear mechanism where both low and high angle impacts are obtainable (108, 193, 230) as shown Fig 9.11. Three regions (Figure 9.11) are typically identified within the surface of the coupon after impingement. Region 1 with high angle impact typically 90-40^{o} is the region closest to the stagnation zone. Near the stagnation zone, there is heavy indentation as a result of the erodent impact. This could lead to the passive film rupture as well as high stress and high strain rate of the layer of the bulk alloy just below the passive film. This high strain rate would lead to severe plastic deformation as reported by Hutchings (231), Figure 9.12. Grains are refined by this heavy impact which would lead to multiple grain boundaries and hence dislocations are hindered from moving. Higher dislocation densities have been reported by Yin *et al.* (229) to increase the activities of electrons and hence higher corrosion activities.

There is also a change of microstructure from FCC austenite to the highly strained BCT martensitic phase especially for a metastable alloy such as the austenitic stainless steel. This markedly affects the resistance of the affected spots to corrosion. More so, the ruptured passive film within the deformed zone would find it

difficult to repassivate as a result of the frequency and energy of the impact. Also, within this region the change in the microstructure, high strain, dislocation density and twin formation would make it more anodic than the other part of the sample. These combined actions on the anodic behaviour would outweigh the positive effect of the fine grains and lower vacancies. Invariably, this zone becomes more prone to further damage by the action of the corrosive medium. The pure-erosion resistance within this zone is, however, enhanced due to the increase dislocation density and hence the work-hardening effects.

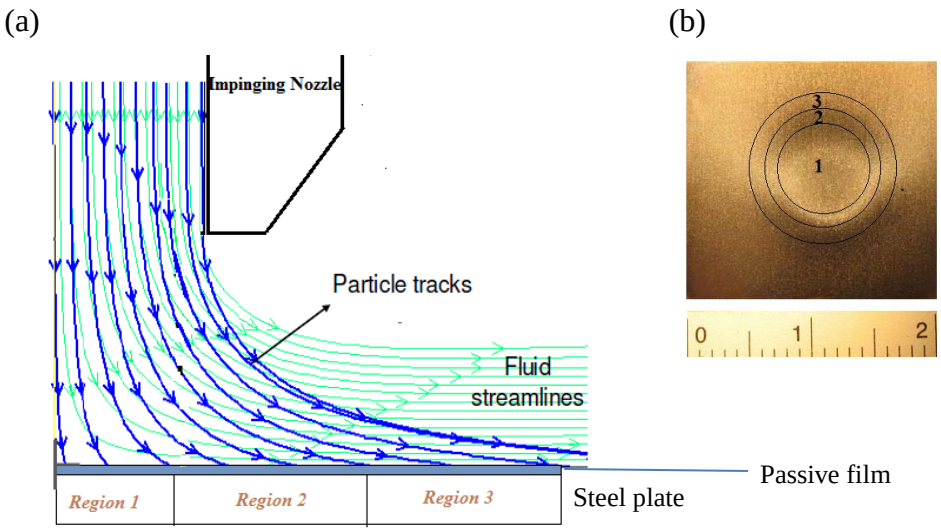

Figure 9.11**:** (a) A half model of the jet impingement showing the motion path of solid particles and fluid streamline. {(Region 1 near stagnation zone; high impact angle); region 2, transition zone; high to low impact angle; region 3, wall jet zone; low impact angle Adapted from Gnanavelu (232) (b) Worn coupon showing the three regions

Region 2 lies between the stagnation zone and the wall jet zone, a mix action of indentation and cutting/ploughing occurs at this region. The transition zone, as it is being referred to, experiences mixed activities combining some of the activities discussed above with the cutting mechanism. Both the subsurface and

ploughing/cutting away of the passive film occur at this zone. Region 3 referred to as the wall jet zone experiences impact at very low angle (usually less than 15^{o}) and the material removal is more of cutting action by the sand grain. Within this zone the passive film is ruptured and cut away. Ability of the bulk alloy to repassivate is thus very important to the material resistance to further degradation within this zone.

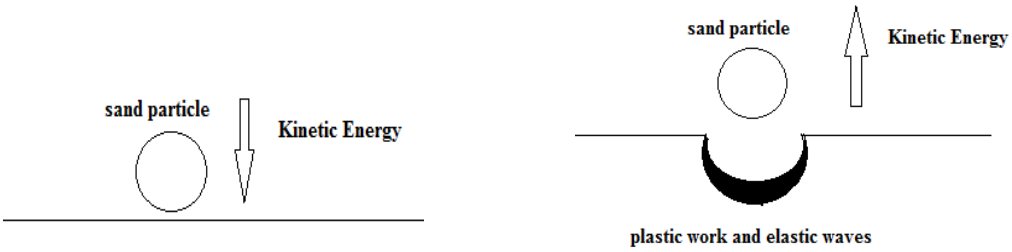

Figure 9.12: Schematic diagram of the plate and sand particle before and after impact at high impact angle shown the dissipation of kinetic energy to plastic and elastic wave (modified from Hutchings, (231))

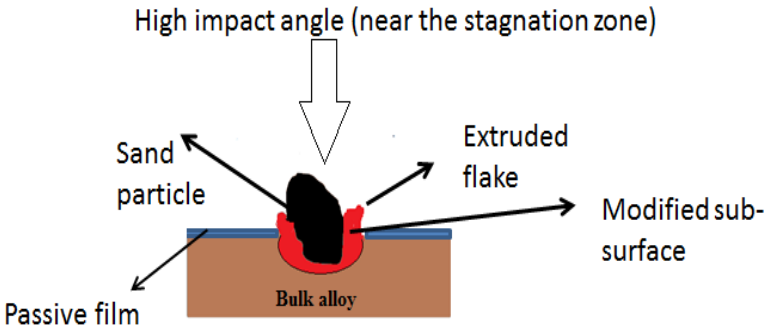

Figure 9.13: Proposed model of the cross-section of the alloy under high frequency impacts and at high angle of impact (region 1 and 2, Figure 9.11)

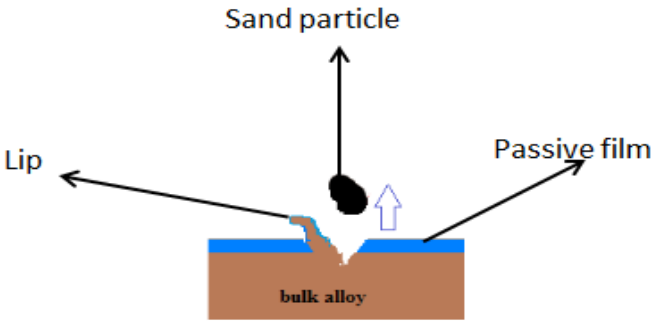

Figure 9.14: Proposed model of the cross-section of the alloy under alloy under high frequency impacts at low angle of impact (region 3, Figure 9.11)

Table 9-2: Proposed mechanism of erosion and erosion-corrosion synergy at the different regions on the coupon under severe impact conditions

	Pure-Erosion	Erosion-enhanced corrosion	Corrosion-enhanced erosion
Region 1(the stagnation zone)	Deformation wear mechanism (231)	Anodic dissolution due to plastic deformation, high dislocation density, martensitic transformation, and fatigue cracks. High stored energy leads to high corrosion activities. (37, 194, 203, 204, 227, 229). Repassivation does not occur at this zone	Corrosion weakens the work-hardened layer and thus enhances erosion, Hardness is weakened by anodic dissolution of the work hardened layer, top layer is roughened by corrosion and thus helps erosion, and secondary phase (ferrite in duplex stainless steel) is preferentially corroded and thus exposed the other phase to erosion. Sub-surface cracks/debonding at crack tips enhances erosion (35, 36, 141, 143, 195, 199, 200, 225, 226)
Region 2 (transition zone)	Deformation and cutting wear mechanism	1. Anodic dissolution due to sub-surface microstructural modification 2. Depassivation and repassivation of the passive film (8, 197)	Same as obtained in region 1. The effects is however milder in this region
Region 3 (wall jet zone)	Cutting and ploughing wear mechanism	Depassivation and repassivation of passive film	Very negligible effect of corrosion on erosion at this zone

Chapter 10. Conclusions and Future Work

10.1 Conclusions

10.1.1 Static Corrosion

The breakdown potential was used to rank the alloys in the static corrosion conditions. Results from the two corrosion media adopted for this research show that the passive film on the entire alloys breakdown at more negative potentials in the CO_2-saturated environment. This behaviour is related to the higher amount of chloride ion adsorbed into the passive film formed in the acidic environment. Open circuit potentials of the lean duplex stainless steels also show that the alloys attained more positive potentials in the aerated environment after exposure for 24 hours. This is despite the higher chloride ion in the bulk solution of the aerated solution.

It is also interesting to find out that lean duplex alloys UNS S32101 and UNS S32304 can be used as substitute alloys for UNS S30403 and UNS S31603 austenitic stainless steels respectively in the CO_2-saturated and aerated conditions. This is because the data available from this research shows that UNS S32101 has a comparable corrosion resistance to UNS S30403 and that UNS S32304 also behaves similar to UNS S31603. Surprisingly also, the lean duplex stainless steel UNS S82441 could be an economic substitute to a standard duplex stainless steel, UNS S32205 at a low temperature in static conditions.

Another interesting result from this chapter is the fact that the Pitting Resistance Equivalent Number (PRE_N) does not seem to be a good parameter to rank the lean

duplex and the austenitic stainless steels when they are considered together. This is because UNS S32101, UNS S31603 and UNS S32304 all have approximately equal PRE_N but UNS S32101 does not have equal resistance to pitting (as evaluated by the breakdown potential) to the other two alloys. Also, UNS S30403 with a PRE_N much lower than that of UNS S32101 has very comparable breakdown potential (even higher breakdown potential in the CO_2-saturated environment) with UNS S32101. However, a critical PRE_N of 35 has been proposed for higher temperature service (50^oC and above) in CO_2 and aerated environments used in this research.

10.1.2 Erosion-Corrosion

Data available from this research shows that the lean duplex stainless steels UNS S32101 and UNS S32304 are promising alloys for erosion-corrosion applications. It is striking to see that UNS S32101 and UNS S32304 show equivalent resistance to UNS S32205 under both pure erosion and erosion-corrosion conditions. Both alloys exhibit better resistance than UNS S30403 under erosion and erosion-corrosion conditions.

10.1.2.1 Erosion-Corrosion and Subsurface Changes

Data from this thesis also show that hardness within the subsurface of an austenitic (UNS S30403) and a lean duplex alloy (UNS S32101) increases during erosion-corrosion degradation. This is established from the micro-hardness data. A change in the microstructure from austenite to strain-induced martensite as a result of the sand impact is also recorded. X-ray diffraction and selected area electron diffraction patterns support these conclusions. Fatigue cracks and grain refinement within the subsurface of the alloys after erosion-corrosion are also seen with the aid

of FIB and TEM. It seems that the sub-surface morphology, microstructure and crystallography changes contribute to the erosion-corrosion synergy. This is also inferred from the fact that UNS S30403 with a more inferior erosion-corrosion resistance suffered more subsurface cracks.

10.1.2.2 Erosion-Corrosion and Repassivation Kinetics of the Passive Film

The submerged impinging jet rig has been successfully adopted to study the repassivation kinetics of passive film under multiple sand impacts. Higher values of repassivation indices were recorded at lower temperature for both alloys. This suggests that the passive film is more compact and the rate of repassivation is faster at lower temperature. Higher repassivation index is recorded for UNS S32101 compared to UNS S30403 at both higher and lower temperatures. This suggests that the passive film formed on UNS S32101 is more compact than the passive film formed on UNS S30403. Also, the passive film on UNS S32101 repassivates faster than the passive film formed on UNS S30403.

Higher current density was observed at 50^{o}C compared to 20^{o}C for both alloys. Also, UNS S30403 also recorded higher current density at both 20 and 50^{o}C. The higher current density recorded for UNS S30403 compared with UNS S32101 is most likely due to the less effective passive film as well as the evolution of less corrosion resistant sub-surface (martensite, high density dislocation, fatigue cracks) which are more pronounced in this alloy than UNS S32101.

The behaviour of passive film on both alloys could thus be related to their erosion-corrosion behaviour. UNS S32101 with faster repassivation rate showed

better erosion-corrosion resistance than UNS S30403 under the same erosion-corrosion conditions.

10.2 Future Work

- Repassivation kinetics of the passive film formed on lean duplex stainless steel in the oilfield environment using single impact method at much lower impinging velocities will be an interesting research area. A miniature submerged impinging jet rig with a smaller capacity, say, 10 litres, driven by a motor would be a good idea. A single impact using either glass bead would then be likelihood with such miniature rig.
- The suggestion above could be supported with a nano-indentation or scratch electrode test method.
- Passive film chemistry of lean duplex stainless steels in CO_2-saturated oilfield environment is suggested to be studied *in situ* using X-ray Photoelectron Spectroscopy (XPS).
- There is still an incomplete understanding of the evolution of subsurface crystallography under erosion-corrosion. A systematic approach to understand the subsurface of each region of the wear coupon under a submerged impinging jet profile is suggested. Ring electrodes representing the stagnation, transition, and wall jet zones should be used. This will ensure no interference from the region that is not under impingement.

- Suggestion above could also be used under multiple impacts to study the repassivation kinetics of the passive film. Current transients from each region can then be separated from each other.

References

1. G2MTLABS. *Cost of corrosion to exceed $1 trillion in the United States in 2012-The future of materials condition assessment* [online]. [Accessed 24/01/2013]. Available from: http://www.g2mtlabs.com/2011/06/nace-cpst-of-corrosion-study-update.
2. REPORT, O.T. *Review of corrosion management for offshore oil and gas processing*. Offshore Technology Report, 2001/044, HSE Offshore Technology, ISBN 0 7176 2096 4, 2001.
3. P.HORROCKS, D. MANSFIELD, K. PARKER, J.THOMSON, T.ATKINSON and J.WORSELY. *Managing ageing plant* [online]. [Accessed 17/09/2013]. Available from: http://www.hse.gov.uk/research/rrpdf/rr823-summary-guide.pdf.
4. OBERNDORFER, M., K. THAYER and W. HAVLIK. Corrosion control in the oil and gas production- 5 successful case histories. *In: NACE corrosion conference, Paper No. 07317*, Nashville, Tennessee. NACE International, 2007.
5. OBERNDORFER, M., M. KAESTENBAUER and K. THAYER. Application limits of stainless steels in the petroleum industry. *In: SPE Annual Technical Conference and Exhibition, Paper No. 56805*, Houston, Texas. 1999.
6. TUTTLE, R.N. Corrosion in oil and gas production. *SPE Journal of Petroleum Technology*, 1987, **39**(7), pp.756-762.
7. ROCHE, M. Corrosion management: A key issue in pipeline integrity. *In: International Petroleum Technology Conference, IPTC 11385*, Dubai, U.A.E., 2007.
8. RINCON, H., J. SHADLEY, K. ROBERTS and E. RYBICKI. Erosion-corrosion of corrosion resistant alloys used in the oil and gas industry. *In: NACE corrosion conference, Paper No. 08571*, New Orleans. NACE International, 2008.
9. SINGH, B., T. FOLK, P. JUKES, J. GARCIA, W. PERICH and D. VAN OOSTENDORP. Engineering pragmatic solutions for CO2 corrosion problems. *In: NACE corrosion conference, Paper No. 07310*, Nashille Tennessee. NACE International, 2007.
10. EZUBAR, H.M. Metallurgical and environmental factors affecting the pitting behaviour of UNS S32205 duplex stainless steel in chloride solutions. *Materials and Corrosion*, 2012, **63**, pp.111-118.
11. RAO.SAITHALA, J., H. SINGH.UBHI, J. D.ATKINSON and A.K. P.PATIL. Pitting corrosion mechanisms of lean duplex, duplex and super duplex stainless steels in chloride solutions. *In: NACE corrosion conference, Paper No. 11255*, Houston, Texas. NACE International, 2011.
12. GUDME, J. and T.S. NIELSEN. Qualification of lean duplex grade LDX 2101 (UNS S32101) for carcass material in flexible pipes. *In: NACE corrosion conference, Paper No. 09075* Atlanta, GA. NACE International, 2009.
13. ROMMERSKIRCHEN, I., S. LEMKEN and R. HOFFMANN. Lean duplex materials for line pipe applications in Sweet and slightly sour environments. *In: International Petroleum Exhibition and Conference, SPE 117147*, Abu Dhabi, UAE. 2008.

14. WEI, Z., J. LAIZHU, H. JINCHENG and S. HONGMEI. Study of mechanical and corrosion properties of a Fe-21.4Cr-6Mn-1.5Ni-0.24N-0.6Mo duplex stainless steel. *Materials Science and Engineering: A*, 2008, **497**(1-2), pp.501-504.
15. ALVAREZ-ARMAS, I. Duplex stainless steels: Brief history and some recent alloys. *Recent patents on mechanical engineering*, 2008, **1**, pp.51-57.
16. IVERSEN, A.K. Stainless steels in bipolar plates--Surface resistive properties of corrosion resistant steel grades during current loads. *Corrosion Science*, 2006, **48**(5), pp.1036-1058.
17. OLSSON, J. and M. SNIS. Duplex -- A new generation of stainless steels for desalination plants. *Desalination*, 2007, **205**(1-3), pp.104-113.
18. MERELLO, R., F.J. BOTANA, J. BOTELLA, M.V. MATRES and M. MARCOS. Influence of chemical composition on the pitting corrosion resistance of non-standard low-Ni high-Mn-N duplex stainless steels. *Corrosion Science*, 2003, **45**(5), pp.909-921.
19. BEREZOVSKAYA, V., M. KOSTINA, E. BLINOV, I. BANNYKH, V. BOBROVA and V. MEL'NIK. Corrosion properties of austenitic Cr-Mn-Ni-N steels with various manganese concentrations. *Russian Metallurgy (Metally)*, 2008, (1), pp.29-33.
20. HWANG, J.-K., G.-J. BANG, M.-I. ROH and K.-Y. LEE. Detailed design and construction of the hull of an FPSO (Floating, Production, Storage, and Off-loading Unit). *In: International Offshore and Polar Engineering Conference*, Osaka, Japan. 2009, pp.151-158.
21. DUNN, J.J. and D.R. HASEK. AL2003 lean duplex case study: Flexible flowlines for an offshore oil field development *In: Stainless Steel World Conference*, The Netherland. 2007, pp.1-14.
22. JORDAN, L.C., MCENERNEY, J.W., MCMANUS J.W. The introduction of alloy 2101 for use as zinc-clad umbilical tubing for deepwater subsea oil and gas development. *acom, a corrosion management and application engineering magazine from outokumpu stainless* 2006, pp.23-30.
23. Y.ZHANG, B., CHEN, L. QUI, T. HILL, M. CASE. State of the art analytical tools to improve optisation of unbounded flexible pipes for deepwater environments. *In: Offshore Technology Conference, OTC 15169*, April 30-May 3, Texas, USA. 2003.
24. OUT, J.M.M. Integrity management of flexible pipe: chasing failure mechanisms. *In: Offshore Technology Conference, OTC-23670*, Houston, Texas, USA. 2012.
25. NEVILLE, A., M. REYES and H. XU. Examining corrosion effects and corrosion/erosion interactions on metallic materials in aqueous slurries. *Tribology International*, 2002, **35**(10), pp.643-650.
26. HU, X. and A. NEVILLE. The electrochemical response of stainless steels in liquid–solid impingement. *Wear*, 2005, **258**(1–4), pp.641-648.
27. NEVILLE, A., T. HODGKIESS and J.T. DALLAS. A study of the erosion-corrosion behaviour of engineering steels for marine pumping applications. *Wear*, 1995, **186-187**(Part 2), pp.497-507.
28. MOHAMMADI, F. and J. LUO. Effect of cold work on erosion–corrosion of 304 stainless steel. *Corrosion Science*, 2011, **53**(2), pp.549-556.

29. CHACON NAVA, J.G., F.H. STOTT and M.M. STACK. The effect of substrate hardness on the erosion-corrosion resistance of materials in low-velocity conditions. *Corrosion Science*, 1993, **35**(5–8), pp.1045-1051.
30. WOOD, R.J.K. Erosion-corrosion interactions and their effect on marine and offshore materials. *Wear*, 2006, **261**(9), pp.1012-1023.
31. BURSTEIN, G.T. and K. SASAKI. Effect of impact angle on the slurry erosion–corrosion of 304L stainless steel. *Wear*, 2000, **240**(1–2), pp.80-94.
32. LI, J., Y.G. ZHENG, J.Q. WANG, Z.M. YAO, Z.F. WANG and W. KE. Depassivation and repassivation of AISI321 stainless steel surface during solid particle impact in 10% H2SO4 solution. *Wear*, 1995, **186-187**(Part 2), pp.562-567.
33. WATSON, S.W., F.J. FRIEDERSDORF, B.W. MADSEN and S.D. CRAMER. Methods of measuring wear-corrosion synergism. *Wear*, 1995, **181-183**(Part 2), pp.476-484.
34. SASAKI, K. and G. BURSTEIN. The generation of surface roughness during slurry erosion-corrosion and its effect on the pitting potential. *Corrosion Science*, 1996, **38**(12), pp.2111-2120.
35. RAJAHRAM, S.S., T.J. HARVEY, J.C. WALKER, S.C. WANG and R.J.K. WOOD. Investigation of erosion–corrosion mechanisms of UNS S31603 using FIB and TEM. *Tribology International*, 2012, **46**(1), pp.161-173.
36. RAJAHRAM, S.S., T.J. HARVEY, J.C. WALKER, S.C. WANG, R.J.K. WOOD and G. LALEV. A study on the evolution of surface and subsurface wear of UNS S31603 during erosion–corrosion. *Wear*, 2011, **271**(9–10), pp.1302-1313.
37. WOOD, R.J.K., J.C. WALKER, T.J. HARVEY, S. WANG and S.S. RAJAHRAM. Influence of microstructure on the erosion and erosion–corrosion characteristics of 316 stainless steel. *Wear*, 2013, **306**(1–2), pp.254-262.
38. E.E. STANSBURY AND R.A. BUCHANAN. *Fundamentals of electrochemical corrosion.* Ohio: ASM International, ISBN 0-87170-676-8, 2000.
39. ROBERGE, P.R. *Handbook of corrosion engineering.* McGraw Hill, ISBN 0-07-076516-2, 2000.
40. DAVIS, J.R. *Corrosion: Understanding the basics.* Materials Park, Ohio, ISBN 978-1-62870-222-4, 2000.
41. NESTOR, P. *Electrochemistry and corrosion science.* Boston: Kluwer Academic Publisher, ISBN 1-4020-7860, 2004.
42. TAIT, W.S. *An introduction to electrochemical corrosion testing for practicing engineers and scientists* Madison, WI,: PaisDocs Publications, ISBN 978-0966020700, 1994.
43. HU, X. *Corrosion and erosion-corrosion behaviour of high alloy stainless steels*. PhD thesis, Heriot Watt University, 2003.
44. TRETHEWEY, K.R. and J. CHAMBERLAIN. *Corrosion for science and engineering.* 2nd ed. UK: Longman Scientific and Technical, ISBN 0-582-238692, 1995.
45. UHLIG, H.H. *Corrosion and corrosion control.* 2nd edition ed. John Wiley & Sons Inc., ISBN 0-471-89563-6, 1971.

46. CHINEDU, O.I. Advances in asset management techniques: an overview of corrosion mechanisms and mitigation strategies for oil and gas pipelines. *International Scholarly Research Network*, 2012, **2012**.
47. BARD, A.J. and L.R. FAULKNER. *Electrochemicals methods: Fundamentals and applications.* John Wiley & Sons, Inc., ISBN 0-471-04372-9, 2001.
48. ROBERGE, P.R. *Corrosion engineering, principles and practice.* McGraw-Hill, ISBN 978-0-07-148243-1, 2008.
49. KAESCHE, H. *Corrosion of metals: Physiochemical principles and current problems.* Berlin Heidelberg: Springer-Verlag, ISBN 3-540-00626-5, 2003.
50. UHLIG, H.H. and R.W. REVIE. *Corrosion and corrosion control: An introduction to corrrosion science and engineering.* John Wiley and Son Inc, ISBN 0-471-07818-2, 1984.
51. STERN, M. and A.L. GEARY. Electrochemical polarization I . A theoretical analysis of the shape of polarization curves. *J. Electrochem. Soc*, 1957, **104** (1), pp.56–63.
52. SCULLY, J.R. Polarization resistance method for determination of instantaneous corrosion rates. *Corrosion*, 2000, **56**(2), pp. 199-221.
53. CHATURVEDI, T.P. *Corrosion behaviour of orthodontic alloys* [online]. [Accessed 27/07/2013]. Available from: http://orthocj.com/2008/01/corrosion-behavior-of-orthodontic-alloys/.
54. EBRAHIMI, N., M.H. MOAYED and A. DAVOODI. Critical pitting temperature dependence of 2205 duplex stainless steel on dichromate ion concentration in chloride medium. *Corrosion Science*, 2011, **53**(4), pp.1278-1287.
55. BARGMANN, I. *Materials selection for erosion corrosion in oil and gas*. PhD thesis, University of Leeds, 2009.
56. OLEFJORD, I. The passive state of stainless steels. *Materials Science and Engineering*, 1980, **42**, pp.161-171.
57. OLDFIELD, J.W. Test techniques for pitting and crevice corrosion resistance of stainless steels and nickel-base alloys in chloride-containing environments. *International Materials Reviews*, 1987, **32**, pp.153-172.
58. BENDALL, K.C. Long term experiences of the use of duplex stainless steel to combat corrosion in the pulp and paper industry. *In: NACE corrosion conference, Paper No. 96469*, Denver, Co. NACE International, 1996.
59. QIU, J.H. Passivity and its breakdown on stainless steels and alloys. *Surface and interface analysis*, 2002, **33**, pp.830-833.
60. OLSSON, C.O.A. and D. LANDOLT. Passive films on stainless steels--chemistry, structure and growth. *Electrochimica Acta*, 2003, **48**(9), pp.1093-1104.
61. NEWMAN, R.C. 2001 WR Whitney award lecture: Understanding the corrosion of stainless steel. *Corrosion Science*, 2001, **57**(12), pp.1030-1041
62. HASSEL, A.W. and J.W. SCHULTZE. Passivity of metals, alloys, and semiconductors *In:* M. STRATMANN and G.S. FRANKEL, eds. *Encyclopedia of Electrochemistry*. Willey, Weinheim, ISBN 978-3-527-30396-0, 2003.

63. HAKIKI, N.E., M.F. MONTEMOR, M.G.S. FERREIRA and M. DA CUNHA BELO. Semiconducting properties of thermally grown oxide films on AISI 304 stainless steel. *Corrosion Science*, 2000, **42**(4), pp.687-702.
64. KELLY, R.G., J.R. SCULLY, D.W. SHOESMITH and G.B. RUDOLPH. *Electrochemical techniques in corrosion science and engineering.* New York: Marcel Dekker Inc, ISBN 0-8247-9917-8, 2003.
65. FERNÁNDEZ-DOMENE, R.M., E. BLASCO-TAMARIT, D.M. GARCÍA-GARCÍA and J. GARCÍA-ANTÓN. Repassivation of the damage generated by cavitation on UNS N08031 in a LiBr solution by means of electrochemical techniques and confocal laser scanning microscopy. *Corrosion Science*, 2010, **52**(10), pp.3453-3464.
66. JEMMELY, P., S. MISCHLER and D. LANDOLT. Electrochemical modeling of passivation phenomena in tribocorrosion. *Wear*, 2000, **237**(1), pp.63-76.
67. GRAHAM, F.G., H.C. BROOKES and J.W. BAYLES. Nucleation and growth of anodic films on stainless steel alloys II. Kinetics of repassivation of freshly generated metal surfaces. *Journal of Applied Electrochemistry*, 1990, **20**, pp.45-53.
68. C.Y. CHAO, L.F. LIN and D.D. MACDONALD. A point defect mode for anodic passive film I. Film growth and kinetics. *Journal of electrochemical Society: Electrochemical Science and Technology*, 1981, **128**(6), pp.1187-1194.
69. STAEHLE, R.W. Transient stability of passive films in aqueous solutions. *Corrosion Science*, 2007, **49**(1), pp.7-19.
70. LEE, J.-B. Effects of alloying elements, Cr, Mo and N on repassivation characteristics of stainless steels using the abrading electrode technique. *Materials Chemistry and Physics*, 2006, **99**(2-3), pp.224-234.
71. ESCRIVÀ-CERDÁN, C., E. BLASCO-TAMARIT, D. GARCÍA-GARCÍA, J. GARCÍA-ANTÓN and A. GUENBOUR. Passivation behaviour of Alloy 31 (UNS N08031) in polluted phosphoric acid at different temperatures. *Corrosion Science*, 2012, **56**, pp.114-112.
72. LILLARD, R., G. VASQUEZ and D. BAHR. The kinetics of anodic dissolution and repassivation on stainless steel 304L in solutions containing nitrate. *Journal of The Electrochemical Society*, 2011, **158**(6), pp.C194-C201.
73. KERMANI, M.B. and A. MORSHED. Carbon dioxide corrosion in oil and gas production - a compendium. *Corrosion*, 2003, **59**(08).
74. MOISEEVA, L.S. Carbon dioxide corrosion of oil and gas field equipment. *Protection of Metals*, 2005, **41**(1), pp.76-83.
75. DAYALAN, E., J.R. SHADLEY, E.F. RYBICKI, S.A. SHIRAZI and F.D.D. MORAES. CO2 corrosion prediction in pipe flow under FeCO3 scale-forming conditions. *In: NACE corrosion conference, Paper No. 98051*, San Diego Ca. NACE International, 1998.
76. KERMANI, B., L.M. SMITH, C. EUROPEAN FEDERATION OF and M. INSTITUTE OF. *A working party report on CO2 corrosion control in oil and gas production design considerations.* London: Maney Publisher, ISBN 978-1861250520, 1997.
77. ORAZEM, M.E. and J. FILHO. Application of a submerged impinging jet to investigate the influence of temperature, dissolved CO2, and fluid velocity on

corrosion of pipeline grade steel in brine. *In: NACE corrosion conference, Paper No. 01058*, Houston, Tx. NACE International, 2001.

78. SCHMITT, G. and M. HORSTEMEIER. Fundamental aspects of CO2 metal loss corrosion - Part II: Influence of different parameters on CO2 corrosion mechanisms. *In: NACE corrosion conference, Paper No. 06112*, San Diego Ca. NACE International, 2006.
79. CHAMBERS, B., R.D. KANE and M. YUNOVICH. Corrosion and selection of alloys for CCS (Carbon Capture and Storage) systems: current challenges. *In: SPE International Conference on CO2 Capture Storage and Utilization, SPE 139521*, New Orleans, Louisiana, USA. Society of Petroleum Engineers, 2010.
80. UEDA, M. and H. TAKABE. Effect of organic acid on CO2 corrosion of carbon and CR bearing steels. *In: NACE corrosion conference, Paper No. 98035*, San Diego Ca. NACE International, 1998.
81. BARDAL, E., J.M. DRUGLI and P.O. GARTLAND. The behaviour of corrosion-resistant steels in seawater: A review. *Corrosion Science*, 1993, **35**(1-4), pp.257-267.
82. FERON, D., N. MARIN and M. ROY. Influence of ageing on corrosion behaviour of stainless steels in sea water. *In: Proceedings of Eurocorr*, Netherlands. 1988, pp.166-171.
83. MANSFELD, F. and B. LITTLE. A technical review of electrochemical techniques applied to microbiologically influenced corrosion. *Corrosion Science*, 1991, **32**(3), pp.247-272.
84. FINNIE, I. Erosion of surfaces by solid particles. *Wear*, **3**(2), pp.87-103.
85. NEILSON, J.H. and A. GILCHRIST. Erosion by a stream of solid particles. *Wear*, 1968, **11**(2), pp.111-122.
86. MCCABE, L.P., G. A. SARGENT and H. CONRAD. Effect of microstructure on the erosion of steel by solid particles. *Wear*, 1985, **105**(3), pp.257-277.
87. SALAMA, M.M. and E.S. VENKATESH. Evaluation of API RP 14E erosional velocity limitations for offshore gas wells. *In: Offshore Technology Conference, OTC 4485*. 1983.
88. FINNIE, I. The mechanism of erosion of ductile metals. *In: Proc. 3rd Nat. Cong. Appl. Mech*. ASME, 1958, pp. 527-532.
89. BITTER, J. A study of erosion phenomena part I. *Wear*, 1963, **6**(1), pp.5-21.
90. ---. A study of erosion phenomena: Part II. *Wear*, 1963, **6**(3), pp.169-190.
91. JORDAN, K.G. Erosion in multiphase production of oil & gas. *In: NACE corrosion conference, Paper No. 98058*, San Diego Ca. NACE International, 1998.
92. MENG, H.C. and K.C. LUDEMA. Wear models and predictive equations: Their form and content. *Wear*, 1995, **181–183, Part 2**(0), pp.443-457.
93. HUTCHINGS, I. *Tribology: friction and wear of engineering materials.* London: Butterworth-Heinemann Ltd, ISBN 978-0340561843, 1992.
94. M.HASHISH. An improved model of erosion by solid particle impact. *In: Proceeding of the 7th international conference on erosion by liquid and solid impact, Paper No. 66*, 1988.
95. SALAMA, M.M. Sand production management. *Journal of Energy Resources Technology*, 1999, **122**(1), pp.29-33.

96. ---. Influence of sand production on design and operations of piping systems. *In: NACE corrosion conference, Paper No. 00080*. NACE International, 2000.
97. X. CHEN, B.S. MCLAURY and S.A. SHIRAZI. Application and experimental validation of a computational fluid dynamics (CFD)-based erosion prediction model in elbows and plugged tees. *Computers & Fluids*, 2004, **33**(10), pp.1251-1272.
98. SALAM, M.M. An alternative to API 14E erosional velocity limits for sand laden fluids. *In: Offshore Technology Conference, OTC 8898*, Houston Texas. 1998.
99. SHIRAZI, S.A., B.S. MCLAURY, J.R. SHADLEY and E.F. RYBICKI. Generalization of the API RP 14E guideline for erosive services. *SPE Journal of Petroleum Technology*, 1995, **47**(8), pp.693-698.
100. RAMACHANDRAN, S., V. JOVANCICEVIC, J. BASSETT and Y.S. AHN. Further advances in the development of erosion corrosion inhibitors. *In: NACE corrosion conference, Paper No. 05292*, Houston, Tx. NACE International, 2005.
101. ROBERGE, P. *Corrosion testing made easy, erosion-corrosion.* NACE International, ISBN 1-57590-173-0, 2004.
102. HE, D.D., X.X. JIANG, S.Z. LI and H.R. GUAN. Erosion-corrosion of stainless steels in aqueous slurries - A quantitative estimation of synergistic effects. *Corrosion*, 2005, **61**(01).
103. MADSEN, B.W. Measurement of erosion-corrosion synergism with a slurry wear test apparatus. *Wear*, 1988, **123**(2), pp.127-142.
104. WANG, C., A. NEVILLE and S. RAMACHANDRAN. Understanding inhibitor action on components of erosion, corrosion and their interactions in CO2-containing slurries. *In: SPE International Symposium on Oilfield Corrosion, SPE 87551*, Aberdeen, United Kingdom. 2004.
105. MCKAY, I., P.R. RUSS and J.W. MOHR. A sand management system for mature offshore production facilities. *In: International Petroleum Technology Conference, IPTC 12784*, Kuala Lumpur, Malaysia. 2008.
106. SHADLEY, J.R., S.A. SHIRAZI, E. DAYALAN and E.F. RYBICKI. Prediction of erosion-corrosion penetration rate in a CO2 environment with sand. *In: NACE corrosion conference, Paper No. 98059* San Diego Ca. NACE International, 1998.
107. EFIRD, K.D. Jet impingement testing for flow accelerated corrosion. *In: NACE corrosion conference, Paper No. 00052*, Orlando, Fl. NACE International, 2000.
108. EFIRD, K.D., J.A. BOROS, T.G. HAILEY and E.J. WRIGHT. Correlation of steel corrosion in pipe flow with jet impingement and rotating cylinder tests. *Corrosion*, 1993, **49**(12).
109. STACK, M.M., S. ZHOU and R.C. NEWMAN. Identification of transitions in erosion-corrosion regimes in aqueous environments. *Wear*, 1995, **186-187**(Part 2), pp.523-532.
110. BABOIAN, R. *Corrosion tests and standards: application and interpretation.* 2nd ed. Baltimore MD, USA: ASTM international, ISBN 0-8031-2098-2, 2005.

111. WOOD, R.J.K. and A.J. SPEYER. Erosion-corrosion of candidate HVOF aluminium-based marine coatings. *Wear*, 2004, **256**(5), pp.545-556.
112. MENG, H., X. HU and A. NEVILLE. A systematic erosion-corrosion study of two stainless steels in marine conditions via experimental design. *Wear*, 2007, **263**(1-6), pp.355-362.
113. NEVILLE, A. and X. HU. Assessing the role of corrosion in erosion-corrosion of high grade alloys in aggressive marine environments. *In: NACE corrosion conference, Paper No. 02189*, Denver, Co. NACE International, 2002.
114. ZU, J., I. HUTCHINGS and G. BURSTEIN. Design of a slurry erosion test rig. *Wear*, 1990, **140**(2), pp.331-344.
115. LILJAS, M. 80 years with duplex steels, a historic review and prospects for the future. *In: 6th European Stainless Steel Conference*, Helsinki. 2008.
116. LO, K.H., C.H. SHEK and J.K.L. LAI. Recent developments in stainless steels. *Materials Science and Engineering: R: Reports*, 2009, **65**(4-6), pp.39-104.
117. HUSSAIN, E. and A. HUSAIN. Erosion-corrosion of duplex stainless steel under Kuwait marine condition. *Desalination*, 2005, **183**(1-3), pp.227-234.
118. GUNN , R.N. *Duplex stainless steels- Microstructure; properties and applications.* Abington Publishing Limited, ISBN 1855 733 188, 1997.
119. FRANCIS, R.B., G. WARBURTON, G. R. Experiences with Zeron 100® super duplex stainless steel in the process industries. *In: Stainless Steel World*: KCL Publishing, 1999, pp.613 - 624.
120. FRANCIS, R., M.N. MALIGAS, G. BYRNE and G.R. WARBURTON. The selection of superduplex stainless steel for oilfield applications. *In: NACE corrosion conference, Paper No. 04123*, New Orleans, La. NACE International, 2004.
121. KARIMI, A. Cavitation erosion of a duplex stainless steel. *Materials Science and Engineering*, 1987, **86**(0), pp.191-203.
122. ATAMERT, S. and J.E. KING. Sigma-phase formation and its prevention in duplex stainless steels. *Journal of Materials Science Letters*, 1993, **12**(14), pp.1144-1147.
123. GHOSH, S.K. and S. MONDAL. High temperature ageing behaviour of a duplex stainless steel. *Materials Characterization*, 2008, **59**(12), pp.1776-1783.
124. NANA, S. and M.B. CORTIE. Microstructure and corrosion resistance of experimental low nickel duplex stainless steels. *J.S Afr. Min. Metall*, 1993, **93**(11/12), pp.307-315.
125. ROMMERSKIRCHEN, I., S. LEMKEN and R. HOFFMANN. Lean duplex grade as longitudinal welded pipes for line pipes in the oil and gas business. *Corrosion Management and Application Engineering Magazine from Outokumpu Stainless Steels*, 2006, pp.2-6.
126. RAGHU, D. and J.B.C. WU. Recent developments in wear and corrosion resistant alloys for oil industry. *In: NACE corrosion conference, Paper No. 97016*, New Orleans, LA. NACE International, 1997.
127. FU, S.-L., J.G. GARCIA and ANTOINE. Corrosion resistance of some downhole tubing materials and inhibitor effectiveness in sweet environments.

In: NACE corrosion conference, Paper No. 96021, Denver, Co. NACE International, 1996.

128. PENDLEY, M.R. meeting the challenge of extremely corrosive service: a primer on clad oilfield equipment. *In: SPE Asia Pacific Oil and Gas Conference, SPE 25345*, Singapore. 1993.
129. UEDA, M. and H. TAKABE. Corrosion resistance of low Cr bearing steel in sour and sweet environments. *In: NACE corrosion conference, Paper No. 02041*, Denver, Co. NACE International, 2002.
130. M.JONES and R.J. LLEWELLYN. Assessing the erosion corrosion properties of materials for slurry transportation and processing in the oil sands industry. *In: NACE corrosion conference, Paper No. 07685*, Nashville, Tennessee. NACE International, 2007.
131. NICOLIO, C. and M. HOLMQUIST. Duplex alloys: challenging corrosion in the new millennium. *In: NACE corrosion conference, Paper No. 02120*, Denver, Co. NACE International, 2002.
132. MARTINS, M. and L.C. CASTELETTI. Microstructural characteristics and corrosion behavior of a super duplex stainless steel casting. *Materials Characterization*, 2009, **60**(2), pp.150-155.
133. CASSAGNE, T. and F. BUSSCHAERT. A review on hydrogen embrittlement of duplex stainless steels. *In: NACE corrosion conference, Paper No. 05098*, Houston, Tx. NACE International, 2005.
134. TAN, H., Y. JIANG, B. DENG, T. SUN, J. XU and J. LI. Effect of annealing temperature on the pitting corrosion resistance of super duplex stainless steel UNS S32750. *Materials Characterization*, 2009, **60**(9), pp.1049-1054.
135. MCKENNIS, J.S., N. BAE and E.J. TERMINE. Carbon dioxide corrosion when least expected: importance of carbonate chemistry in stress corrosion cracking on the external surfaces of martensitic stainless-steel production tubing and low-alloy carbon steel pipeline. *In: SPE Annual Technical Conference and Exhibition, SPE 135217*, Florence, Italy. 2010.
136. BARGMANN, I., A. NEVILLE, S. HERTZMAN, F. REZA and X. HU. Erosion-corrosion in oil and gas-stainless steel under de-aerated slurry impingement attack. *In: NACE corrosion conference, Paper No. 09483*, Atlanta, GA. NACE International, 2009.
137. OH, K.-T., K.-N. KIM, M. LEE and Y.-S. PARK. Corrosion wear of high molybdenum and nitrogen stainless steel for biomedical applications. *Journal of The Electrochemical Society*, 2002, **149**(4), pp.B146-B153.
138. HABERL, J., G. MORI, P. WAGNER, W. HAVLIK and P. HOSEMANN. How do microstructure and PREN affect the erosion corrosion behaviour of stainless steels? *In: NACE corrosion conference, Paper No. 09480*, Atlanta, GA. NACE International, 2009.
139. JOHANSSON, E. and T. PROSEK. Stress corrosion cracking properties of UNS S32101 -A new duplex stainless steel with low nickel content. *In: NACE corrosion conference, Paper No. 07475*, Nashville, Tennessee. NACE International, 2007.
140. IVERSEN, A., R. QVARFORT and A. BERGQVIST. Corrosion properties of S32101 - A new duplex stainless steel, with Low nickel content for use as reinforcement in concrete. *In: NACE corrosion conference, Paper No. 05260*, Houston,Texas NACE International, 2005.

141. M.O. MATSUMURA, H. HIURA and M. YANO. The role of passivation film in preventing slurry erosion corrosion of austenitic stainless steel. *ISIJ International*, 1991, **31**(2), pp.168-176.
142. LU, X.C., S.Z. LI, X.X. JIANG and T.C. ZHANG. Effect of γ phase on corrosive wear of duplex stainless steel in sulfuric acid solution. *Corrosion*, 1995, **51**(6), pp.456-462.
143. LIU, W., Y.G. ZHENG, C.S. LIU, Z.M. YAO and W. KE. Cavitation erosion behavior of Cr–Mn–N stainless steels in comparison with 0Cr13Ni5Mo stainless steel. *Wear*, 2003, **254**(7–8), pp.713-722.
144. KWON, H.S., E.A. CHO and K.A. YEOM. Prediction of stress corrosion cracking susceptibility of stainless steels based on repassivation kinetics. *Corrosion*, 2000, **56**(01), pp.32-40.
145. CABRERA, N. and N. MOTT. Theory of the oxidation of metals. *Reports on Progress in Physics*, 1949, **12**(1), p.163.
146. KIRCHHEIM, R. Growth kinetics of passive films. *Electrochimica Acta*, 1987, **32**(11), pp.1619-1629.
147. BURSTEIN, G. and A. DAVENPORT. The current-time relationship during anodic oxide film growth under high electric field. *Journal of The Electrochemical Society*, 1989, **136**(4), pp.936-941.
148. LANDOLT, D., S. MISCHLER and M. STEMP. Electrochemical methods in tribocorrosion: A critical appraisal. *Electrochimica Acta*, 2001, **46**(24-25), pp.3913-3929.
149. KIM, J.S., P.J. XIANG and K.Y. KIM. Effect of tungsten and nickel addition on the repassivation behavior of stainless steel. *Corrosion*, 2005, **61**(02), pp.174-183.
150. NEWMAN, R.C. The dissolution and passivation kinetics of stainless alloys containing molybdenum--1. Coulometric studies of Fe-Cr and Fe-Cr-Mo alloys. *Corrosion Science*, 1985, **25**(5), pp.331-339.
151. HASHIMOTO, K., K. ASAMI and K. TERAMOTO. An X-ray photo-electron spectroscopic study on the role of molybdenum in increasing the corrosion resistance of ferritic stainless steels in HC1. *Corrosion Science*, 1979, **19**(1), pp.3-14.
152. IHSAN-UL-HAQ TOOR, K.J. PARK and H. KWON. Manganese effects on repassivation kinetics and SCC susceptibility of high Mn-N austenitic stainless steel alloys. *Journal of The Electrochemical Society*, 2007, **154**(9), pp.C494-C499.
153. YAMAMOTO, T., K. FUSHIMI, M. SEO, S. TSURI, T. ADACHI and H. HABAZAKI. Depassivation-repassivation behavior of type-312L stainless steel in NaCl solution investigated by the micro-indentation. *Corrosion Science*, 2009, **51**(7), pp.1545-1553.
154. PHADNIS, S.V., A.K. SATPATI, K.P. MUTHE, J.C. VYAS and R.I. SUNDARESAN. Comparison of rolled and heat treated SS304 in chloride solution using electrochemical and XPS techniques. *Corrosion Science*, 2003, **45**(11), pp.2467-2483.
155. MAZZA, B., P. PEDEFERRI, D. SINIGAGLIA, A. CIGADA, G.A. MONDORA, G. RE, G. TACCANI and D. WENGER. Pitting resistance of cold-worked commercial austenitic stainless steels in solution simulating

seawater. *Journal of The Electrochemical Society*, 1979, **126**(12), pp.2075-2081.

156. HODGKIESS, T. and A. NEVILLE. An XPS study of passive films on stainless steels and a high-grade Ni-base alloy in seawater environments. *In: NACE corrosion conference, Paper No. 99317*, San Antonio TX. NACE International, 1999.
157. OLEFJORD, I. and L. WEGRELIUS. Surface analysis of passive state. *Corrosion Science*, 1990, **31**(0), pp.89-98.
158. WEGRELIUS, L. and I. OLEFJORD. Dissolution and passivation of stainless steels exposed to hydrochloric acid. *Materials Science Forum*, 1995, **185**, pp.347-356.
159. DONIK, Č., A. KOCIJAN, D. MANDRINO and M. JENKO. X-ray photoelectron spectroscopy depth profiling of electrochemically prepared thin oxide layers on duplex stainless steel. *Metallurgical and Materials Transactions B*, 2011, **42**(5), pp.1044-1050.
160. FREDRIKSSON, W., K. EDSTRÖM and C.O.A. OLSSON. XPS analysis of manganese in stainless steel passive films on 1.4432 and the lean duplex 1.4162. *Corrosion Science*, 2011, **52**(7), pp.2505-2510.
161. TOOR, I.-U.-H., K.J. PARK and H. KWON. Manganese effects on repassivation kinetics and SCC susceptibility of high Mn-N austenitic stainless steel alloys. *Journal of The Electrochemical Society*, 2007, **154**(9), pp.C494-C499.
162. ZHANG, Y., X. ZHU, M. LIU and R. CHE. Effects of anodic passivation on the constitution, stability and resistance to corrosion of passive film formed on an Fe-24Mn-4Al-5Cr alloy. *Applied Surface Science*, 2004, **222**(1), pp.89-101.
163. ANSELMO, N., J.E. MAY, N.A. MARIANO, P.A.P. NASCENTE and S.E. KURI. Corrosion behavior of supermartensitic stainless steel in aerated and CO2-saturated synthetic seawater. *Materials Science and Engineering: A*, 2006, **428**(1-2), pp.73-79.
164. SH. ENDO, M.N. Ferrite–martensite dual phase anti-erosion steel. *ISIJ International*, 1996, **36** pp.95–100.
165. QIONG-LI, W. Wear resistance of steels under wet-abrasive erosion conditions. *Wear*, 1986, **112**(2), pp.207-216.
166. BÜSCHER, R. and A. FISCHER. The pathways of dynamic recrystallization in all-metal hip joints. *Wear*, 2005, **259**(7–12), pp.887-897.
167. BIDIVILLE, A., M. FAVERO, P. STADELMANN and S. MISCHLER. Effect of surface chemistry on the mechanical response of metals in sliding tribocorrosion systems. *Wear*, 2007, **263**(1–6), pp.207-217.
168. IVES, L.K. and A.W. RUFF. Electron microscopy study of erosion behaviour in copper. *In:* W.F. ADLER, ed. *Erosion: Prevention and useful applications*. American Society for Testing and Materials ASTM STP 664, ISBN 04-664000-29, 1979, pp.5-35. .
169. EDINGTON, J.W. and I.G. WRIGHT. Study of particle erosion damage in Haynes Stellite 6B I: Scanning electron microscopy of eroded surfaces. *Wear*, 1978, **48**(1), pp.131-144.
170. ---. Study of particle erosion damage in Haynes Stellite 6B II: Transmission electron microscopy. *Wear*, 1978, **48**(1), pp.145-155.

171. LU, X.-C., K. SHI, S.-Z. LI and X.-X. JIANG. Effects of surface deformation on corrosive wear of stainless steel in sulfuric acid solution. *Wear*, 1999, **225–229, Part 1**(0), pp.537-543.
172. ZHANG, Y.S., X.M. ZHU, M. LIU and R.X. CHE. Effects of anodic passivation on the constitution, stability and resistance to corrosion of passive film formed on an Fe-24Mn-4Al-5Cr alloy. *Applied Surface Science*, 2004, **222**(1–4), pp.89-101.
173. LU, B., J. LUO, F. MOHAMMADI, K. WANG and X. WAN. Correlation between repassivation kinetics and corrosion rate over a passive surface in flowing slurry. *Electrochimica Acta*, 2008, **53**(23), pp.7022-7031.
174. FUSHIMI, K., K.-I. TAKASE, K. AZUMI and M. SEO. Current transients of passive iron observed during micro-indentation in pH 8.4 borate buffer solution. *Electrochimica Acta*, 2006, **51**(7), pp.1255-1263.
175. SUN, D., J. WHARTON and R. WOOD. Micro- and nano-scale tribo-corrosion of cast CoCrMo. *Tribology Letters*, 2011, **41**(3), pp.525-533.
176. FUSHIMI, K., T. SHIMADA, H. HABAZAKI, H. KONNO and M. SEO. Mechano-electrochemistry of a passive surface using an in situ micro-indentation test. *Electrochimica Acta*, 2011, **56**(4), pp.1773-1780.
177. SEO, M., M. CHIBA and K. SUZUKI. Nano-mechano-electrochemistry of the iron (100) surface in solution. *Journal of Electroanalytical Chemistry*, 1999, **473**(1), pp.49-53.
178. SMITH, A.J., M. STRATMANN and A.W. HASSEL. Investigation of the effect of impingement angle on tribocorrosion using single impacts. *Electrochimica Acta*, 2006, **51**(28), pp.6521-6526.
179. BARKER, R.J. *Erosion-corrosion of carbon steel pipework on an offshore oil and gas facility*. PhD thesis, University of Leeds, 2012.
180. LAYCOCK, N. Effects of temperature and thiosulfate on chloride pitting of austenitic stainless steels. *Corrosion*, 1999, **55**(6), pp.590-595.
181. NATISHAN, P., W. O'GRADY, F. MARTIN, R. RAYNE, H. KAHN and A. HEUER. Chloride interactions with the passive films on stainless steel. *Journal of The Electrochemical Society*, 2011, **158**(2), pp.C7-C10.
182. NEVILLE, A., F. REZA, S. CHIOVELLI and T. REVEGA. Erosion–corrosion behaviour of WC-based MMCs in liquid–solid slurries. *Wear*, 2005, **259**(1), pp.181-195.
183. WOOD, R. and D. WHEELER. Design and performance of a high velocity air-sand jet impingement erosion facility. *Wear*, 1998, **220**(2), pp.95-112.
184. LIEBHARD, M. and A. LEVY. The effect of erodent particle characteristics on the erosion of metals. *Wear*, 1991, **151**(2), pp.381-390.
185. *Research Equipment Facilities* [online]. [Accessed 21/11/2013]. Available from: http://www.engineering.leeds.ac.uk/lennf/facilities/index.shtml.
186. *The principle of FIB* [online]. [Accessed 15-12-2013]. Available from: http://en.wikipedia.org/wiki/Focused_ion_beam.
187. LUO, H., C. DONG, K. XIAO and X. LI. Characterization of passive film on 2205 duplex stainless steel in sodium thiosulphate solution. *Applied Surface Science*, 2011, **258**(1), pp.631-639.
188. ABREU, C., M. CRISTÓBAL, R. LOSADA, X. NÓVOA, G. PENA and M. PÉREZ. Long-term behaviour of AISI 304L passive layer in chloride containing medium. *Electrochimica Acta*, 2006, **51**(8), pp.1881-1890.

189. *Bragg's Law* [online]. [Accessed 06-05-2013]. Available from: http://serc.carleton.edu/research_education/geochemsheets/BraggsLaw.html.
190. ELSENER, B., D. ADDARI, S. CORAY and A. ROSSI. Nickel-free manganese bearing stainless steel in alkaline media-Electrochemistry and surface chemistry. *Electrochimica Acta*, 2011, **56**(12), pp.4489-4497.
191. LEVY, A.V., N. JEE and P. YAU. Erosion of steels in coal-solvent slurries. *Wear*, 1987, **117**(2), pp.115-127.
192. LEVY, A.V. and P. YAU. Erosion of steels in liquid slurries. *Wear*, 1984, **98**, pp.163-182.
193. CLARK, H.M. The influence of the flow field in slurry erosion. *Wear*, 1992, **152**(2), pp.223-240.
194. HEIDEMEYER, J. Influence of the plastic deformation of metals during mixed friction on their chemical reaction rate. *Wear*, 1981, **66**(3), pp.379-387.
195. JIANG, J., M. STACK and A. NEVILLE. Modelling the tribo-corrosion interaction in aqueous sliding conditions. *Tribology International*, 2002, **35**(10), pp.669-679.
196. CHEN, J.F., E.F. RYBICKI and J.R. SHADLEY. Activation/repassivation behavior of 13Cr in CO2 and sand environments using a modified electrochemical noise technique. *In: NACE corrosion conference, Paper No. 02494*, Denver, Colorado. NACE International, 2002.
197. RINCON, H., J.R. SHADLEY and J.F. CHEN. Erosion corrosion phenomena of 13Cr alloy in flows containing sand particles. *In: NACE corrosion conference, Paper No. 02493*, Houston, Texas. NACE International, 2002.
198. LU, X.-C., T.-C. ZHANG, X.-X. JIANG and S.-Z. LI. Effect of g phase on corrosive wear of duplex stainless steel in sulfuric acid solution. *Corrosion*, 1995, **51**(06).
199. YAUN QING-LONG and M.M. STACK. Effect of preferential dissolution on erosion-corrosion for chromium steel in alkali slurry. *Trans.Nonferrous Met. Soc*, 2002, **12**(5), pp.931-935.
200. AL-HASHEM, A., P. CACERES, A. ABDULLAH and H. SHALABY. Cavitation corrosion of duplex stainless steel in seawater. *Corrosion*, 1997, **53**(2), pp.103-113.
201. KARAMAN, I., H. SEHITOGLU, Y.I. CHUMLYAKOV and H.J. MAIER. The deformation of low-stacking-fault-energy austenitic steels. *JOM*, 2002, **54**(7), pp.31-37.
202. SCHRAMM, R. and R. REED. Stacking fault energies of seven commercial austenitic stainless steels. *Metallurgical Transactions A*, 1975, **6**(7), pp.1345-1351.
203. MARSHALL, P. *Austenitic stainless steels: Microstructure and mechanical properties.* Springer, ISBN 0-85334-277-6, 1984.
204. RAVI KUMAR, B., MAHATO, B, AND SINGH R. Influence of cold worked structure on electrochemical properties of austenitic stainless steels. *Metallurgical and Materials Transactions A*, 2007, **38A**, pp.2085-2093.
205. KWOK, C.T., H.C. MAN and F.T. CHENG. Cavitation erosion of duplex and super duplex stainless steels. *Scripta Materialia*, 1998, **39**(9), pp.1229-1236.

206. CHUI, P., K. SUN, C. SUN, X. YANG and T. SHAN. Effect of surface nanocrystallization induced by fast multiple rotation rolling on hardness and corrosion behavior of 316L stainless steel. *Applied Surface Science*, 2011, **257**(15), pp.6787-6791.
207. NOVA´K, P. and A. MACENAUER. Erosion-corrosion of passive metals by solid particles. *Corrosion Science*, 1993, **35**(1–4), pp.635-640.
208. PITT, C.H., Y.M. CHANG, M.E. WADSWORTH and D. KOTLYAR. Laboratory abrasion and electrochemical test methods as a means of determining mechanism and rates of corrosion and wear in ball mills. *International Journal of Mineral Processing*, 1988, **22**(1–4), pp.361-380.
209. JIANG, X.X., S.Z. LI, D.D. TAO and J.X. YANG. Accelerative effect of wear on corrosion of high-alloy stainless steel. *Corrosion*, 1993, **49**(10), pp.836-841.
210. ITAGAKI, M., R. OLTRA, B. VUILLEMIN, M. KEDDAM and H. TAKENOUTI. Quantitative analysis of iron dissolution during repassivation of freshly generated metallic surfaces. *Journal of The Electrochemical Society*, 1997, **144**(1), pp.64-72.
211. HUMPHREY, J. Fundamentals of fluid motion in erosion by solid particle impact. *International Journal of Heat and Fluid Flow*, 1990, **11**(3), pp.170-195.
212. BROWN, G. Erosion prediction in slurry pipeline tee-junctions. *Applied mathematical modelling*, 2002, **26**(2), pp.155-170.
213. RAJAHRAM, S.S. *Erosion-corrosion mechanism of stainless steel UNS S31603*. PhD thesis, University of Southampton, 2010.
214. KIM, J.-D. and S.-I. PYUN. The effects of applied potential and chloride ion on the repassivation kinetics of pure iron. *Corrosion Science*, 1996, **38**(7), pp.1093-1102.
215. LAKATOS-VARSÁNYI, M., F. FALKENBERG and I. OLEFJORD. The influence of phosphate on repassivation of 304 stainless steel in neutral chloride solution. *Electrochimica Acta*, 1998, **43**(1), pp.187-197.
216. HUBSCHMID, C., D. LANDOLT and H.J. MATHIEU. XPS and AES analysis of passive films on Fe-25Cr-X (X = Mo, V, Si and Nb) model alloys. *Fresenius' Journal of Analytical Chemistry*, 1995, **353**(3-4), pp.234-239.
217. LANDOLT, D., S. MISCHLER, A. VOGEL and H. MATHIEU. Chloride ion effects on passive films on FeCr and FeCrMo studied by AES, XPS and SIMS. *Corrosion Science*, 1990, **31**, pp.431-440.
218. VIRTANEN, S., E. MOSER and H. BÖHNI. XPS studies on passive films on amorphous Fe-Cr-(B, P)-C alloys. *Corrosion Science*, 1994, **36**(2), pp.373-384.
219. LORANG, G., M.D.C. BELO, A. SIMOES and M. FERREIRA. Chemical composition of passive films on AISI 304 stainless steel. *Journal of The Electrochemical Society*, 1994, **141**(12), pp.3347-3356.
220. ELSENER, B., D. ADDARI, S. CORAY and A. ROSSI. Stainless steel reinforcing bars – reason for their high pitting corrosion resistance. *Materials and Corrosion*, 2011, **62**(2), pp.111-119.
221. ERNST, P. and R.C. NEWMAN. Pit growth studies in stainless steel foils. I. Introduction and pit growth kinetics. *Corrosion Science*, 2002, **44**(5), pp.927-941.

222. ERNST, P., N.J. LAYCOCK, M.H. MOAYED and R.C. NEWMAN. The mechanism of lacy cover formation in pitting. *Corrosion Science*, 1997, **39**(6), pp.1133-1136.
223. PISTORIUS, P. and G. BURSTEIN. Metastable pitting corrosion of stainless steel and the transition to stability. *Philosophical Transactions of the Royal Society of London. Series A: Physical and Engineering Sciences*, 1992, **341**(1662), pp.531-559.
224. BROWN, R., S. KOSCO and E.J. JUN. The effect of particle shape and size on erosion ofaluminum alloy 1100 at 90° impact angles. *Wear*, 1983, **88**(2), pp.181-193.
225. GUO, H., B. LU and J. LUO. Interaction of mechanical and electrochemical factors in erosion–corrosion of carbon steel. *Electrochimica Acta*, 2005, **51**(2), pp.315-323.
226. LI, Y., BURSTEIN G.T., HUTCHINGS I.M. The influence of corrosion on the erosion of aluminium by aqueous silica slurries. *Wear*, 1995, **186-187**, pp.515-522.
227. YIN, S. and D. LI. Effects of prior cold work on corrosion and corrosive wear of copper in HNO3 and NaCl solutions. *Materials Science and Engineering: A*, 2005, **394**(1), pp.266-276.
228. CHEN, J., J.R. SHADLEY and E.F. RYBICKI. Effect of temperature on the erosion-corrosion of 13Cr. *In: NACE corrosion conference, Paper No. 03320*. NACE International, 2003.
229. YIN, S., D. LI and R. BOUCHARD. Effects of the strain rate of prior deformation on the wear–corrosion synergy of carbon steel. *Wear*, 2007, **263**(1), pp.801-807.
230. LAPIDES, L. and A. LEVY. The halo effect in jet impingement solid particle erosion testing of ductile metals. *Wear*, 1980, **58**(2), pp.301-311.
231. HUTCHINGS, I. A model for the erosion of metals by spherical particles at normal incidence. *Wear*, 1981, **70**(3), pp.269-281.
232. GNANAVELU, A.B. *A geometry independent integrated method to predict erosion wear rates in a slurry environment*. PhD thesis, University of Leeds, 2010.